Journal of Networks

Contents

Special Issue: Transparent Optical Networking
Guest Editors: Carmen Mas Machuca and Norbert Hanik

Special Issue on Transparent Optical Networking

Guest Editorial

Transparent optical-fiber based transmission and networking with transmission capacity of Terabit/s per optical fibre have revolutionized modern telecommunications and consequently have influenced dramatically the working methods and everyday life of societies and individuals. The ongoing research and development efforts in this extremely innovative field are reflected in this Special Issue on *Transparent Optical Networking* which contains nine carefully selected papers based on the contributions to the 12th International Conference on Transparent Optical Networks ICTON 2010, Munich, Germany, June 27- July 1, 2010, www.itl.waw.pl/icton. ICTON is receiving technical co-sponsorship by the IEEE Photonics Society (formerly LEOS).
All papers in this Special Issue have been submitted by Editors' invitations.

   The first paper entitled *Design Considerations and Performance Comparison of High-Order Modulation Formats using OFDM* by A. Ali, J. Leibrich, and W. Rosenkranz, addresses OFDM transmission over optical links with high spectral efficiency. 32*10.7 Gb/s optical WDM-OFDM over 3200km SSMF with direct detection are achieved.

   The second paper on the *Dimensioning of Optical Codes in OCDM/WDM Optical Packet Switches* by V. Eramo, L. Piazzo, A. Germoni, A. Cianfrani, and M. Listani, investigates the performance of an Optical Code Division Multiplexing/Wavelength Division Multiplexing (WDM/OCDM) Optical Packet Switch when impairments due to both Multiple Access Interference and Beat noise are taken into account. A Packet Loss Probability of the OCDM/WDM switch of 10^{-9} is demonstrated when M=16 wavelengths, Gold code of length L=511 and only 24 wavelength converters are used in the switch.

   The third paper on the *Performance of Stereo Multiplexing in Single Channel and DWDM Systems Using Direct Detection with Optimum Dispersion maps* by O. Gaete, L. Coelho and B. Spinnler, compares the performance of Stereo Multiplexing, a novel technique that permits simultaneous direct detection of two modulated optical carriers, with single-carrier DQPSK and dual carrier DQPSK for single channel and DWDM transmission of 55.5 Gb/s through 1040 km of SMF. It is shown that the best performance and robustness is obtained by sharing the information between two carriers, Stereo being only 1dB below dual-carrier NRZ-DQPSK.

   The fourth paper on *Adaptive Data Rates for Flexible Transceivers in Optical networks* by B. Teipen, M. H. Eiselt, K. Grobe, J.-P. Elbers, discusses possibilities and advantages of reconfigurable and dynamically-adaptive transceivers, and their potential applications in future optical networks. These software-defined transceiver configurations support a set of specific modulation formats, with corresponding data rates and tolerances to system impairments, as well as sets of electronic digital signal processing schemes chosen to best function in a given network environment

   The fifth paper entitled *Optimization Framework for Supporting 40 Gbit/s and 100Gbit/s Services over Heterogeneous Optical Transport Networks* by J. Santos, J. Pedro, P. Monteiro, and J. Pires presents a novel hybrid optimization framework, which is based on an iterative combination of linear programming and rounding algorithms for the demand routing, with graph coloring heuristics for the wavelength assignment. The performance of this framework is assessed and compared with a similar approach that resorts to an integer linear programming (ILP) model to route the demands.

   The sixth paper entitled *Scalability Analysis of Optical Intrasystem Interconnects* by S. Aleksić and N. Ferhatović investigates requirements and limitations of large-scale optical interconnects. Various point-to-point interconnects and two optically switched interconnection options were studied with regard to their scalability by considering various impairments on the optical signal, required number of fiber links and power consumption.

   The seventh paper addresses *Heuristic Approaches for Periodic Reconfiguration of Lightpath-based Networks under Multi-hour Traffic*. Authors are R. Aparicio-Pardo, B. Garcia-Manrubia, N. Skorin-Kapov, and P. Pavon-Marino. This paper presents and compares two algorithms for planning a reconfigurable virtual topology suitable for exploring the trade-off between lower network costs obtained through better resource allocation and undesired traffic disruptions. The merits of both algorithms are assessed for moderate network sizes through comparison with analytical lower bounds and exact solutions obtained by a MILP formulation.

   The eighth paper entitled *Delay-Constrained Admission and Bandwidth Allocation for Long-Reach EPON* by B. Kantarci and H. T. Mouftah presents a delay-constrained admission control mechanism and adapts this scheme to a previously proposed bandwidth allocation technique, called Delay-Constrained Periodic GATE Optimization (DC-PGO). Through simulations it is shown that DC-PGO enhances the performance of multi-threaded polling in long-reach Ethernet PON when packets of differentiated service classes arrive with pre-specified delay requirements.

The ninth paper entitled *Energy Efficient Optical Networks with Minimized Non-renewable Power Consumption* by X. Dong, T. El-Gorashi and J. M. H. Elmirghani introduces a Linear Programming (LP) model and a novel heuristic to minimize the non-renewable power consumption in the "hybrid-power" IP over WDM network. The performance of the network is studied considering two topologies, the NSFNET and the USNET. Compared with routing in the electronic layer, the results show that routing in the optical layer coupled with using renewable energy significantly reduces the CO_2 emissions of the IP over WDM network by up to 73% for the NSFNET and 69% for the USNET.

Guest Editors:

Carmen Mas Machuca received the Dipl.-Ing. Degree in telecommunications engineering from the Universitat Politècnica de Catalunya (UPC), Spain in 1996 and the Dr.-Ing. Degree from the Swiss Federal Institute of Technology (EPFL), Switzerland in 2000 on "Fault Location Algorithms for Optical Networks". From 2000 to 2002, she was project coordinator at Intracom S.A., Greece, of several Eurescom and European projects. In 2002 she joined Athens Information Technology (AIT) Centre as researcher and in 2004 she became assistant professor. Since December 2005, she is senior researcher and member of the teaching staff at the Institute for Communication Networks at TUM. Her main research interests are in the area of optical networks and techno-economic studies. Dr. Mas Machuca has published more than 60 papers in scientific conferences and journals. She is member of several technical program committees such as ONDM, ICTON, ACP, etc. as well as chair of several workshops. She is a member of IEEE.

Norbert Hanik received the Dipl.-Ing. degree in electrical engineering from the Technische Universität München (TUM), with a thesis on Digital Spread Spectrum Systems. From 1989 to 1995 he was a research associate at the Institute for Telecommunications, TUM, where he worked in the field of Optical Communications. In 1995 he received the Dr.-Ing. degree with a thesis on Non-linear effects in Optical Signal Transmission. From 1995 to 2004 he was with the Technologiezentrum of Deutsche Telekom, heading the research group "System Concepts of Photonic Networks". From January to March 2002 he was engaged as a Visiting Professor at Research Center COM of Technical University of Denmark, Copenhagen. During his work Norbert Hanik contributed to a multitude of Telekom-internal, national and international R&D-projects, both as scientist and project leader. As of April 2004, Dr. Hanik holds an Associate Professorship at TUM in the field of wired and optical signal transmission. His primary research interests are in the fields of physical design and optimization of optical communication systems and networks.

Design Considerations and Performance Comparison of High-Order Modulation Formats using OFDM

Abdulamir Ali, Jochen Leibrich and Werner Rosenkranz
University of Kiel, Chair for Communications, Kaiserstr. 2, 24143 Kiel, Germany
Email: {aal, jol, wr}@tf.uni-kiel.de

Abstract— **This paper addresses OFDM transmission over optical links with high spectral efficiency, i.e. by using high-order QAM-modulation schemes as a mapping method prior to the OFDM multicarrier representation. Low and moderate cost optics which is mandatory in access and in metro applications is assumed. Here we address especially direct detection receivers using photo detectors without the need for local lasers at the transmitter side. In addition, we show 32×10.7 Gb/s optical WDM-OFDM over 3200km SSMF with direct detection.**

Index Terms— **optical communications, modulation, QAM, OFDM, direct detection, WDM.**

I. INTRODUCTION

Orthogonal Frequency Division Multiplexing (OFDM) is currently considered as an interesting alternative transmission scheme in optical communications [1-4]. This holds not only for long haul high-capacity networks, but also for the metro and even the access network. There are two strategies for transmitting the quasi-analogue OFDM signal over optical fiber. One solution is given by optical I-Q-modulation in conjunction with coherent detection (CO-OFDM) [2, 3]. A second method restricts to a real-valued OFDM signal transmitted with intensity modulation and direct detection and is called optical DD-OFDM [1]. The latter requires substantially less complexity in the optical domain and in this paper the focus is thus put on this scheme. OFDM offers a simple possibility to adapt the modulation format to various channel conditions as both transmitter and receiver are basically software defined, i.e. digital signal processing is employed. A high-order modulation format, as e.g. 64-QAM, would result in a high spectral efficiency and is thus efficient in terms of bandwidth. However the noise performance is poor. Vice versa, we achieve high noise resistance if we allow for more bandwidth as e.g. with binary PSK-modulation. Therefore the well known principle in communications, namely the possibility to exchange noise performance against bandwidth is nicely implemented in a practical system.

The paper investigates square QAM modulation constellations from 4-QAM up to 64-QAM. We start with a description of the DD-OFDM system setup. Results are given for the Peak-to-Average Power Ratio (PAPR) and

for the impact of the drive conditions of the Mach-Zehnder modulator (MZM) on the system performance. A complete investigation on the sensitivity for the various number of modulation levels is given. Also, we investigate the system in a dispersive transmission scenario based on an optimized system design. As an extension to our previous work [5], the fiber nonlinearity effect on the system performance has been investigated for a specific modulation format, 4-QAM, in Wavelength-Division-Multiplexing (WDM) optical OFDM transmission and experimental results are presented for 4 and 16-QAM modulation formats.

II. OPTICAL-OFDM SYSTEM

Optical-OFDM is based on electronic signal processing before the optical modulator and after the photo-detector. The modulation and demodulation processes are performed in the electrical domain, and the optical components are used just for converting the electrical OFDM signal into an optical signal at the transmitter for transmission through an optical fiber and for converting the received optical signal back into the electrical domain at the receiver. This has a big advantage because the microwave devices are much more mature than their optical counterparts. The schematic diagram of an optical-OFDM is shown in Fig. 1.
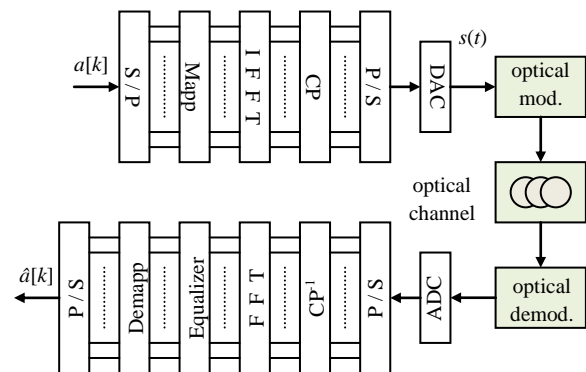

Figure 1. Schematic diagram of optical-OFDM system.

In this paper, direct detection optical-OFDM (DD-OFDM) is considered. The main requirements for a DD-OFDM system are:

- *Bias*: to generate the carrier (DC) required for DD, because an electrical OFDM time signal is quasi-analog with zero mean.
- *Frequency gap (W_g)*: the OFDM signal spectrum (B_{ofdm}) is displaced by a frequency gap from the optical carrier to ensure that the second order inter-modulation distortion (IMD), due to the photo-detector, fall outside the signal spectrum.
- *SSB transmission*: to avoid the power null fading due to the chromatic dispersion and to enable a powerful and simple equalization method.

III. SIMULATION RESULTS

The general DD-OFDM system setup is shown in Fig. 2. The real valued, up-converted to f_{Rf} OFDM signal is generated by using a complex conjugate extension and appropriate zero padding for the input to IFFT [6]. This can also be achieved by using an electrical I-Q modulator. The resulting signal has to be biased for driving an external optical MZM in order to achieve sufficient carrier power for direct detection. A Single-Side-Band (SSB) optical filter is used to transmit only one sideband together with the optical carrier. The optical transmission line consists of spans of 80 km of Standard Single-Mode Fiber (SSMF) without Dispersion Compensating Fiber (DCF). Span loss is compensated for by means of inline optical amplifiers. For the receiver, a variable optical attenuator (VOA) in front of the optical preamplifier, (Erbium Doped Fiber Amplifier, EDFA), allows for OSNR tuning. OFDM demodulation is performed including removing of cyclic prefix (CP^{-1}), Serial-to-Parallel (S/P) conversion, FFT, post detection OFDM equalization, symbol de-mapping and parallel-to-serial conversion (P/S) (see Fig. 1).
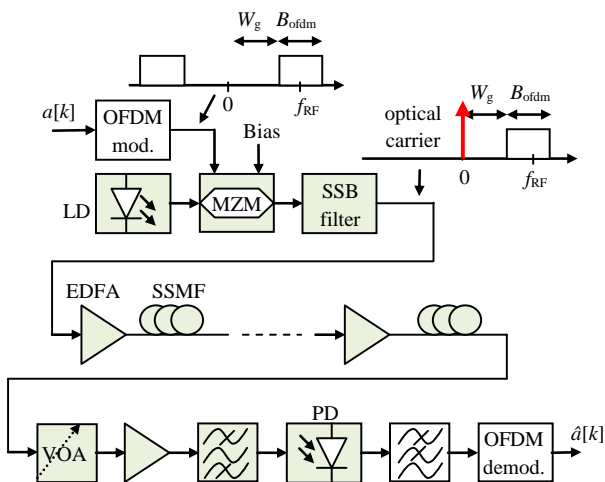

Figure 2. DD-OFDM system setup.

A Baud rate of 5.35GBaud/s including 7% overhead for Forward Error Correction (FEC) is used as this is compatible with existing component technology. The received raw Baud rate after FEC decoding and removing of cyclic prefix is 5 GBaud/s . In our investigation we examine the system performance with different modulation formats but with the same Baud rate, i.e.

bitrates vary between 10 Gbit/s (4-QAM) and 30 Gbit/s (64-QAM).

A. Peak-to-Average Power Ratio (PAPR)

An OFDM signal consists of a number of independently modulated subcarriers, which can give a large PAPR when added up coherently [7]. As a result, the DAC, ADC, amplifiers and optical modulators like MZM need to have large dynamic range, which leads to an inefficiency of power and cost.

The PAPR of the transmitted signal can be calculated by interpolating the IFFT output at least by a factor of 4 (i.e. oversampling factor=4). It also is advantageous to examine the PAPR behavior for different modulation formats. Simulation is carried out for different modulation formats and number of subcarriers (N). Fig. 3 shows the PAPR distribution results for 100,000 OFDM symbols with 8-times oversampling, where the probability that PAPR exceeds a specific threshold value PAPR$_{TH}$ is plotted. Obviously, for a given number of subcarriers, the PAPR behavior is the same for different modulation formats, however is strongly dependent on N.
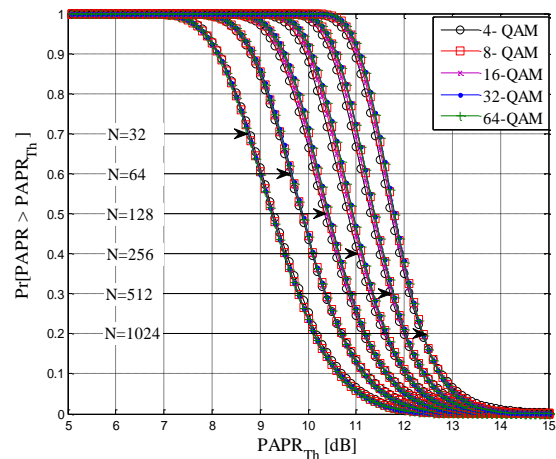
Figure 3. PAPR distribution for different modulation formats and different number of subcarriers.

B. MZM Nonlinearity (B2B Transmission)

The sensitivity of an OFDM signal to MZM nonlinearity for different modulation levels is examined next. The simulation parameters are: N=512, relative CP=1/8 of OFDM symbol duration, Baud rate of 5.35GBaud/s, carrier to single sideband power ratio (PR)=1 for each modulation format to achieve optimum receiver sensitivity [8].

Fig. 4(a) shows the simulation results, where the required OSNR at BER=10^{-3} is plotted for different modulation formats and different Optical Modulation Indexes (OMI), which is defined as the standard deviation of the OFDM driving signal σ_s divided by the switching voltage V_π. From Fig. 4(a) we can see that the effect of the nonlinearity of the MZM is very severe for higher levels M of modulation formats. This could be attributed to the increased influence of the neighbor symbols. Therefore, in order to avoid these nonlinear distortions, suitable driving amplitude has to be chosen for each

modulation format. Fig. 4(b) shows the received constellations for different modulation formats and different OSNR at BER≈10^{-3}.

(a)

(b)
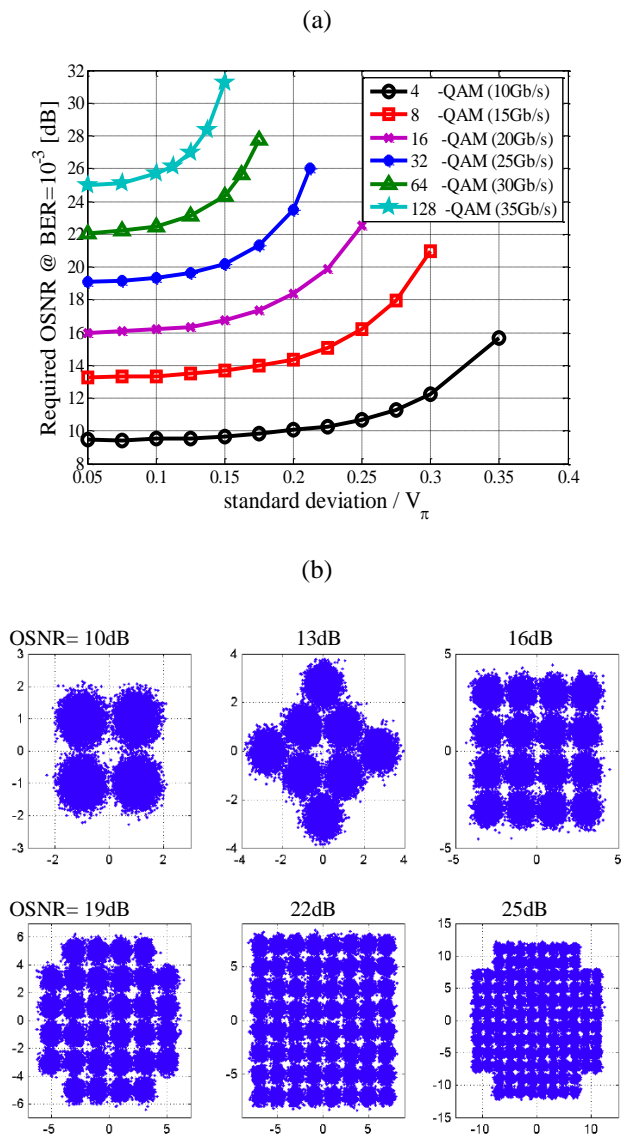
Figure 4. Impact of MZM nonlinearity (a). Received constellations for different OSNR and modulation formats at BER≈10^{-3}(b).

C. Receiver Sensitivity (B2B Transmission)

The noise performance of the system in terms of receiver sensitivity is investigated for different modulation formats. The simulation parameters are the same as in sec. 3.2, except that an OMI is set to 0.1 to avoid the MZM nonlinearity.

The sensitivity penalties for different modulation formats compared to 4-QAM are calculated to make a comparison with the simulation results. For example, doubling the bandwidth efficiency by doubling the digital modulation format from 4-QAM to 16-QAM results in a mean power of $5d^2/2$ per symbol compared to $d^2/2$ for 4-QAM, where d is equal to the minimum Euclidian distance between two symbols. Using the approximation that the BER only depends on d when comparing several formats, a factor of 5 (≡7dB) higher signal-to-noise ratio is required to achieve the same BER compared to 3 dB

increase in data throughput [9]. Fig. 5(a) shows approximate penalties compared to 4-QAM for several modulation formats. Fig. 5(b) shows the simulation results for the receiver sensitivity. For the same BER (e.g. BER=10^{-3}), doubling the constellation size from 4-QAM to 16-QAM requires 7dB higher OSNR, 3dB for doubling the data throughput and 4dB sensitivity penalty which confirms the calculation results in Fig. 5(a).

(a)

(b)
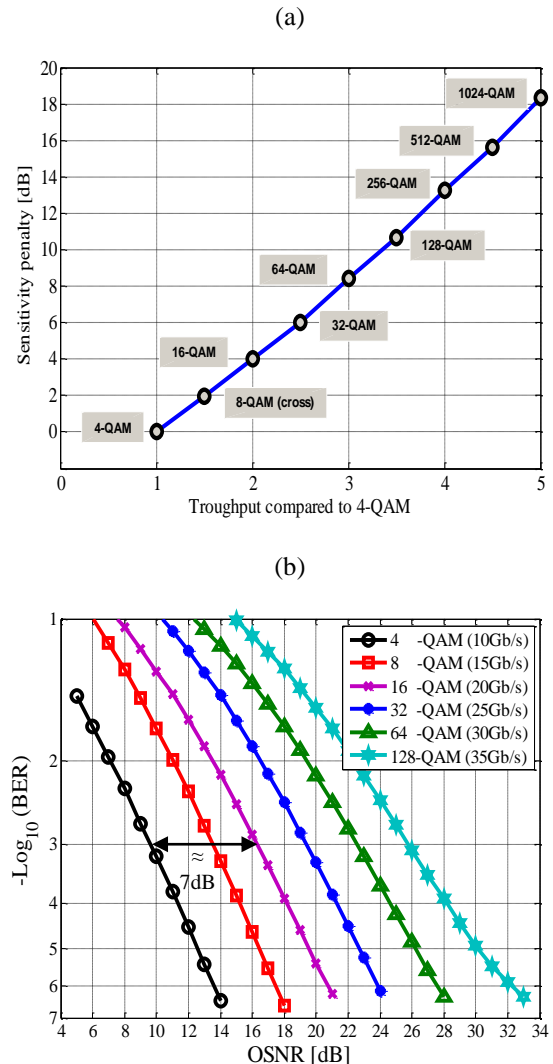
Figure 5. Sensitivity penalty for different modulation formats (a). Receiver sensitivity for different modulation formats (b).

D. Chromatic Dispersion

The benefit of the cyclic prefix (CP) in OFDM, to minimize the chromatic dispersion induced inter-symbol-interference (ISI), is examined here. Linear fiber model is considered with chromatic dispersion of 17 ps/nm/km. The number of subcarriers used here is N=512, the SSB and ASE optical filters are Gaussian filters of 5th order and each of 15GHz FWHM bandwidth. The electrical filter after the photodiode is a 5th order Butterworth filter with 3dB cutoff frequency of 15GHz. The net Baud rate for each modulation format after extracting the CP and FEC overhead is 5GBaud/s (i.e. 10, 15, 20, 25 and 30Gb/s for 4, 8, 16, 32 and 64-QAM respectively).

Fig. 6 shows the results for the maximum reach that can be obtained for all M-QAM when the relative CP=1/8. It is obvious from Fig. 6 that transmission is possible up to 12000km for all cases. This is an optimized result, after optimization of the synchronization, compared to the results of our previous work [5]. Longer transmission reach can be obtained by increasing the cyclic prefix.
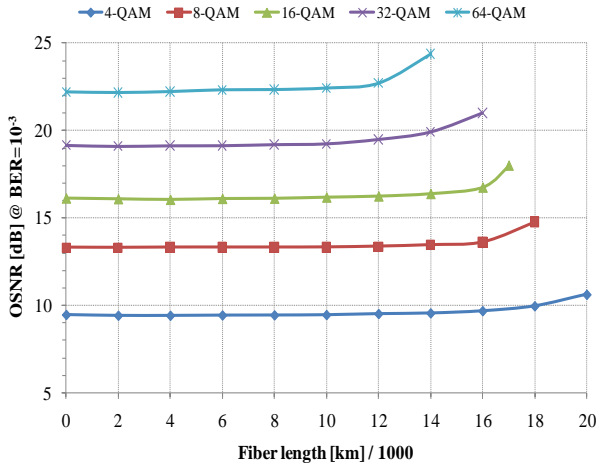
Figure 6. Required OSNR at BER=10^{-3} vs. fiber length for relative CP=1/8.

D. Fiber Nonlinearity

Simulation was carried out also to investigate the effect of fiber nonlinearity, impact of input optical power and number of WDM channels are treated here. In a single channel transmission, the main nonlinear effect is Self-Phase-Modulation (SPM) while in WDM transmission, the main additional limiting factors are Cross-Phase-Modulation (XPM) and Four-Wave-Mixing (FWM).

In out setup according to Fig. 2, up to 32 channels (each of 10.7Gb/s and 512 QPSK-modulated subcarriers) are combined using optical multiplexer (OPTMUX) to generate a WDM-SSB-OFDM comb with a channel spacing of 20GHz. The OMI is set to 0.1 to minimize the effect of MZM nonlinearity and the PR is set to one for optimum receiver sensitivity.

The fiber link consists of 80-km spans of 17 ps/nm/km dispersion fiber with 0.2 dB/km loss, a nonlinear refractive index of 3.2×10^{-20} m^2/W and A_{eff} of 8×10^{-11}m^2. The loss of each span is compensated with an optical amplifier with a noise figure of 5 dB. The Amplified Spontaneous Emission (ASE) noise is included also in the inline optical amplifiers to consider the mixing of the noise with the signals due to fiber nonlinearity. The WDM channels were demultiplexed using a 15-GHz FWHM bandwidth Gaussian optical filter. The performance of a transmission system is specified in terms of the Q-value. The q-factor was calculated as $q^2 = |\mu|^2/\sigma^2$, where μ and σ^2 are the mean-value and variance of a particular cluster with $\mu = \mu_R + j\mu_I$, and Q is defined as $Q_{(dB)} = 20 \cdot \log_{10}(q)$, The bit error ratio (BER) [10] can be estimated using $0.5 \text{erfc}(q/\sqrt{2})$. For simulations with

multiple WDM channels, q was averaged in a linear scale over all channels.

The simulation result for a single channel is shown in Fig. 7 where the system Q-value is plotted versus the input power. It can be seen that, for low optical power the system is limited by ASE noise, while for high input power the system is limited by nonlinear effects. In the noise limit regime, The Q-value increases by 1dB as the input power increased by 1dBm, while in the nonlinear limit regime, the Q-value decreases by 2dB as the input power increases by 1dBm. Also, for each system length, there is an optimum input power (for which a maximum system Q-value is achieved) which decreases slightly with the system length. Therefore, for a given system setup, transmission performance is optimized by realizing a compromise between noise limit and nonlinear limit given by the optimal input power.
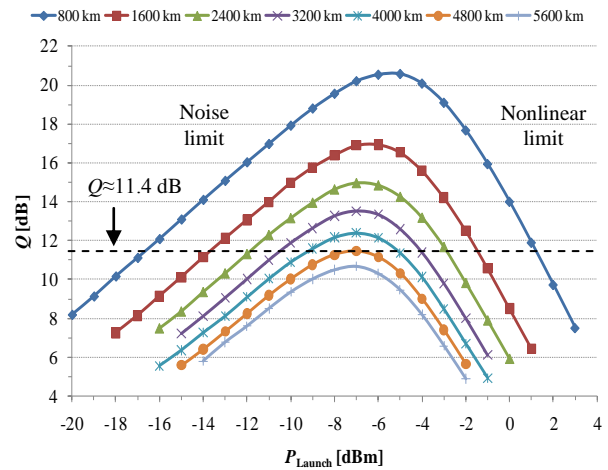
Figure 7. System Q-value versus optical input power for single channel and different fiber lengths.
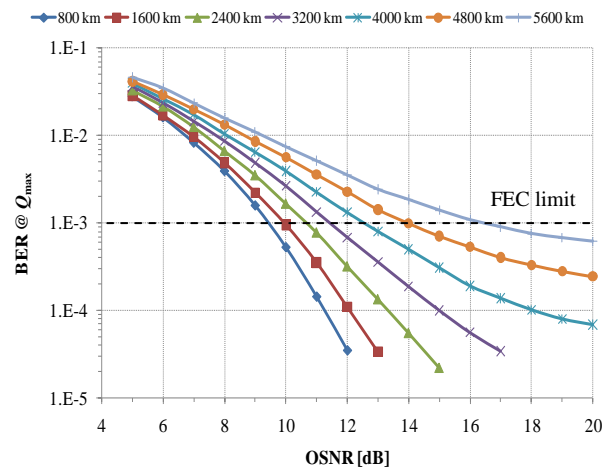

Figure 8. Receiver sensitivity at maximum Q-value for different fiber lengths.

Fig. 8 shows the BER curve versus OSNR for different fiber lengths at optimal input optical power (i.e. at maximum system Q-value) for each distance. For long distances (like 4800km and 5600km), an error floor emerges owing to fiber nonlinearity and chromatic

dispersion after exhaustion of the cyclic prefix. Transmission is possible up to 5600km at which the required OSNR at BER=10^{-3} is $\approx$ 16dB.

Simulation for WDM-OFDM was already carried out in [11] with an assumption of linearized optical modulator (MZM). In our simulation the MZM nonlinearity is also included to make our system more realistic. The plot of the system Q-value versus the optical input power per channel for 8-WDM channels is shown in Fig. 9. The optimal input power (for maximum Q-value) is decreased in 8-WDM system compared with the optimum input power in a single channel.
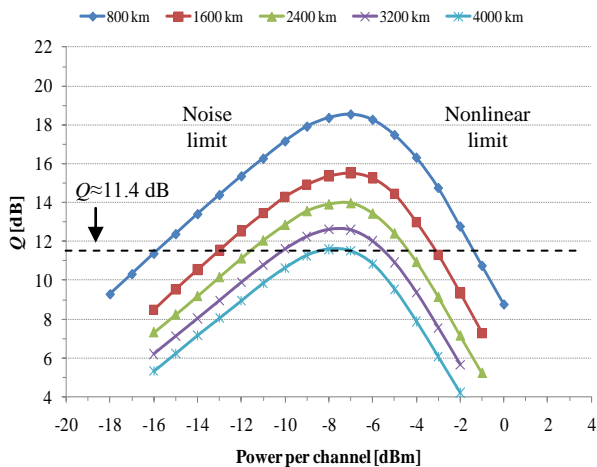
Figure 9. System Q-value versus input power per channel for 8-WDM channels and different fiber lengths.

To determine the Non-Linear Threshold (NLT) of our system, the maximum power (nonlinear limit) and minimum power (noise limit) per channel that gave $Q \approx 11.4$ dB (which corresponds to BER$\approx 10^{-4}$) are plotted against the system length for different numbers of WDM channels in Fig. 10.
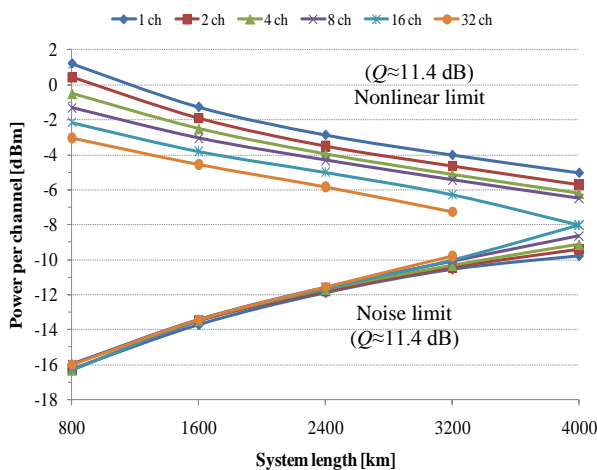
Figure 10. Power per channel vs. system length for different numbers of WDM channels.

In the noise limit regime, it is obvious that increasing the number of WDM channels has no effect on the noise limit, except when the NLT is approached, while in the

nonlinear limit regime, the nonlinear limit decreases with increasing the number of WDM channels and reduces approximately 2 dB with each doubling of the system length. For system length of 4000km with 32 WDM channels $Q \approx 11.4$ dB could not be achieved.

The influence of the number of WDM channels has been investigated, too. Fig. 11 plots the maximum Q-value (for an optimum input power) versus number of WDM channels for each fiber length. For small number of channels, the impact of nonlinearity is strong and the Q falls rapidly, while when increasing the number of channels, the decrement of the Q-value is less rapid, because the impact of nonlinearity is reduced for the outer channels.
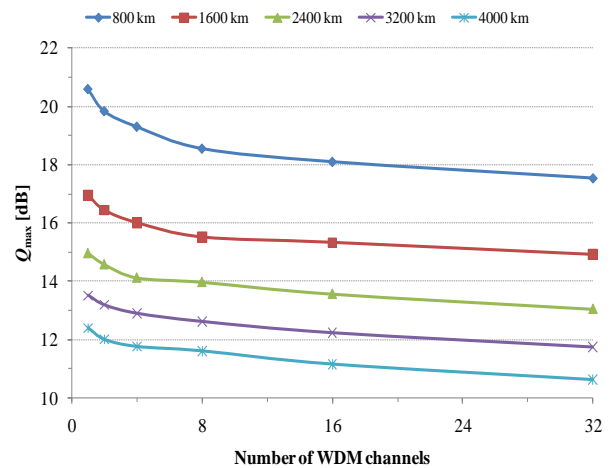
Figure 11. Q_{max} vs. number of WDM channels for different system lengths.

IV. EXPERIMENTAL RESULTS

The experimental system setup is the same as Fig. 2. The real valued OFDM signal is generated offline in MATLAB with the following parameters; number of subcarriers N=256, FFT size is 2048 and CP=1/8 of the useful OFDM symbol duration. The OFDM signal, which occupies the frequency range from 2.5 to 5 GHz, is displaced by frequency gap W_g=2.5 GHz for the reason mentioned previously. The signal is then downloaded to an arbitrary waveform generator (AWG7102) which is used in an interleaved mode to give a sampling rate of 20 GS/s. The resolution of the digital-to-analog converter of the AWG is 8 bits. The nominal baud rate is then 2.5GBaud/s. The output signal from the AWG is then amplified to drive the single drive MZM. For SSB transmission, a tunable optical filter (0.2 nm) is used to suppress one sideband and the signal is then boosted with an optical amplifier.

At the receiver, the signal is preamplified, a fiber Bragg Grating (0.2 nm FWHM) is used as an ASE filter and the optical signal is detected by 12GHz photoreceiver. The received data is captured using digital sampling oscilloscope (Tektronix DPO72004) of 50GS/s. A post processing is performed offline in MATLAB including up/down sampling, synchronization and OFDM demodulation and equalization.
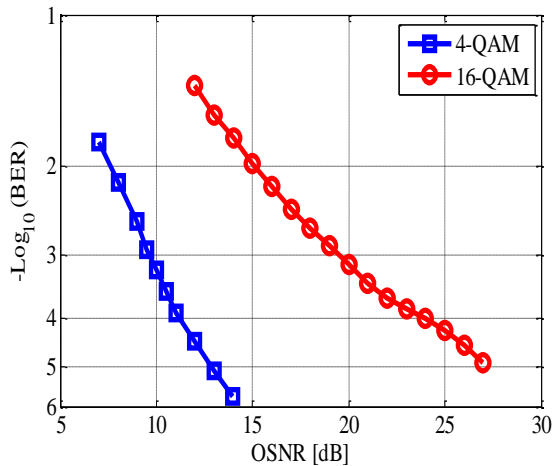
Figure 12. Receiver sensitivity of 4 and 16-QAM for B2B.

1000 OFDM symbols were transmitted. 4 and 16-QAM modulation formats were considered here. The OSNR was measured within 0.1 nm resolution bandwidth.

Fig. 12 shows the results for B2B transmission where the BER curves are plotes versus OSNR. It can be seen from Fig. 12 that at BER=10^{-3}, the required OSNRs are ~ 9.5dB and 19.5dB for 4-QAM and 16-QAM respectively, that is the OSNR penalty is ~10dB when we move from 4 to 16-QAM, which is 3dB more compared to the simulation results (see Fig. 5). This can be attributed to the impacts of DAC filtering (suppression of high frequency subcarriers) and MZM nonlinearity. These impacts become high as the modulation level increases, and as a result more 3dB OSNR is required. Fig. 13 shows the results after 100km transmission. It is obvious that no OSNR penalty is obtained compared with B2B transmission.
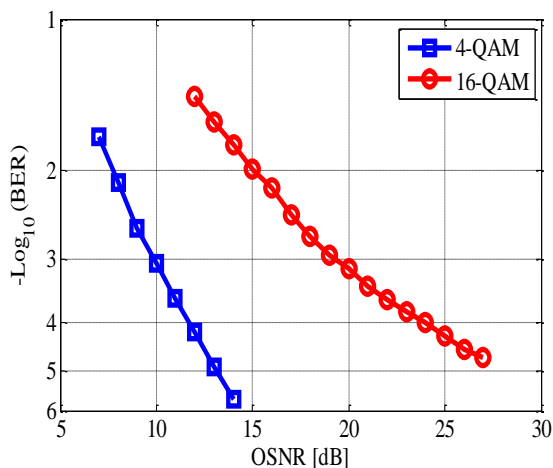
Figure 13. Receiver sensitivity of 4 and 16-QAM after 100km SMF transmission.

VI. CONCLUSIONS

We demonstrate and investigate the behavior of DD-OFDM with different high-order modulation formats, ranging from 4-QAM up to 64-QAM. The investigations are based on the assumption that the optical and electronic devices are all 10 Gbit/s equipment irrespective of the modulation level. Thus we automatically increase the bitrate up to a factor of three without requesting more bandwidth or higher speed components. From the given results one can estimate the OSNR-requirements for all those constellations. We observe roughly a 3-dB degradation per doubling of the constellation size. Moreover, we investigate the impact of fiber nonlinearity for 4-QAM modulation format in long-haul WDM-OFDM transmission with direct detection. Transmission of 32×10.7 Gb/s over 3200km SSMF is possible. Finally, experimental results for 4-QAM and 16-QAM are demonstrated.

REFERENCES

[1]   A. Lowery and J. Armstrong, "Adaptation of orthogonal frequency division multiplexing (OFDM) to compensate impairments in optical transmission systems," *ECOC*, vol. 2, pp. 121-152, 2007.

[2]   S. Jansen, I. Morita, H. Tanaka, "10x121.9-Gb/s PDM-OFDM transmission with 2-b/s/Hz spectral efficiency over 1,000 km of SSMF," *OFC*, paper PDP2, 2008.

[3]   Q. Yang, Y. Ma, W. Shieh, "107 Gb/s coherent optical OFDM reception using orthogonal band multiplexing," *OFC*, paper PDP7, 2008.

[4]   I. B. Djordjevic and B. Vasic, "Orthogonal frequency division multiplexing for high-speed optical transmission, " *Optics Express*, vol. 14, no. 9, pp. 3767-3775, May 2006.

[5]   W. Rosenkranz, A. Ali and J. Leibrich, "Design Considerations and Performance Comparison of High-Order Modulation Formats using OFDM, " *ICTON* Munich, Germany, Invited paper Tu.D1.3, 2010.

[6]   A. Ali, J. Leibrich and W. Rosenkranz, "Impact of Nonlinearities on Optical OFDM with Direct Detection, " *ECOC*, Paper P095, 2007.

[7]   R. V. Nee and R. Prasad, *OFDM for Wireless Multimedia Communications*, Artech House, Boston . London, 2000.

[8]   A. Ali, J. Leibrich and W. Rosenkranz, "Spectral Efficiency and Receiver Sensitivity in Direct Detection Optical-OFDM, " *OFC,* San Diego, USA, Paper OMT7, 2009.

[9]   J. Leibrich, A. Ali and W. Rosenkranz, "Single Polarization Direct Detection Optical OFDM with 100 Gb/s Throughput: A Concept Taking into Account Higher Order Modulation Formats, " *SPPCom*, Karlsruhe, Germany, paper SPThC4, 2010.

[10] A. J. Lowery, L. B. Du and J. Armstrong, "Orthogonal Frequency Division multiplexing for Adaptive Dispersion Compensation in Long Haul WDM Systems, " *OFC*, paper PDP39, 2006.

[11] A. Lowery, L. B. Du and J. Armstrong, "Performance of Optical OFDM in Ultralong-Haul WDM Lightwave Systems, " *Journal of Lightwave Technology*, Vol. 25, No. 1, Jan. 2007.

Abdulamir Ali was born in Babel, Iraq. He received the B.Sc degree from the University of Technology, Iraq, in Electronics and communications engineering and M.Sc. degree in digital communications from Christian-Albrechts-Universität zu Kiel, Germany, in 2006. He is currently working toward the Ph.D degree at the chair for communications. His research interest is Optical-Orthogonal Frequency Division Multiplexing with Direct-Detection (DD-OFDM).

Jochen Leibrich (S'01-M'07) received the Dipl.-Ing. degree from Technische Universität Darmstadt, Germany in 1998 and the Dr.-Ing degree from Christian-Albrechts-Universität zu Kiel, Germany, in 2007. His main research focus was in the area of modeling and simulation of optical transmission systems as well as on modulation formats with high spectral efficiency. Since 2007 he holds a position as Senior Researcher at the Chair for Communications, Christian-Albrechts-Universität zu Kiel, where he is primarily engaged in orthogonal frequency-division multiplexing and digital signal processing for high-speed data transmission.

Werner Rosenkranz studied Electrical Engineering at University of Erlangen-Nürnberg, Erlangen, Germany. There he received the Ph.D. and the Habilitation at the Lehrstuhl für Nachrichtentechnik. He worked on Phase-locked Loops, digital FM-systems, and Digital Signal Processing. In 1989 he joined Philips Kommunikations Industrie / Lucent Technologies in Nürnberg, Germany, where he was responsible for a transmission research group in the basic development lab, working on the development of wireless and optical communication transceivers. As a full Professor for the Chair of Communications at the University of Kiel, Kiel, Germany since 1997, he is leading a research group in the field of fiber optic transmission. As a project leader he is/was responsible for numerous research and development projects with co-operation partners from industry, with German Science Foundation, European Commission, and government funded projects. Werner Rosenkranz is a member of the IEEE, OSA and VDE. He serves in the ITG-VDE committee "Optical Communications". He has authored and co-authored over 180 book chapters, journal and conference papers. He holds currently 14 patents. He serves as a referee for several IEEE journals and he is/was a member of the Technical Program Committee in various international conferences such as OFC and ECOC. He is currently the General Co-chair for the 2011 SPPCom (Signal Processing in Photonic Communications) organized within the OSA Optics & Photonics Congress.

Dimensioning of Optical Codes in OCDM/WDM Optical Packet Switches

V. Eramo, L. Piazzo, A. Germoni*, A. Cianfrani, , M. Listanti

DIET, Sapienza University of Roma, Via Eudossiana 18 - 00184 Rome, Italy

*Co.Ri.Tel., Via Cavour 256 - 00184 Rome, Italy

Email: Vincenzo.Eramo@uniroma1.it

Abstract— **In this paper we investigate the performance of an Optical Code Division Multiplexing/Wavelength Division Multiplexing (WDM/OCDM) Optical Packet Switch when impairment due to both Multiple Access Interference and Beat noise are taken into account. Analytical models are introduced to dimension the switch resources, in particular the number of optical codes carried on each wavelength. The Packet Loss Probability due to output packet contentions is evaluated as a function of the main switch and traffic parameters when Gold coherent optical codes are adopted. The Packet Loss Probability of the OCDM/WDM switch can reach 10^{-9} when M=16 wavelengths, Gold code of length L=511 and only 24 wavelength converters are used in the switch.**

Index Terms— **Bufferless Optical Packet Switch, Wavelength Conversion, Optical Code Division Multiplexing Performance Evaluation.**

I. INTRODUCTION

The switching speed of Internet router directly impacts the performance of the entire network. To improve switching speed and the bandwidth utilization, all-optical routers such as multiprotocol MPλS, Optical Packet Switching (OPS) and so on are proposed [1]–[5] to avoid the electricity switching bottleneck. MPλS [3] uses a wavelength as an optical channel in the router, but the capacity granularity MPλS may sometimes be too large to accommodate the traffic between node pairs. In the OPS [6]–[8], the label is attached to the head of a packet and routing of packets is based on label switching. The throughput is restricted because the packets are carried in serial on the same wavelength. Optical Code Division Multiplexing (OCDM) paths were proposed in [9]–[11] where each bit in the packet, including the header is encoded by a specific optical code. The OCDM paths can overlap with each other and that enables the router to process packets in parallel. To achieve satisfactory performance in the OCDM system, coherent time-spread optical-Code (OC) generation and recognition based upon

Superstructure Fiber Bragg Gratings (SSFBG) using the gold code is employed [12]–[16]. The combination of OC- and wavelength-based routing has been presented in [9] where it is shown that the joint use of WDM/OCDM improves the efficiency of bandwidth utilization and obtains high flexibility in providing stable service owing to its independence of burst duration time and a simple architecture with nonbuffer operation.

In this paper we propose an analytical model, validated by simulation, to dimension the Optical Codes on any wavelength of a WDM/OCDM system so that the Packet Loss Probability due to both Multiple Access Interference (MAI) and beat noise is limited to a given threshold value. Next we evaluate the performance of a bufferless WDM/OCDM switch [17] using Gold Optical Codes dimensioned according to the proposed analytical model. The output packet contentions in the switch are solved in both the code and wavelength domains.

The organization of the paper is as follows. In Section 2 we describe the WDM/OCDM switch in question. The analytical model introduced to dimension the Optical Codes is introduced in Section 3. We discuss the effectiveness of the WDM/OCDM technique in solving output packet contentions in Section 4. Our main conclusions and further research topics are discussed in Section 5.

II. WDM/OCDM OPTICAL PACKET SWITCH ARCHITECTURE

We consider the WDM/OCDM optical packet switch with N Input/Output fibers (IF/OF) reported in Fig. 1. Each fiber supports M wavelengths denoted $\lambda_1, \cdots, \lambda_M$. On each wavelength up to F packets are carried out by using Optical Code Division Multiplexing. Let L be the code length and $\{OC_k, k = 1, \ldots, F\}$ the set of Optical Codes (OC) of a wavelength on which the packets can be carried. An input (or output) channel is identified by the triple (i, λ_j, OC_k), where i $(i = 1, \cdots, N)$ identifies one of the input (or output) fibers, λ_j $(j = 1, \cdots, M)$ identifies one of the wavelengths on that IF (OF) and OC_k $(k = 1, \cdots, F)$ identifies one of the optical codes on that wavelength.

The operation mode of the architecture is synchronous, meaning that all arriving packets have a fixed size and their arrival on each input channel is synchronized on a time-slot basis. The synchronization operation, not shown
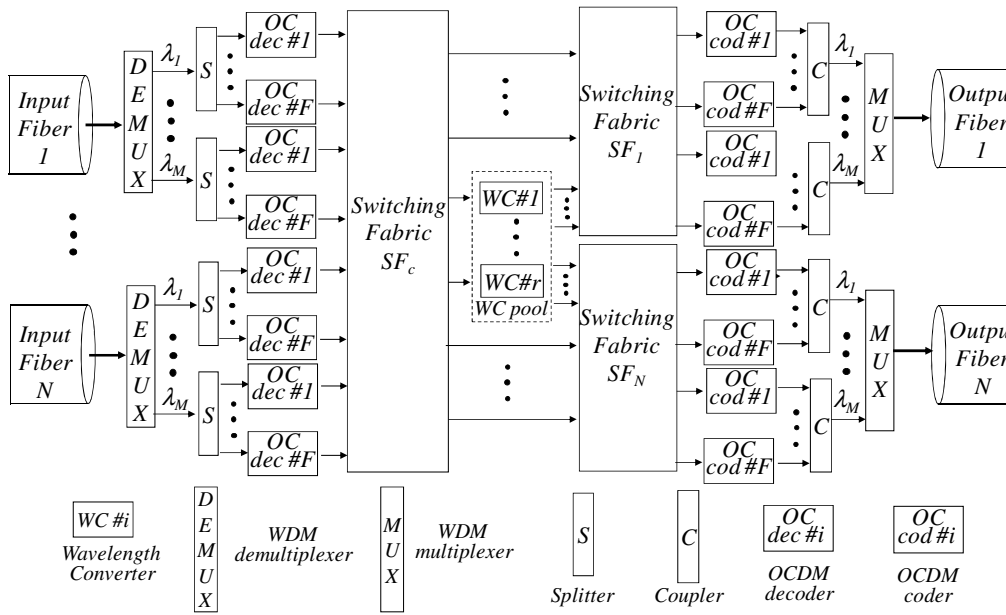
Figure 1. WDM/OCDM Optical Packet Switch.

in Fig. 1, is realized by means of synchronizers located at the ingress of the switch.

The WDM/OCDM optical packet switch illustrated in Fig. 1 performs the following operations: i) the packets are wavelength demultiplexed and code decoded by means of one WDM demultiplexer and $M \cdot F$ OC decoders for each IF; ii) the unit control, not shown in Fig. 1, processes the packet headers and decides which packets have to be wavelength converted and which Output Wavelength Channels (OWC) and Output Optical Codes (OOC) are assigned to the packets to transmit; iii) the Switching Fabric SF_c routes the packets towards either the bank of r Wavelength Converters (WC) or the Output Switching Fabrics SF_i $(i = 1, \cdots, N)$ according to decisions taken by the control unit; iv) the converted packets are routed towards the SF_i $(i = 1, \cdots, N)$ where in output the packets are code and wavelength multiplexed by means of $M \cdot F$ OC coders and one WDM multiplexer.

One of the advantages of the proposed OPS is to reduce the number of WCs used because the control algorithm [18] first tries to solve the contention in code domain by changing the packet code and only if this operation is unsuccessful, the contention is solved in wavelength domain by using one WC of the shared pool. This strategy, preferring the use of passive devices like OC decoders and coders rather than active elements like WCs, allows for the reduction of the switch cost.

III. ANALYTICAL MODEL FOR THE DIMENSIONING OF OPTICAL CODES

We propose an analytical model to dimension the number F of codes so that the Packet Loss Probability P_{loss}^{noise} due to both Multiple Access Interference (MAI) and beat noise on each wavelength is limited to a given

threshold value. In the proposed analytical model, P_{loss}^{noise} is evaluated as a function of the following traffic and switch parameters: i) N is the number of IF/OF; ii) M is the number of wavelengths; iii) F is the number of codes carried on each wavelength; iv) p is the offered traffic offered to each input channel; v) L is the code length; vi) H is the packet length. In particular the evaluation of P_{loss}^{noise} for a target user has been carried out under the assumptions that coherent OCDM techniques are considered and the coding is based upon optical amplitude, where each chip in a code sequence can have a phase 0 or π with a Binary-Phase-Shift-Keying (BPSK) scheme [16]. Gold Codes are assumed that leads to a maximum number of codes equal to $L+2$ [19]. We also assume that users tranmsit bit '0' and '1' with equal probability $\frac{1}{2}$.

Due to the synchronous operation mode of the switch, we can express P_{loss}^{noise} by conditioning to the number i of packets arriving on any input wavelength [18]. We obtain the following expression:

$$P_{loss}^{noise} = \sum_{i=2}^{F} \binom{F}{i} p^i (1-p)^{F-i} \left(1 - (1 - P_{E,i})^H \right).$$
(1)

where $P_{E,i}$ is the probability that a bit transmitted by a target user is corrupted for MAI and beat noise when i packets are arriving on any input wavelength. Its expression is given by Eq. (2) reported at page 3 where $P_{E,i,h}^{'target'}$ is the probability that a bit transmitted by a target user is corrupted by MAI and beat noise when exactly h interfering users transmit bit '1'.

To evaluate $P_{E,i,h}^{'target'}$ we report the receiver model of a target user in Fig. 2 [16], [20]. Three different kinds of noise sources should be taken into account: MAI noise

$$P_{E,i} = \begin{cases} 0 & i = 0,1 \\ \left(\frac{1}{2}\right)^{i-1} \sum_{h=0}^{i-1} \binom{i-1}{h} P'^{target'}_{E,i,h} & i = 2, \cdots, F \end{cases} \quad (2)$$

arising from the network, beat noise at the detector and electrical receiver noise (thermal and shot noise). The bandwidth of the receiver is limited to the chip rate and thus is equivalent to an integration over one-chip interval and a thresholder. In this paper, we will focus on MAI
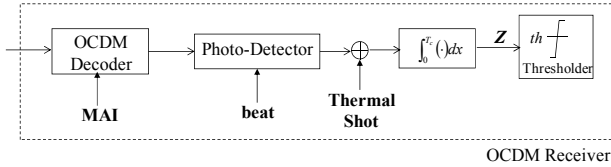

Figure 2. OCDM Receiver model and noise sources.

and beat (both Primary and Secondary) noise, which are the two most important performance limitations. Other receiver noises such as shot and thermal noise will be discussed in succeeding paper. In this case, if chip-rate square-low photodetector is used, the output signal $Z_{a,h}$ from the integrator when the 'target' user transmits bit a ($a = 0,1$) and exactly h interfering users transmit bit 1 is given by the Eq. (3) at pag. 3 [16], [20], wherein:

- $\Re$ is the responsivity of the detector;
- T_c is the chip duration;
- a is the variable that assumes value 1 if target user transmits bit '1', otherwise assumes value 0;
- S_{ac} is the autocorrelation of the sequence associated to the target user; if Gold codes are used we have $S_{ac} = L$ [19]:
- $S_{cc,j}$ is the cross-correlation between the sequences associated to the target user and the $j-th$ interfering user; in order to evaluate $P'^{target'}_{E,i,h}$ [18], we need to calculate the $S_{cc,j}$'s average quadratic value $m_{S^2_{cc,j}}$ and the $S^2_{cc,j}$'s variance $\sigma^2_{S^2_{cc,j}}$; if Gold codes are used, these terms can be evaluated by taking into account that the random variables $S_{cc,j}$ ($j = 1, \cdots, h$) are identically distributed with probabilities [19]:

$$S_{cc} = \begin{cases} -1+t & with\ probability\ \frac{\alpha}{L} \\ -1 & with\ probability\ \frac{\beta}{L} \quad (4) \\ -1-t & with\ probability\ \frac{\gamma}{L} \end{cases}$$

with $n = log_2(L+1)$, $t = 2^{\frac{n+1}{2}}$, $\alpha = 2^{n-2} + 2^{\frac{n-3}{2}}$, $\beta = 2^n - 2^{n-1} - 1$, $\gamma = 2^{n-2} - 2^{\frac{n-3}{2}}$.
According to Eq. (4) after some algebra we obtain the following expressions for $m_{S^2_{cc}}$ and $\sigma^2_{S^2_{cc}}$:

$$m_{S^2_{cc}} = L + 1 - \frac{1}{L}. \quad (5)$$

$$\sigma^2_{S^2_{cc}} = L^2 + 2L - \frac{2}{L} - \frac{1}{L^2}. \quad (6)$$

- $\varphi_{d,j} = \varphi_d - \varphi_j$, $\varphi_{j,u} = \varphi_j - \varphi_u$ with φ_d and φ_s ($s = 1, \ldots, h$) being the carrier phase of the target and $s-th$ interfering users respectively. In coherent systems we can assume the random variables $\varphi_{d,j}$ and $\varphi_{j,u}$ as uniformly distributed in the interval $[-\pi, \pi]$ [20].

Let $f_{Z_{a,h}}(x)$ ($a = 0,1; h = 0,1,\ldots i-1$) define the $Z_{a,h}$'s probability density. The expressions (7)-(8) reported at page 4 hold for the $Z_{a,h}$'s average value $m_{Z_{a,h}}$ and variance $\sigma^2_{Z_{a,h}}$ ($a = 0,1$).

Let us assume that the target user transmits bit '0' and '1' with equal probability $\frac{1}{2}$. We can write for $P'^{target'}_{E,i,h}$ the following expression:

$$P'^{target'}_{E,i,h} = \frac{1}{2} \int_{th_i}^{+\infty} f_{Z_{0,h}}(x)dx + \frac{1}{2} \int_{-\infty}^{th_i} f_{Z_{1,h}}(x)dx. \quad (9)$$

where th_i is the receiver threshold when i packets are transmitted on any wavelength.

If the interfering MAI and beat noises are modeled as Gaussian noise, we obtain the simple expression for $P'^{target'}_{E,i,h}$ [20]:

$$\begin{aligned} P'^{target'}_{E,i,h} &= \frac{1}{4}erfc\left(\frac{th_i - m_{Z_{0,h}}}{\sqrt{2}\sigma_{Z_{0,h}}}\right) + \\ &+ \frac{1}{4}erfc\left(\frac{m_{Z_{1,h}} - th_i}{\sqrt{2}\sigma_{Z_{1,h}}}\right). \end{aligned} \quad (10)$$

The probability $P'^{target'}_{E,i,h}$ has been evaluated in [18] when the simple threshold $th_i^{(s)}$ is chosen:

$$th_i^{(s)} = \frac{\sigma_{Z_{0,\frac{1}{2}(i-1)}} m_{Z_{1,\frac{1}{2}(i-1)}} + \sigma_{Z_{1,\frac{1}{2}(i-1)}} m_{Z_{0,\frac{1}{2}(i-1)}}}{\sigma_{Z_{0,\frac{1}{2}(i-1)}} + \sigma_{Z_{1,\frac{1}{2}(i-1)}}}. \quad (11)$$

A procedure has been identified in [21] allowing us to determine the optimum threshold when i is lower than or equal to a maximum value M_{max} depending on the code length L. In particular the evaluation of the optimum threshold $th_i^{(OT)}$ is regulated by the following Lemma.
$Lemma$: If $i \leq M_{max} = \lfloor min(1 + \beta, \frac{L^2}{L+1-1/L} - \beta) \rfloor$, with:

$$\beta = \frac{L^2}{(L+1-1/L)(1 + \sqrt{1 + \frac{2L^2(L+1-1/L)}{L^2+2L-2/L-1/L^2}})} \quad (12)$$

then the optimum receiver threshold $th_i^{(OT)}$ is obtained by finding the unique root in the interval $\Phi = [\frac{1}{2}i(L+1-1/L), \frac{1}{2}L^2]$ of the following function $f_{E,i}(x)$ expressed

$$Z_{a,h} = \overbrace{\frac{1}{2}a\Re T_c S_{ac}^2}^{signal} + \overbrace{\frac{1}{2}\Re T_c \sum_{j=1}^{h} S_{cc,j}^2}^{MAI\ noise} + \overbrace{a\Re T_c \sum_{j=1}^{h} S_{ac}S_{cc,j}\cos\Delta\varphi_{d,j}}^{Primary\ Beat\ noise} + \overbrace{\Re T_c \sum_{j=1}^{h-1}\sum_{u=j+1}^{h} S_{cc,j}S_{cc,u}\cos\Delta\varphi_{j,u}}^{Secondary\ Beat\ noise}. \quad (3)$$

$$m_{Z_{a,h}} = \frac{1}{2}a\Re T_c L^2 + \frac{1}{2}h\Re T_c\left(L+1-\frac{1}{L}\right). \quad (7)$$

$$\sigma_{Z_{a,h}}^2 = \Re^2 T_c^2\left(\frac{1}{4}h\left(L^2+2L-\frac{2}{L}-\frac{1}{L^2}\right) + \frac{1}{2}ahL^2\left(L+1-\frac{1}{L}\right) + \frac{1}{4}h(h-1)\left(L+1-\frac{1}{L}\right)^2\right). \quad (8)$$

by:

$$f_{E,i}(x) = \left(\frac{1}{2}\right)^{i-1}\sum_{m=1}^{i-1}\frac{\binom{i-1}{m}}{\sqrt{8\pi}}\left(\frac{e^{-\frac{(\alpha_{1,m}-x)^2}{2\sigma_{1,m}^2}}}{\sigma_{1,m}} + \right.$$
$$\left. - \frac{e^{-\frac{(x-\alpha_{0,m})^2}{2\sigma_{0,m}^2}}}{\sigma_{0,m}}\right) \quad (13)$$

IV. NUMERICAL RESULTS

This section will be devoted to cope with the following issues: i) validation of the proposed model by means of a Quasy Analytical model; ii) performance evaluation of WDM/OCDM switches as a function of the main traffic and switch parameters when the Optical Codes are optimally dimensioned according to the procedure illustrated in Section III.

The Gaussian Analytical (GA) model introduced to evaluate the Packet Loss Probability P_{loss}^{noise} has been validated by following a Quasy Analytical (QA) approach. The probability densities $f_{Z_{0,h}}(x)$ and $f_{Z_{1,h}}(x)$ [22] appearing in Eq. (9) have been estimated. To this end for any given value h and transmitted bit '0' and '1' of the 'target' user, we simple produce Q instances of the users' phases φ_d, φ_s $(s = 1, \ldots, h)$ and crosscorrelation $S_{cc,h}$ $(s = 1, \ldots, h)$ appearing in Eq. (3), use these instances in Eq. (3) to produce Q samples of $Z_{0,h}$ and $Z_{1,h}$ and build an histogram approximating $P_{E,i,h}^{'target'}$. The histogram can be used in Eq. (2) to estimate the Bit Error Rate (BER) that is the probability $P_{E,i}$ $(i = 2, \ldots, F)$ that a bit transmitted by a target user is corrupted for MAI and beat noise when i packets are arriving on any input wavelength.

The comparison between the GA and QA models in the case L=511 and L=1023 is shown in Fig. 3 where we report the probability $P_{E,i}$ as a function of the number i of the packets arriving on any wavelength. For both the models we perform the analysis when the optimum receiver threshold is taken into account. From Fig. 3 we can notice that the values obtained by the Gaussian and Quasy Analytical models are close and conclude that the GA approach can be exploited in order to estimate the BER of a dynamic threshold system provided that the threshold curve is properly selected. Notice that the conclusion does not contradict the one reported in

[16] where the Gaussian approximation does not hold because the comparison between analytical and simulation results is performed when the receiver threshold is not optimized. Because the GA approach is less complex and more informative than the QA one, next we use the Gaussian analytical model to evaluate the performance of the WDM/OCDM systems.
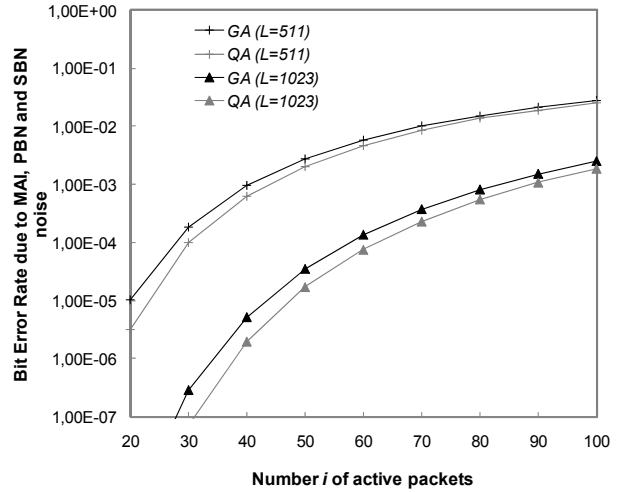
Figure 3. Validation of the analytical model by means of a Quasy Analytical model. The Bit Error Rate (BER) is reported for L=511 and L=1023 as a function of the number of packets arriving on any wavelength.

Next we show how the choice of the optimum receiver threshold expressed by Eq. (13) allows us to obtain better switch performance because a more effective code dimensioning may be accomplished.

First of all we show in Fig. 4 the Packet Loss Probability P_{loss}^{noise} due to MAI, Primary Beat Noise (PBN) and Secondary Beat Noise (SBN) versus the number F of OCs supported on each wavelength. Notice that P_{loss}^{noise} is the probability that at least a bit of a packet is affected by an error due to MAI and beat noise. It depends on $P_{E,i}$ and the offered traffic to each input wavelength according to Eq. (1) reported in Section III. We have evaluated P_{loss}^{noise} for offered traffic p varying from 0,3 to 0,9 and packet length H equal to 500 bytes. The code length L is chosen to be 511. For each value of traffic

we report two curves: the first one is obtained when the receiver threshold $th_i^{(s)}$ $(i = 2, \cdots, F)$ expressed by Eq. (11) is used, the second one reports the results when the threshold $th_i^{(OT)}$ $(i = 2, \cdots, F)$ is chosen according to the procedure illustrated in Section III. We have applied the Newton-Raphson method to evaluate the root of the function $f_{E,i}(x)$. From Fig. 4 you can notice how, when a given P_{loss}^{noise} is fixed, a higher number of codes can be carried on each wavelength if the receiver threshold optimization is performed. For instance, when p equals 0,5 and P_{loss}^{noise} is around 10^{-7}, we have that 4 and 10 codes can be carried on each wavelength in the cases in which the thresholds $th_i^{(s)}$ and $th_i^{(OT)}$ $(i = 2, \cdots, F)$ are used respectively.

Figure 5. Packet Loss Probability P_{loss}^{opc} due to output packet contentions as a function of the number r of used WCs. The curves labeled with OT report the results when the Optimized Threshold is used.

Figure 4. Packet Loss Probability due to MAI and beat noise as a function of the number F of Optical Codes for L=511, H=500 byte and p varying from 0,3 to 0,9. The curves labeled with OT report the results when the Optimized Threshold is used.

The choice of an optimized receiver threshold impacts on the OCDM/WDM switch performance allowing for a reduction of the Packet Loss Probability P_{loss}^{opc} due to output packet contentions [18]. P_{loss}^{opc} is reported in Fig. 5 as a function of the number r of used WCs for H=500 bytes, N=8, M=16, L=511 and p=0,3, 0,5, 0,7. The number F of used OCs for each wavelength is chosen so that the threshold Packet Loss Probability P_{loss}^{noise} due to MAI and beat noise is not greater than 10^{-9}. For each value of traffic, we report P_{loss}^{opc} when the receiver threshold $th_i^{(s)}$ and $th_i^{(OT)}$ $(i = 2, \cdots, F)$ are used. We can notice that better performance is obtained when the threshold is chosen according to the procedure illustrated in Section III. For instance when p=0,7 and r=28, P_{loss}^{opc} equals $9,58*10^{-7}$ and $3,87*10^{-10}$ in the cases in which the receiver thresholds $th_i^{(s)}$ and $th_i^{(OT)}$ $(i = 2, \cdots, F)$ are used respectively. Obviously the better performance is due to the higher number of codes that is possible to carry on each wavelength and consequently a higher probability in solving output packet contentions.
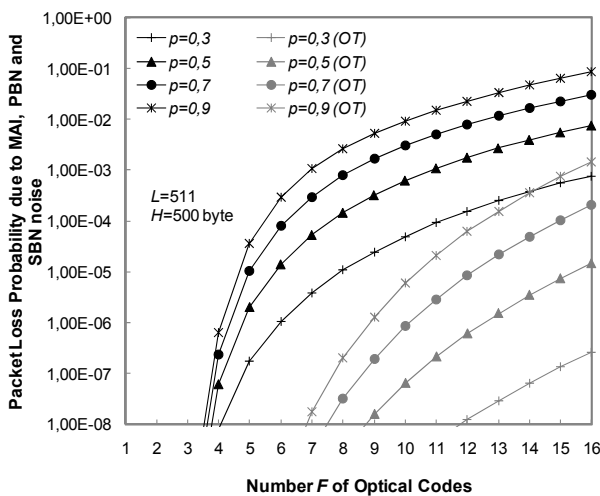
V. CONCLUSION

The WDM/OCDM optical packet switch performance has been analytically investigated by introducing an analytical model to dimension the optical codes carried on each wavelength. The dimensioning has been performed in the cases in which a simple and an optimized receiver threshold are used. We have shown that the switch can reach acceptable performance, in particular for offered traffic p equal to 0,5, the packet loss probability equals 10^{-9} when the number M of wavelengths equals 16, the code length L is 511 and only 24 wavelength converters are used.

REFERENCES

[1] A. Teixeira, T. Silveira, A. Ferreira, R. Nohueira, P. Andrea, M. Lina, P. Monteriro, and J. Da Rocha, "All optical router based on OCDMA codes and SOA based devices," in *7th Int. Conf. on Transparent Optical Networks*, June 1999, pp. 183–188.

[2] I. Saeki, S. Nishi, and M. Murakami, "All-optical code division multiplexing switching network based on self-routing principle," *IEICE Transactions Communications*, vol. E82-B, pp. 239–245, 1999.

[3] D. Hsu, "A novel photonic label switching based on optical code division multiplexing," in *10th Int. Conf. on Telecommunications*, June 2003, pp. 634–640.

[4] J. Bannister, J. Touch, and A. Willner, "How many wavelengths do we really need? A study of the performance limits of packets over wavelengths," *Optical Networks Magazine*, vol. 1, pp. 17–28, 2000.

[5] D. Blumenthal, G. Rossi, and T. Dimmick, "All-optical label swapping networks and technologies," *IEEE Journal of Lightwave Technology*, vol. 18, pp. 2058–2074, 2000.

[6] V. Eramo, M. Listanti, C. Nuzman, and P. Whiting, "Optical switch dimensioning and the classical occupancy problem," *International Journal Communications Systems*, vol. 15, pp. 69–80, 2002.

[7] V. Eramo, A. Germoni, M. Savi, and C. Raffaelli, "Multi-fiber shared-per-wavelength all-optical switching: Architectures, control, and performance," *IEEE/OSA Journal Lightwave of Technology*, vol. 26, pp. 537–551, 2008.

[8] V. Eramo and M. Listanti, "Wavelength converter sharing in a WDM optical packet switch: dimensioning and performance issues," *Elsevier Computer Networks*, vol. 32, pp. 633–651, 2000.

[9] S. Huang and K. Kitayama, "Variable-bandwidth optical paths: Comparison between optical code-labeled path and OCDM path," *IEEE/OSA Journal Lightwave of Technology*, vol. 24, pp. 3563–3573, 2006.

[10] Y. Wang and B. Li, "Optical code-labeled router based on OCDM," *IEEE/OSA Journal Of Optical Communications and Networking*, vol. 2, pp. 111–116, 2010.

[11] N. Wada, "Optical code processing system, device and its application," *Journal of Networks*, vol. 5, pp. 242–250, 2010.

[12] P. Teh, P. Petropoulos, M. Ibsen, and D. Richardson, "A comparative study of the performance of seven and 63-chip optical code division multiple access encoders and decoders on superstructured fiber bragg gratings," *IEEE/OSA Journal Lightwave of Technology*, vol. 19, pp. 1352–1365, 2001.

[13] P. Teh, M. Ibsen, L. Fu, J. Lee, Z. Yusoff, and D. Richardson, "A 16-channel OCDMA system (4 OCDM×4 WDM) based on 16-chip, 20 Gchip/s superstructure fiber bragg gratings and DFB fiber laser transmitters," in *Optical Fiber Communication Conference*, 2002, pp. 600–601.

[14] X. Wang, K. Matsushima, A. Nishiki, N. Wada, F. Kubota, and K. Kitayama, "High performance optical code generation and recognition using 511-chip 640 Gchip/s phase-shifted superstructured FBG," *Optics Letters*, vol. 30, pp. 355–357, 2005.

[15] X. Wang, K. Matsushima, N. Wada, and K. Kitayama, "Dispersion-flattened-fiber-based optical thresholder for multiple-access-interference suppression in OCDMA System," *OSA Optics Express*, vol. 13, pp. 5499–5505, 2005.

[16] X. Wang and K. Kitayama, "Analysis of beat noise in coherent and inchoerent time-spreading OCDMA," *IEEE Journal of Lightwave Technology*, vol. 22, pp. 2226–2234, 2004.

[17] V. Eramo, L. Piazzo, M. Listanti, A. Germoni, and A. Cianfrani, "Performance evaluation of an optical packet switch using wavelength and code domain to solve output contentions," in *12th Int. Conf. on Transparent Optical Networks*, 2010, pp. 600–601.

[18] V. Eramo, "Impact of the mai and beat noise on the performance of OCDM/WDM optical packet switches using gold codes," *Optics Express*, vol. 18, pp. 17 897–17 912, 2010.

[19] D. Sarwate and M. Pursley, "Crosscorrelation properties of pseudorandom and related sequences," *Proceedings of the IEEE*, vol. 68, pp. 593–619, 1980.

[20] T. Pu, H. Zhang, Y. Guo, and Y. Li, "Evaluation of beat noise in OCDMA system with non-gaussian approximated method," *IEEE Journal of Lightwave Technology*, vol. 24, pp. 3574–3582, 2006.

[21] V. Eramo and L. Piazzo, "Evaluation of optimum threshold in OCDM/WDM optical packet switches," *IEEE Communication Letters*, vol. 15, pp. 755–57, 2011.

[22] L. Piazzo, V. Eramo, and A. Aceto, "Performance analysis of an OCDMA system by means of the quasy analytical and the gaussian approaches," in *12th Int. Conf. on Transparent Optical Networks*, 2010, pp. 392–295.

Vincenzo Eramo received his "Laurea" degree in Electronics Engineering in 1995 and his "Dottorato di Ricerca" (PhD degree) in Information and Communications Engineering in 2001, both from the University of Roma "La Sapienza". From June 1996 to December 1996 he was a researcher at the Scuola Superiore Reiss Romoli. In 1997, he joined the Fondazione Ugo Bordoni as a researcher in the Telecommunication Network Planning group. From November 2002 to July 2010 he was currently an Assistant Professor in the INFOCOM Department of the University of Rome La Sapienza. Actually he is Aggregate Professor in the Department of Information, Electronics and Telecommunications Engineering. His current research interests are focused on resource dimensioning techniques in Optical Packet Switches and performance evaluation of routing protocols in software router. These activities have been carried out also in the framework of national (MIUR) and international (European Union) projects. Dr. Eramo was Chairman in some international conferences (ICC 2003, EuroIMSA 2005). He has published more than sixty papers on international journals and conference proceedings.

Lorenzo Piazzo received the "Laurea" degree (cum laude) and PhD Degree in Telecommunications from the university of Rome "La Sapienza" in 1991 and 1995 respectively. From 1997 he is assistant professor at the university of Rome "La Sapienza". His research interests include speech and channel coding, OFDM, UWB and optical communications, Infrared images processing and Multi-Hop networks.

Angelo Germoni received the Laurea (M.Sc.) degree (cum laude) in Telecommunications Engineering from the University of Rome "La Sapienza", Italy in 2006. He got a Ph.D student in Information and Communication Engineering at INFOCOM Dept. of the same university in 2010. He is currently collaborating with the CoRiTeL (Consorzio di Ricerca sulle Telecomunicazioni) research consortium since October 2008. His current research interests are in the fields of all-optical networks and switching architectures. He is a member of the European Network of Excellence IST-FP7 BONE.

Antonio Cianfrani was born in Isernia, Italy, in 1980 and he received the M.S. degree in Telecommunications Engineering and the Ph.D degree in Information and Communication Engineering from the University of Rome Sapienza, Italy, in 2004 and 2008, respectively. He is currently working in the Department of Information, Electronics and Telecommunications Engineering of the University of Rome La Sapienza. His main scientific contribution are on performance evaluation of Software Router and on incremental routing algorithms in IP networks. His current research interests are focused on switching architectures in OPS networks and on Routing and Wavelength Assignment problem in OTDM/WDM all optical networks. He is currently involved in the EU-funded IST BONE Network of Excellence project.

Marco Listanti received his Dr. Eng. degree in electronics engineering from the University La Sapienza of Roma in 1980. In 1981, he joined the Fondazione Ugo Bordoni, where has been leader of the group "TLC network architecture" until 1991. In November 1991 joined the INFOCOM Dept. of the University of Roma "La Sapienza", where he is Professor of Switching Systems. Since 1994, he also collaborates with the Electronic Department of the University of Roma Tor Vergata where he holds courses in Telecommunication networks. Actually he is Assistant Professor in the Department of Information, Electronics and Telecommunications Engineering of the University of Rome La Sapienza. He participated at several international research project supported by EEC and ESA and is author of several papers published on the most important technical journals and conferences in the area of telecommunication networks. His current research interests focus on traffic control in IP networks and on the evolution of techniques for optical networking. Mr. Listanti has been representative of Italian PTT administration in international standardization organizations (ITU, ETSI). Mr. Listanti is also a member of IEEE Communications and Computer Societies.

Performance of Stereo Multiplexing in Single Channel and DWDM Systems Using Direct Detection with Optimum Dispersion Maps

Oscar Gaete, Leonardo Coelho, Bernhard Spinnler*

Institute for Communications Engineering, Technische Universität München, Germany

*Nokia Siemens Networks GmbH & Co. KG, München, Germany

Email: {Oscar.Gaete, Leonardo.Coelho}@tum.de and Bernhard.Spinnler@nsn.com

Abstract— We present Stereo Multiplexing, a novel technique that permits simultaneous direct detection of two modulated optical carriers. This is accomplished by modulating the optical carriers with the difference and the sum of two signals. The linear performance of Stereo-multiplexed DQPSK signals is compared to single-carrier DQPSK and dual-carrier DQPSK. Subsequently, by means of simulations, the robustness of each format is compared for single channel and DWDM transmission of 55.5 Gb/s through 1040 km of SMF. This is done by searching the optimum dispersion map and input powers for each format and looking at the stability of the performance around the optimum. We show that the best performance and robustness is obtained by sharing the information between two carriers, and that Stereo is only 1dB below dual-carrier NRZ-DQPSK. We discuss the penalty associated with designing a DWDM system based only on the optimization of transmission of single channel.

Index Terms— modulation formats, direct detection, DQPSK, optimum dispersion maps

I. Introduction

The increasing capacity requirements in optical networks demand the use of spectrally efficient transmission formats at very high data rates. This supposes a big challenge concerning both transmission performance and hardware requirements. Lately, much interest has been put in schemes that reduce the symbol rate by sharing the transmitted data in two optical wavelengths [1]–[4]. By doing so, not only the bandwidth requirements of the components are relaxed, but it is also expected a gain in robustness against impairments that scale with the symbol rate, e.g., dispersion. In dual-carrier transmission using coherent detection, demultiplexing is carried out electrically, resulting in great performance but at expense of increased complexity in the receiver structure [1]. On the other hand, complexity can be kept low in direct detected systems; however, the optical carriers must be detected and demodulated separately, which increases the receiver hardware and the overall cost [2].

In [5] we proposed Stereo Multiplexing, a novel transmission format that allows the simultaneous reception and electrical demultiplexing of two optical carriers using direct detection. In [6] we compared the performance of Stereo-multiplexed DQPSK signals against its single-carrier and dual-carrier equivalent, using RZ-50% and NRZ pulse shaping. This was done for DWDM signals

regarding the linear performance in back-to-back configuration, and after 1040 km of transmission in standard single-mode fiber (SMF). For a fair comparison the optimum dispersion map of each modulation format was found using the global optimization algorithm introduced in [7] and [8]. Subsequently, we analysed the robustness of the dispersion maps for each format.

In this contribution, we are interested in the optimization process that led to the mentioned results. Optimization of dispersion maps for DWDM requires a significant effort regarding simulation time, and often, the process is simplified by analysing the transmission of a single channel, either simulating it or using approximated models for the performance of the system [9]. Here we look at the penalty involved between optimization of single channel versus optimization of a DWDM system. For this purpose, we compare in detail the optimum dispersion maps and overall performance of single channel transmission with DWDM transmission of 7 optical channels.

In section II, a brief introduction to Stereo Multiplexing is given and section III shows the system design for the compared formats. In section IV, the algorithm for optimizing the dispersion maps is described and the results of the simulations are discussed.

II. Stereo Multiplexing

In a conventional dual-carrier transmission system, two data streams modulate two optical carriers independently. In Stereo Multiplexing, the sum and the difference of two modulated signals are conveyed in two optical carriers respectively. Taking on-off keying (OOK) as example, the Stereo-multiplexed optical signal can be described as

$$x_o(t) = (A + B)\, e^{j(\omega_1 t + \phi_1)} + (A - B)\, e^{j(\omega_2 t + \phi_2)} \quad (1)$$

where A and B are OOK base-band signals that modulate two complex optical fields at angular frequencies ω_1 and ω_2, and phases ϕ_1 and ϕ_2 respectively. After direct detection, the electrical signal is directly proportional to the squared magnitude of the complex optical signal

$$x_e(t) = \left(|A|^2 + |B|^2\right) + \left(|A|^2 - |B|^2\right)\cos\left(\Delta\omega t + \Delta\phi\right). \quad (2)$$
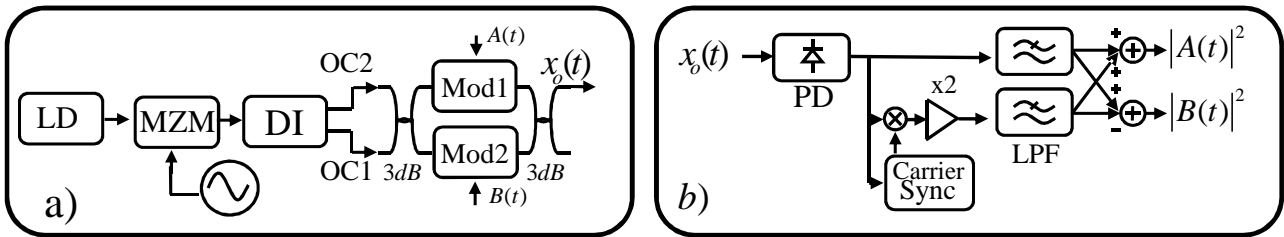
Figure 1: Transmitter (*a*) and receiver (*b*) for OOK-Stereo-multiplexed signals.
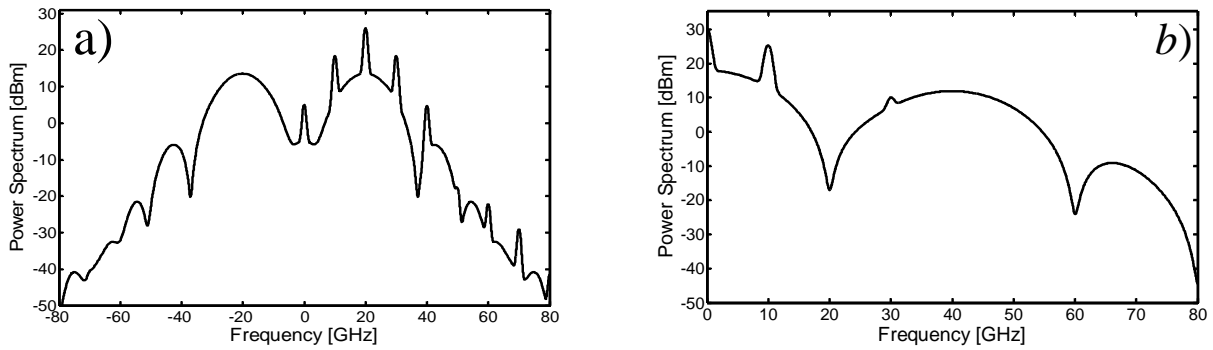

Figure 2: Spectrum of the optical OOK-Stereo-multiplexed signal (*a*) and of the signal after detection (*b*).

By recovering the band-pass part of the electrical signal and combining it with the base band, the intensities of the original data signals can be demultiplexed and used for decision or further processing in the electrical domain. Figure 1a illustrates one possible realization of the Stereo-multiplexed signal at the transmitter side. The two optical carriers OC1 and OC2 can be generated using a Mach-Zehnder modulator (MZM) driven by a sinusoidal signal with half the frequency of the desired sub-carrier separation, followed by a Mach-Zehnder interferometer-based filter used to separate both of them [3]. After being generated, the optical carriers must be added with a phase shift of 90° between them, for example by means of a 3 dB optical coupler. Then, both sub-carriers are simultaneously modulated with two different data patterns and the signals at the output of the modulators are added again using a coupler. The receiver is shown in Fig. 1b. Figure 2a depicts the optical spectrum of a 10 Gb/s OOK-Stereo-multiplexed signal and the spectrum of the received electrical signal. In this example, the frequency deviation of the optical carriers from the center frequency is twice the symbol rate.

The proposed technique can also be implemented with phase modulation. In this case interferometric detection must be performed first. Thanks to the periodicity of the transfer function of the delay interferometer (DI), it is possible to demodulate the two carriers simultaneously [4], provided that the frequency separation between them is an integer number of the free spectral range of the DI. In any case, the multiplexing stage in the transmitter is independent of the modulation format. Hence, with single ended MZM (as depicted in Fig.1a) OOK or DPSK can be generated. Optical IQ modulators would be required to generate DQPSK.

III. SYSTEM DESIGN AND LINEAR PERFORMANCE

Figure 3 depicts a block representation of the three simulated systems. The DQPSK modulation is accomplished by using nested Mach-Zehnder modulators. The demodulators consist of Mach-Zehnder delay interferometers followed by balanced detection and a 5th order Bessel low pass filter (B = 0.75*symbol rate) before final symbol decisions. In each case a PRQS of length 4^6 is used to modulate the optical carriers. The total data rate is 55.5 Gb/s. The transmitters generate 7 WDM channels in a 50 GHz grid. The center channel is extracted by means of a 42 GHz optical band pass filter (2nd order, Gauss) and the required OSNR for a BER of 10^{-4} is calculated. The BER is calculated in all cases with the Karhunen-Loéve method [10]. RZ-50% and NRZ pulses are simulated for each modulation format. When two optical carriers are used to convey the data (dual-carrier and Stereo), they have a frequency separation of twice the symbol rate. In dual-carrier DQPSK, band pass optical filters are used to separate the optical carriers. It was found that the optimum bandwidth of the filters for the single channel case is 25 GHz for RZ-50% and 19.4 GHz for NRZ; and for the DWDM case is 13.8 GHz for RZ-50% and 20.8 GHz for NRZ. In Fig. 4 the BER curves and the dispersion tolerance for the back-to-back configuration are shown. It is possible to observe, that single-carrier and dual-carrier NRZ share the best back-to-back sensitivity and that Stereo-NRZ is only half decibel away, and as expected, Stereo-NRZ and dual-carrier-NRZ have an increased tolerance to dispersion. Formats with two carriers and RZ-50% pulses have a degraded sensitivity due to the cross-talk between carriers and they will not be considered for the rest of the simulations.
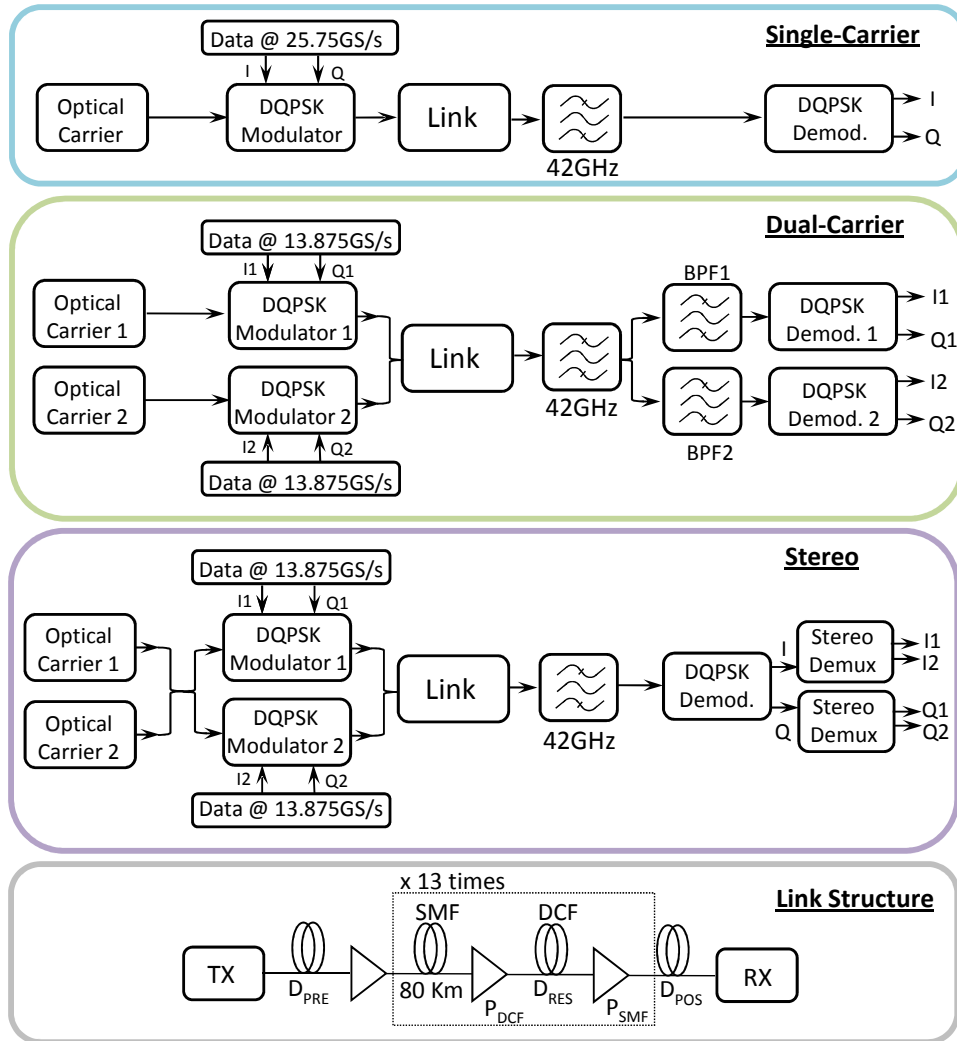
Figure 3: System design for each modulation format and structure of the link.

IV. OPTIMIZATION OF DISPERSION MAPS

A. The Optimization Algorithm

In optimizing a communication system, we are concerned with the problem of finding the best suitable set of parameters that leads to the best performance in the transmission, e.g., the lowest required OSNR. In this paper we do this by independently varying four parameters of the transmission link (see Fig.3): average input power levels into the SMF and DCF (P_{SMF}, P_{DCF}), amount of pre-compensation (D_{PRE}) and residual dispersion per span (D_{RES}). Post-compensation (D_{POS}) sets the accumulated dispersion back to zero. The usual approach is to carry out a grid search, in other words, to simulate every possible combination of parameters and choose the one that gives the best result. However, due to the long transmission distances and the extremely large bandwidth of the signals, the simultaneous optimization of several parameters often translates into prohibitive simulation times. In such scenarios advanced optimization algorithms prove to be an attractive alternative to the conventional grid search.

In [7] and [8] we have presented a novel algorithm especially appropriate for the optimization of optical communication systems. It is independent of external parameters and converges rapidly to the global optimum of the system, drastically reducing the number of required simulation. The algorithm works as follows: After an interval for each parameter is set (thus defining the search space), the algorithm starts by simulating the 2^4 boundary points. Then it divides the search space into a set of simplexes. For each simplex, the unknown objective function (the required OSNR after 1040 km) is modeled as a Gaussian stochastic process and its mean and variance are used to find the next set of input parameters, which will most probably improve the currently best solution already found. After a certain number of iterations the global optimization algorithm determines the lowest required OSNR and the set of parameters that defines the optimum dispersion map.

B. Simulation results

The algorithm is set to find the optimum dispersion map for each modulation format in 75 iterations (plus the initial 16 boundary points). The link is depicted in Fig. 3. The total field transmission is simulated using the non-
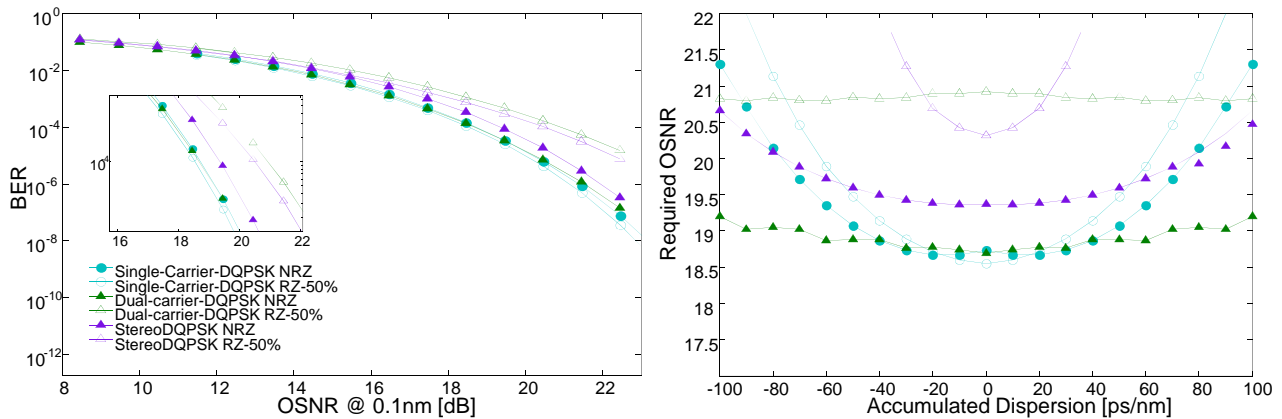
Figure 4: BER curves and dispersion tolerance for DWDM.

linear Schrödinger equation and the symmetrized split-step Fourier method. Only dispersion, attenuation and Kerr nonlinearities are investigated. Polarization mode dispersion and nonlinear phase noise are not considered. The nonlinearity of the pre- and post-compensation fibers is neglected, but their attenuations are taken into account. EDFA's have a noise figure of 6 dB.

Table I summarizes the results for the optimization of each transmission format. Subsequently, the robustness of each optimum dispersion map is investigated. This is done by fixing the optimal input powers and varying the pre-compensation and residual dispersion per span around the optimum values shown in the previous table. Results are shown in Fig. 5 for the single channel case and Fig. 6 for DWDM. The contour plot represents the required OSNR in dB, for a BER of 10^{-4}.

By optimizing the dispersion maps, a fair comparison can be done regarding the overall performance of a transmission format. From Table I, one can observe that by optimizing the dispersion map, the performance of the transmission after 1040 km is comparable to the back-to-back case. Results show that the required OSNR for single-carrier and for dual-carrier are approximately the same, and for Stereo is about 1 dB more than the rest of the formats. The results depicted in Fig. 5 and 6 show the robustness of each modulation format to variations in the optimum parameters of the dispersion map.

As expected RZ-50% is more robust than NRZ to variations in the amount of residual dispersion per span, and pre compensation. It is also possible to observe that by sharing the transmitted data in two optical carriers, the robustness of the dispersion map is greatly improved. This is true for dual carrier and for Stereo. Robustness to input power in the SMF seems to increase as well. Dual-carrier-DQPSK using NRZ pulses has the best performance and greatest robustness. However, this comes at the expense of doubling the required hardware. Stereo-multiplexed signals, on the other hand, trade around 1 dB in performance against increased robustness in the dispersion map and reduced hardware requirements at the receiver side.

It is worth mentioning that the values in Table I are the ones given by the optimization algorithm. After sim-ulating around these values, it is possible to observe that even smaller required OSNRs are found. The difference between them and the ones from Table I are, in any case, very small.

As mentioned before, the evaluation of the optimum dispersion maps in the case of WDM systems can be extremely time consuming. This causes that sometimes, the parameters of a system are set to optimize the single channel case, and one hopes that the penalty of transmitting WDM channels instead, is tolerable. It is therefore interesting, to investigate the penalty that one occurs in transmitting DWDM channels with the optimum parameters obtained from the optimization of single channel transmission. The values for the parameters are shown in Table I. The result is shown in Table II. As observed, the penalty is small; always less than one deci-bel. This indicates that the optimization of single channel transmission is a good starting point for transmission of WDM channels. It is also worth noting that the biggest difference between the dispersion maps in single channel and in DWDM is that transmission close to where there is zero residual dispersion per span should be avoided due to enhanced cross-phase modulation between the channels.

TABLE II.: Performance of DWDM
with Parameters for Single Channel

Format	Required OSNR (dB)
Single-Carrier NRZ	18.86
Single-Carrier RZ-50%	19.05
Dual-Carrier NRZ	18.48
Stereo NRZ	20.60

V. CONCLUSION

In this paper, Stereo-multiplexed-DQPSK has been introduced and its performance has been analysed and compared to single-carrier and dual-carrier DQPSK, with NRZ and RZ-50% pulses. With the help of an algorithm for the global optimization of the dispersion maps, we have found that dual-carrier DQPSK has the best performance and the most robust dispersion map of all,

TABLE I.: Minimum Required OSNR (dB) and Optimum Parameters for DQPSK

	Single-Carrier NRZ		Single-Carrier RZ-50%		Dual-Carrier NRZ		Stereo NRZ	
	Single-Channel	DWDM	Single-Channel	DWDM	Single-Channel	DWDM	Single-Channel	DWDM
Back-to-back	17.5	18.5	17.7	18.7	17.7	18.6	18.8	19.3
After 1040 km	17.6	18.7	17.7	18.8	17.7	18.5	19.1	20.0
P_{SMF} (dBm)	-3	-3	-3	-2.7	-3	-2.9	-3	-3
P_{DCF} (dBm)	-10	-9.5	-9,6	-9.9	-9.8	-9.8	-9.9	-10
D_{PRE} (ps/nm)	-431.6	-166	-99,6	-66.4	431.6	-166	-166	-33.2
D_{RES} (ps/nm)	26.56	-26.56	0.0	13.28	-66.4	-66.4	-13.28	-66.4
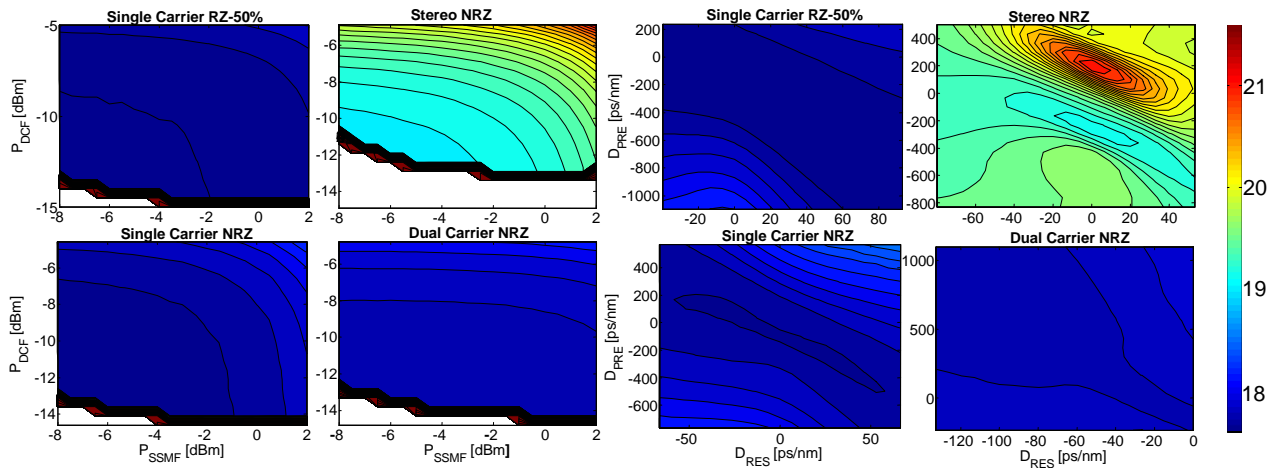
Figure 5: Robustness of optimum dispersion maps for single channel
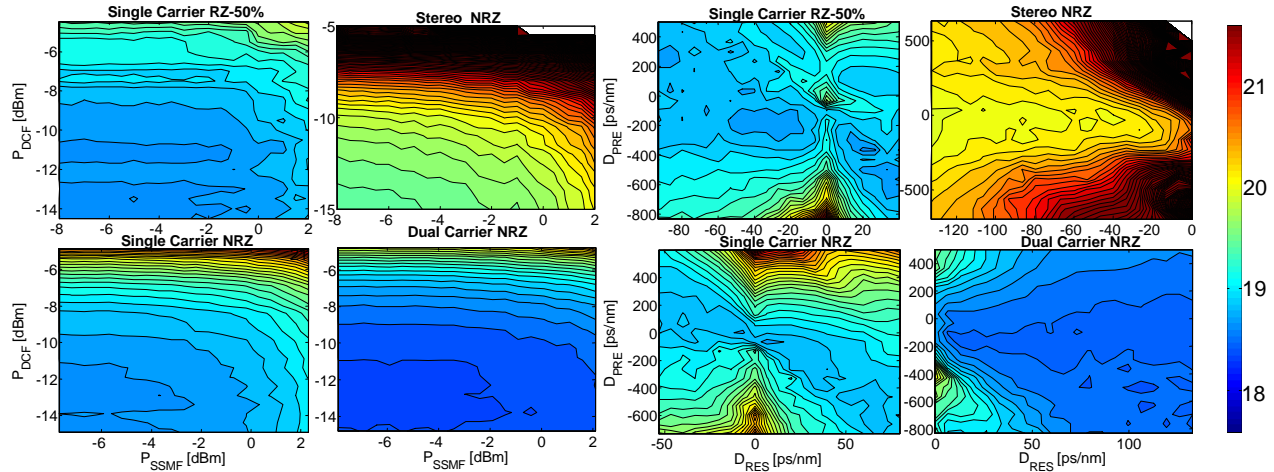
Figure 6: Robustness of optimum dispersion maps for DWDM

but at the expense of doubling the required hardware at the transmitter and receiver. On the other hand, Stereo-DQPSK using NRZ pulses is an alternative if robustness of the dispersion map needs to be increased, and costs must be kept low.

We also verified that optimizing single channel transmission, is a good starting point for transmission of DWDM channels, and that in the case of the investigated formats, a penalty of less than one decibel can be expected.

REFERENCES

[1] E. Yamada *et al*, "1 Tb/s (111 Gb/s/ch x 10ch) No-Guard-Interval CO-OFDM Transmission over 2100 km DSF," in *Opto-electronics and Communications Conference*, Sydney, 2008.

[2] T. Kobayashi *et al*, "Electro-optically multiplexed 110 Gbit/s optical OFDM signal transmission over 80 Km SMF without dispersion compensation," *IEEE Electronics Letters*, vol. 44, no. 3, 2008.

[3] A. Sano *et al*, "30x100-Gb/s all optical OFDM transmission

over 1300 km SMF with 10 ROADM nodes," in *European Conference on Optical Communications*, Berlin, 2007.

[4] D. Caplan *et al*, "High-Sensitivity Demodulation of Multiple-Data-Rate DPSK Signals using a Single Interferometer," in *Optical Fiber Conference*, Anaheim, CA, 2007.

[5] O. Gaete *et al*, "Stereo Multiplexing for Direct Detected Optical Communication Systems," in *Optical Fiber Conference*, San Diego, CA, 2009.

[6] ——, "Performance of Stereo Multiplexing in Systems Using Direct Detection with Optimum Dispersion Maps," in *International Conference on Transparent Optical Networks*, Munich, 2010.

[7] ——, "Global Optimization of Optical Communication Systems," in *European Conference on Optical Communications*, Brussels, 2008.

[8] L. Coelho, O. Gaete, and N. Hanik, "An Algorithm for Global Optimization of Optical Communication Systems," *AEU-International Journal of Electronics and Communications*, vol. 67, no. 7, 2009.

[9] R. Killey *et al*, "Reduction of Intrachannel Nonlinear Distortion in 40 Gb/s based WDM Transmission over Standard Fiber," *IEEE Photonic Technology Letters*, vol. 12, no. 12, 2000.

[10] A.H. Gnauck, *et al*, "Optical phase shift keyed transmission," *IEEE Journal of Lightwave Technology*, vol. 23, no. 115, 2005.

Oscar Gaete was born in Viña del Mar, Chile, in 1981. He received the Dipl.-Ing. degree in Electrical Engineering from the Pontificia Universidad Catolica de Valparaiso, Chile in 2005 and the M.Sc. degree from the HTW-Aalen in 2007, Germany working on indoor optical communications.

He was a visiting researcher at the University of Melbourne, Australia, in late 2010 and is currently working toward the Ph.D. degree at the Technische Universität München. His main research interests include optimization of fiber-optic communication systems, robust modulation formats for high speed transmission and equalization of system impairments.

Leonardo D. Coelho was born in Recife, Brazil, in 1979. He received the B.Sc. degree in Electrical Engineering from the Universidade Federal de Pernambuco, Recife, Brazil in 2003, the M.Sc. and Ph.D. degree from the Technische Universität München (Munich, Germany) in 2005 and 2010, respectively, studying advanced modulation formats for high-speed optical transmission systems.

He currently holds a postdoctoral position at the Institute for Communicaitons Engineering, Technische Universität München. His main research interests include simulation and optimization of optical communication systems, transmitter and receiver modeling for new modulation formats and nonlinear signal propagation in fiber-optic transmission systems.

Bernhard Spinnler was born in Erlangen, Germany, in 1968. He received the Dipl.-Ing. degree in communications engineering and the Dr.-Ing. degree with a thesis on noncoherent detection of continuous phase modulation from the University of Erlangen-Nrnberg, Germany, in 1994 and 1997, respectively.

Since 1997, he worked on low-complexity modem design of wireless radio relay systems at Siemens AG, Information and Communication Networks. In 2002, he joined the optical networks group of Siemens Corporate Technology, which later merged into Nokia Siemens Networks. There he is working on robust and tolerant design of optical communications systems. His interests focus on advanced modulation, forward error correction, and equalization.

Adaptive Data Rates for Flexible Transceivers in Optical Networks

Brian T. Teipen [1], Michael H. Eiselt [1], Klaus Grobe [2], Jörg-Peter Elbers [2]

[1] ADVA AG Optical Networking, Advanced Technology Group, Meiningen, Germany

[2] ADVA AG Optical Networking, Advanced Technology Group, Martinsried, Germany

Email: bteipen@advaoptical.com

Abstract— **Efforts towards commercializing higher-speed optical transmission have demonstrated the need for advanced modulation formats, several of which require similar transceiver hardware architecture. Adaptive transceivers can be built to have a number of possible operational configurations selected by software. Such software-defined transceiver configurations can create specific modulation formats to support sets of data rates, corresponding tolerances to system impairments, and sets of electronic digital signal processing schemes chosen to best function in a given network environment. In this paper, we discuss possibilities and advantages of reconfigurable, bit-rate flexible transceivers, and their potential applications in future optical networks.**

Index Terms — **bit-rate flexible transceivers, software-defined optics, dynamic networks, transmission constraints**

I. INTRODUCTION

In conventional optical networks, channels, once initially provisioned, are seldom reconfigured until they are decommissioned at end-of-life. Network operators manage the system capacity via such channels in multiples of the SONET/SDH or OTN data rate, and the capacity and reach of a given provisioned channel is static and dependent on the specific transceiver interface being used and the network environment, respectively. Relatively recent concepts could change such fixed properties of optical channels.

One concept is the introduction of dynamic optical networks [1], where channels are configured on demand and might remain configured for only a relatively short duration, for example on the order of a number of hours. A second concept concerns the data rates of the optical channels. To date, the optical telecom industry has been accustomed to fixed line rates near 2.5 Gb/s, 10 Gb/s, or 40 Gb/s. Recently, fixed line rates at approximately 100 Gb/s for Ethernet and OTN applications have seen industry-wide engineering development. By contrast, in several recent wireless applications, variable channel data rates are used; if the transmission quality for a given channel deteriorates, the data-rate is reduced. Extending this to optical networks, an optical channel's data rate can be adapted based on performance characteristics such as the optical signal-to-noise ratio (OSNR).

Taken together, the implementation of these concepts requires a system that can optimize transmission for reach, data rate, and spectral occupancy. These concepts could be addressed via a software-based configuration or implementation of the operating function of a given transceiver. Such a flexible transceiver would enable operation at one of multiple data rates, by changing at least one parameter such as the symbol encoding modulation format, symbol rate, or possibly the number of subcarriers used for an aggregate channel. This flexibility could be realized using a common, fixed hardware configuration, with functionality selected via software commands, giving rise to the term software-defined optics (SDO) [2]. This distinctly differs from software control, i.e. the tuning of operating set-points. For wireless and radio applications, similar functionality for transceivers has been commercialized [3].

II. APPLICATIONS FOR FLEXIBLE TRANSCEIVERS

The concept of transceivers capable of operating with flexible bit-rates, together with the relationships between performance characteristics (e.g. equivalent OSNR) and optical impairments, leads to a number of applications in optical networks which can be attractive from both a technical and an economical point of view.

One motivation for designing bit-rate flexible optical transceivers includes the reduction of costs (operating expenses) which could result from having fewer types of transceivers, in turn facilitating increased efficiency in network planning and reducing operational sparing of equipment. A larger portion of cost savings is expected to come from the ability to more fully use the available OSNR margin in a system. Currently, optical transmission systems are designed using given device specifications, while individual device performance lies somewhere within the statistical ensemble of manufactured components. The optical device and sub-module supply chain anticipates how performance-data could fluctuate over the period of manufacturing, and applies a margin to define specifications that can be achieved. Deployed channels have OSNR margins that, across a statistical distribution, are above operational and planning requirements. When this OSNR margin can be used towards a higher per-channel data rate, fewer transceivers are required per capacity requirement.

Several applications follow from the characteristic that bit-rate flexible transceivers have an increased distance reach while operating at lower line rates. This suits a

typical requirement of large corporate networks – as well as managed-service providers – because traffic volume is approximately inversely proportional to transport distance. Examples of this behavior are cited by enterprises [4] with cloud computing applications. An application using a single type of bit-rate flexible transceiver would ease network/link planning and sparing requirements, thereby reducing operating expenses.

Another particular application relates to resilience against fully disruptive failures (e.g. fiber breaks) which force protection (or possibly restoration) switching. In most cases, a protection path is longer than the original working path. In order to achieve protection capacity equal to the initial working capacity, transceivers with an increased distance reach are required to operate over the protection path; if the same fixed transceiver design is to be used for both working and protection paths, the working transceivers are over-designed with respect to the working-path lengths. With a flexible bit-rate design, all transceivers can be economically unified, at the cost of the protection-path capacity being less than the original working capacity in most cases. Note however, that the initial ability to increase the working-path capacity with respect to the protection-path capacity is what would be initially gained over a fixed-rate transceiver scenario, because performance margin gained from the lesser working path distance is then exchanged for a higher transmission rate. This mode of operation could be acceptable for many applications, given the fact that at least a throttled protection capacity would be available, and given that cost (capital expenses) could be saved with respect to the interfaces.

A decrease in the overall line rate could yield performance margin to be re-used for longer protection paths or could be used as margin towards dynamic impairments. An example is polarization-mode dispersion (PMD), which tends to vary significantly over several days or weeks in certain unstable fiber links [5]. Instead of 'over-engineering' a link with interfaces, the bandwidth could be throttled adaptively in cases of increasing impairments. For applications with moderate-availability requirements, this might be an attractive scenario compared to either the cost of requiring full protection or the cost associated with designing for additional margin to accommodate exceptional events.

It follows that bit-rate flexible transceivers could also be used to accommodate multiple levels of service. Under normal working conditions, the respective working transceivers could carry high-priority traffic plus low-priority (so-called 'best-effort') traffic, and under failure conditions the respective protection interfaces would carry only the high-priority traffic. Best-effort transmission might require new service models, but might be accounted for in a similar fashion as existing extra traffic scenarios in which lower priority traffic occupies the protection path facilities as long as working path options are stable and operational.

As we explore further in Section III, another trait of flexible transceivers is that, depending on the specific implementation, a change in the bit-rate or modulation format of a flexible transceiver can change the spectral bandwidth of the signal. As a channel's spectral bandwidth changes, its slot width could be made flexible, to adaptively utilize the spectral gain width of the optical amplifiers in the system. An application based on this would require supporting flexible grid (filter) hardware.

In the next section of the paper, we discuss methods to create certain modulation formats and data rate flexibility, discuss approaches regarding the symbol rate, and describe differences in OSNR margin required for given modulation formats.

III. APPROACHES FOR FLEXIBLE DATA RATES AND SOFTWARE-DEFINED OPTICS

There are approaches for implementing flexible data rates with software-defined transceivers which could operate at a constant symbol rate or which could change between two or more symbol rates. Given either of these approaches, a number of subcarriers might be used to construct an aggregate channel, a so-called superchannel, which would then be filtered or optically switched through a network as a single entity. The superchannel could be transmitted in an optical OFDM format [6] or in a Nyquist-WDM format [7].

We discuss some possible implementations and approaches in the following subsections of the paper. In Section III A, we introduce a set of possible modulation formats that are suitable to be used by a software-defined transceiver for flexible data rates. These modulation formats can be constructed from a fixed hardware configuration, and we show two such possible fixed configurations. In Section III B we discuss the constant-symbol-rate approach, and then discuss the flexible-symbol-rate approach in Section III C. Both constant- and flexible-symbol-rate approaches will be discussed in the context of a single carrier as well as the more generalized case in which multiple subcarriers are used. In Section III D we discuss bit-rate scaling that is achievable, given a common symbol rate, by changing the modulation format.

A. Modulation Formats and Data Rate Flexibility

M-ary Quadrature Amplitude Modulation (QAM) formats generated for an optical carrier are excellent modulation format candidates for flexible transceivers. The optical I-Q modulators which are used for the polarization-multiplexed quadrature phase-shift keying (PM-QPSK) modulation format (which is currently being widely developed for 100 Gb/s long-haul transmission) can also be used to generate various QAM formats. A given data rate is then possible by supplying appropriate multi-level drive voltages, at particular baud rates, to the embedded Mach-Zehnder (MZ) modulators.

Figure 1a shows a digital-to-analog converter (DAC) which is used to generate binary or multi-level RF signals for the inputs of a parallel MZ modulator structure. As an example, by using the DAC to create six-levels for each embedded modulator, a 36QAM format can be created (Figure 1b). Through proper encoding, any of the constellation points can be purposely avoided. Typically

the four corner points would not be created for a 32QAM format. Figure 1c shows a 16QAM format created from a four-level drive to each modulator, and correspondingly Figure 1d show a 4QAM format (otherwise known as QPSK) created with binary drives to each modulator.
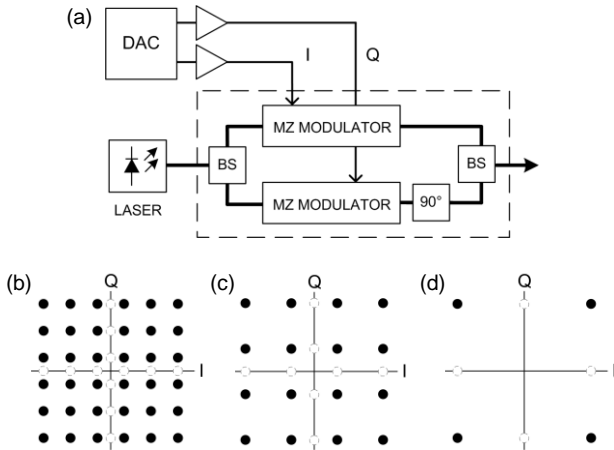

Figure 1. (a) Parallel modulator architecture that can be used to generate various QAM formats: (b) 36QAM or alternatively generation of 32QAM by ensuring through encoding that four (usually the corner) constellation points are not created; (c) 16QAM; (d) 4QAM (QPSK). Open circles indicate respective drive signals to I and Q modulators. Digital-to-Analog Converter DAC; In-phase I; Quadrature phase Q; Mach-Zehnder MZ; Beam Splitter BS; 90° polarization rotator

Given the ability to flexibly change the modulation format between 32QAM, 16QAM, and 4QAM, and thereby change the bit-per-symbol encoding, a system can be operated in various ways. The operational mode would depend on whether the symbol rate is kept constant or has the ability to change, and would also depend on whether the channel is built up from several sub-carriers to construct a superchannel. Given a superchannel, flexibility can come from constructing specific data rates for the channel by allowing the number of sub-carriers to increase or decrease.

In Figure 2, an alternative hardware configuration is shown for generating a set of modulation formats, in which binary signals drive each MZ modulator input. By using drive amplitudes for I1 and Q1 which are equal to half the drive amplitudes for I2 and Q2, 16QAM can be generated. To generate 4QAM, the drive I1 and Q1 could then simply be turned off. Note that with this hardware configuration as shown, the 36QAM or 32QAM format is not generated; however, this could be implemented by using dual-drive MZ modulators to receive a more complex binary drive scheme in place of the I1 and Q1 drive signals.

There is a trade-off in the simplicity of the binary drive input and the increase in complexity of the hardware configuration (as compared to the DAC and dual parallel MZ modulator structure, respectively, in Figure 1). While the quad-parallel modulator architecture is feasible, one complexity that this option brings with it is the proper

biasing of additional MZ modulators as well as the balancing of drive amplitudes and timing between the drive signals.
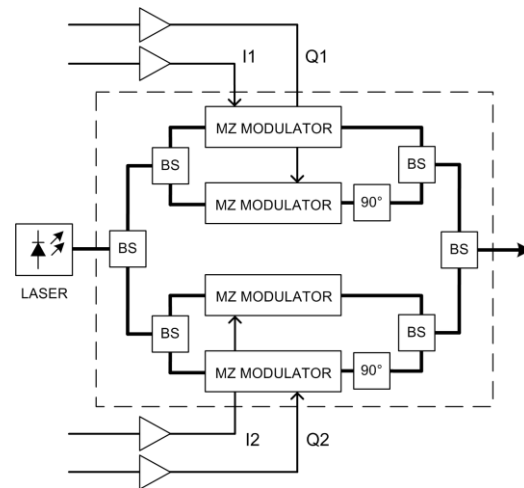
Figure 2. Quad-parallel modulator configuration which uses four separate input binary drive signals. Inputs I1 and Q1 are used to create a QPSK at the combined output of the upper two MZ modulators; correspondingly, inputs I2 and Q2 are used to create a QPSK at the combined output of the lower two MZ modulators. By using drive amplitudes for I1 and Q1 which are equal to half the drive amplitudes for I2 and Q2, 16QAM can be generated.

B. Constant-Symbol-Rate Approach

The electrical and electro-optical components used in a given transceiver each have a limited bandwidth which in part determines the maximum symbol rate that can be achieved for an optical signal. In this section we consider the flexibility of a given software-defined transceiver that operates at a fixed symbol rate which is determined by the respective integrated hardware components.

Flexibility in the transceiver can be implemented in a straight-forward manner by using software-defined components, e.g. FPGA or DSP chips. An increase in the transported data rate can then be achieved with a constant symbol rate by increasing the number of bits encoded within each symbol.

Figure 3 (a-d) shows aggregate channels that can be built up from one or more subcarriers, with flexibility in capacity, bandwidth occupancy, and spectral efficiency; however in each case, baud rate per sub carrier remains a constant value.

Considering Figure 3a, subcarriers modulated with QPSK at 28 Gbaud symbol rate comprise a 400 Gb/s channel given polarization multiplexing (actually a 448Gb/s channel including FEC and OTN framing overhead, but for simplicity we use approximate data payload rates). Subcarriers modulated with 16QAM at the same 28 Gbaud symbol rate then comprise an 800 Gb/s channel (with polarization multiplexing) due to the doubling of encoded bits per symbol (2 bits/symbol per polarization and 4 bits/symbol per polarization,

respectively). In this manner, with a constant symbol rate, flexibility in data rate and spectral efficiency is achievable.

In Figure 3b, a constant data rate is demonstrated by changing the modulation format and changing the number of subcarriers. In this manner, with a constant symbol rate, a constant data rate is maintained while flexibility in the spectral efficiency is achievable.

Figure 3. Flexible modulation and flexible subcarrier count can be combined to create a rate- and/or bandwidth-adaptive channel using the (a-d) constant-symbol-rate approach, or the (e-h) flexible-symbol-rate approach. Aggregate data rates are calculated considering polarization multiplexing.

Figure 3c shows data rate reduction by simply leaving the modulation format constant and reducing the number of subcarriers. While this does not change the spectral efficiency, it may free up spectral occupancy that could be put to use with an addition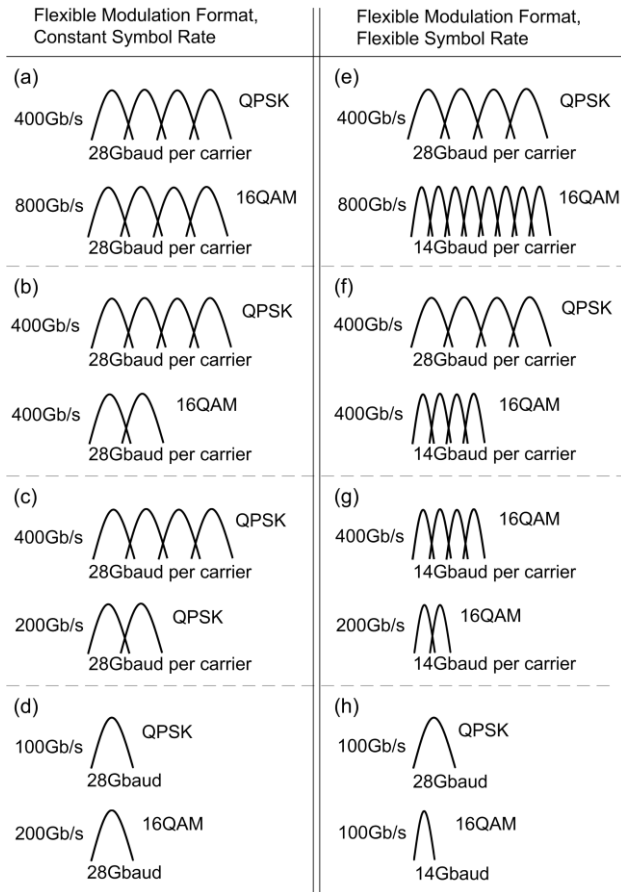al, possibly higher-revenue bearing channel. Note that further bandwidth could be made available if the two-subcarrier QPSK channel were replaced with a single carrier 16QAM channel. This implementation and others depend on the available OSNR margin available or the required OSNR needed by a channel with given reach requirements. This will be further explored in Section III D.

Finally, we consider a single carrier in Figure 3d. In this case, maintaining a constant baud rate necessarily means that the data rate must change.

C. Flexible-Symbol-Rate Approach

Figure 3 (e-h) shows aggregate channels that can be built up from one or more subcarriers, with flexibility in capacity, spectral occupancy, and spectral efficiency, with hardware components in the transceiver that also support a change in the baud rate.

In Section III B, it was already shown that when subcarriers comprise an aggregate channel, flexible bandwidth and flexible grid concepts can be used. What is additionally possible with flexible symbol rates in the context of such aggregate channels is the finer granularity in the steps for flexible data rates. For example, considering the 800 Gb/s option depicted in Figure 3e (vs. the 800 Gb/s option depicted in Figure 3a), and noting that the signal is generated with eight subcarriers, each modulated with a 16QAM format at 14 Gbaud, the aggregate channel can flexibly have its data rate modified in steps of 100 Gb/s via changing to a different number of subcarriers.

Note that with the option to change the symbol rate, it can of course also remain fixed and operate in each of the same conditions as the fixed data rate implementation. That which can be additionally advantageous is the finer granularity in data rate steps as well as the corresponding finer granularity in using flexible amounts of the grid.

D. Modulation Format and Relative OSNR Penalty

Figure 4 shows an estimate of the achievable increase in transmission distance, when variable level m-QAM is used. The OSNR penalty for a number M constellation points [8] versus 4-QAM is approximated as

$$OSNR_{pen} \approx 10\log_{10}\left(\frac{M-1}{3}\right). \quad (1)$$

The data rate that can be transported with M-QAM is

$$R_M = R_4 \frac{ld(M)}{2} , \quad (2)$$

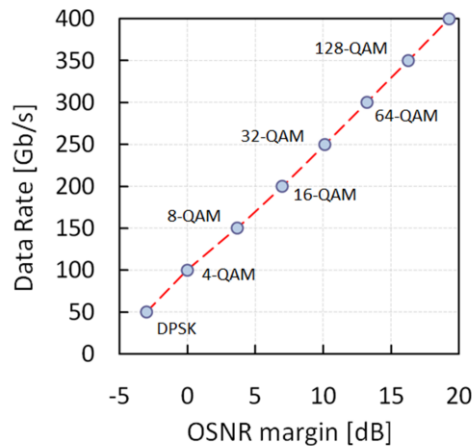where the baseline data rate R_4 is chosen to be 100 Gb/s.

Figure 4. Scalable bit-rate as a function of available OSNR margin. OSNR margins should be evaluated between formats using equal symbol rates, e.g. 50Gbaud, or alternatively 25Gbaud with the use of polarization multiplexing. Note that 56Gbaud and 28Gbaud are line rates used after FEC and OTN framing are considered.

Because 4-QAM encodes two bits per symbol, the symbol rate is 50 Gbaud, or 25 Gbaud if polarization multiplexing is used. Note that 56Gbaud, or 28 Gbaud, respectively, would be actual line rates when FEC and OTN framing are considered. Given an expendable OSNR margin of 13 dB, the transmitted bit-rate can be increased threefold using 64-QAM, while maintaining a constant symbol rate. However, if the OSNR is not sufficient for 100 Gb/s transmission with 4-QAM modulation, the transceiver can operate with halved data rate using DPSK modulation to compensate for 3 dB of OSNR.

The adaptation of the data rate can be done solely by adapting the encoding program in an FPGA. If the number of constellation points is not a power of two, multiple symbols can be combined to yield a better utilization of the channel capacity. However, combining multiple symbols increases the complexity of the signal processing. Consider briefly the case for which we allow a maximum of two symbols to be combined. For instance, the 25-QAM format has an information capacity of 4.64 bits per symbol. The combination of two adjacent symbols enables the encoding of 9 bits per symbol pair, while the remaining information capacity of 0.14 bits per symbol (corresponding to a rate of 7 Gb/s in this example) is discarded.

Depending on the quality of the optical link, the system control plane could trigger an increase in data rate. For dynamic networks, the link quality could be predicted before the channel is turned up, and the expected data rate would be set by software control of the transceiver.

IV. EXPERIMENTAL DEMONSTRATION OF A BIT-RATE FLEXIBLE TRANSCEIVER

Flexibility of the transmission rate and the related OSNR tolerance of a channel can be achieved by a bit-rate flexible transceiver by modifying the number of utilized constellation points in the modulation format. In the laboratory, we assembled a modulation format combining both differential phase-shift keying (DPSK) and multi-level amplitude-shift keying (mASK).

We began by constructing an RZ-DPSK-3ASK modulated optical signal [9] whereby we were able to change the available number of the symbol states via a simple method. We configured our laboratory system using a DPSK transceiver sub-module, with the output signal shaped to return-to-zero (RZ) pulses at the output of a separate MZ modulator and subsequently amplitude modulated in an additional MZ modulator [10].

The amplitude modulation was constructed by driving a push-pull, dual-drive MZ modulator. In this work the drive consisted of two PRBS signals, creating three optical amplitude levels in the signal at the output of the dual-drive MZ modulator. Therefore, the two initial phase constellation points from the DPSK sub-module were each amplitude-modulated to one of three levels, to create the six-point format shown in Figure 5a. The symbol rate was 43 Gbaud, such that, given proper encoding of the binary drives to the dual-drive MZ modulator, a 107 Gb/s signal was achieved.

By turning off one of the drive amplifiers to an RF port of the dual-drive MZ modulator, the input DPSK optical signal was modulated into two amplitude levels, rather than three levels. By reducing the symbol set (constellation points) in this manner, we could eliminate two constellation points from the constellation diagram in Figure 5a, and we also could increase the symbol distance between the two center-most symbols, i.e., the DPSK eye opening was increased by changing the DC bias to the ASK modulator. Figure 5c shows a schematic of the approximate constellation diagram and Figure 5d shows the resulting optical signal magnitude of the RZ-DPSK-2ASK that resulted from turning off a drive amplifier to the dual-drive MZ modulator.

We note here that the ASK signal encoding needed to change when the flexible transceiver moved from a six-point, 3ASK format, to a four-point, 2ASK format. However, the DPSK signal encoding did not need any change. Given a network scenario where an adaptive DPSK-3ASK transceiver is switched to the DPSK-2ASK format, there could be a seamless, error-free transition with respect to the DPSK transmission. The same is true for the reverse course of action, in the scenario where symbol states are added.
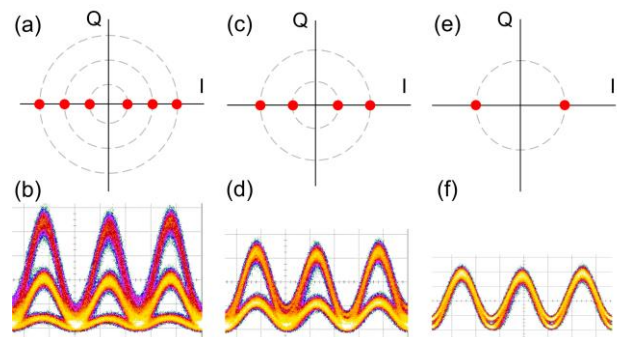
Figure 5. Constellation diagrams and directly detected optical signals, for RZ-DPSK-mASK with m=3, (a) and (b), respectively; m=2, (c) and (d), respectively; and m=1, (e) and (f), respectively.

Note also that both inputs to the dual-drive modulator could be turned off, leaving the system operating with two constellation points for standard DPSK modulation (Figure 5e). The DPSK eye was further increased in this case. Figure 5f shows the RZ-DPSK signal before it was demodulated by a delay line interferometer; therefore the DPSK eye was not directly observed but the height of the lowest amplitude level from a null level corresponded to DPSK eye opening.

We measured BER vs. OSNR for DPSK-3ASK, DPSK-2ASK, and DPSK (Figure 6). The BER for the DPSK signal was measured via the reported pre-FEC (forward error correction) errors in a FEC chip, and the BER for the ASK-encoded data was measured for the ASK eyes with a BER tester (BERT). The 3ASK signal has an upper and a lower ASK eye. Results in Figure 6 report the aggregate ASK BER performance.

The step from DPSK-3ASK to DPSK-2ASK increased the 2ASK eye opening as well as having increased the

DPSK eye opening. The DC bias was subsequently adjusted to improve the DPSK-2ASK performance. The performance could have been further increased by changing the drive amplitude but was not done for this work. At a BER of 10^{-3}, a 5 dB OSNR margin is gained by changing from the 107 Gb/s RZ-DPSK-3ASK signal to the 86 Gb/s RZ-DPSK-2ASK signal; an additional 7 dB OSNR margin is gained by changing to the 43 Gb/s RZ-DPSK signal.
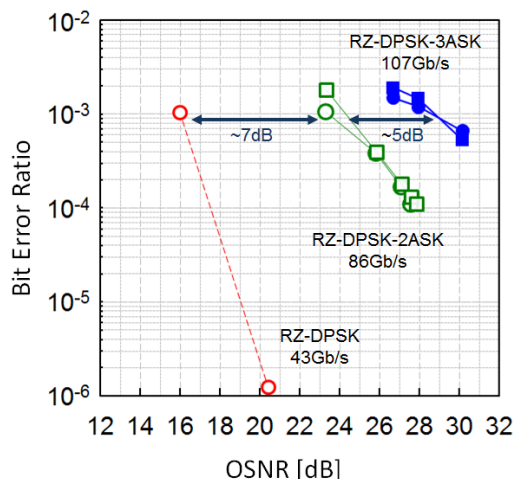
Figure 6. OSNR (0.1nm noise bandwidth) tolerances for DPSK-3ASK, DPSK-2ASK, and DPSK. For each format, the BER results of the data encoded with DPSK are the circle data markers.

These measurements demonstrate a possible adaptive receiver functionality that could be used to enable a set of modulation/demodulation formats, each supporting a specific data rate and different tolerances to system impairments. Data rates could then be chosen based on the specific network environment.

V. NETWORK IMPACT OF DATA RATE FLEXIBILITY

Given the data rates discussed, minimum transparent transmission distances which are at least several hundred kilometers in length would allow for several operation modes (e.g., short distance with high bandwidth vs. long distance with lower bandwidth), thus taking advantage of rate-flexible designs. Additionally, a programmable channel bandwidth scheme with a flexible grid [11] would be an advantageous way to benefit from the variation in spectral occupancy which in several scenarios would accompany flexible data rate operation. This would mark a necessary change from today's WDM grid, i.e., ITU-T G.694.1 with 50 GHz or 100 GHz channel spacing.

Modifications in traditional network architectures would also be required relating to the interfacing between the optical transport layer and the Layer-1/2/3 clients (e.g., electrical cross connects, switches, or routers). Today, in a typical scenario, interfaces run at fixed bit-rates, for example 10G (examples are STM-64, ODU2/OTU2, and 10GbE LAN PHY), although some mechanisms exist for aggregate payload flexibility,

namely the ITU-T G.7042 Link Capacity Adjustment Scheme (LCAS). Without LCAS or similar Ethernet (Layer-2) mechanisms, flexible bit-rates are not supported by the clients. In order to make use of bit-rate flexible transceivers, client interfaces need to support rate adaptation as well.

In addition, a paradigm shift might be required concerning Quality-of-Service (QoS) and the related service-level agreements (SLAs) between a service provider and its customers. For example, SLAs may need to change from guaranteed availabilities for fixed bandwidths to a combined guaranteed Availability x Bandwidth (A x B) product. While this is not commonplace today, it nonetheless has market potential due to the potential for lower cost, and as such may be an attractive solution alternative for innovative network operators and service providers.

VI. CONCLUSIONS

Adaptive optical transmission can be made possible through the use of flexible bit-rates over varying transmission distances, with the flexibility determined in part by OSNR margins and the spectral occupancy of the channel. In dynamic optical networks, this methodology could be used to decrease the cost of transmission. M-ary QAM formats, with varying M, are well suited for such bit-rate flexible transceivers, due to the ability to change modulation formats with a fixed hardware configuration. Additionally, we presented experimental results from a DPSK-*m*ASK modulation format, where *m* unipolar ASK levels were used to step between line rates having different OSNR performance. In the network context, new models with regard to QoS and related SLAs may be required in order to make full use of the potential savings offered by bit-rate flexible transceivers.

REFERENCES

[1] S. Azodolmolky et al., "A Dynamic Impairment-Aware Networking Solution for Transparent Mesh Optical Networks," *IEEE Commun. Mag.*, vol. 47, pp. 38-47, May 2009.

[2] I. Baldine, R. Dutta, G. Rouskas, "A unified architecture for cross layer design in the future optical internet," *Proc. ECOC 2009, 35th European Conference on Optical Communication*, 2009.

[3] A. Kaul, "Software-Defined Radio: The Transition from Defense to Commercial Markets," *Proceeding of the SDR 07 Technical Conference and Product Exposition*, 2007.

[4] B. Koley, "100GbE in Datacenter Interconnects: When, Where," *Presentation ECOC 2009*, Online. Available: http://conference.vde.com/ecoc-2009/programs/ documents/ecoc09-100g-ws-google-koley.pdf

[5] M. Karlsson, J. Brentel, and P. A. Andrekson, "Long-Term Measurement of PMD and Polarization Drift in Installed Fibers," *J. Lightwave Technol.*, vol. 18, pp. 941-951, 2000.

[6] S. Chandrasekhar, X. Liu, "Terabit Superchannels for High Spectral Efficiency Transmission," *Proc. ECOC 2010, 36th European Conference on Optical Communication, 2010.*

[7] G. Bosco, V. Curri, A. Carena, P. Poggiolini, F. Forghieri, "On the Performance of Nyquist-WDM Terabit Superchannels Based on PM-BPSK, PM-QPSK, PM-8QAM or PM-16QAM," *IEEE Lightwave Technolog.,* vol. 29, pp. 53-61, 2011.

[8] J. G. Proakis, *Digital Communications, Fourth Edition*, New York, McGraw-Hill, 2001.

[9] M. Eiselt, B. Teipen, "Cost-effective 100Gbps Optical Modulation Format for Metro Networks," in *Proc. ITG-Fachbericht 207 Photonische Netze*, pp. 61-65, April 2008.

[10] M. Eiselt and B. Teipen, "Requirements for 100-Gb/s Metro Networks," in *Proc. OFC 2009*, paper OTuN6.

[11] S. Gringeri, B. Basch, V. Shukla, R. Egorov, T.J. Xia, "Flexible Architectures for Optical Transport Nodes and Networks," *IEEE Commun. Mag.,* vol. 48, pp. 40-50, July 2010.

Brian T. Teipen received the B.S. degree in physics from Indiana University, Bloomington in 1995, and the Ph.D. in electrical engineering from The University of Texas at Dallas in 2000.

From 2000 to 2007, he held positions in the telecommunications industry in roles dedicated to testing, designing and planning optical transport networks. In 2007 he joined the Advanced Technology group at ADVA AG Optical Networking in Meiningen, Germany to focus on 100 Gbit/s research objectives, and since 2011 has been with ADVA Optical Networking in Norcross, Georgia, USA as Principal Engineer Advanced Technology.

Dr. Teipen is a member of the IEEE Photonics Society, OSA (The Optical Society of America), and VDE-ITG Information Technology Society.

Michael H. Eiselt received the Dipl.-Ing. degree in electrical engineering from University Hannover, Germany in 1989 and the Dr.-Ing. degree from Technical University Berlin, Germany in 1994.

From 1989 to 1997, Dr. Eiselt was a research staff member at Heinrich-Hertz-Institute, Berlin. In 1995/96, he spent a year as a visiting scientist with AT&T Bell Labs, Crawford Hill Labs, Holmdel, NJ. From 1997 to 2000, Dr. Eiselt was with the Lightwave Network Research dept. of AT&T Labs-Research in Middletown, NJ, and from 2000 to 2005, he was a Principal Architect for Celion Networks, designing ultra-long haul optical transmission systems. In 2005, he joined ADVA AG Optical Networking in Meiningen, Germany, where he is currently a Director in the Advanced Technology department. Dr. Eiselt has authored or co-authored more than 100 scientific papers and holds 26 patents. He is a Fellow of the Optical Society of America, a Senior Member of the IEEE Photonic Society, and a Member of the German Society for Information Technology (VDE-ITG).

Klaus Grobe received the Dipl.-Ing. and Dr.-Ing. degrees in electrical engineering from Leibniz University, Hannover, Germany, in 1990 and 1998, respectively.

From 1990 to 1993, he worked on fiber-optic telemetry and surveillance systems for deep-sea research. From 1998 to 2000, he worked for German and pan-European network operators where he designed WDM transport networks. Since 2000, he is with ADVA AG Optical Networking where he is now working in the Advanced Technologies group. Dr. Grobe authored and co-authored more than 70 scientific publications as well as three book chapters on WDM and PON technologies.

Dr. Grobe is member of the IEEE Photonics Society, the German VDE ITG (German Association for Electrical, Electronic & Information Technologies), ITG Study Group 5.3.3 on Photonic Networks, and OFC Sub-Committee F. He is also working in FSAN NG-PON2 activities.

Jörg-Peter Elbers received the diploma and the Dr.-Ing. degree in electrical engineering from Dortmund University, Germany, in 1996 and 2000, respectively.

From 1999-2001 Dr. Elbers was with Siemens AG – Optical Networks, last as Director of Network Architecture in the Advanced Technology Department. In 2001 he joined Marconi Communications (now Ericsson) as Director of Technology in the Optical Product Unit. Since September 2007 he is with ADVA AG Optical Networking, where he is currently Vice President Advanced Technology in the CTO office.

Dr. Elbers authored and co-authored more than 70 scientific publications and 14 patents. He is member of the IEEE LEOS as well as the German VDI (Association of German Engineers) and VDE (German Association for Electrical, Electronic & Information Technologies). Dr. Elbers is a frequent reviewer of technical publications and serves in technical program committee of the European Conference on Optical Communication (ECOC). He is also member of the VDE expert committee for optical communications engineering.

Optimization Framework for Supporting 40 Gb/s and 100 Gb/s Services over Heterogeneous Optical Transport Networks

João Santos[1,2*], João Pedro[1,2], Paulo Monteiro[1,3], João Pires[2]

[1] Nokia Siemens Networks S.A., R. Irmãos Siemens 1, 2720-093 Amadora, Portugal
[2] Instituto de Telecomunicações, Instituto Superior Técnico, Av. Rovisco Pais 1, 1049-001 Lisboa, Portugal
[3] Instituto de Telecomunicações, Universidade de Aveiro, Campus de Santiago, 3810-193 Aveiro, Portugal
* Tel: +351 21 4167130, Fax: +351 21 4242082, e-mail: joao.santos@nsn.com

Abstract—**Continuous traffic growth and crunched profit margins are leading network operators to deploying high-capacity backbone infrastructures with minimal capital investment. However, the cost-effective design of optical transport networks (OTNs) remains a complex challenge subjected to multiple constraints, e.g., maximum bit rate per channel, electrical multiplexing capabilities, wavelength count per fiber, optical interface cost, maximum transparent reach, etc. To efficiently solve this multi-constrained dimensioning problem in presence of heterogeneous client demands and optical channel rates of 40 Gb/s and 100 Gb/s, this paper presents a novel hybrid optimization framework. The proposed approach is based on an iterative combination of linear programming and rounding algorithms for the demand routing, with graph coloring heuristics for the wavelength assignment. The performance of this framework is assessed and compared with a similar approach that resorts to an integer linear programming (ILP) model to route the demands. The results obtained show that our proposal is able to reach the same low network expenditures as the ILP while requesting less computation time. We also confirm that the most cost-effective network solutions are attained when optical line rate heterogeneity is jointly applied with diverse multiplexing capabilities at the OTN electrical layer, such as grooming and inverse-multiplexing.**

Index Terms—**network dimensioning, optical transport network, Ethernet, routing and wavelength assignment.**

I. INTRODUCTION

The increased adoption of IP-based applications in both business (e.g., cloud computing, VPN services) and residential (e.g., social networking, IPTV, file sharing) areas is leading to a significant growth of traffic over the existing telecom networks. At the customer premises, broadband access connectivity is guaranteed by recent fiber (PONs), copper (xDSL), and wireless (HSPA, LTE) technology deployments. Moreover, novel high-speed Ethernet interfaces of 40 Gb/s (40G) and 100 Gb/s (100G), recently standardized by IEEE [1], are expected to be deployed at the network aggregation segment in order to meet the rapidly growing traffic requirements. Concurrently, the capacity of optical transport network (OTN) systems has been upgraded by ITU-T with the addition of the 100 Gb/s digital container specification for long-haul transmission [2], [3]. However, the increasing market competition is putting service providers under continuous economical pressure. As a result, the adoption of novel optical technologies is hampered by the impact they have on currently deployed fiber infrastructure. Therefore, in order to abide to the engineering rules established for 10 Gb/s and 40 Gb/s network design, 100 Gb/s optical systems require the use of advanced modulation formats (e.g., CP-QPSK) and intensive digital signal processing to mitigate the impact of chromatic and polarization mode dispersion. For these reasons, innovative component design, integration, and packaging techniques are required for complying with the new transceiver architectures devised for these next-generation systems. Thus, the ongoing research and development efforts could be materialized into a first breed of 100 Gb/s products but at the expense of higher costs. In this scenario, the cost of one 100 Gb/s interface may surpass that of one, two, or even more 40 Gb/s interfaces, compromising the massive proliferation of these systems.

Capital expenditures (CAPEX) in long-haul optical networks are typically dominated by transceiver and regenerator costs [4]. Still, optical interface cost and line rate capacity are not the only factors needed to make a consistent decision about the most cost-efficient network design. In addition, the network planner must account for the following factors: optical transmission performance, which determines the maximum transparent reach and the number of required regenerators; wavelength count limit, that upper-bounds the number of optical channels traversing any given fiber link; the type of client service requests, which define the granularity of the traffic flows carried over the optical network; mixed line rate (MLR) capabilities, which imposes an heterogeneity in the bandwidth of the available optical channels; and traffic engineering techniques, that indicate the type of multiplexing procedures applicable at the electrical processing layer, such as grooming or inverse-multiplexing. The combined influence of these design aspects has been repeatedly neglected in the existing literature [5-7]. In [5], [6] an ILP model and a heuristic method are described to cost-effectively design

MLR networks. However, such proposals assume that only transparent lightpaths can be established, thus neglecting the important contribution of the regeneration equipment to the final network cost estimation and the use of translucent paths to satisfy the demands. Furthermore, a set of fixed cost relations are assumed between the different optical interfaces. Although such assumption may be acceptable in a very specific scenario, these prices have a tendency to vary along the commercial life of the transmission equipment. The authors of [7] present a heuristic solution that also uses the maximum optical reach constraint for solving the MLR problem. However, channel rate heterogeneity is only allowed for different links, i.e., all the lighpaths passing through a given link are required to have the same capacity over that fiber segment. This assumption limits the full application of the MLR concept and requires additional signal processing equipment for forwarding traffic between links of different capacities. Moreover, the aforementioned publications [5-7] also neglect the application of inverse-multiplexing for transmitting large traffic demands over cost-effective optical channels of lower capacity.
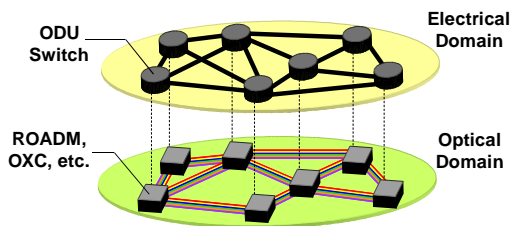

Figure 1.   Optical transport network architecture.

Our previous work [8], presented an optimization framework targeting the dimensioning of an OTN-based infrastructure for 40G and 100G service demands while taking into consideration the relative price and optical reach of the 40G and 100G optical interfaces. With the objective of minimizing the inherent expenditures, the total network cost accounted the transceiver and regenerator costs for each optical technology. In addition, some typical OTN functionalities, such as traffic grooming and inverse-multiplexing, were employed to encapsulate the traffic demands onto the channels offering the lowest cost figures. The design problem, which was formulated as an integer linear programming (ILP) model, was basically restricted to service provisioning at the optical channel data unit (ODU) network layer. In this case, and since wavelength assignment was neglected, the wavelength count limit per link was seen as a bound to the maximum number of ODU circuits supported in each link. However, when this solution is applied to a realistic OTN network scenario that includes the optical domain (see Fig. 1), two evident drawbacks can arise. Firstly, the paths provisioned at the electrical ODU level cannot be immediately transposed to the optical layer without being assigned a specific wavelength. This process imposes the wavelength continuity constraint and the result of performing wavelength assignment after routing may lead to a

number of required wavelengths that surpasses the maximum wavelength count per link. This outcome can be even more problematic if the regenerators are inhibited from performing any wavelength conversion because the same wavelength needs to be reserved on the entire path. Secondly, considering the routing and the wavelength assignment together significantly increases the number of variables and constraints of the ILP model. This makes the problem intractable for networks of reasonable size.

In view of these limitations, this paper proposes an alternative approach which separates routing from wavelength assignment while guaranteeing that a specific number of maximum wavelengths per fiber is not exceeded on both procedures via an iterative process. At the routing and interface selection stage, two distinct methods are applied: the previously proposed ILP model [8], and a linear programming model combined with rounding heuristics (LP+R). The latter approach can, in theory, require less computation time than the former to solve the same dimensioning problem. However, and since the integral constraints are relaxed, variable rounding may lead to a solution less than optimal. At the second stage, a set of known heuristics solves the wavelength assignment problem in network scenarios where the maximum number of required wavelengths per link is expected to remain equal to the wavelength count limit initially imposed during the routing. In case of the initial wavelength limit being exceeded, the procedure is repeated, by decreasing the number of wavelengths available for routing, until the initial wavelength count is satisfied after the wavelength assignment procedure. During this process, and when the wavelength count is decremented, the routing methods are expected to find a new solution (either by modifying the paths selected or by employing a distinct type of multiplexing) that ensures the demand satisfaction. The performance of this optimization framework is conveniently assessed in two reference topologies, considering heterogeneous (40G and 100G) demands as well as heterogeneous optical channel capacities.

This article is organized as follows. Section II introduces the OTN multiplexing hierarchy and the functionalities applicable in our optimization framework. Section III presents and describes an optimization procedure for designing MLR networks under multiple constraints, such as wavelength count, optical interface cost, and optical transparent reach. The design of two backbone networks is pursued in section IV to deliver an adequate comparison between the ILP and LP+R methods and demonstrate the benefits derived from optimized MLR implementations. Finally, the main conclusions from this work are crystallized in section V.

II. TRAFFIC MULTIPLEXING IN OPTICAL TRANSPORT NETWORKS

The OTN is a circuit-switched technology that offers connectivity between higher layer services and the underlying optical domain [9]. Such services comprise a large diversity of technologies, ranging from Ethernet to SONET/SDH, Fibre-Channel (FC), and Multi-Protocol

Label Switching (MPLS). To deliver these services with the required efficiency, OTN was defined as a layered hierarchy (see Fig. 2) where each layer is dedicated to a set of specific functionalities. The different layers are defined and distributed between an electrical switching domain and an optical switching domain.
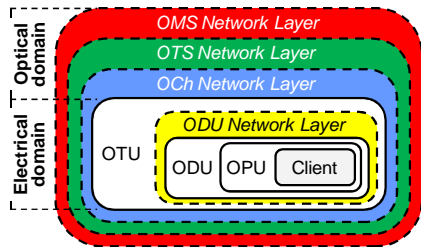

Figure 2.   OTN layered architecture

At the electrical OTN layer, a group of digital framing structures (also called containers) are used to encapsulate the client traffic, such as the optical channel payload unit (OPU), the ODU (both within the ODU network layer), and the optical channel transport unit (OTU). These containers are electrically processed and support several functions, e.g., client signal adaptation to the OTN channel, multi-domain route tracing, signal supervision, FEC processing, etc [3]. The ODU network layer further includes the inverse-multiplexing protocol, named virtual concatenation (VCAT), and the link capacity adjustment scheme (LCAS), permitting to adjust the capacity allocated to a given service by dynamically adding/deleting channels from a concatenation group. At the optical domain, the optical channel (OCh) layer is responsible for managing the signal transmission between 3R (regeneration) points, while the optical transmission section (OTS) and the optical multiplex section (OMS) are dedicated to managing the multi-wavelength signals between the line amplifiers of a single optical span and between multiple optical spans delimited by optical multiplexing equipment, respectively. In such layers, signal quality monitoring and implementation of reliable protection mechanisms are also implemented.
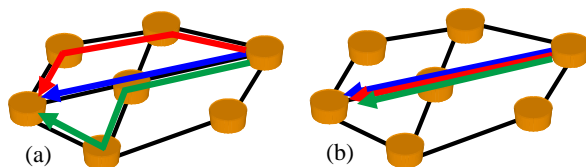

Figure 3.   (a) Multipath and (b) single-path ODU routing.

OTN has also been specified to support a wide range of bit-rate capacities [3]. For each container type, the bit rate capacity is identified by its order k. For the basic framing structure, the OPUk, the bit-rates supported vary from 2.488 Gb/s (k=1), 9.995 Gb/s (k=2), 40.150 Gb/s (k=3), to 104.355 Gb/s (k=4). When VCAT is applied, a set of OPUk containers are grouped to form the augmented OTN channel OPUk-Xv, where X represents the number of OPUk units in the concatenation group. Note that when VCAT is used, the OPUk containers of each group are viewed and handled as independent elements by the following ODU and OTU layers.

Importantly, after mapping each container into an independent optical channel, the concatenation group can be routed in a multipath (diverse-path routing) or single-path (co-routing) fashion, as shown in Fig. 3.
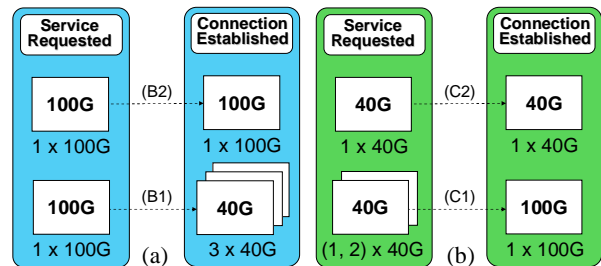
Figure 4.   100G and 40G service multiplexing alternatives.

Essentially, the subject of this study relies on an optical network implemented accordingly to the OTN layered architecture (see Fig. 2) for supporting 100 Gb/s and 40 Gb/s services, e.g., high-speed Ethernet flows [10], over heterogeneous optical interfaces. To account for the multiplexing flexibility available in OTN, each service type, either 100G or 40G, can be transported over the optical domain by one of two different ways. As observed in Fig. 4(a), if the request from the Ethernet layer comprises a 100G flow, it can be either forwarded directly through a 100G optical channel (with OPU4 wrapping) or virtually-concatenated over three 40G optical channels (OPU3-3v solution). As mentioned, the latter case enables the use of multipath routing, if required. On the other hand, as shown in Fig. 4(b), each 40G request can be directly mapped into a 40G optical channel (OPU3 container) or up to two 40G signals can be multiplexed (groomed) into a single 100G wavelength (OPU4 container). Thus, the number of wavelengths allocated at the optical domain will be dependent on the type of multiplexing procedure selected at the OTN electrical layer. In terms of network dimensioning, the quantity of channels required is reflected on a given cost (according to the interface type) and on a certain number of wavelengths that need to be available in the fiber links.

III. HYBRID OPTIMIZATION FRAMEWORK

As previously mentioned, our optimization strategy is based on a combination of linear programming and heuristic procedures. Linear programming techniques are applied in both ILP and LP+R models. Fundamentally, the LP+R approach aims at relaxing the ILP model to avoid using time-consuming enumeration techniques (e.g., branch-and-bound). The integrality of the variables is obtained after applying a rounding procedure to the LP solution. The proposed framework, described in Fig. 5, receives as input several parameters, among which the wavelength count limit per fiber W. The first stage selects the optical interface capacity and the routing paths used to transmit the client data while minimizing the total network cost. During this stage, the number of ODUs occupying each fiber link is limited to W and the multiplexing schemes of the demands applied at the OTN electrical layer (e.g., direct mapping, grooming, or inverse-multiplexing) are also selected. Since wavelength

assignment is not considered in this stage, the underlying optical layer is viewed as being opaque (where any wavelength assignment restrictions are neglected). On the other hand, the number of regenerators required in each path is included in the network cost estimation. As output, a set of routing paths (consisting of links and nodes traversed) is delivered to the subsequent optimization stage, where wavelength assignment is then carried out. Here, known graph coloring heuristics [11], [12] are employed to sort the wavelength associated to each routing path and minimize the number of different wavelengths used. In this case, both the wavelength uniqueness per link and the wavelength continuity constraints are enforced. Although the existence of regenerators is included for cost estimation purposes, the possibility of doing wavelength conversion in this equipment is not assumed. Hence, the wavelength assignment of the routing paths is done transparently, i.e., the same wavelength selection is maintained over the set of links composing each path. By separating the wavelength assignment from the routing process, there is a possibility that the number of different wavelengths allocated to the routing paths surpasses W. Whenever this occurs, the value of W at the routing stage is decremented and the dimensioning process is repeated until the initial W is satisfied by the number of wavelengths assigned. If the new values of W prevent the routing stage from establishing all the demands, the iterative dimensioning process is terminated.
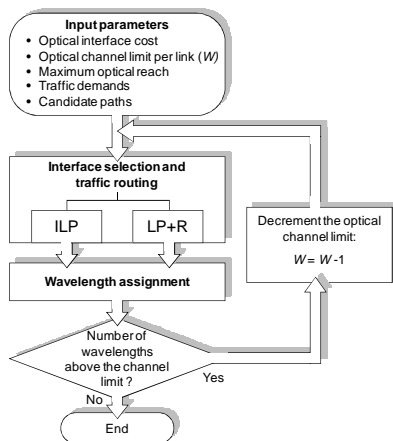

Figure 5. Optimization framework flowchart.

The routing and interface selection stage can be executed in two different ways: through an ILP model or via the LP+R approach. The ILP model is explained as follows. As input, the network topology is given to the ILP model as a graph $G(V, E)$, where V and E comprise the non-empty sets of vertices and edges, respectively. Two demand matrices, each dedicated to a different client traffic type, containing the number of flows t^{sd} exchanged between each source s and destination d node pairs, are also provided. In detail, the subsequent sets of parameters, constants and variables are used:

Parameters:

W: maximum number of wavelengths per link

K: number of shortest paths computed for each sd node pair

α: cost relation between 100G and 40G interfaces (see (1))

β: relation between the maximum transparent reach for 40G and 100G interfaces (see (2))

Constants:

$C_{100}^{TxRx}, C_{40}^{TxRx}$: transceiver cost for 100G/40G optical interfaces

$D_{100}^{\max}, D_{40}^{\max}$: maximum reach for 100G/40G optical interfaces

$Reg_{100}^{sd,k}, Reg_{40}^{sd,k}$: number of regenerators required in the k-th 100G/40G path between the sd node pair

$D^{sd,k}$: length of the k-th path between the sd node pair

$t_{100}^{sd}, t_{40}^{sd}$: number of 100G/40G flows exchanged between the sd node pair

$\delta_{ij}^{sd,k}$: equal to 1 if the link between ij nodes is traversed in the k-th path between the sd node pair, and 0 otherwise

Variables:

$total\_cost$: total network cost, accounting for the price of transceivers and regenerators

$x_{100,n}^{sd,k}, x_{40,n}^{sd,k}$: equal to $t_{100,n}^{sd} / \left\{1, ..., 3t_{100,n}^{sd}\right\}$ if the k-th 100G/40G path is used to transport the n-th 100G service flow between the sd node pair, and 0 otherwise

$y_{100,m}^{sd,k}, y_{40,m}^{sd,k}$: equal to $1 / \left\{1, ..., t_{40,m}^{sd}\right\}$ if the k-th 100G/40G path is used to transport the m-th 40G service flow between the sd node pair, and 0 otherwise

The ILP model aims at minimizing the cost of the network while resorting to both 40G and 100G optical technology. In order to differentiate the capital expenditures related with each option we define a cost model based on the transceiver cost ratio (1), identified as α, and on the maximum optical distance without regeneration ratio (2), denoted as β. In essence, an increase in α reflects a transceiver cost increase for the 100G interfaces in comparison with the 40G ones. Conversely, an increase of β above the unitary value means that the maximum optical reach of 40G transceivers surpasses the one provided by 100G equipment. The maximum optical reach of each transceiver type is used in (3) to calculate the minimum number of 3R regenerators required in a given path and for a given optical channel capacity. This number is obtained by relating the path distance with the maximum reach of the optical interface. For the sake of simplicity, it is also assumed that the cost of one regenerator corresponds to that of two transceivers. Additionally, the traffic demand of each sd pair for 100G demands is

divided in (4) into N multiples of unitary 100G flows. For 40G requests, (5) partitions the traffic demand into M multiples of two 40G flows to enable grooming of up to two flows into each 100G channel.

$$C_{100}^{TxRx} = \alpha \cdot C_{40}^{TxRx} \qquad (1)$$

$$D_{40}^{\max} = \beta \cdot D_{100}^{\max} \qquad (2)$$

$$Reg_{100}^{sd,k} = \left\lceil \frac{D^{sd,k} - D_{100}^{\max}}{D_{100}^{\max}} \right\rceil, \quad Reg_{40}^{sd,k} = \left\lceil \frac{D^{sd,k} - D_{40}^{\max}}{D_{40}^{\max}} \right\rceil \qquad (3)$$

$$t_{100,n}^{sd} = \begin{cases} 1, & \text{if } n <= t_{100}^{sd} \\ 0, & \text{otherwise} \end{cases} \quad \forall_n \qquad (4)$$

$$t_{40,m}^{sd} = \begin{cases} 2, & \text{if } \left(\text{mod}_2\left(t_{40}^{sd}\right) = 1 \wedge m < \left\lceil t_{40}^{sd}/2 \right\rceil \right) \vee \\ & \left(\text{mod}_2\left(t_{40}^{sd}\right) = 0 \wedge m <= \left\lceil t_{40}^{sd}/2 \right\rceil \right) \\ 1, & \text{if } \text{mod}_2\left(t_{40}^{sd}\right) = 1 \wedge m = \left\lceil t_{40}^{sd}/2 \right\rceil \\ 0, & \text{otherwise} \end{cases} \quad \forall_m \qquad (5)$$

The objective function and the constraints of the proposed ILP model are presented and explained hereafter:

Objective:

$$\min \ total\_cost \qquad (6)$$

Subject to:

$$\frac{1}{3} \sum_k x_{40,n}^{sd,k} + \sum_k x_{100,n}^{sd,k} = t_{100,n}^{sd}, \quad \forall_n \forall_{sd} \qquad (7)$$

$$\sum_k y_{40,m}^{sd,k} + \sum_k \left(t_{40,m}^{sd} \cdot y_{100,m}^{sd,k} \right) = t_{40,m}^{sd}, \quad \forall_m \forall_{sd} \qquad (8)$$

$$\sum_{sd} \sum_k \sum_n \left(x_{40,n}^{sd,k} + x_{100,n}^{sd,k} \right) \cdot \delta_{ij}^{sd,k} + \\ \sum_{sd} \sum_k \sum_m \left(y_{40,m}^{sd,k} + y_{100,m}^{sd,k} \right) \cdot \delta_{ij}^{sd,k} \le W, \ \forall_{ij} \qquad (9)$$

$$total\_cost = \sum_{sd} \sum_k \sum_n \left[C_{40}^{TxRx} \left(x_{40,n}^{sd,k} + y_{40,n}^{sd,k} \right) \cdot \left(Reg_{40}^{sd,k} + 1 \right) \right] \\ + \sum_{sd} \sum_k \sum_n \left[C_{100}^{TxRx} \left(x_{100,n}^{sd,k} + y_{100,n}^{sd,k} \right) \cdot \left(Reg_{100}^{sd,k} + 1 \right) \right] \qquad (10)$$

This model consists of a multi-commodity formulation where both the objective function and the constraints are expressed as linear functions. The objective function (6) aims at minimizing the total network expenditures *total_cost* of the network. At the output, the ILP model returns the routing of all 100G and 40G demands using integer variables x and y, respectively. For satisfying the

100G demands, each 100G signal may be sent over a single 100G channel, or via three 40G channels when exploiting VCAT. Therefore, constraint (7) is simultaneously used for assuring that the traffic demand is satisfied and for opting between single-channel or inverse-multiplexed transmission. In addition, expression (7) enables to individually select the routing path of each ODU, thereby determining if the virtually concatenated ODUs are co-routed or diversely routed. The 40G demands may be directly transmitted over 40G channels or groomed into 100G channels, as defined in constraint (8). Constraint (9) guarantees that the maximum number of optical channels per fiber link is not exceeded. Finally, in (10) the *total_cost* is associated to the set of transceivers and regenerators required to satisfy all the traffic demands.
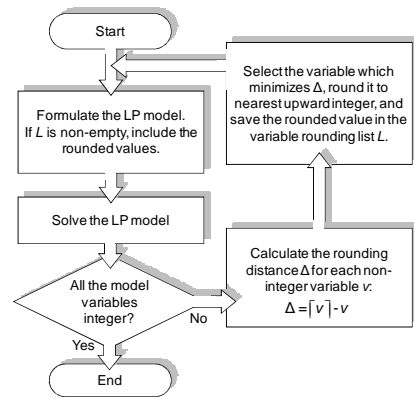
Figure 6.   LP+R routing routine flowchart.

Alternatively to solving the ILP model, the LP+R method may result in a less time consuming procedure if recurrent routing executions are needed to satisfy the wavelength link capacity bound. Transforming the ILP problem into an LP formulation basically consists in relaxing the integrality characteristic from the decision variables ($x_{100,n}^{sd,k}$, $x_{40,n}^{sd,k}$, $y_{100,m}^{sd,k}$, and $y_{40,m}^{sd,k}$). Eventually, the LP solution may deliver non-integral variables that cannot be used for dimensioning purposes. For this reason, as depicted in Fig. 6, the LP+R method is implemented as an iterative procedure that rounds the routing variables to its nearest integrals while satisfying the remaining constraints of the model. Importantly, this is an incremental method, i.e., it only rounds one variable per iteration, enabling the following LP execution to take into account previous rounding decisions while minimizing the network cost.

After concluding the routing of the demands, the wavelength assignment for each optical channel is processed through two consecutive steps. In the first step, three graph coloring algorithms (Largest First, Smallest Last, and Color Degree) [11] are concurrently employed to obtaining an initial solution to the wavelength assignment problem. With this strategy, it is assured that the results are not biased by any particular graph coloring algorithm. In the second step, an iterative algorithm (known as Iterated Greedy [12]) is applied to further reduce, if possible, the amount of necessary colors (wavelengths).

IV. RESULTS AND DISCUSSION

The performance of our optimization framework is assessed in the 19-node EON and the 24-node UBN reference networks (both depicted in Fig. 7). About 80% of the existing node pairs are randomly selected to exchange 1x100G and 4x40G services. The resulting traffic matrices can be viewed in Fig. 8. For each node pair, 5 candidate paths are pre-computed using a K-shortest paths algorithm. The maximum optical reach for 100G systems is assumed to be 1000 km while 40G technology is able to extend this reach by 30%. The interface cost of 40G systems is fixed with a unitary value while 100G prices vary from 1 to 4 units. Due to space restrictions, the results shown for each W are representative of the averaged results obtained for the different 100G interface prices. Each execution of the ILP model was upper-bounded to one hour to prevent unacceptable running times. In the cases where the ILP interruption is forced, the best solution obtained up to that moment is used. Both ILP and LP problems are solved with *lp_solve* [13].
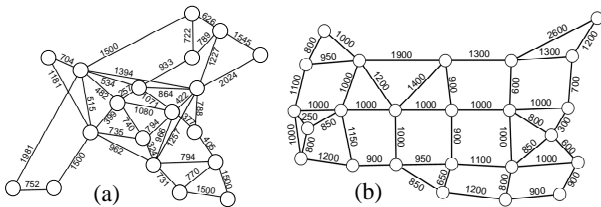
Figure 7.   (a) EON and (b) UBN topologies (distances in km).
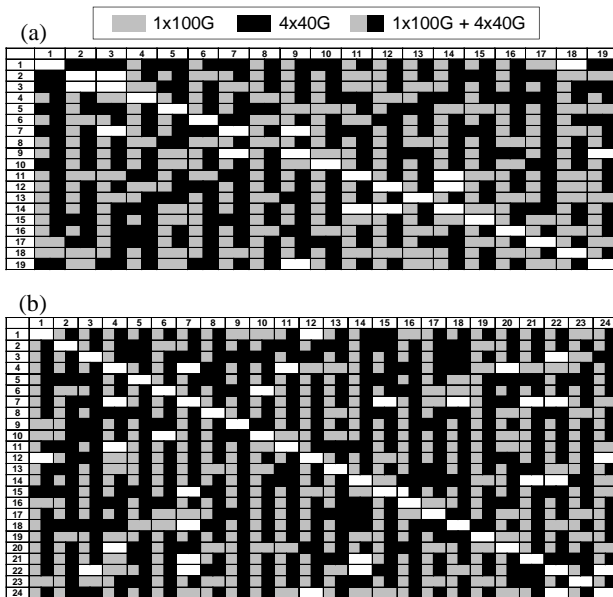
Figure 8.   (a) EON and (b) UBN static Ethernet demands.

The average results obtained for both topologies are depicted in the figures below. Several line rate scenarios are evaluated: the case in which both 100G and 40G optical technologies coexist (100G/40G); the case in which only 100G interfaces are available; and the scenario where only 40G-based channelization is applicable. The possibility of having full or limited

multiplexing functionalities (grooming, VCAT) will also be considered.
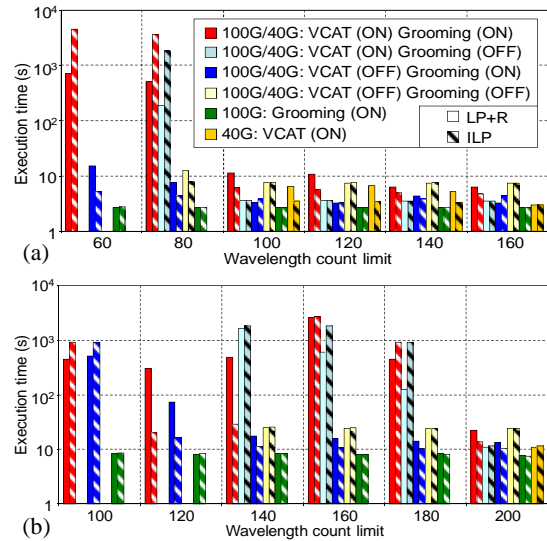
Figure 9.   Execution time for (a) EON and (b) UBN.

Fig. 9 exhibits the computation time requested by each optimization method employed at the routing stage. As expected, the LP+R approach typically requires less time to solve the complete optimization problem. Note that the computation time advantage of LP+R over ILP is expected to be more pronounced in case the ILP execution time is not upper-bounded and the problem size is augmented. In general, the 100G/40G scenarios exploiting VCAT are the ones which demand the highest computational effort, as a result of the larger number of variables required. In contrast, the smallest execution times are obtained with the single line rate solutions.
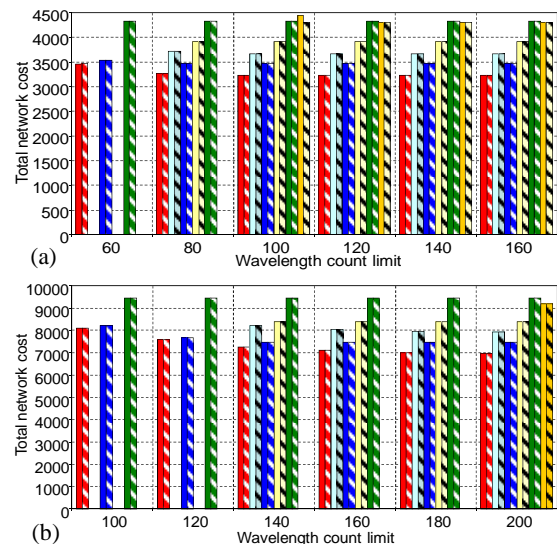
Figure 10. (a) EON and (b) UBN network cost.

Regarding the network cost minimization, whose results are reproduced in Fig. 10, the difference between the ILP and LP+R approaches is practically negligible for the cases studied in both topologies. Thus, in terms of cost-effectiveness, both strategies compute adequate

solutions for the service provisioning problem. Additional considerations can be made by observing Fig. 10. For instance, the satisfaction of the traffic demands with lower values of W is only feasible if grooming is employed. This behavior attends to the fact that up to two 40G services can be multiplexed and transmitted over a single 100G wavelength. Hence, by leveraging important savings in terms of wavelength count, grooming enables the support of more traffic demands with the same network capacity. Interestingly, the worst cost values are obtained when only one type of optical technology is available, clearly favoring the adoption of MLR architectures.
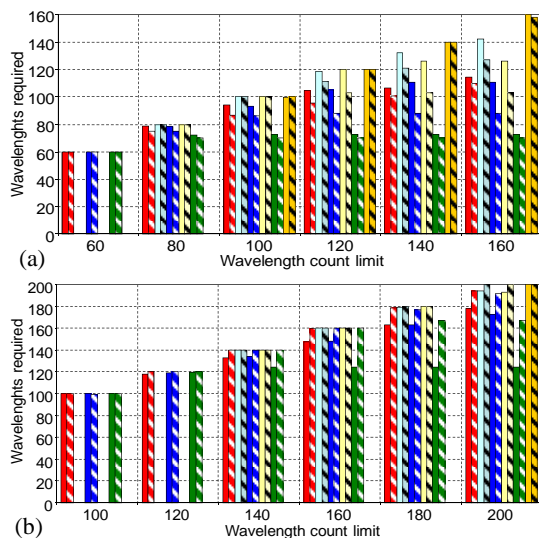
Figure 11. Number of wavelengths required for (a) EON and (b) UBN.
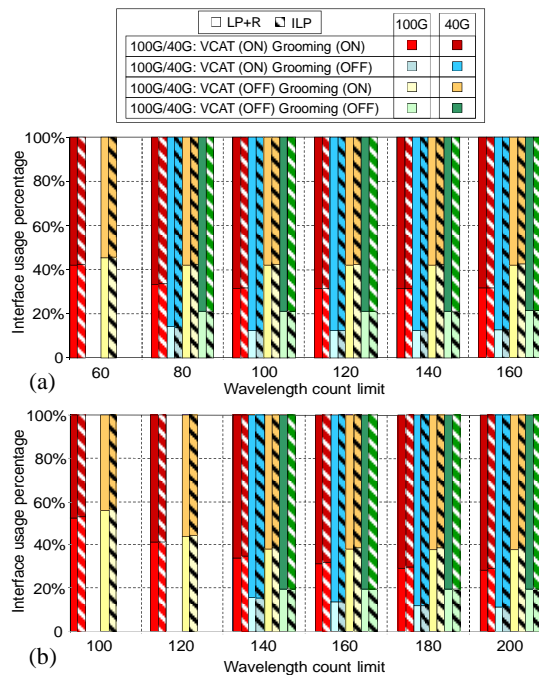
Figure 12. Interface selection distribution for (a) EON and (b) UBN.

Fig. 11, which depicts the wavelength usage, highlights pertinent differences between the ILP and LP+R approaches. In the EON case, the ILP model

typically requires fewer wavelengths for routing the demands. Conversely, in UBN the LP+R approach provides the smallest amount of occupied wavelengths. These differences illustrate the diverse routing solutions obtained when using the ILP and LP+R methods. Noteworthy, although both approaches can produce significantly different values in the number of wavelengths used, the total network cost is not impacted. In general, as W increases, so does the number of wavelengths used as a way of benefiting from the low-cost and long-reach 40G interfaces. When grooming is disabled, smaller W can lead to unfeasible planning solutions due to the lack of available transmission channels. This effect is also evident in networks configurations where only 40G optical interfaces exist.

Lastly, Fig. 12 exhibits the average optical interface usage when different multiplexing functionalities are available at the OTN electrical layer. As observed, the interface distribution remains almost constant for high values of W (140 for UBN and 80 for EON). However, for smaller W, the amount of 100G transceivers increases as a way of exploiting the grooming of 40G services to save on wavelength channels. In addition, we can notice that the difference between ILP and LP+R is almost unperceivable. Interestingly, it is also possible to infer that the optimum mix of interfaces is dependable on several aspects, such as the network topology, the wavelength count per link, and the traffic multiplexing abilities.

V. CONCLUSIONS

This work has introduced and evaluated an optimization framework for dimensioning cost-effective optical transport networks with capabilities for supporting high-speed data services of 100 Gb/s and 40 Gb/s (e.g., Ethernet). The availability of both 40 Gb/s and 100 Gb/s optical technology and the possibility of using traffic grooming and inverse-multiplexing techniques are also explored. Two routing methods, based on an ILP model and a LP model combined with a rounding algorithm, are complemented with proper wavelength assignment heuristics for full resource provisioning at both electrical and optical layers. The results obtained demonstrate that the LP+R approach can obtain the same network cost levels as the ILP alternative while benefiting from smaller execution times. The number of wavelengths allocated is shown to depend heavily on the network topology while the amount of optical interfaces employed remains very close between both approaches. Moreover, the scenario where heterogeneous line rates are combined with VCAT and grooming functionalities was shown to yield the lowest cost over the other scenarios in which some multiplexing abilities are inhibited or only one type of line rate is available at the optical layer.

REFERENCES

[1] IEEE Std 802.3ba, Amendment 4: Medium access control parameters, physical layers and management parameters for 40 Gb/s and 100 Gb/s operation, June 2010.

[2] S. Trowbridge, "High-speed Ethernet transport", in IEEE Communications Magazine, vol. 45, no. 12, pp. 120-125, 2007.

[3] ITU-T G.709, Interfaces for the Optical Transport Network (OTN), 2009.

[4] A. Morea, and J. Poirrier, "A critical analysis of the possible cost savings of translucent networks", in Proc. DRCN 2005, pp. 311-317.

[5] A. Nag, M. Tornatore, and B. Mukherjee, "Optical network design with mixed line rates", in Elsevier Optical Switching and Networking, vol. 6, no. 4, pp. 227-234, 2009.

[6] A. Nag, M. Tornatore, and B. Mukherjee, "Optical network design with mixed line rates and multiple modulation formats", in IEEE Journal of Lightwave Technology, vol. 28, no. 4, pp. 466-475, 2010.

[7] M. Batayneh, et al., "Optical network design for a multiline-rate carrier-grade Ethernet under transmission-range constraints", in IEEE Journal of Lightwave Technology, vol. 26, no. 1, pp. 121-130, 2008.

[8] J. Santos, J. Pedro, P. Monteiro, and J. Pires, "Simplified framework for optimal support of 40 Gb/s and 100 Gb/s services over OTN exploiting grooming and VCAT", in Proc. OFC 2009, paper NThE4.

[9] D. Cavendish, "Evolution of optical transport technologies: from SONET/SDH to WDM," in IEEE Communications Magazine, vol. 38, no. 6, pp. 164–172, 2000.

[10] J. Roese, R. Braun, M. Tomizawa, and O. Ishida, "Optical transport network evolving with 100 gigabit Ethernet," in IEEE Communications Magazine, vol. 48, no. 3, pp. S28-S34, March 2010.

[11] D. Matula, G. Marble, and J. Isaacson, "Graph-coloring algorithms", in Graph Theory and Computing, pp. 109-122, 1972.

[12] J. Culberson, and F. Luo, "Exploring the k-colorable landscape with Iterated Greedy", in Cliques, Coloring, and Satisfiability: Second Dimacs Implementation Challenge, 1996.

[13] Lp_solve reference guide, Available at: http://lpsolve.sourceforge.net/5.5/

João Santos received the diploma in electrical and computer engineering from the Instituto Superior Técnico (IST), Technical University of Lisbon, Portugal, in 2006. He is currently working towards a Ph.D. in IST and Nokia Siemens Networks Portugal, where he studies methods for optimizing the transport of Ethernet traffic over optical transmission networks. He is also interested in routing algorithms, optimization methods, multilayer network design, and optical access networks.

João Pedro (S'07) received the diploma, M.Sc. and Ph.D. degrees in electrical and computer engineering from the Instituto Superior Técnico (IST), Technical University of Lisbon, Portugal, in 2001, 2004 and 2011, respectively. Currently, he is with Nokia Siemens Networks (NSN), where he designs network planning tools. He has authored or coauthored more than 50 publications in international conferences and journals and is currently involved in the large-scale integrating project FUTON (FP7 ICT-2007–215533). His research interests include routing, and wavelength assignment and 3R placement algorithms, multilayer optimization and advanced optical networking paradigms (burst/packet switching), .

Paulo Monteiro (M'87) received the diploma and Ph.D. degrees in electronics and telecommunications from the University of Aveiro, Portugal, and the M.Sc. degree from the University of Wales, U.K. He is the Optical Networks Technology Manager in the Transport, Aggregation, and Fixed Access Department, Nokia Siemens Networks. He is also an Associate Professor at the University of Aveiro and researcher at the Instituto de Telecomunicações. His main research interests include high-speed communications for access and core optical networks and fixed-mobile convergence. He has participated in several national and European projects and is currently the project coordinator of the large-scale integrating project FUTON (FP7 ICT-2007–215533). He has authored/co-authored more than 18 patent applications and over 200 refereed papers and conference contributions.

João Pires (M'87) received the Ph.D. degree in electrical and computer engineering from the Technical University of Lisbon, Portugal, in 1993. He is currently an Assistant Professor at the Instituto Superior Técnico, Technical University of Lisbon. From 1991 to 1999, he worked on a number of European-funded projects, including RACE and ACTS projects. He is the author or co-author of more than 60 papers in international journals and conference proceedings. At present, his research interests are mainly in the area of optical transport networks and optical broadband access networks.

Scalability Analysis of Optical Intrasystem Interconnects

Slavisa Aleksic and Naida Fehratovic

Vienna University of Technology / Institute of Telecommunications, Vienna, Austria

Email: {slavisa.aleksic, naida.fehratovic}@tuwien.ac.at

Abstract— **Architecture of network elements such as large routers and switches is becoming more and more complex due to the constantly increasing requirements on both capacity and performance. Already today, high-performance routers having capacities of more than several Tb/s can not be packaged in a single rack of equipment. Complex and spatially distributed multirack routers comprising a large number of line cards, switching modules and high-speed ports have already become reality. A consequence of this trend is that internal interconnecting system also becomes large and complex. Interconnection distances, total number of cables and power consumption increase rapidly with the increase in capacity, which can cause limitations in scalability of the whole system. This paper addresses requirements and limitations of large-scale optical interconnects. Various point-to-point interconnects and two optically switched interconnection options were studied with regard to their scalability by considering various impairments on optical signal, required number of fiber links and power consumption. Results of this study are presented and discussed in this paper.**

Index Terms—**Optical interconnects, scalability, power consumption, optical switching, optically switched interconnects.**

I. INTRODUCTION

New generation routers require several racks for housing a large number of switching modules and line cards in order to achieve large capacities of more than several Tb/s. For this reason, the most of the high-performance routers currently being developed are multi-rack systems. Since the internal interconnection network becomes more critical when increasing the number of switching chips, line cards, and racks, the high-capacity network elements are often limited by the maximum achievable size of the interconnection network. Thus, a scalable interconnection system is a crucial prerequisite for implementing high-capacity, efficient and scalable routers and switches. The intrasystem interconnection network is usually limited by the maximum data rate per link and per cable, required number of cables and required length of a single interconnection link. Additionally, a large number of high-capacity links and an increased distance always results in large power consumption because a large number of high-speed transceivers is needed. Due to the fact that optical transmission and switching technologies

are generally able to provide higher data rates over longer transmission distances than electrical transmission systems, a natural answer to the scalability problem could be to use optical transmission and switching systems in order to relax the limitations and to improve the scalability of internal interconnects.

This paper addresses requirements of different state-of-the-art and advanced optical interconnect technologies and compares them with each other with respect to power consumption and scalability limitations. The paper is organized as follows: Section II reviews current trends in optical interconnects for large-scale network elements and high-performance computers. Section III describes main characteristics of electrical and optical interconnects and gives a brief overview on current technologies for optical point-to-point interconnects. Technologies and limitations of optically switched interconnects are discussed in Section IV. The considered architecture for large-scale interconnection systems based on a non-blocking 3-stage Clos network is presented in Section V, while Section VI describes the model and presents results on scalability concerning power consumption and required number of fiber links. Finally, Section VII summarizes and concludes this paper.

II. CURRENT TRENDS

Extensive research has been conducted on the relieving bandwidth bottlenecks related to current electronic point-to-point interconnects. Electrical interconnects suffer from high crosstalk as well as distance and frequency dependent attenuation due to dielectric losses coupled with high frequencies. Hence, very high data rates over copper-based cables and PCB traces are hardly achievable. In fact, recent high-capacity routers and switches, supercomputers, and data centers are increasingly relying on optical point-to-point interconnection links that typically support up to 10 Gb/s data rate per channel. Standard optical point-to-point links are based on directly modulated 850 nm vertical cavity surface emitting lasers (VCSEL) and multimode fibers (MMFs) [1-6]. The capacity of such interconnects is limited both by modulation bandwidth of the laser and by the intermodal dispersion in MMFs [7]. Recently, various methods have been proposed and investigated in order to enable transmission at higher data rates: i) increasing the modulation rate of the laser [8,9], ii) using multiple fibers and transceivers in a parallel manner [10-12], iii) using advanced signal formats such as optical

orthogonal frequency division multiplexing (OOFDM) and high-order modulation formats [7,13-18].

According to [19], communication networks of today are responsible for about 2% of the global carbon emissions. Therefore, power consumption demands a lot of attention when considering scaling of the network and managing elements to future required aggregate capacities. Figure 1a) shows the estimated total power consumption of electronic routers for capacities up to 100 Tb/s with some examples of current high-performance routers [20]. Thus, power consumption increases linearly with bandwidth and each new generation of high-capacity routers consumes more power than the previous one.

State-of-the-art electronic core routers providing Tb/s capacity consume about 8-11 kW per rack. For a total capacity of 100 Tb/s, the power to be supplied to such a system is in the order of 1 MW. The second most consuming part of such a large electronic router is the subsystem comprising intrasystem interconnects and switching fabrics [20]. A straightforward scaling of current routers to higher capacities would result in a very high total power consumption of order of several MW and a very large number of internal interconnection links. Additional to the increased number of links, also their length increases due to the increased size of the entire system, which consequently leads to an increase in power consumption because more transceivers providing both high-bandwidth and large signal power are needed.
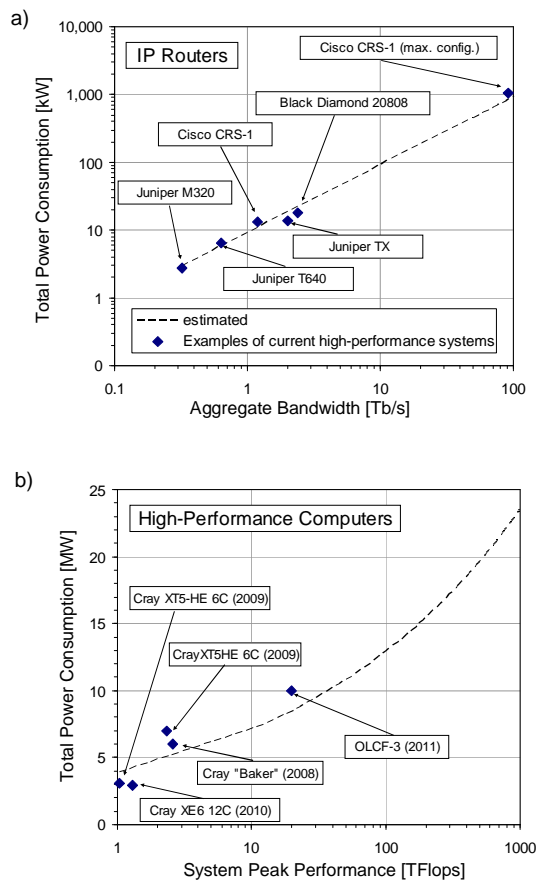

Figure 1. Trends and projections for power consumption of a) high-performance routers [20] and b) high-performance computers according to data from [21].

Similar issues are faced by interconnection networks used in data centers and high performance computing (HPC) systems. In fact, data centers are experiencing a heavy increase in the amount of traffic to store and process. Optical cables have been used to interconnect racks of equipment within data centers, and within high performance computer clusters.

Figure 1b) represents historic trends and projections for power consumption of high-performance computers (HPCs). It is evident that already today HPC systems consume several MW of electricity [21]. Future Exascale computer systems will probably consume more than 20 MW, which will set very high requirements on power supply and cooling systems. Therefore, a large effort has to be put into research and development of more energy efficient structures and technologies in order to make possible further scaling in both capacity and performance.

III. OPTICAL POINT-TO-POINT INTERCONNECTS

As the need for higher system capacities becomes ever greater, a lot of efforts have been made by standardization bodies such as IEEE 802.3ba Ethernet Task Force [22], Optical Internetworking Forum (OIF) [23], Fiber Channel (FC), InfiniBand (IB) [24], Rapid IO Trade Association [25] and PCI Express [26] in order to achieve an improvement in existing interconnecting technologies regarding data rate and efficiency. The IEEE 802.3ba Ethernet Task Force has already finished the work on the standardization of 40 Gb/s (40GbE) and 100 Gb/s Ethernet (100GbE). The Physical and Link Layer (PLL) Working Group of the OIF developed the physical specifications CEI-25G and CEI-28G for achieving lane signaling rate of up to 28 Gbaud/s [23,27]. It is intended for next generation chip-to-chip and chip-to-module as well as for backplane applications that support transmission at 100 Gb/s. InfiniBand has announced future plans in terms of EDR (Enhanced Data Rate) systems with 1×20 Gb/s per lane that is planned for the year 2011 [28]. Similarly, the PCI-SIG group has also released the final specifications for PCI Express 3.0 with improved data rates [29]. Rapid IO focuses on higher data rates which will come with the serial Rapid IO 3.0 specification [30]. A question that arises is which of these technologies is the most suitable for intermodule interconnects regarding overall system scalability and power dissipation.

Main characteristics of electronic and optical interconnections with respect to serial (single-channel) and parallel (multi-channel) transmission are presented in Table I. The potential benefits of optics over electronics, as outlined in Table I, lead to the capability of optical interconnects to overcome most of the physical limitations associated with the electronic interconnects such as interconnection density, timing, signal integrity as well as power consumption. A detailed overview of requirements for optical interconnects for chip-chip and on chip interconnects can be found in [31].

Table II briefly outlines various options for point-to-point optical interconnects and summarizes some important parameters. Each interconnection technology is

upper-bounded regarding transmission distance and number of channels/lanes provided. Please note that the values for power consumption listed in Tables II and III are obtained by averaging power consumption values given in data sheets of a number of components either currently available on the market or presented in the research literature.

TABLE I. BASIC PHYSICAL DIFFERENCES BETWEEN ELECTRONIC AND OPTICAL INTERCONNECTS.

Interconnection	Physical Effects	Electrical	Optical
Serial (Single-Channel) Interconnection	Transmission Line Effects	• Distance and frequency dependent attenuation due to two kinds of losses coupled with high frequencies: 1. **Dielectric loss** in PCB substrates 2. **Skin-effect** in coaxial cables	• Low-loss propagation media (silica with 0.2 dB/km) • **no frequency-dependent loss** • Higher carrier frequency of light, shorter wavelength ($\lambda = c/f$) and larger photon energy ($E = h \cdot f/e$; h is Planck´s constant and e is electronic charge).
	Synchronization	Low clock jitter and skew needed in order to achieve synchronous clock distribution	The use of short optical pulses could ensure system synchronization in terms of signal and clock skew elimination
	Noise	**Thermal noise**	**Quantum noise**
Parallel (Multichannel) Interconnection	Crosstalk	Limits interconnect density	Relevant for WDM interconnects, spectral characteristics of optical filters, nonlinear effects,…
	Interconnect Density ("**Aspect Ratio**")	The limit on the number of bits per second that can be sent thorough the electrical interconnect, given the ISI from frequency-dependent loss and distortion.	Do not have this aspect ratio limit at all
	Dispersion		One of the rear drawbacks of optical-based transmission

TABLE II. CONSIDERED POINT-TO-POINT OPTICAL INTERCONNECTION TECHNOLOGIES.

Interconnection Technologies	Net Channel Data Rate (R_{TRX}) [Gb/s]	Total Net Data Rate [Gb/s]	Maximum Distance [m]	Power Consumption per TX/RX Pair (P_{TRX}) [W]
10G XAUI	10	10	< 300	1.89
4xSDR InfiniBand (IB)	2	8	200	0.9
4xDDR InfiniBand (IB)	4	16	200	1.63
4xQDR InfiniBand (IB)	8	32	150	2
40G parallel	10	40	100	2.61
40G WDM	10	40	10 k	6

IV. OPTICALLY SWITCHED INTERCONNECTS

A. Optical Switching Technologies

Optical switching technologies for the use in optical interconnection systems can be classified based upon underlying physical effect that is used for the switching process, i.e. into electro-optic (EO), acusto-optic (AO), thermo-optic (TO) and opto-mechanical (OM) switching. The EO, AO and TO effects rely on refractive index changes of the matter through application of an external physical field or action.

In the EO effect, an applied electrical field induces change in the index of refraction, which then channels light to the appropriate port. LiNbO$_3$ is unique crystal that shows large EO effect, AO effect, TO effect and nonlinear effects. EO device based on this substrate have very fast response, small dielectric constant and relatively low power dissipation [32]. Another EO switches are based on liquid-crystals and exhibit high extinction ratio, high reliability and low power consumption.

Semiconductor optical amplifiers (SOAs) can also be used as an ON-OFF switch by varying its bias current. By reduced bias voltage, no population inversion is achieved and device rather absorbs input signal thereby building the off-state. In contrary, if a sufficiently high bias voltage is applied, input signal will be amplified and, thus, the on-state is achieved. However, EO switches suffer from high insertion loss and possible polarization dependent loss (PDL) [33]. PDL can be combat at the cost of higher driving voltage, and consequently lower switching speed, which is not desirable.

The changes of refractive index due to the interaction between acoustic and optical waves in the crystal are utilized in the AO switches. The switching time is limited by the propagation speed of acoustic waves [33]. AO switches can also be implemented on Lithium Niobate.

The TO effect utilizes the temperature dependence of the refractive index. The advantage of thermo-optical switches is its generally small size, but high driving power and high power dissipation make such switches highly impractical. Crosstalk and insertion loss values are

also not satisfactory. Mostly used materials for TO switching implementations are silica and polymers.

Opto-mechanical (OM) switching is based on mechanics and free-space optics and switching is performed by some electro-mechanical means such as by moving mirrors or directional couplers. Regarding its optical performance parameters, OM switches have low insertion loss, low PDL and low crosstalk [34]. Drawbacks of this type of switches are its relatively low switching speed in the order of few milliseconds which could be unacceptable for some specific applications. MEMS (Micro Electro Mechanical System) switches form a subcategory of the OM switches. In particular, 3-D MEMS is the most promising option for telecommunication applications, where large port counts are desired and a low switching speed is not an issue. By nature, MEMS devices are compact and consume low power. Challenges regarding MEMS are mirrors maintenance, fabrication and packaging, as well as implementation. As already mentioned before, OM switches, and thus optical switches based on MEMS, provide low switching speeds, which makes this type of switches less suitable for application in dynamic and fast packet –switched systems.

Arrayed waveguide grating (AWG) based switches are gaining a particular attention for large-scale switching fabrics and there are a lot of architectures that base upon these particular elements. Since they are passive elements, they provide low power switching. However, additional elements such as wavelength converters (WCs) are needed to implement switching operation, which do consume power. A limiting factor is the lack of mature and commercially available all-optical wavelength converters needed for the AWG-based switch realization.

Each of the switching technologies is characterized by its switching time, insertion loss, crosstalk and PDL. According to these parameters, a technology is more or less suitable for a particular application. For example, required switching time for fast packet switching applications should be small compared to packet length and in the order of nanoseconds or less. Optimally, optical devices should be designed taking into account already available or near-to-mature optical switching technologies in order to ensure their feasibility on a large scale.

In our study, we consider two particular realization options for optical switched interconnects, namely one based on semiconductor optical amplifiers as shown in Figure 2a) and another using arrayed waveguide gratings (AWGs) and tunable wavelength converters (TWCs) as presented in Figure 2b). Since we are concentrating on a dynamic and fast switching operation needed for packet switching, thermo-optical and opto-mechanical switches are not considered because they are not able to provide short enough switching times needed for such applications.

Figure 2. Examples of 4x4 switching elements based on a) semiconductor optical amplifiers (SOAs) and b) arrayed waveguide gratings (AWGs) with tunable wavelength converters (TWCs).

B. Scalability of Optical Switching Elements

Scalability of optical switching elements is mostly influenced by physical impairments on optical signals that set limits on maximum size of switching elements. We assume in this study that those impairments can be compensated by means of optical signal regeneration, but we still should look at the maximum switch size, i.e., at the maximum number of cascaded switching elements after which signal regeneration has to be performed. Therefore, we carried out physical layer simulations by using the VPISystems simulation tool and by taking into account all relevant effects such as attenuation, dispersion, noise accumulation, nonlinear effects and crosstalk. For a more detailed description of the performed simulations including specification of parameters please refer to [34].

The results presented in Figure 3 show the degradation of optical signals when transmitted through SOA-based and AWG-based switches of different sizes. The maximum achievable number of ports is obtained at the line data rate of 40 Gb/s by assuming a target upper bound on eye closure penalty of 4 dB. The AWG-based switch shows the worst scalability when inband crosstalk is considered. For an AWG switch having 16 ports, an eye closure penalty (ECP) of about 4 dB was obtained. On the other hand, an ECP below 4 dB was obtained for up to 10 cascaded SOA gates, which corresponds to a switch size of 32×32 ($N = 2^{10/2} = 32$). Thus, the signal has to be regenerated after each 10th SOA gate. If the inband crosstalk in the AWG switch is mitigated, which can be achieved by a careful design and an optimal configuration of the switch, very large switches of more than several hundreds of ports are imaginable. It should be mentioned at this point that the largest scalability could be achieved

when using micro-electro-mechanical-systems (MEMS) switches [34]. However, optical MEMS switches are not considered in this study because of their large switching time that makes them less suitable for implementing dynamic packet-switched fabrics.
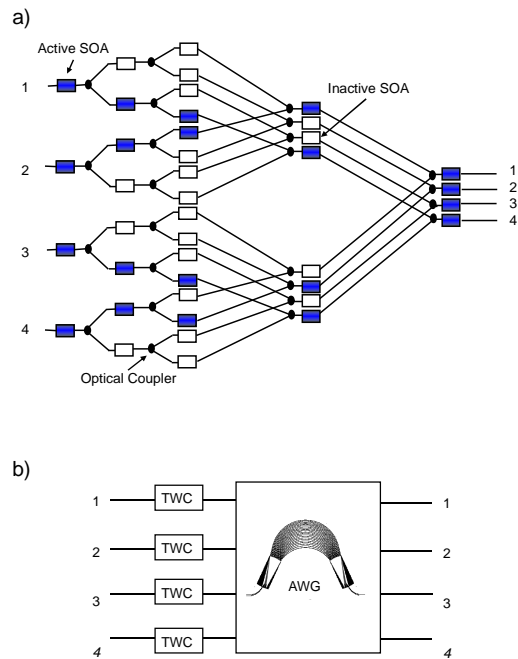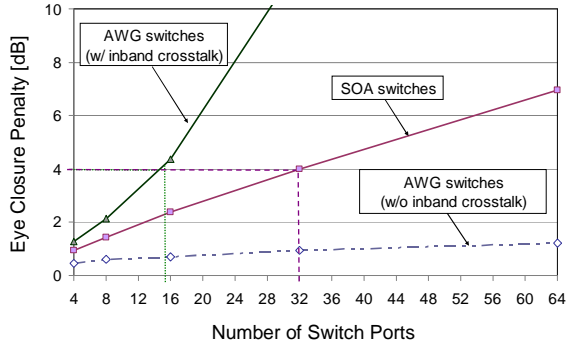

Figure 3. Scalability of switching elements based on semiconductor optical amplifiers (SOAs) and arrayed waveguide gratings (AWGs) with tunable wavelength converters (TWCs) as shown in Figure 2.

V. CONSIDERED INTERCONNECTION ARCHITECTURE

There are various architectures of internal switching fabrics, and hence of internal interconnects, currently used in high-performance routing and switching elements. In most cases, switching fabrics are realized using a multistage architecture. In the architecture that we consider in our study, line cards are equipped with optoelectronic transmitters/receivers that send/receive the optical signal to/from a large packet switching fabric. The large packet switching fabric is realized using a number of smaller switching elements interconnected in a 3-stage strictly non-blocking Clos network as shown in Figure 4. We assume the minimal non-blocking arrangement, in which $k = 2n - 1$ and $n = \sqrt{N/2}$ [36].
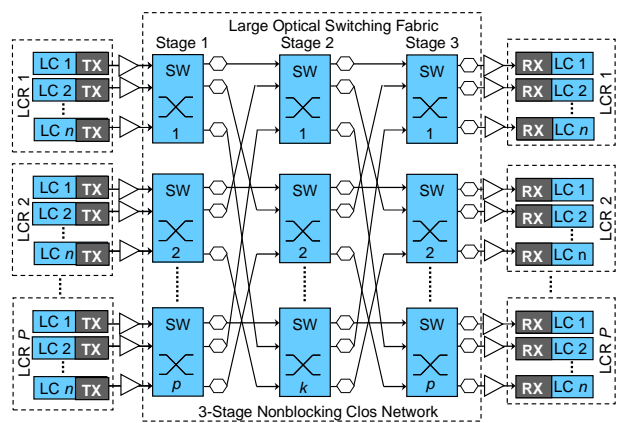
Figure 4. Considered interconnection arrangement based on a 3-stage Clos network. The total number of ports is $N = np$. (LC: Line Card, LCR: Line Card Rack, SW: Switch, TX: Transmitter, RX: Receiver)

We consider two different realization options: the first one uses electronic switching elements and optical point-to-point interconnects and the second one is an optically switched interconnect comprising switching elements based either on arrayed waveguide gratings (AWGs) or

semiconductor optical amplifiers (SOAs). The first option requires optoelectronic transceivers to be deployed within the Clos network because the electronic switching elements are interconnected with optical links. Optically switched interconnects make use of optical switches so that no optoelectronic transceivers are needed within the Clos network, but the impairments on the optical signal such as attenuation, noise accumulation, cross-talk and nonlinear effects have to be compensated by optical amplifiers and all-optical 3R signal regenerators. The considered structures of all-optical wavelength converters and 3R regenerators are shown in Figure 3, while power consumption values for other components used in the model are listed in Table III.
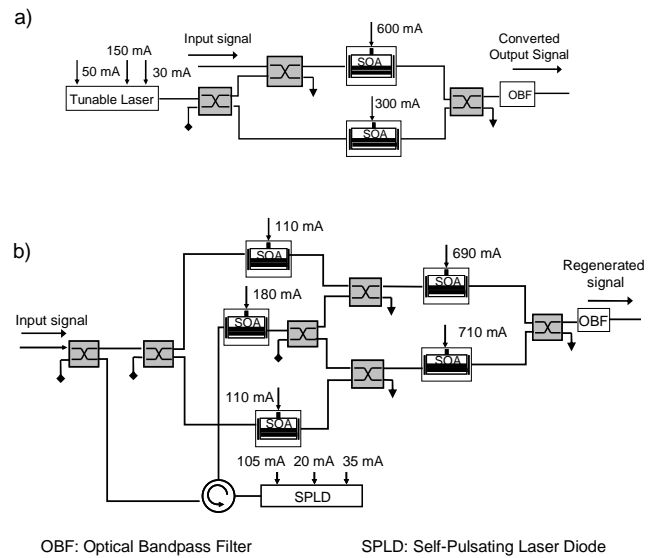
Figure 5. Structures of a) tunable wavelength converters (TWCs) and b) all-optical 3R regenerators.

Please note that only active elements on signal paths through the switch are assumed to consume power. We also assume one temperature stabilization circuit (TEC) per one switching unit (for both SOA and AWG-based switches).

TABLE III. POWER CONSUMPTION VALUES USED FOR OPTICALLY SWITCHED INTERCONNECTS

Component	Power Consumption [W]
SOA	0.24
3R Regenerator	2.78
Tunable Wavelength Converter (TWC)	1.69
40G Optical Transceiver (TRX_opt)	14
Optical Amplifier (P_{out}=21 dBm, G=23 dB)	14
TEC for SOAs and AWGs	4

We further assume line cards operating at 40 Gb/s and optical links between line cards and switching fabric as well as within the Clos network at the same data rate. Since different point-to-point interconnection technologies provide different maximum data rates per

channel or per fiber, the number of fibers per link, and thus the number of transceivers needed, is calculated such that the aggregate capacity of each link is 40 Gb/s.

VI. SCALABILITY OF LARGE OPTICAL INTERCONNECTS

Two important scalability limitations of point-to-point interconnecting technologies are the required number of fiber links and the maximum supported transmission distance. One can calculate the number of required fibers for different interconnection technologies in a multi-stage arrangement such as e.g. the Clos network. The number of required fibers for different interconnection technologies in a 3-stage Clos can be calculated as follows:

$$N_{fiber} = \frac{2pR_{line}(n+k)}{R_{TRX}},\qquad(1)$$

where n, p and k are the parameters of the Clos network (see Figure 4), R_{line} is the line data rate (in our case it is set to 40 Gb/s) and R_{TRX} is the data rate supported by transceivers of the considered interconnection technologies (see Tables II and III).

As it can be seen form Figure 6, the largest number of fiber links is needed for options providing low data rates per channel such as SDR InfiniBand (IB). For example, more than 100,000 fiber links are required if 4×SDR IB is used in a 100 Tbit/s switch. The total number of fibers can be reduced by either increasing the data rate per channel or transmitting a number of channels over a single fiber in a wavelength-division multiplexed manner. Thus, optically switched interconnects require the minimum number of fiber links because they can potentially support very high data rates per switching port. In this case, the minimum number of fibers required for 100 Tbit/s in a 3-stage Clos arrangement becomes less than 10,000.
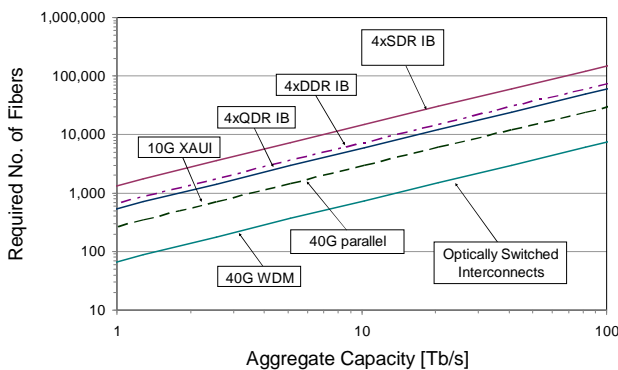
Figure 6. Required number of fibers for optical interconnects in a 3-stage Clos arrangement.

Using the values from Tables II and III, considering the architecture depicted in Figure 5 and taking into account the scalability limitations of optically switched interconnects as determined in Section IV B., we can estimate the total power consumption of different options for implementing large-scale optical interconnects.

A. Power Consumption of Point-to-Point Interconnects

The total power consumption of point-to-point optical interconnects is obtained by summing up the total power consumed by all transceivers (P_{TRX_p-t-p}) and that consumed by the electronic switching elements (P_{el_sw}), i.e.,

$$P_{tot\_p-t-p} = P_{TRX\_p-t-p} + P_{el\_sw}.\qquad(2)$$

The power consumption of electronic switching elements is taken into account because optically switched interconnects already provide the switching functionality. In order to fairly compare the two different interconnect options, we need to include the switching functionality to the point-to-point interconnects by considering the use of electronic packet switches according to the arrangement shown in Figure 4. Here we assume that a current electronic packet switch consumes 8 W per 80 Gb/s bidirectional switching capacity.

The total power consumed by transceivers of a point-to-point interconnect is given by:

$$P_{TRX\_p-t-p} = \frac{2pR_{line}\cdot(n+k)}{R_{TRX}}\cdot P_{TRX},\qquad(3)$$

where P_{TRX} is the power consumption of a single optical transceiver. Similarly, the total power consumed by electronic switching elements is calculated using:

$$P_{el\_sw} = 3pk\cdot P_{sw\_port},\qquad(4)$$

where P_{sw_port} is the power consumption of an input/output port of the electronic switch.

B. Power Consumption of Optically Switched Interconnects

The total power consumption of SOA-based optically switched interconnects is determined by considering the contributions of active SOAs within the Spanke-type switching elements (P_{active_SOA}), TEC elements (P_{TEC_tot}), 3R regenerators (P_{3R_tot}), optical amplifiers (P_{OA_tot}) and transceivers (P_{TRX_opt}), i.e.,

$$\begin{aligned}P_{tot\_SOA} &= P_{active\_SOA} + P_{TEC\_tot} + P_{3R\_tot}\\ &\quad + P_{OA\_tot} + P_{TRX\_opt}\end{aligned}\qquad(5)$$

The individual contributions to the power consumption of a large SOA-based interconnect – which is realized as a Clos network of smaller Spanke-type SOA switching elements as shown in Figure 2a) – are calculated according to the following formulae [20]:

$$\begin{aligned}P_{active\_SOA} &= N_{active\_SOA}\cdot P_{SOA}\\ &= 2pn\cdot\log_2\left[p\cdot(k-1)^2\right]\cdot P_{SOA}\end{aligned},\qquad(6)$$

$$P_{TEC\_tot} = (2p+k)\cdot P_{TEC},\qquad(7)$$

$$P_{3R\_tot} = \frac{N_{active\_SOA}}{10} \cdot P_{3R}, \tag{8}$$

$$P_{OA\_tot} = 2 pn \cdot P_{OA}, \text{ and} \tag{9}$$

$$P_{TRX\_opt} = pn \cdot P_{TRX\_opt}. \tag{10}$$

In case of an AWG-based large interconnect, the total power consumption is given by:

$$P_{tot\_AWG} = P_{WC\_tot} + P_{TEC\_tot} + P_{OA\_tot} + P_{TRX\_opt}. \tag{11}$$

where P_{WC_tot} is the total power consumption of wavelength converters, i.e.,

$$P_{WC\_tot} = 2p \cdot (n+k) \cdot P_{WC}. \tag{12}$$

C. Results on Power Consumption of Optical Interconnects

The results on power consumption of optical point-to-point and optically switched interconnects are presented in Figure 7a) and b). As it can be seen from Figure 7a), power consumption of low data rate point-to-point interconnects such as 4×SDR IB increases rapidly with the increase in aggregate capacity. This is because at large aggregate capacities, a very large number of transceivers are required when R_{TRX} is low. Similar to the conclusions regarding the required number of fibers, an improvement of energy efficiency can be achieved by increasing data rate per channel and transmitting several channels over a single fiber. Both considered optically switched interconnection options (SOA-based and AWG-based) consume three to four times less power than the low data-rate point-to-point interconnects (e.g. 4×SDR IB) and at least 30% less power than the most efficient realization of the considered optical point-to-point interconnects (4×QDR IB).

When including the results obtained for intrasystem interconnects into the model for power consumption of current electronic routers presented in [20], we can obtain the contribution of the considered interconnects to the total power consumption of conventional electronic routers. Thus, an internal interconnection system based on a low-speed point-to-point interconnect would contribute by about 18% to the total power consumption of large-scale routers. Other higher-speed and parallel point-to-point interconnect technologies contribute by approximately 9% to 12%, while the contribution of the optically switched interconnects would be only about 6% of the total power consumed. Thus, optically switched interconnects have the potential to reduce the total power consumption of large-scale network elements.

Figure 8 shows the total power consumption of 100 Tb/s switched intrasystem interconnects when considering different realization options. In the case of point-to-point optical interconnects, the contributions of the large electronic switch and the fiber-based point-to-

point links are separately shown. It can be observed that although fast optical packet switches do not necessarily consume considerably less power than their electronic counterparts [37], the large-scale optically switched interconnects are more power efficient than the electronic switching fabrics interconnected by means of optical point-to-point interconnects. For example, a SOA-based interconnect consume about 30% less power than the most power efficient point-to-point option (4×QDR IB). Moreover, an AWG-based interconnect is able to provide even better energy efficiency; it shows an improvement in energy efficiency of about 25% with regard to an SOA-based interconnection system.
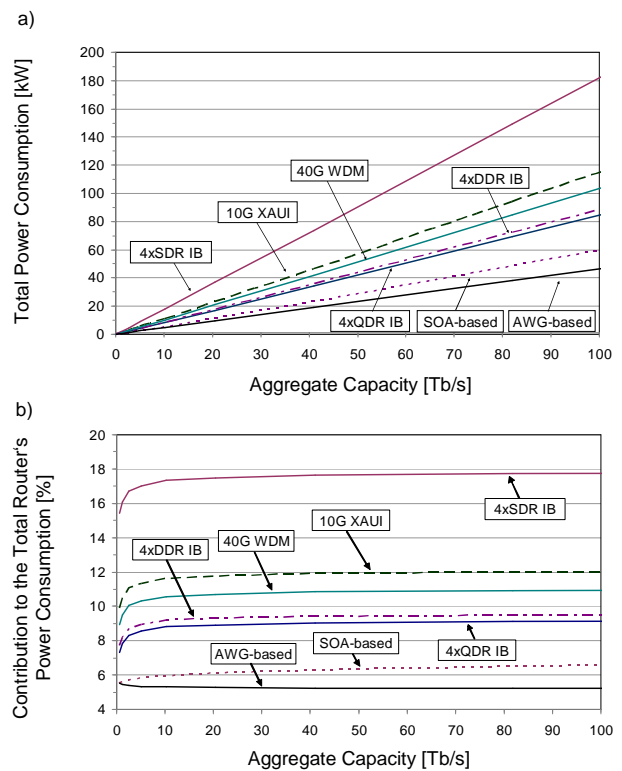

Figure 7.   a) Total power consumption vs. aggregate capacity and b) estimated contribution of optical interconnects to the total power consumption of conventional electronic routers.
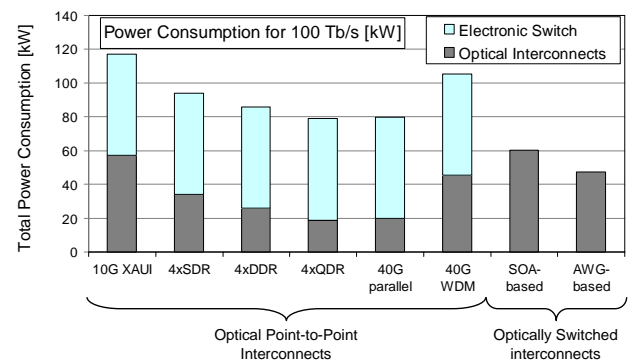

Figure 8.   Power consumption of the considered optically switched interconnects and optical point-to-point interconnects for an aggregate capacity of 100 Tb/s.

VII. CONCLUSIONS

In conclusion, we evaluated the scalability of various optical point-to-point and optically switched interconnects by taking into account peculiarities of each considered technology. Optical point-to-point interconnects require a large number of fiber links, especially the options providing low data rate per channel. The total number of fibers can be reduced by increasing the data rate per channel and by transmitting several channels over a single fiber in a WDM manner. On the other hand, optically switched interconnects require the lowest numbers of both interconnecting fibers and transceivers. We presented a model for evaluation of power consumption of large-scale interconnection systems. Similar to the conclusions regarding the required number of fibers, an improvement of energy efficiency can be achieved by increasing data rate per channel and transmitting several channels over a single fiber. The results of our study showed that optically switched interconnects have the potential to improve the energy efficiency of high-capacity switches and routers. However, their scalability is mainly limited by optical impairments that need to be effectively compensated.

REFERENCES

[1] Finisar Corporation, "10Gb/s 850 nm Multimode XENPAK Transponder", Data Sheet, Product FTLX8561E2, online available under: http://www.finisar.com/products/.

[2] OpNext SFP+, "Transceiver Product TRS20A0EN", Data, Sheet, online available under: http://www.opnext.com.

[3] ExceLight Communications Inc., "10Gb/s SFP Optical Transceiver Module, Product SPP5101SR-GL (10GBASE-SR, 850nm VCSEL, PIN-PD)", online available under: http://www.excelight.com/products/productindex.asp

[4] K. Schmidtke, F. Flens, "Trends and Future Directions in optical Interconnects for Datacenter and Computer Applications", OFC 2010, San Diego, California, USA, March 21-25, 2010, paper OTuP4.

[5] R. Michalzik, A. Kern, M. Stach, F. Rinaldi and D. Wahl, "True bidirectional optical interconnects over multimode fiber", Proc. SPIE 7607, 76070B, San Francisco, California, USA, January 2010.

[6] D. Wahl, A. Kern, M. Stach, F. Rinaldi, R. Rösch and R. Michalzik, "VCSELs with monolithically integrated photodiodes for single-fiber bidirectional data transmission in the Gbit/s range", Elsevier Journal of Crystal Growth, doi:10.1016/j.physletb.2003.10.071.

[7] Y. Benlachtar, R. Bouziane, R. I. Killey, C. Berger, P. A. Milder, R. Koutsoyannis, J. C. Hoe, M. Püschel and M. Glick, "Optical OFDM for the Data Center", ICTON 2010, Munich, Germany, June 27 -July 1, 2010, paper We.A4.3.

[8] J.S. Gustavsson, S.B. Heall, P. Westbergh, A. Haglund, A. Larsson, E.P. O'Reilll, "Optimized Active Region Design for High Speed 850 nm VCSELs", CLEOE-EQEC 2009, Munich, Germany, 14-19 June 2009, pp. 1-1.

[9] P. Westbergh, J.S. Gustavsson, A. Haglund, A. Larsson, F. Hopfer, G. Fiol, D. Bimberg and A. Joel, "32 Gbit/s multimode fiber transmission using high-speed, low current density 850 nm VCSEL", Electronics Letters, Vol. 45, No. 7, pp. 366-368, March 2009.

[10] ReflexPhotonics, "100G Ethernet CFP Transceiver Module", Product brief, online available under: http://www.reflexphotonics.com/.

[11] N. Y. Li et al., "High-Performance 850 nm VCSEL and Photodetector Arrays for 25 Gb/s Parallel Optical Interconnects", OFC 2010, San Diego, California, USA, March 21-25, 2010, paper OTuP2.

[12] Petar Pepeljugoski et al., "Low Power and High Density Optical Interconnects for Future Supercomputers", OFC 2010, San Diego, California, USA, March 21-25, 2010, paper OThX2.

[13] J. M. Tang, P. M. Lane, and K. A. Shore, "High-Speed Transmission of Adaptively Modulated Optical OFDM Signals Over Multimode Fibers Using Directly Modulated DFBs", Journal of Lightwave Technology, Vol. 24, No. 1, pp. 429 - 441, 2006.

[14] M. Glick, Y. Benlachtar, R. I. Killey, "Performance and Power Consumption of Digital Signal Processing Based Transceivers for Optical Interconnect Applications", ICTON 2009, Azores, Portugal, June 28 -July 2, 2009, paper We.B2.3.

[15] H. Yang, S.C.J. Lee, E. Tangdiongga, F. Breyer, S. Randel, A.M.J. Koonen "40-Gb/s Transmission over 100m Graded-Index Plastic Optical Fiber based on Discrete Multitone Modulation", OFC 2009, San Diego, CA, USA, March 2009, paper PDPD8.

[16] A. J. Lowery and J. Armstrong, "10 Gbit/s multimode fiber link using power efficient orthogonal-frequency-division multiplexing", Optics Express, Vol. 13, Issue 25, Part 2, pp. 10003-10009, 2005.

[17] S. C. J. Lee et al., "24-Gb/s Transmission over 730 m of Multimode Fiber by Direct Modulation of an 850-nm VCSEL using Discrete Multi-Tone Modulation", OFC 2007, Anaheim, California, USA, March 25-29 2007, paper PDP6.

[18] N. E. Jolley et al. "Generation and propagation of a 1550 nm 10 Gb/s optical orthogonal frequency division multiplexed signal over 1000 m of multimode fiber using a directly modulated DFB", OFC 2005, Anaheim, California, USA, March 6-11 2005, paper OFP3.

[19] The Climate Group: "SMART 2020: Enabling the low carbon economy in the information age", GLobal eSustainability Initiative, Techn. Rep. 2008.

[20] S. Aleksic, "Analysis of Power Consumption in Future High-Capacity Network Nodes", IEEE Journal of Optical Communications and Networking (JOCN), Vol. 1, No. 3, pp. 245 - 258, August 2009.

[21] Top500 Computer Sites, "Statistics on high-performance computers", online available under; http://www.top500.org/.

[22] IEEE 802.3ba Ethernet Task Force, online available under: http://www.ieee802.org/3/ba/.

[23] Optical Internetworking Forum (OIF), Ethernet Alliance, "CEI-28G: Paving the Way for 100 Gigabit", white paper, online available under: http://www.oiforum.com.

[24] InfiniBandSM Trade Association, "InfiniBandTM Architecture Specification, Volume 2, Release 1.2, October 2004.

[25] RapidIO Trade Association, "RapidIO Interconnect Specification Rev. 2.0", 03/2008.

[26] PCI-SIG, PCI Express 3.0, online available under: http://www.pcisig.com.

[27] E. A Donnay, J. R Goergen, "CEI-25G-LR Baseline Clause Proposal", Physical Link Layer (PLL) Working Group, July 23, 2008.

[28] InfiniBand Trade Association, online available under: http://www.infinibandta.org/.

[29] PCI-SIG, PCI Express 3.0, online available under: http://www.pcisig.com.

[30] Serial RapidIO 3.0, online available under: http://www.rapidio.org/specs/current.

[31] D. A. B. Miller, "Device Requirements for Optical Interconnects to Silicon Chips", Proceedings of the IEEE, Vol. 97, No. 7, pp. 1166 - 1185, July 2009.

[32] T. S. El-Bawab, "Optical Switching ", Springer, 2006.

[33] G. I. Papadimitriou, C. Papazoglou, A. S. Pomportsis, "Optical Switching: Switch Fabrics, Techniques, and Architectures", Journal of Lightwave technology, Vol. 21, No.2, pp. 384-405, February 2003.

[34] N. Fehratovic and S. Aleksic, "Power Consumption and Scalability of Optically Switched Interconnects for High-Capacity Network Elements", in Proceedings of Optical Fiber Communication Conference and Exposition (OFC 2011), Los Angeles, CA, USA, pp. JWA84-1 - JWA84-3, March 2011.

[35] S. Aleksic and N. Fehratovic, "Requirements and Limitations of Optical Interconnects for High-Capacity Network Elements", (invited), in Proceedings of 12th International Conference on Optical Trans-parent Networks (ICTON 2010), Munich, Germany, paper We.A1.2, June 2010.

[36] C. Clos, "A study of non-blocking switching networks," Bell Syst. Tech. J., vol. 32, pp. 406–424, 1953.

[37] S. Aleksic, "Electrical Power Consumption of Large Electronic and Optical Switching Fabrics", IEEE Winter Topicals 2010, Majorca, Spain; pp. 95 – 96, January 2010.

Naida Fehratovic received BSc and MSc (Dipl.-Ing.) degrees in electrical engineering from Vienna University of Technology, Austria, in 2008 and 2010, respectively. Her current research topics include network elements in the core area, interconnects for high-capacity routers and switches, and energy efficiency. The title of her master thesis is "Power Consumption Analysis of Advanced Interconnection Systems within High-Capacity Switching Elements". She has authored and coauthored several papers in highly recognized international conferences and peer-reviewed journals.
Dipl.-Ing. Fehratovicis a student member of the Optical Society of America (OSA).

Slavisa Aleksic received MSc (Dipl.-Ing.) and Ph.D. (Dr. techn.) degrees in electrical engineering from Vienna University of Technology (TUW), Austria, in 1999 and 2004, respectively. His current research interests include communication networks, photonic networks, energy efficiency in communication networks, high-speed optical and electrical signal processing systems, as well as high-speed media access control (MAC) protocol design and implementation. He is author or co-author of more than 70 scientific publications including book chapters, papers in peer-reviewed scientific journals, and contributions to internationally recognized conferences. He has experience in both research and industrial fields through successfully managing and conducting many projects related to communication networks including two projects funded by the Austrian Science Fund (FWF) and a number of projects in collaboration with several Austrian and European academic institutions and companies. He was Austrian representative in COST action no. 291 "Towards Digital Optical Internet" and in the EU Network of Excellence "e-Photon/One". Currently, he is leading the TUW's research group within the EU Network of Excellence "BONE" and within the national project "HOME-ICT" funded by the Austrian Fund for Climate and Energy.
Dr. Aleksic is a senior member of the IEEE and a member of the OVE and the IEICE. He has received several international awards, grants, and recognitions.

Heuristic Approaches for Periodic Reconfiguration of Lightpath-based Networks under Multi-hour Traffic

Ramon Aparicio-Pardo
Universidad Politécnica de Cartagena/Dept. Information and Communication Technologies, Cartagena, Spain
Email: ramon.aparicio@upct.es

Belen Garcia-Manrubia
Universidad Politécnica de Cartagena/Dept. Information and Communication Technologies, Cartagena, Spain
Email: belen.garcia@upct.es

Nina Skorin-Kapov
University of Zagreb/Faculty of Electrical Engineering and Computing (FER), Zagreb, Croatia
Email: nina.skorin-kapov@fer.hr

Pablo Pavon-Marino
Universidad Politécnica de Cartagena/Dept. Information and Communication Technologies, Cartagena, Spain
Email: pablo.pavon@upct.es

Abstract—**Periodic lightpath reconfiguration of virtual topologies in transparent optical networks has been recently investigated as a mechanism to more efficiently adapt the network to predictable periodic traffic variations along a day or week. Scheduling periodic reconfigurations involves tuning a trade-off between a lower network cost obtained through better resource allocation, and undesired traffic disruptions that these reconfigurations may cause. This paper presents and compares two algorithms for planning a reconfigurable virtual topology suitable for exploring this trade-off. The first is based on a Lagrangean Relaxation of the planning problem, and the second is based on a Tabu Search meta-heuristic. The merits of both algorithms are assessed for moderate network sizes through comparison with analytical lower bounds and exact solutions obtained by a MILP formulation.**

Index Terms—**virtual topology design, network planning, multi-hour traffic, Lagrangean Relaxation, Tabu Search.**

I. INTRODUCTION

Optical networks based on Wavelength Division Multiplexing (WDM) have become an accepted solution for today's high-speed backbone networks [1]. In such networks, traffic is carried over lightpaths. A lightpath is defined as a transparent all-optical connection between an optical transmitter in the originating node and an optical receiver in the terminating node using a wavelength channel in each traversed physical link. Since lightpaths allow bypassing the electronic processing of the traffic at intermediate nodes, savings with respect to electronic switching equipment are achieved. In order to carry a given set of traffic demands (in Gbps), a set of lightpaths, comprising a so-called virtual topology, is established over the physical topology. Therefore, the Virtual Topology Design (VTD) problem implies solving a multilayer routing problem consisting of two layers. The upper layer problem involves routing traffic flows (demands) over the virtual topology; while the lower layer problem implicates finding a Routing and Wavelength Assignment (RWA) [2] of lightpaths over the physical topology. We must note that in this work we focus only on the upper layer routing problem and we assume a feasible RWA solution exists for each lightpath in the virtual topology. This assumption can realistically depict several network scenarios, such as metro-area optical networks with an over-dimensioned fiber plant.

In this paper, we address a variant of the aforementioned VTD problem, where we assume that the traffic varies along a given period of time (e.g. a day) following a repetitive pattern, i.e., that the traffic is periodic. Therefore, the traffic demand can be represented as a temporal sequence of matrices, where each matrix is associated to a time slot. This variant is denoted as Multi-Hour Virtual Topology Design (MH-VTD) [3]. Real traffic traces, such as the Abilene backbone network [4] and GEANT backbone network [5], support this assumption of the periodic nature of traffic.

The MH-VTD problem can be classified into: (i) the MH-VTD-NR (non-reconfigurable) problem, where the virtual topology cannot be changed along time, which means that we determine a static set of lightpaths capable of routing all the traffic as it varies over all time slots;

and (ii) the MH-VTD-R (reconfigurable) problem where the virtual topology changes along time to follow the multi-hour traffic variations. In both problem variants, the main objective is to minimize the number of optical transceivers in the network as a measure of the network cost. In the reconfigurable case, the number of reconfigurations associated with the evolution of the virtual topology is also minimized as a second optimization criterion. Considering these two objectives, we aim to take into account the trade-off existing between resources (optical transceivers) and reconfiguration costs. On the one hand, the reconfiguration of the virtual topology design along time may involve savings in optical resources since traffic is sent (received) to (from) different nodes at different peak hours. On the other hand, a reconfigurable virtual topology incurs extra costs provoked by the signaling complexity of the traffic adaptation and also by the disruptions in the existing traffic connections.

In this case, we focus on the MH-VTD-R problem assessing the minimization of the number of transceivers achieved via lightpath reconfiguration, against the amount of reconfigurations required. Since the MH-VTD-R problem is clearly NP-hard, like the single traffic matrix VTD problem (integer capacity planning) [6], heuristic algorithms are required to handle large-sized problems. To this aim, we present two heuristic approaches to handle the multihour problem: (i) a Lagrangean Relaxation via Subgradient optimization method (denoted as *LR*), and (ii) an algorithm based on a Tabu Search (denoted as *TS*).

The work presented in this paper is an extension of the works in [27] and [23], where the aforementioned algorithms were initially proposed. In this paper, we expand the algorithm descriptions, specifically elaborating upon on the theoretical steps that support the LR method. Furthermore, we perform a new series of tests, both for synthetically generated traffic and traffic traces from reference topologies, to better assess the behavior and quality of the algorithmic approaches. We also include new results obtained by solving exact MILP formulations for networks of moderate sizes. For cases when the MILP becomes intractable, we compare with lower bounds on the optimal number of transceivers required in the network.

The rest of the paper is organized as follows. Section II presents the state-of-the-art of multihour planning. Section III proposes an application to MH-VTD-R problems of the well-known Lagrangean Relaxation via Subgradient Optimization. Section IV describes a Tabu Search heuristic approach for the MH-VTD-R problem with penalization of reconfiguration. Section VI shows the results of the case studies considered and, finally, Section VII concludes the paper.

II. RELATED WORK

Multi-hour network design has been researched for multiple network technologies [7]-[27] (see [10] for a

comprehensive survey). If we focus on optical networks, the first investigations of MH planning were targeted towards the design of virtual topologies in multi-hop networks based on passive stars [7].

However, in the last decade, the interest of the optical community has shifted to lightpath-based transparent optical networks [3],[8],[11]-[27]. Initial investigations on virtual topology reconfiguration consider solely the case of one-time adaptations. In such cases, a change in traffic is known and procedures adapt the existing VTD to this change, without considering periodic (multi-hour) traffic trends [8],[11]-[14]. In all these works, a common objective is to minimize the number of lightpath reconfigurations in the VTD so as to reduce disruptions in the traffic connections.

Recently, other strategies have been attracting the interest of the research community considering periodicity in transparent optical networks planning [3], [15]-[27]. Most such research efforts have been centered on planning in the lower layer, i.e., finding an RWA for a given sequence of virtual topology designs corresponding to MH traffic. This is based on the Scheduled Lightpath Demand (SLD) model proposed in [15] where the evolution of individual lightpaths is known in advance. The planning problem then consists of finding a set of valid RWA solutions for the input VTDs, optimizing several network performances, such as the number of wavelengths used in the highest loaded fiber link. The SLD model enables more efficient utilization of resources by exploiting the temporal relationship between lightpaths. In [15], a branch and bound algorithm and Tabu Search heuristic were proposed for the Routing and Wavelength Assignment of a set of SLDs. An enhanced Tabu Search algorithm and efficient greedy algorithms for the same problem were proposed in [16]. Fault tolerant RWA was studied in [17] where the authors propose a Simulated Annealing algorithm using channel re-use and back-up multiplexing. Fault-tolerant RWA SLDs under single component failure was considered in [18]. They develop ILP formulations for the problem with dedicated and shared protection. In [19], the authors indicate some drawbacks in the formulations from [18], and give new ILP formulations for survivable service provisioning in networks with wavelength conversion. Their objective is to minimize the number of wavelength-links used by primary and secondary paths with guaranteed restoration in case of single failures.

A more general model, called the sliding scheduled traffic model was proposed in [20]. In this model, the set-up and holding times of lightpath demands are known in advance, but they are allowed to slide within a predefined window. Consequently, service provisioning consists not only of solving the RWA problem, but also scheduling demands in time subject to the sliding window constraints with the objective to minimize demand overlap. In [20], they solve the problems subsequently: first tackling scheduling using a demand time conflict reduction algorithm, and then solving RWA with two proposed approaches. Fault tolerant RWA for the sliding scheduled traffic model in networks without wavelength

conversion was considered in [21]. They also propose a two-phase approach: time conflict resolution followed by RWA. ILP formulations which jointly solve lightpath scheduling and RWA for the sliding scheduled traffic model are given in [22], along with a faster two-step optimization approach for larger problems.

In contrast to the above detailed works, this paper is centered on the upper layer multihour problem, i.e. determining the evolution of the virtual topology from the MH traffic. To the best of our knowledge, the only work previous in the literature on the MH-VTD-R problem variant is [23] which presents a naïve approach for the reconfigurable problem where the VTDs are independently planned in each time interval.

In the last years, we have been intensively investigating different MH-VTD problem variants presented in [3],[25]-[27]. In [25] a set of MILP formulations is proposed to solve several MH-VTD-NR and MH-VTD-R problem variants minimizing solely the number of transceivers. In [26], a set of Tabu Search based heuristic algorithms solving the previous problems is presented. In [3], we focus on the comparison of a set of variants of the non-reconfigurable problem, with and without flow routing reconfiguration. A set of MILP formulations for the problem and a 3-step algorithm which is based on the concept of traffic domination [28] are proposed.

Finally, in [27] we center on the reconfigurable problem, minimizing both transceiver and reconfiguration cost. We present two families of heuristic algorithms. One family of algorithms is based on the Tabu Search approach from [26], and the other one is based on a decomposition consisting of a Lagrangean Relaxation and a subgradient optimization of the dual problem.

Concerning to the application of similar heuristic approaches to network planning, we have already quoted above some examples of Tabu Search algorithms proposed for optical networks planning ([15], [16]). The Lagrangean Relaxation approach, on the other hand, has been applied previously in [10], [30] to solve multihour capacity design problems in dynamically reconfigurable ATM-based broadband networks. In these works, time-fixed modular capacities were assigned to an underlying and given physical topology, whereas time-varying virtual ATM paths were routed over these modular capacities. This problem is equivalent to the MH-VTD-NR problem, a problem variant not addressed herein, considering the time-fixed modular capacities as non-reconfigurable lightpaths, and the virtual ATM paths as non-defined higher layer traffic flows. On the contrary, in this work the algorithm is applied to the optical MH-VTD-R problem as formulated in Section III. In this MH-VTD problem variant, we attempt to minimize the number of optical transceivers and lightpath reconfigurations in a reconfigurable (time-varying) virtual topology.

III. LAGRANGEAN RELAXATION (LR) APPROACH

This section describes the application of the well-known *Lagrangean Relaxation via Subgradient Optimization* method [29] to multihour problems in optical networks. We refer to this approach as *LR* in the rest of this paper. This optimization method is based on relaxing the MH-VTD-R problem formulated as a MILP model. Therefore, we will introduce a formal model for the MH-VTD-R considered in this paper before describing the LR approach proposed.

A. MILP Formulation

In this subsection, we show an exact MILP formulation proposed for the MH-VTD-R problem which penalizes number of lightpath reconfiguration frequency.

Let N be the number of nodes in the network, and T the number of time slots in the multihour traffic. Let $i, j, s, d, n = \{1...N\}$ be the indices for the nodes, and $t = \{1...T\}$ be the index for the time slots Note that we assume that the last time interval $t = T$ is followed by the first time interval $t = 1$, since traffic is periodic. Let h^t denote the traffic matrix at time slot t, and $h_{sd}{}^t$ denote the traffic demand (measured in Gbps) from node s to node d, during time interval t). Let C denote the lightpath capacity in Gbps. The cost of each transmitter and receiver is considered equal, and is represented by c_1. An artificial cost of reconfiguring (setting up or turning down) a lightpath is denoted as c_2.

The decision variables of the MH-VTD-R problem are:

- $\mathbf{f} = (f_{ij}{}^{sdt}) \in [0, 1]$. Fraction of the total traffic demand $h_{sd}{}^t$ from node s to node d that is routed on the existing lightpaths from node i to node j.
- $\mathbf{p} = (p_{ij}{}^t) = \{0, 1, 2, ...\}$. Number of lightpaths from node i to node j, required during time interval t.
- $\mathbf{tx} = tx_n = \{0, 1, 2, ...\}$. Number of transmitters installed in node n.
- $\mathbf{rx} = rx_n = \{0, 1, 2,...\}$. Number of receivers installed in node n.
- $\mathbf{r}^+ = (r^+{}_{ij}{}^t) = \{0, 1, 2, ...\}$. Number of new lightpaths set up at time t with respect to the number of existing lightpaths at time t-1 (or time T if t=1) between the nodes (i, j).
- $\mathbf{r}^- = (r^-{}_{ij}{}^t) = \{0, 1, 2, ...\}$. Number of lightpaths torn down at time t with respect to the number of existing lightpaths at time t-1 (or time T if $t = 1$) between the nodes (i, j)

Then, the problem formulation is given by (1).

$$\min c_1 \sum_n (tx_n + rx_n) + c_2 \sum_{i,j,t} r^+{}_{ij}{}^t \tag{1a}$$

Subject to

$$\sum_{s,d} \{h_{sd}{}^t \cdot f_{ij}{}^{sdt}\} \le C \cdot p_{ij}{}^t, \quad i, j = \{1,...,N\}, \ t = \{1,...,T\} \tag{1b}$$

$$\sum_j f_{nj}^{sdt} - \sum_i f_{in}^{sdt} = \begin{cases} 1, if \ n = s \\ -1, if \ n = d, \ n, s, d = \{1,...,N\}, \\ 0 \ otherwise \end{cases} \quad (1c)$$

$$t = \{1,...,T\}$$

$$tx_n \geq \sum_j p_{nj}^t, \ n = \{1,...,N\}, \ t = \{1,...,T\} \quad (1d)$$

$$rx_n \geq \sum_i p_{in}^t, \ n = \{1,...,N\}, \ t = \{1,...,T\} \quad (1e)$$

$$p_{ij}^t - p_{ij}^{t-1} = r^+{}_{ij}^t - r^-{}_{ij}^t, \ i, j = \{1,...,N\}, t = \{2...,T\} \quad (1f)$$

$$p_{ij}^1 - p_{ij}^T = r^+{}_{ij}^1 - r^-{}_{ij}^1, \ i, j = \{1,...,N\} \quad (1g)$$

The objective function (1a) minimizes the total cost of the *transmitters* and *receivers* (c_1) and the artificial *lightpath reconfiguration* cost (c_2). Constraints (1b) and (1c) are the standard link capacity and link-flow conservation constraints, respectively. Constraints (1d) and (1e) guarantee that, at any time, the number of transmitters (receivers) installed at a node n is sufficient to establish the decided number of lightpaths originating (terminating) at n, respectively. And, finally, constraints (1f) and (1h) links the $\mathbf{r^+}$ and $\mathbf{r^-}$ variables with the accounting for the absolute increase and decrease, respectively, in the number of lightpaths between nodes i,j, at time t.

B. Lagrangean Relaxation via Dual Subgradient Optimization Algorithm

The Lagrangean Relaxation approach proposed herein uses the same general procedure described in [10] and [29],[30]. We will describe the application of this procedure to the MH-VTD-R problem, but we encourage the interested reader to consult these works for the detailed mathematical foundations about duality concepts.

The philosophy of the method is based on the idea of solving the MILP formulation (1), denoted in the remaining subsection as *primal problem*, in the dual variable space. The resulting dual problem consists of the maximization of a non-differentiable concave function. Therefore, the problem can be solved by using a standard iterative subgradient algorithm.

The minimization primal problem (1) is transformed into a maximization *dual problem* by "relaxing" (or "dualizing") a specially chosen subset of primal constraints. This "relaxation" is performed by adding these constraints to the primal objective function (1a) weighted by "Lagrangean multipliers" (also named "dual variables"). Then, the so-obtained *Lagrangean Relaxed Problem* is still a minimization problem in the primal variable space but parameterized by the dual multipliers. The optimization of this problem generates a value of the dual objective. Since *Lagrangean Relaxed Problem* is parameterized by the dual multipliers, the value of dual function will depend on the particular values of the multipliers. Consequently, to solve the dual problem, we are interested in finding those dual variables (or multipliers) maximizing the dual function. The exploration of the dual variable space can be carried out through a heuristic subgradient optimization method, since the dual function is concave. In such a method, we jump from a dual solution to other by following the direction of the subgradient vector of the dual function. The newly found values for the dual multipliers are employed to define a new instance of the *Lagrangean Relaxed Problem*, which is solved in the next iteration to find a new dual function value. Therefore, the overall method is based on successive iterations, each one of them consisting of a minimization step of the *Lagrangean Relaxed Problem*; and, a maximization step of the *Dual Problem* via a subgradient optimization. During these steps, the best primal and dual solutions are stored. We must recall from duality theory that the maximal value of best dual solution constitute a lower bound on the optimal primal objective function value. As a consequence, the method provides us a sub-optimality gap along the iterations. Finally, the algorithm finishes when the sub-optimality gap falls below a threshold or a maximal number of iterations is reached. In the next paragraphs, we will detail these aspects.

The *Lagrangean Relaxed Problem* appears when the constraints (1b), (1d) and (1e) are "relaxed" (or "dualized") by adding them (weighted by Lagrangean multipliers) to the objective function (1a) and eliminating them of the total set of constraints of (1b)-(1h). Let $\boldsymbol{\lambda} = (\lambda_{ij}^t)$, $\boldsymbol{\mu} = (\mu_i^t)$ and $\mathbf{v} = (v_j^t)$ be the Lagrangean (or dual) multipliers associated with the constraints (1b), (1d) and (1e), respectively. Then, the Lagrangean function $L(\boldsymbol{\lambda}, \boldsymbol{\mu}, \mathbf{v}, \mathbf{f}, \mathbf{p}, \mathbf{tx}, \mathbf{rx}, \mathbf{r^+})$ resulting of the relaxation is:

$$L(\boldsymbol{\lambda}, \boldsymbol{\mu}, \mathbf{v}, \mathbf{f}, \mathbf{p}, \mathbf{tx}, \mathbf{rx}, r+) =$$

$$= c_1 \sum_n \{tx_n + rx_n\} + c_2 \sum_{i,j,t} r^+{}_{ij}^t +$$

$$+ \sum_{i,j,t} \lambda_{ij}^t \cdot \left\{ \sum_{s,d} \{h_{sd}^t \cdot f_{ij}^{sdt}\} - C \cdot p_{ij}^t \right\} +$$

$$+ \sum_{i,t} \mu_i^t \cdot \left\{ \sum_j p_{ij}^t - tx_i \right\} +$$

$$+ \sum_{j,t} v_j^t \cdot \left\{ \sum_i p_{ij}^t - rx_j \right\} =$$

$$= \sum_n \left\{ c_1 - \sum_t \mu_n^t \right\} \cdot tx_n +$$

$$+ \sum_n \left\{ c_1 - \sum_t v_j^t \right\} \cdot rx_n +$$

$$+ \sum_{t,i,j} \lambda_{ij}^t \cdot \left\{ \sum_{s,d} \{h_{sd}^t \cdot f_{ij}^{sdt}\} \right\} +$$

$$+ c_2 \sum_{i,j,t} r^+{}_{ij}^t + \sum_{t,i,j} \left\{ \mu_i^t + v_j^t - C \cdot \lambda_{ij}^t \right\} \cdot p_{ij}^t =$$

$$= L_1(\boldsymbol{\mu}, \mathbf{tx}) + L_2(\mathbf{v}, \mathbf{rx}) +$$

$$+ L_3(\boldsymbol{\lambda}, \mathbf{f}) + L_4(\boldsymbol{\lambda}, \boldsymbol{\mu}, \mathbf{v}, \mathbf{r}^+, \mathbf{p}) \qquad (2)$$

And the *Lagrangean Relaxed Problem* is:

$$W(\boldsymbol{\lambda}, \boldsymbol{\mu}, \mathbf{v}) =$$

$$\min_{\mathbf{f}, \mathbf{p}, \mathbf{tx}, \mathbf{rx}, \mathbf{r}^+} \left\{ \begin{array}{l} L(\boldsymbol{\lambda}, \boldsymbol{\mu}, \mathbf{v}, \mathbf{f}, \mathbf{p}, \mathbf{tx}, \mathbf{rx}, \mathbf{r}^+) \\ \text{subject to} \\ \text{constraints (1c),(1f) and (1g)} \end{array} \right\} \qquad (3)$$

Where $W(\boldsymbol{\lambda}, \boldsymbol{\mu}, \mathbf{v})$ is the dual function, and the *dual problem* to solve via subgradient optimization is:

$$\max_{\boldsymbol{\lambda}, \boldsymbol{\mu}, \mathbf{v}} \left\{ W(\boldsymbol{\lambda}, \boldsymbol{\mu}, \mathbf{v}) \mid \boldsymbol{\lambda} \geq \mathbf{0}, \boldsymbol{\mu} \geq \mathbf{0}, \mathbf{v} \geq \mathbf{0} \right\} \qquad (4)$$

The minimization problem (3) of the Lagrangean function $L(\boldsymbol{\lambda}, \boldsymbol{\mu}, \mathbf{v}, \mathbf{f}, \mathbf{p}, \mathbf{tx}, \mathbf{rx}, \mathbf{r}^+)$ can be decoupled into four sets of separate minimization subproblems since the relaxation of the constraints (1b), (1d) and (1e) has broken the dependencies among some primal decision variables. The first and second sets of subproblems are associated to the variables $\mathbf{tx}$ and $\mathbf{rx}$, respectively. The third set of subproblems corresponds to the variables $\mathbf{f}$ solely restrained by the constraints (1c). And, finally, in the fourth set of subproblems the variables $\mathbf{p}$, $\mathbf{r}^+$ and $\mathbf{r}^-$ remain linked trough the constraints (1f) and (1g).

$$W(\boldsymbol{\lambda}, \boldsymbol{\mu}, \mathbf{v}) =$$

$$= \min_{\mathbf{f}, \mathbf{p}, \mathbf{tx}, \mathbf{rx}, \mathbf{r}^+} \left\{ \begin{array}{l} L(\boldsymbol{\lambda}, \boldsymbol{\mu}, \mathbf{v}, \mathbf{f}, \mathbf{p}, \mathbf{tx}, \mathbf{rx}, \mathbf{r}^+) \\ \text{subject to} \\ \text{constraints (1c),(1f),(1g)} \end{array} \right\} =$$

$$= \min_{\mathbf{tx}} \left\{ L_1(\boldsymbol{\mu}, \mathbf{tx}) \right\} + \min_{\mathbf{rx}} \left\{ L_2(\mathbf{v}, \mathbf{rx}) \right\} +$$

$$+ \min_{\mathbf{f}} \left\{ \begin{array}{l} L_3(\boldsymbol{\lambda}, \mathbf{f}) \\ \text{subject to} \\ \text{constraints (1c)} \end{array} \right\} +$$

$$+ \min_{\mathbf{p}, \mathbf{r}^+} \left\{ \begin{array}{l} L_4(\boldsymbol{\lambda}, \boldsymbol{\mu}, \mathbf{v}, \mathbf{p}, \mathbf{r}^+) \\ \text{subject to} \\ \text{constraints (1f),(1g)} \end{array} \right\} =$$

$$= W_1(\boldsymbol{\mu}) + W_2(\mathbf{v}) + W_3(\boldsymbol{\lambda}) + W_4(\boldsymbol{\lambda}, \boldsymbol{\mu}, \mathbf{v}) \qquad (5)$$

If we analyze these subproblems, we observe that solutions $\mathbf{tx}^*$, $\mathbf{rx}^*$ and $\mathbf{f}^*$ to the first (W_1), second (W_2) and third (W_3) subproblems, respectively, can be easily computed. For each group (s,d,t), the solutions $f^*_{ij}{}^{sdt}$ is the shortest path between node s and d in network with link

weights $\lambda_{ij}{}^t$. The solutions tx^*_n can be trivially obtained by setting:

$$tx_n{}^* = \begin{cases} UB_{TX}, \text{if } c_1 < \sum_t \mu_n^t \\ LB_{TX}, \text{if } c_1 \geq \sum_t \mu_n^t \end{cases}, n = \{1...N\} \qquad (6)$$

Whereas, the solutions rx^*_n can be trivially obtained by:

$$rx_n{}^* = \begin{cases} UB_{RX}, \text{if } c_1 < \sum_t v_n^t \\ LB_{RX}, \text{if } c_1 \geq \sum_t v_n^t \end{cases}, n = \{1...N\} \qquad (7)$$

where UB_{TX} and UB_{RX} are upper bounds on the number of transmitters and receivers, respectively. These upper bounds may be artificially large enough values.

Conversely, LB_{TX} (or LB_{RX}) represents lower bounds on the number of transmitters (or receivers); and, for each node n, we can take the minimum number of transmitters (or receivers) that the node n requires, i.e., the largest number of lightpaths required to add (or drop) the total traffic generated by (or targeted to) the node in any time slot t. Thus, these lower bounds can be calculated as follows.

$$LB_{TX}(n) = \max_{t=1...T} \left\{ \sum_{j=1}^N \left\lceil \frac{h_{n,j}^t}{C} \right\rceil \right\} \qquad (8)$$

$$LB_{RX}(n) = \max_{t=1...T} \left\{ \sum_{i=1}^N \left\lceil \frac{h_{i,n}^t}{C} \right\rceil \right\} \qquad (9)$$

Finally, the solution $\mathbf{p}^*$, $\mathbf{r}^{*+}$ and $\mathbf{r}^{*-}$ are obtained by solving the fourth set of ILP subproblems W_4 in (5). Although solving these subproblems implies to solve ILP formulations, we must note that they suppose an important reduction on complexity with respect to the original unrelaxed primal one.

Once we have found a solution ($\mathbf{f}^*$, $\mathbf{p}^*$, $\mathbf{tx}^*$, $\mathbf{rx}^*$, $\mathbf{r}^{*+}$, $\mathbf{r}^{*-}$) that minimizes the *Lagrangean function* $L(\boldsymbol{\lambda}, \boldsymbol{\mu}, \mathbf{v}, \mathbf{f}, \mathbf{p}, \mathbf{tx}, \mathbf{rx}, \mathbf{r}^+)$ (2), the *dual function* is totally characterized. Further, we must note that *dual function* is a piecewise linear concave function, since it is the minimum of the linear functions appearing in the solutions of the subproblems. This is the key point of the method. We have transformed a mixed-integer problem into a convex problem (maximization of a concave function) where a local solution is also a global one. On the other hand, the new concave problem is not differentiable (the objective function is piecewise). Thus, the dual space could not be explored with a classical gradient optimization step but with a subgradient one. The subgradient vector $\mathbf{g}$, used as search direction, is computed as follows:

$$\mathbf{g} = \nabla W(\boldsymbol{\lambda},\boldsymbol{\mu},\mathbf{v});$$

$$\mathbf{g} = \begin{bmatrix} \mathbf{g}^1 & \mathbf{g}^2 & \mathbf{g}^3 \end{bmatrix}$$

$$\mathbf{g}^1 = \left(g^1_{ijt}\right) = \sum_{s,d}\left\{h^t_{sd}\cdot f^{sdt}_{ij}\right\} - C\cdot p^t_{ij};\ i,j=\{1,...,N\},\ t=\{1,...,T\}$$

$$\mathbf{g}^2 = \left(g^2_{it}\right) = \sum_{j} p^t_{ij} - tx_i;\quad i=\{1,...,N\},\ t=\{1,...,T\}$$

$$\mathbf{g}^3 = \left(g^3_{jt}\right) = \sum_{i} p^t_{ij} - rx_j;\quad j=\{1,...,N\},\ t=\{1,...,T\} \tag{10}$$

Then, the new triple ($\boldsymbol{\lambda}$, $\boldsymbol{\mu}$, $\mathbf{v}$) in the dual space in the next iteration $k+1$ is updated by the subgradient step as:

$$\boldsymbol{\lambda}^{k+1} = \max\left\{\boldsymbol{\lambda}^k + s_k\cdot\mathbf{g}^1,\ \mathbf{0}\right\} \tag{11}$$

$$\boldsymbol{\mu}^{k+1} = \max\left\{\boldsymbol{\mu}^k + s_k\cdot\mathbf{g}^2,\ \mathbf{0}\right\} \tag{12}$$

$$\mathbf{v}^{k+1} = \max\left\{\mathbf{v}^k + s_k\cdot\mathbf{g}^3,\ \mathbf{0}\right\} \tag{13}$$

where the step size s_k is given by :

$$s_k = p\cdot\frac{\left(\overline{W} - W(\boldsymbol{\lambda}^k,\boldsymbol{\mu}^k,\mathbf{v}^k)\right)}{\left\|\nabla W(\boldsymbol{\lambda}^k,\boldsymbol{\mu}^k,\mathbf{v}^k)\right\|^2} \tag{14}$$

where $\overline{W}$ is the best dual function value found along the algorithm's iterations and p is parameter initiated to p_0 value and halved after a certain number of iterations k_p without improvement in the dual objective, without becoming less than a minimal value p_{min}.

The new dual multipliers ($\boldsymbol{\lambda}^{k+1}$, $\boldsymbol{\mu}^{k+1}$, $\mathbf{v}^{k+1}$) are replaced in the Lagrangean function (2), given rise to a new instance of the *Lagrangean Relaxed Problem* (3) for the $k+1$ iteration. Then, after solving the new *Lagrangean Relaxed Problem*, a new *subgradient optimization* step follows. During the algorithm's iterations, we store the best primal and dual solutions found and update the corresponding suboptimality gap from them. The method continues until a stoping rule such as maximum number of iterations $k_{maz} > k_p$ is reached; or, the suboptimality gap becomes negligible.

Finally, and before concluding this subsection, we must note that the minimal solution (**f***, **p***, **tx***, **rx***, **r***⁺, **r***⁻) that optimizes the *Lagrangean Relaxed Problem* (3) might be not feasible from the point of view of the *primal problem* (i.e. *primal unfeasible*), since we have relaxed some constraints in (1). Therefore, we need to find a *primal feasible* solution (**f***, **p^pf**, **tx^pf**, **rx^pf**, **r***⁺, **r^+pf**, **r^-pf**). This solution can be generated from the minimal solution **f*** following the next steps. Unlike the solutions **p***, **tx*** , **rx***, and **r⁺***; the solutions **f*** is also *primal feasible*. For this reason, we may use initially **f*** in (1b) to compute a primal-feasible solution **p^pf**. Then, this solution **p^pf** will be replaced in (1d) and (1e) to derivate primal-feasible **tx^pf** and **rx^pf**; and, in (1f) and (1g) to derivate primal-feasible **r^+pf** and **r^-pf**.

IV. Tabu Search (TS) Approach

In this section, a Tabu Search heuristic algorithm, denoted as *TS* in the remainder of this paper, is proposed to address the MH-VTD-R problem with penalization of lightpath reconfiguration. This is an adaptation of the approach presented in [16] to include the minimization of the reconfigurations in the virtual topology. Tabu Search is an iterative meta-heuristic where the exploration of the solution space is controlled by a memory structure called a tabu *list*. The *tabu list* stores a certain number of the last visited solutions, prohibiting the search to reconsider them for as long as they remain in the list. With this, we prevent the search from cycling between neighboring solutions around a local optimum.

First, the algorithm starts with an initial current solution. Then, in each iteration, the algorithm explores all the neighboring solutions with respect to the current one, except those memorized in the *tabu list*. In our approach, we explore a reduced neighborhood to alleviate the computational load. The solutions explored in the neighborhood are computed by a single-time slot MILP formulation, which constraints the number of available transceivers at a given node n in a given time slot t. All the neighboring solutions explored in the iteration are evaluated with a fitness function. The best one becomes in the new current solution in the next iteration. After each iteration, the *tabu list* and the best found solution overall, called the *incumbent* solution, are updated. The algorithm terminates according to a predefined termination criterion, in our case, the number of iterations without improvement.

A. Solution Computation

A solution in *TS* consists of T virtual topology designs, one for each time slot $t = 1, ..., T$. Each one of these VTDs is computed by the single time slot MILP formulation (14). This formulation receives as input a single traffic matrix and a set of upper bounds on the number of transceivers at each node. It calculates a virtual topology and its corresponding flow routing with the objective to minimize electronic switching, i.e., to minimize the number of lightpaths traversed by a unit of traffic in the network.

The decision variables are:

- $\mathbf{f} = (f^{sd}_{ij}) \in [0, 1]$. Fraction of the total traffic demand h_{sd} from node s to node d that is routed on the existing lightpaths from node i to node j.
- $\mathbf{p} = (p_{ij}) = \{0, 1, 2, ...\}$. Number of lightpaths from node i to node j.

The objective function and the set of constraints are described in (14), for the problem associated with a time slot $t = 1, ..., T$:

$$\min \sum_{i,j,s,d} f^{sd}_{ij} \tag{14a}$$

Subject to

$$\sum_{s,d}\left\{h_{sd}\cdot f_{ij}^{sd}\right\}\le C\cdot p_{ij},\quad i,j=\{1,...,N\}\qquad(14b)$$

$$\sum_{j} f_{nj}^{sd} - \sum_{i} f_{in}^{sd} = \begin{cases} 1, if\ n=s \\ -1, if\ n=d, \\ 0\ otherwise \end{cases}\qquad(14c)$$

$$n,s,d=\{1,...,N\}$$

$$\sum_{j} p_{nj} \le UB_{TX}(n),\ n=\{1,...,N\}\qquad(14d)$$

$$\sum_{i} p_{in} \le UB_{RX}(n)\ n=\{1,...,N\}\qquad(14e)$$

Constraints (14b) represent the capacity constraints, and equations (14c) are the flow conservation constraints. Constraints (14d) and (14e) ensure that the number of lightpaths originating (terminating) at a given node, must be below the pre-fixed upper bounds on number of transmitters (receivers) at that node.

The initial solution in *TS* is obtained by solving the formulation (14) separately for each time slot $t = \{1...T\}$, setting to infinity the upper bounds on the transceivers per node $UB_{TX}(n)$ (or $UB_{RX}(n)$).

B. Solution Space Exploration

Herein, we introduce some concepts and notations required for a better understanding of the algorithm description:

- *Activity matrices*: For a given solution composed of *T* virtual topologies, we define a (*NxT*) matrix named *Active Transmitters* (**AT**) *matrix*. $AT(n,t) = \{0, 1, 2, …\}$ represents the number of transmitters that are active at node *n* in time slot *t* in that solution. In other words, a row *n* shows how the number of active transmitters at node *n* varies over time. A column *t* shows the number of active transmitters at all nodes in time slot *t*. The necessary number of transmitters per node is shown as a vector $T(n) = \max(t)\{AT(n,t)\}$, i.e. the maximum element in each row *n*. The total number of transmitters needed in the network corresponding to that solution is $T_{tot} = \text{sum}(n)\{T(n)\}$. Consider the following example. Suppose there are 3 nodes and 4 time slots, i.e. N = 3, T = 4, with an *Active Transmitters matrix* of a potential solution as shown below.

$$\mathbf{AT}=\begin{pmatrix} 3 & 1 & 1 & 2 \\ 2 & 2 & 1 & 1 \\ 1 & 2 & 0 & 4 \end{pmatrix}$$

Figure 1. An example of an **AT** matrix.

In this example, value $AT(1,4) = 2$ indicates that in the fourth time slot there are 2 transmitters active at node 1. The number of necessary transmitters per node is: $T(n) = [3\ 2\ 4]$, while the total number of transmitters required is $T_{tot} = 11$.

We do the same for receivers to get activity matrix Active Receivers (**AR**), the necessary number of receivers per node **R**(*n*), and the total required receivers R_{tot}.

- *Utilization matrices*: For a given solution, we define a (*NxT*) matrix, which we denote as Utilization of Transmitters (**UT**) matrix. It is obtained from matrix **AT** by subtracting from each element in **AT**, the value of the maximal element in its row except itself. In other words,

$$UT(n_i,t_i)=AT(n_i,t_i)-\max_{t|t\ne t_i}(AT(n_i,t))\qquad(15)$$

According to the above definition, the utilization matrix for the previous example is:

$$\mathbf{UT}=\begin{pmatrix} 1 & -2 & -2 & -1 \\ 0 & 0 & -1 & -1 \\ -3 & -2 & -4 & 2 \end{pmatrix}$$

Figure 2. An example of an **UT** matrix.

The positive elements in this matrix indicate the number of transmitters that are only used in a single time slot, i.e. are not very efficiently utilized. For example, $UT(3, 4) = 2$ indicates that in time slot 4 at node 3, there are 2 transmitters that are only used in this time slot. Intuitively, trying to rearrange these poorly utilized transmitters may lead to better results. We do the same for receivers from **AR** to get a matrix Utilization of Receivers (**UR**).

TS explores the solution space as follows. The heuristic iteratively solves smaller MILP formulations (14) limiting the number of transceivers for independent time intervals in order to jump between neighboring solutions, and, thus, explore the solution space in a directed manner.

After solving (14), without limiting the number of transceivers, for each time slot $t = \{1...T\}$ to create an initial solution, Tabu Search iterations are run alternating between limiting the total number of transmitters and the total number of receivers until the maximal number of iterations without improvement of the best solution is met. Upon termination, the incumbent (i.e., best visited) solution is deemed the final result. During these iterations, two tabu lists are maintained, realized as FIFO (First In First Out) queues of finite size corresponding to either transmitters (tabu list TL_{TX}) or receivers (tabu list TL_{RX}). Each entry in TL_{TX} (or TL_{RX}) is a node *n* where the transmitters (or receivers) cannot be further reduced as long as *n* remains in the list.

In each iteration, we consider neighboring solutions of a current solution to be all those one changed in only one time slot *t*, i.e., solely a virtual topology and a flow routing at a time slot *t* is different between two neighbors, whereas the *VTDs* for the remaining time slots are equal between them. Since there are a large number of such solutions, we propose a neighborhood reduction

technique to consider those solutions more likely to improve the incumbent solution.

Firstly, if the number of transmitters (or receivers) at some node in the current solution is already at its lower bound according to (8) (or (9)), there is no need to consider neighboring solutions with less transmitters or receivers, respectively. If we consider that we are searching for virtual topologies which use the minimum number of transceivers required to carry the offered periodic traffic, reducing the number of transceivers at highly utilized nodes does not seem very useful. A reduction of these transceivers will need compensation in several time slots. Conversely, reducing a transmitter (receiver) at nodes where transmitters (receivers) are used only in one single time slot can more easily be compensated for. In other words, we think eliminating poorly utilized transceivers where feasible should yield better results.

Consequently, we perform a neighborhood reduction as follows. For each node $n = \{1...N\}$, we choose one time slot t with poorly utilized transmitters, excepting for those nodes forbidden by the tabu list TL_{TX}. These pairs (n, t) correspond to those neighboring solutions taken as candidates *with respect to transmitters*. Thus, the total number of candidates *with respect to transmitters* is N minus the size of the tabu list TL_{TX}. Analogously, we can define candidates *with respect to receivers*. Note that candidates cannot include nodes at time slots for which the lower bound on transmitters/receivers is reached.

To choose the set of candidates (n, t) *with respect to transmitters*, we consider only *strictly positive*, i.e. poorly utilized, elements in **UT**, for which $AT(n,t) > LB_{TX}(n)$. For each node n, we choose randomly one such element which is not forbidden by the tabu list. If there are no positive elements in **UT**, we choose a random time slot corresponding to one of the elements with zero value zero. For each obtained candidate (n, t), we run the formulation (14) for the traffic matrix at time t but limiting the maximum number of transmitters at node n to $AT(n, t)$-1. Receivers at node n, along with transmitters and receivers at all other nodes, are also limited to their maximal value along time in the current solution. The new virtual topology obtained by solving the formulation (14) replaces the virtual topology at corresponding time slot t in the current solution, giving the new neighboring solution. The same is done to obtain neighbors from candidates (n, t) *with respect to receivers*, chosen analogously from non-negative elements of **UR** for which $AR(n,t) > LB_{RX}(n)$.

In our example, assuming no violation of the lower bound and tabu list constraints, we would have three neighbors with respect to transmitters obtained from candidates (1, 1), (2, 1 or 2) and (4, 3), which correspond to elements $UT(1, 1)$, $UT(2, 1)$ or $UT(2, 2)$, and $UT(4, 3)$, respectively. If all neighboring solutions in the reduced neighborhood are infeasible in one iteration, the neighborhood is increased to $2 \cdot T \cdot N$ where candidates correspond to *all* nodes and *all* time slots for both transmitters and receivers, and with no constraints imposed by the tabu list.

The quality of all the candidates is assessed by means of a *fitness function*. The best neighboring solution among these candidates, according to the *fitness function*, becomes the new current solution in the next iteration. The used fitness function is defined as:

$$c_1 \sum_n \left\{ \max_t \sum_{j, j \neq n} p_{nj}^t \right\} + c_1 \sum_n \left\{ \max_t \sum_{i, i \neq n} p_{in}^t \right\} + c_2 \sum_{i,j,t} \left| p_{ij}^t - p_{ij}^{t-1} \right| \quad (16)$$

where p_{ij}^t is the number of lightpaths established between nodes i and j at the time slot t, c_1 is the cost of one transceiver (or receiver), and c_2 is the cost of one lightpath reconfiguration.

This fitness function aims to minimize both the number transceivers and the lightpath reconfigurations, assuming reconfigurable equipment, i.e., the same transceivers can be used for different lightpaths as long as they are in different time slots. The lightpath reconfigurations are computed as the increases or decreases in the number of lightpaths between consecutive time slots.

We can observe that (16) matches with (1a) expressed in terms of p_{ij}^t, since solutions constructed by the Tabu Search algorithm in each iteration are derived from single time interval MILP formulations (14) for all t.

After each iteration, if the new current solution selected as above is better than the incumbent solution, the incumbent solution is updated accordingly. In addition to this, the tabu lists TL_{TX} and TL_{RX} are updated to include the node n of the best neighbor in the last iteration.

Finally, the Tabu Search terminates when a maximum number of iterations without improvement is reached.

V. RESULTS

This section presents the results of extensive tests conducted to assess the performance of the proposed algorithms, compared with those obtained by the exact MILP formulations (in small networks) and lower bounds to the network cost (for larger networks). The algorithms were implemented in the MatplanWDM tool [31] which links to the TOMLAB/CPLEX library [32] to solve the MILP formulations.

Since we follow the assumption of a sufficient number of wavelengths established in Section I, any VTD has a feasible RWA solution. Thus, the optimization problem is independent of the physical network topology. Therefore, the multihour demand is the only input data to the planning problem. Under these considerations, the Lagrangean Relaxation (LR)-based and the Tabu Search (TS)-based approaches are tested and compared for six network traffic data scenarios: a) three small-sized scenarios based on artificial networks; and, b) three larger-sized scenarios based on reference networks brought from literature. In all these scenarios, the multihour traffic consists of 24 matrices used to illustrate hourly fluctuations over the course of a day. All the

simulations were run on an Intel Core2 Duo CPU P8400 2.26 GHz processor.

The small non-real network scenarios consist of three networks of $N = \{4, 6, 8\}$ nodes, respectively. For each network case, five multi-hour sequences were generated randomly using the model described in the equations (17)-(18).

$$m_{ij}^t = b_{ij} \cdot \text{activity}(t) \cdot rf(R), \quad \forall i, j, t. \tag{17}$$

According to the model, the traffic between two nodes at a given time $m_{i,j}^t$ was calculated as the product of three factors. First, factor $b_{i,j}$ gives the (i,j) coordinate of a base traffic matrix computed for the sequence as follows. 80% of the values in matrix b (randomly chosen) were set to one, while the remaining 20% were set to two. This is meant to capture the effect of non-uniformities in the generated traffic matrices. Secondly, activity factor $activity(t)$ in equation (17) intends to capture the effect of traffic intensity variation along the day. Our intensity variation scheme is described by equation (18), based on the intensity model presented in [33].

$$\text{activity}(t) = \begin{cases} 0.1 \, \text{if } t \in [1,6] \\ 1 - 0.9 \cdot \left(\cos\left(\frac{\text{mod}(t,T) - 6}{18} \cdot \pi \right) \right)^{10} \text{ otherwise} \end{cases} \tag{18}$$

where $t = 1, ..., T$

Factor $rf(R)$ in (17) is a random value, uniformly distributed over interval $[1-R, 1+R]$. A new independent sample of the $rf(R)$ factor was used for each value $m_{i,j}^t$. The purpose of the rf factor is to include a randomness effect in the traffic intensity. In our tests R was set to 0.2.

Besides the above commented scenarios, three larger scenarios based on more realistic networks are studied: the Abilene ($N = 11$), NSFNET ($N = 14$) and 15-node worldwide networks. In these three cases, the physical topologies span over several time zones in order to investigate the temporal mismatch of the most loaded traffic hour.

In the Abilene network scenario, we used data from a real traffic trace, publicly available at [1]. This data consists of traffic matrices spanning several weeks. Thus, we averaged all values of the trace taken at the same time in the day to obtain a sequence of 24 matrices illustrating typical hourly fluctuations in a day.

For the NSF net case, a unique multi-hour sequence was generated using the aforementioned model described in equations (17)-(18), using as basis matrix b, the reference matrix in [34]. As before, R was set to 0.2.

Finally, the last scenario corresponds to synthetic multi-hour traffic generated for a 15-node worldwide network. The physical topology is described in Table I and Fig. 3. The traffic was generated using the multi-hour model proposed in [33], for which the traffic between two nodes is proportional to the product of the two node populations; the variation of the traffic activity along the

day in a node evolves according to expression (18); and, the traffic demand between a pair of nodes depends of the activity of both end nodes.

In all the scenarios, the sequences of traffic matrices were normalized by multiplying them with a normalization factor (nf) given in equation (19). Value nf was calculated such that the average traffic between two nodes in the most loaded time slot is equal to $\rho \cdot C$, where C is the lightpath capacity, and ρ is a traffic load parameter. The values tested in our study were for $\rho = \{0.1, 1, 10\}$. A value of $\rho = 0.1$ corresponds to the case when the average traffic between two nodes in the most loaded time slot is only 10% of a single lightpath capacity. On the contrary, a value of $\rho = 10$ captures cases in which the average traffic between two nodes in the most loaded time slot is the capacity of ten lightpaths.

$$h_{ij}^t = m_{ij}^t \cdot nf(\rho), \qquad \forall i, j, t$$

$$\text{where } nf(\rho) = \frac{n \cdot (n-1) \cdot \rho \cdot C}{\max_t \left\{ \sum_{i,j} m_{ij}^t \right\}} \tag{19}$$
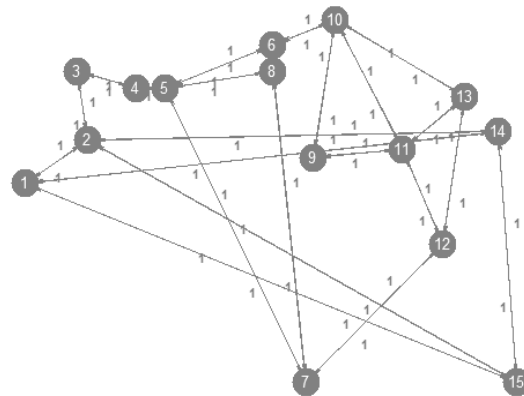
Figure 3. 15-node Worldwide Network Topology.

TABLE I.
DATA OF 15-NODE WORLDWIDE NETWORK TOPOLOGY.

Node	Name	Population	Timezone
1	Honolulu	378155	-11
2	Los Angeles	3789981	-8
3	Vancouver	545671	-8
4	Chicago	2886251	-6
5	New York	8084316	-5
6	London	6638109	0
7	Cape Town	2415408	1
8	Paris	2125246	1
9	Athens	745514	2
10	Moscow	10101500	3
11	New Delhi	12791458	4
12	Beijing	13820000	7
13	Singapore	4017733	7
14	Tokyo	8134688	8
15	Sydney	3997321	9

TABLE II.
NUMBER OF TRANSCEIVERS (AND RECONFIGURATIONS) OBTAINED FOR
SMALL NETWORK SCENARIOS

N	ρ	LB	MILP	TS	LR
4	0.1	8	8 (1.2)	8 (45.6)	21.4 (34.8)
	1	28.2	28.2 (0.4)	28.4 (35.2)	36.6 (15.2)
	10	263.8	263.8 (7.4)	266.6 (237.2)	272.2 (235.2)
6	0.1	12	16 (1.2)	18.4 (96.4)	54.8 (152.6)
	1	71.2	71.8 (4.4)	71.8 (91.6)	91.4 (34.8)
	10	654.2	656.6 (17.8)	662 (616.6)	679.2 (612.8)
8	0.1	16	- (-)	31.6 (147.8)	105.6 (313.4)
	1	127.6	129.8 (5.2)	132.6 (172.2)	167.2 (74.6)
	10	1199.8	1203.2 (71.6)	1212.6 (1141.8)	1249.8 (1143)

TABLE III.
NUMBER OF TRANSCEIVERS (AND RECONFIGURATIONS) OBTAINED FOR
LARGE NETWORK SCENARIOS

Network	ρ	LB	TS	LR
Abilene (N=11)	0.1	36	52 (201)	93 (40)
	1	248	260 (219)	369 (97)
	10	2385	2392 (1078)	2497 (1048)
NSF (N=14)	0.1	56	235 (574)	309 (483)
	1	406	424 (550)	585 (301)
	10	3959	3972 (3855)	4132 (3879)
Worldwide (N=15)	0.1	66	104 (499)	290 (210)
	1	506	516 653)	774 (232)
	10	4920	4924 (3331)	5134 (3092)

Tables II and III summarize all the performed tests. In Table II, the heuristic approaches are studied for each of the small networks ($N = \{4, 6, 8\}$) with synthetic traffic. For each network size N and network load ρ, we generated five independent sequences of traffic matrices. The columns correspond to:

- LB: lower bounds (LB) on the optimal number of transceivers in the network computed, calculated as:

$$LB = \sum_{n=1}^{N} \left\{ LB_{TX}(n) + LB_{RX}(n) \right\} \quad (20)$$

where LB_{TX} and LB_{RX} are computed according to (8) and (9).

- MILP: exact solutions of the MILP formulation (1), for those cases where the solver found a solution.
- TS: approximate solutions provided by the TS approach. The stopping criterion was fixed to 20 iterations without improving the best solution found and the size of the *tabu list* was set to 3, 4 and 5, respectively.
- LR: approximate solutions provided by the LR approach. The total number of iterations was set to 1000 (although the best solution was reached after 50 iterations). The initial and minimal values of step-size parameter p were fixed to 2 and 0.005, respectively; and, the maximum number of iterations without improvement to halve p was set to 10.

In all the approaches, the cost of one transceiver (c_1) was fixed to 1, whereas the cost of reconfiguring a lightpath c_2 was set to a sufficiently small fraction ($\sim 10^{-5}$) of the cost c_1, so that the cost of the transceivers dominates the optimization, minimizing the number of transceivers as main objective.

Each cell in Table II shows the average number of transceivers used in the solutions obtained for each of the five sequences corresponding to the same network and load ρ. In parenthesis, we include the number of reconfigurations, averaged over the five sequences. The cells marked with (-/-) represent cases where the associated approach was not able to obtain a solution in reasonable time (250000 s ≈ 3 days).

Table III collects the results for the scenarios based on realistic networks: Abilene, NSFNET and the 15-node worldwide network. Herein, for each network and a network load ρ, a unique multi-hour traffic sequence is used. The columns of Table III are the same as Table II, excepting the MILP column. In this case, the formulation (1) becomes intractable for the network sizes. On the other hand, the same values as Table I were used for the algorithm parameters, apart from the size of the *tabu list* in TS. This parameter was set to 7, 8 and 9 for the 11-node Abilene network, 14-node NSFNET network and the 15-node worldwide networks, respectively.

The results in both tables show that TS outperforms LR in terms of the number of transceivers, while, with respect to reconfiguration frequency, LR obtains similar results for high loads; and, generally better results for medium and low loads. However, these solutions require significantly more transceivers (between 25% and 234%) with respect to the TS solutions. These extra transceivers enable a VTD reconfigurable design with fewer reconfigurations. Furthermore, we can observe that the transceiver performance of LR versus TS worsens with load parameter ρ.

Finally, the optimality of the TS solutions in terms of the number of transceivers (total transceiver cost) is studied in Tables IV and V for small and large networks, respectively. In Table IV, two sub-optimality gaps are computed with respect to: (i) the optimal MILP solutions for four-, six- and eight-node networks (Gap TS-MILP); and, (ii) the lower bounds (Gap TS-LB) for all the networks. In Table V, the sub-optimality gaps with respect to the lower bounds (Gap TS-LB) are the only one. The analysis of these gaps in the tables confirm that TS is able to provide good approximate solutions for loads $\rho = 1$ and $\rho = 10$ in general; and, even quasi-optimal solutions for $\rho = 10$ and for small sized networks. However, for a load of $\rho = 0.1$ and large networks ($N \geq 8$), it is difficult to conclude whether the lower bound is weak or the heuristic solutions are far from optimal, as the suboptimal Gap TS-LB is not negligible and exact MILP solutions were not able to finish for all the cases. Moreover, the only two low load cases ($N = 4$, $N = 6$) where both gaps are available are contradictory, making it hard to assess the weakness of the lower bounds. For $N = 4$, the optimal solutions and lower bounds were equal; whereas for $N = 6$, the optimal solutions were one third larger than the lower bounds.

TABLE IV.
OPTIMALITY GAPS OF THE TOTAL TRANSCEIVER COST OF THE TS
SOLUTIONS FOR SMALL NETWORK SCENARIOS

N	ρ	Gap TS-MILP (%)	Gap TS-LB (%)
4	0.1	0.00%	0.00%
	1	0.70%	0.70%
	10	1.05%	1.05%
6	0.1	13.04%	34.78%
	1	0.00%	0.84%
	10	0.82%	1.18%
8	0.1	-	49.37%
	1	2.11%	3.77%
	10	0.78%	1.06%

TABLE V.
OPTIMALITY GAPS OF THE TOTAL TRANSCEIVER COST OF THE TS
SOLUTIONS FOR LARGE NETWORK SCENARIOS

Network	ρ	Gap TS-LB (%)
Abilene (N=11)	0.1	30.77%
	1	4.62%
	10	0.29%
NSF (N=14)	0.1	76.17%
	1	4.25%
	10	0.33%
Worldwide (N=15)	0.1	36.54%
	1	1.94%
	10	0.08%

VI. CONCLUSIONS

In this paper, two heuristic algorithms based on a Lagrangean Relaxation (LR) and a Tabu Search (TS) approach are proposed to solve the Reconfigurable Multi-Hour Virtual Topology Design (MH-VTD-R) problem assuming two optimization criterions. Both the number of optical transceivers required at the nodes and the number of lightpath reconfigurations necessary to handle the traffic variations over time are minimized as primary and secondary objectives, respectively.

Several test cases are conducted to compare the performance of the two proposed algorithms. The results reveal the superiority of the TS approach with respect to the LR approach in terms of reconfiguration cost. However, LR improves upon TS with respect to reconfiguration performance.

Additionally, the optimality of the heuristic solutions found by the proposed approaches is compared with (i) analytical lower bounds for all the cases; and (ii) exact MILP solutions, for small networks. From these studies, the excellent sub-optimality of the TS solutions in terms of number of transceiver for middle and high traffic loads is demonstrated, while for low loads results are inconclusive due to presumably weak analytical bounds. This sub-optimality, however, comes at the cost of higher reconfiguration frequency.

ACKNOWLEDGMENT

REFERENCES

[1] J. Berthold, A. A. M. Saleh, L. Blair, and J. M. Simmons, "Optical Networking: Past, Present, and Future," in *IEEE J. Lightw. Technol.*, vol. 26, no. 9, pp.1104-1118, May 2008.

[2] H. Zang, J. P. Jue, and B. Mukherjee, "A Review of Routing and Wavelength Assignment Approaches for Wavelength-Routed Optical WDM Networks," *Optical Network Magazine*, pp. 47-59, Jan. 2000.

[3] P. Pavon-Marino, R. Aparicio-Pardo, B. Garcia-Manrubia, and N. Skorin-Kapov, "Virtual topology design and flow routing in optical networks under multihour traffic demand," *Photonic Network Communications*, vol. 19, no. 1, pp. 42-54, Feb. 2010.

[4] TOTEM Project: Toolbox for Traffic Engineering Methods [Online]. Available: http://totem.run.montefiore.ulg.ac.be/datatools.html

[5] S. Uhlig, B. Quoitin, J. Lepropre, S. Balon, "Providing public intradomain traffic matrices to the research community," *ACM SIGCOMM Computer Communication Review*, vol. 36, no. 1, pp. 83-86, January 2006.

[6] B. Mukherjee, D. Banerjee, S. Ramamurthy, A. Mukherjee, "Some Principles for Designing a Wide-Area WDM Optical Network," *IEEE/ACM Transactions on Networking*, vol. 4, vo. 5, pp. 684-696, Oct. 1996.

[7] G. Rouskas, M. H. Ammar, "Dynamic Reconfiguration in Multihop WDM Networks," *Journal of High Speed Networks*, vol. 4, no. 3, pp. 221-238, 1995.

[8] I. Baldine and G. N. Rouskas, "Traffic adaptive WDM networks:A study of reconfiguration issues," *Journal of Lightwave Technology*, vol. 19, pp. 433–455, Apr. 2001.

[9] G. R. Ash, R. H. Cardwell, and R. P. Murray, "Design and optimization of networks with dynamic routing," *Bell Systems Technical Journal*, vol. 60, pp. 1787-1820, Oct. 1981.

[10] M. Pioro and D. Medhi, *Routing, Flow and Capacity Design in Communication and Computer Networks*. San Francisco, CA: Morgan Kaufmann, 2004, pp. 455–474.

[11] A. Gencata, B. Mukherjee, "Virtual-Topology Adaptation for WDM Mesh Networks under Dynamic Traffic," *IEEE/ACM Transactions on Networking*, vol. 11, no. 2, pp. 236-247, Apr. 2003.

[12] D. Banerjee, B. Mukerjee, "Wavelength-Routed Optical Networks: Linear Formulation, Resource Budgeting Tradeoffs, and a Reconfiguration Study," *IEEE/ACM Transactions on Networking*, vol. 8, pp. 598-607, 2000.

[13] B. Ramamurthy, A. Ramakrishnan, "Virtual Topology Reconfiguration of Wavelength-Routed Optical WDM Networks," *IEEE Globecom 2000*, 2000.

[14] K. Liu, C. Liu, J. Pastor, A. Roy, J. Wei, "Performance and Testbed Study of Topology Reconfiguration in IP over Optical Networks," *IEEE Transactions on communications*, vol. 50, no. 10, pp. 1662-1679, Oct. 2002.

[15] J. Kuri, N. Puech, M. Gagnaire, E. Dotaro, and R. Douville, "Routing and wavelength assignment of scheduled lightpath demands," *IEEE Journal on Selected*

Areas in Communications, vol. 21, pp. 1231–1240, Oct. 2003.

[16] N. Skorin-Kapov, "Heuristic algorithms for the routing and wavelength assignment of scheduled lightpath demands in optical networks," *IEEE Journal on Selected Areas in Communication*, vol. 24, pp. 2–15, 2006.

[17] J. Kuri, N. Puech, and M. Gagnaire, "Diverse routing of scheduled lightpath demands in an optical transport network," in *Proc. Design of Reliable Communication Networks (DCRN2003)*, pp. 69–76, Oct. 2003.

[18] C. V. Saradhi, L. K. Wei, and M. Gurusamy, "Provisioning fault-tolerant scheduled lightpath demands in WDM mesh networks", in *Proc. of BroadNets 2004*, San Jose, Cal. USA, pp. 150-159, Oct. 2004.

[19] B. Wang, T. Li., C. Xin, X. Zhang, "On survivable service provisioning in WDM networks under a scheduled traffic model", in *Proc. of Globecom 2005*, St. Louis, MO, USA , pp. 1900-1904, Nov.-Dec. 2005.

[20] B. Wang, T. Li, X. Luo, Y. Fan, and C. Xin, "On service provisioning under a scheduled traffic model in reconfigurable WDM optical networks" in *Proc. Of BroadNets 2005*, Boston, USA, pp 13-22, Oct. 2005.

[21] C. V. Saradhi, M. Gurusamy, and R. Piesiewicz, "Routing fault-tolerant sliding scheduled traffic in WDM optical mesh networks" in *Proc. of BroadNets 2008*, London, UK, pp.197-202, Sept. 2008.

[22] A. Jaekel, Y. Chen, "Resource provisioning for survivable WDM networks under a sliding cheduled traffic model", *Optical Switching and Networking*, Vol. 6, pp. 44-54, 2009.

[23] F. Ricciato, S. Salsano, A. Belmonte, and M. Listanti, "Off-line Configuration of a MPLS over WDM Network under Time-Varying Offered Traffic," *IEEE Infocom*, pp. 57-65, 2002.

[24] G. Agrawal and D. Medhi, "Lightpath Topology Configuration for Wavelength-Routed IP/MPLS Network for Time-Dependent Traffic", *Proc. of IEEE Globecom 2006*, San Francisco, Nov-Dec 2006.

[25] B. Garcia-Manrubia, R. Aparicio-Pardo, P. Pavon-Marino, N. Skorin-Kapov, and J. Garcia-Haro, "MILP Formulations for Scheduling Lightpaths under Periodic Traffic," in *Proc. 11th International Conference on Transparent Optical Networks*, ICTON 2009, Island of São Miguel, Azores, Portugal, June 2009.

[26] N. Skorin-Kapov, P. Pavon-Marino, B. Garcia-Manrubia, and R. Aparicio-Pardo, "Scheduled Virtual Topology Design Under Periodic Traffic in Transparent Optical Networks," in *Proc. 6th ICST International Conference on Broadband Communications, Networks and Systems*, *BroadNets 2009*, Madrid, Spain, Sept. 2009.

[27] R. Aparicio-Pardo, P. Pavon-Marino, N. Skorin-Kapov, B. Garcia-Manrubia, and J. Garcia-Haro, "Algorithms for virtual topology reconfiguration under multi-hour traffic," in *Proc. 12th International Conference on Transparent Optical Networks*, *ICTON 2010*, Munich, Germany, June 2010, p. We.B1.2.

[28] G. Oriolo, "Domination between traffic matrices," *Mathematics of Operations Research*, vol. 33, no. 1, pp. 91-96, Feb. 2008.

[29] M. Pioro and D. Medhi, *Routing, Flow and Capacity Design in Communication and Computer Networks*. San Francisco, CA: Morgan Kaufmann, 2004, pp. 178–184.

[30] D. Medhi and D. Tipper, "Some approaches to solving a multihour broadband network capacity design problem with single-path routing," *Telecommunication Systems*, vol. 13, no. 2-4, pp. 269-291, Jul. 2000.

[31] MatPlanWDM, Web Site, [Online], Available: http://ait.upct.es/~ppavon/matplanwdm/ Accessed 10 January 2012.

[32] TOMLAB Optimization. Available: http://tomopt.com/. Accessed 10 January 2012.

[33] J. Milbrandt, M. Menth, S. Kopf, "Adaptive Bandwidth Allocation: Impact of Traffic Demand Models for Wide Area Networks," in *19th International Teletraffic Congress (ITC19)*, Beijing, China, 2005.

[34] R. Ramaswami, K.N. Sivarajan, "Design of Logical Topologies for Wavelength-routed Optical Networks," *IEEE J. Select. Areas Commun.*, vol. 14, no. 5, pp. 840–851, Jun. 1996.

Ramon Aparicio-Pardo received the Engineering degree in Telecommunications and the Ph.D. degree from the Universidad Politécnica de Cartagena (UPCT), Spain, in 2006 and 2011, respectively. He has visited the Networks Lab (University of California at Davis) leaded by Prof. Biswanath Mukherjee from August 2011 to December 2011. His research interests include planning and performance evaluation of optical switching networks.

Belen Garcia-Manrubia received the Engineering degree in Telecommunication and the M.Sc. degree from the Technical University of Cartagena (UPCT), Spain, in 2007 and 2008, respectively. She received the PhD. degree from the same university in 2012. Her research interests include planning and performance evaluation of optical networks, especially cross-layer planning under wavelength-routing paradigm.
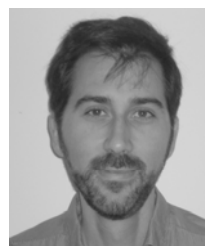
Nina Skorin-Kapov received the Dipl.-Ing. and Ph.D. degrees in electrical engineering from the University of Zagreb, Zagreb, Croatia, in 2003 and 2006, respectively. She has been working as an Assistant Professor at the Department of Telecommunications at the same university since 2008. She completed a Post-Doctoral Fellowship at Télécom ParisTech (formerly ENST) in Paris, France ,in academic year 2006-7. Her main research interests include optimization of communication networks and network security.

Pablo Pavon-Marino received his Telecommunications Engineering degree from the University of Vigo (Spain) in 1999. In 2000 he joined the Universidad Politécnica de Cartagena (Spain), where he received his Ph.D. degree in Telecommunications in 2004. In 2010 he received his degree in Mathematics from the UNED University (Spain). He is Associate Professor in the Department of Information Technologies and Communications. His research interests include performance evaluation and optimization of communication networks

Delay-Constrained Admission and Bandwidth Allocation for Long-Reach EPON

Burak Kantarci, Hussein T. Mouftah

School of Electrical Engineering and Computer Science, University of Ottawa, Ontario, Canada

Email: {kantarci, mouftah}@site.uottawa.ca

Abstract— Next generation Passive Optical Network (PON) technology has been evolving to consolidate the metro and access networks in order to offer enhanced capacity, high split ratio and reduced deployment cost per subscriber. However, transmission of the signals to long distances up to 100km leads to increased propagation delay whereas high split ratio may lead to long cycle times resulting in large queue occupancies and long packet delays. In this article, we present a delay-constrained admission control mechanism and adapt this scheme to our previously proposed bandwidth allocation technique, namely Periodic GATE Optimization (PGO). We call this new scheme Delay-Constrained Periodic GATE Optimization (DC-PGO). DC-PGO is designed to run for multiple service classes as it inherits the advantages of PGO by periodically building and solving an ILP formulation at the OLT in order to obtain the appropriate credit values for the overloaded ONUs. At the ONU side, DC-PGO runs an admission control scheme before pushing the arriving packets in the sub-queues. The admission control scheme uses statistical information consisting of the local data at the ONU and the previously received GATE messages from the OLT. Through simulations, we show that DC-PGO enhances the performance of multi-threaded polling in long-reach Ethernet PON when packets of differentiated service classes arrive with pre-specified delay requirements.

Index Terms— Dynamic bandwidth allocation, Ethernet PON, long-reach passive optical networks, multi-threaded polling

I. INTRODUCTION

Optical Access Networks form a great portion of the telecommunication networks as they serve in the *last mile* of the Internet service provisioning. Passive Optical Networks (PONs) have emerged as a promising technology by offering high capacity and low power budget solutions [1]. Deployment of high capacity and low cost solutions in the last mile is required due to the increasing bandwidth demand and differentiated real-time service level requirements of the end user applications such as Internet Protocol (IP) telephony, video on-demand, online gaming and http [2]. ATM-PON (APON), Ethernet PON (EPON) and Gigabit PON (GPON) are current passive optical network technologies that are standardized in ITU-T G.983, IEEE 802.3ah and ITU-T G.984, respectively. Basically a PON consists of an Optical Line Terminal (OLT) where the access network meets the metropolitan
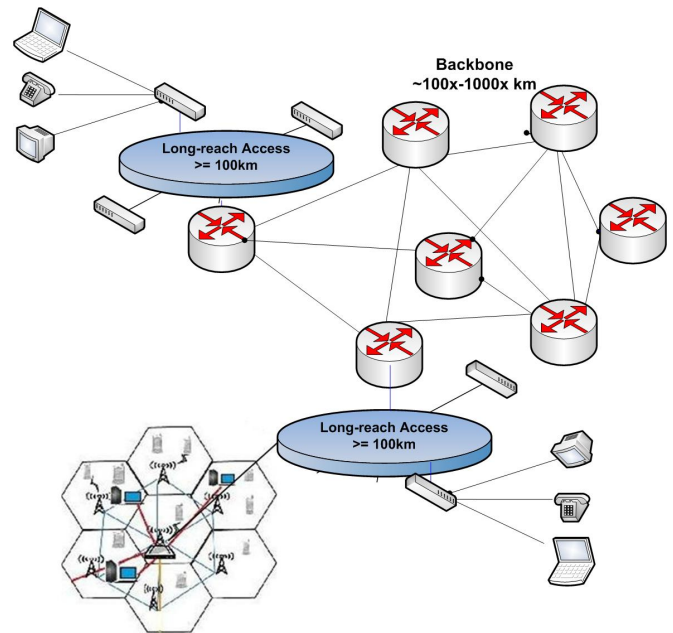
Figure 1. New infrastructure of the telecom network by the employment of LR-PON.

area network and several Optical Network Units (ONUs), and the end users are connected to the ONUs through wired (fiber, copper, etc) or wireless (WiFi, WIMAX, etc) links. A feeder fiber runs from the OLT to a passive splitter (coupler) which splits (couples) the signal on N distribution fibers each of which is connected to an ONU.

Recently, Long-Reach PON (LR-PON) technology has been developed to combine the capacities of metro and access networks by extending the reach of the feeder and increasing the split ratio [3]. Conventional PON lies on a maximum feeder distance of 20km while LR-PON aims to extend this distance to 100km and even longer [4]–[7]. Figure 1 illustrates two LR-PONs having ring topologies of ONUs in a distance longer than 100km. As seen in the figure, the access network is not connected to a metro ring network but it is connected to the Internet directly through the edge routers of the backbone. Thus, by deployment of LR-PON, not only metro and access network capacities are combined but also the telecommunication network infrastructure is simplified [8].

Hardware demonstrations have already been introduced to implement the LR-PON technology [9], [10] however, long-reach and high split ratio of LR-PON introduces

a significant drawback in terms of packet delay if conventional Multi Point Control Protocol (MPCP) signaling [11] and bandwidth distribution schemes [12]–[14] are employed. Those existing solutions have initially been proposed for the conventional feeder distances (up to 20km) which are considerably shorter than the aimed distance of LR-PONs. As it is stated in [15], [16], round trip time of a single frame increases up to 1ms in an extended reach of 100km, and considering the REPORT-GATE messaging of the MPCP, the ONU is expected to introduce further delay to an arriving user frame since the arriving frame will be granted after sending a REPORT message from the ONU which will be followed by a GATE message from the OLT.

There are several other types of long-reach optical access networks such as long-reach GPON [17], long-reach DWDM PON [18], hybrid long-reach TDM/DWDM PON [3], and radio over fiber through long-reach PON [19]. However, the scope of this article is limited to Long-Reach EPON (LR-EPON).

In this paper, we present an admission control mechanism which is adapted from our previously proposed scheme, Periodic GATE Optimization with Quality of Service (QoS)-Awareness (PGO-QoS) [20], [21] where the packets arrive at the ONUs with pre-specified delay bounds. Our new scheme is called Delay-Constrained Periodic GATE Optimization (DC-PGO), and it has initially been proposed in [22]. Here, we present this scheme in more details and evaluate its delay, utilization, packet loss and queue length performance by running extensive simulations. In PGO-QoS, the OLT polls the ONU requests in a multi-threaded way while periodically running an optimization model that re-adjusts the credits for the overloaded ONUs in order to minimize the average packet delay. The ONUs run a burstification (intra-ONU scheduling) module in order to prioritize the de-queuing procedure of the high-priority SLA sub-queues and aid the optimization building process of the OLT. DC-PGO employs an admission control module at each ONU in front of the burstification module, and based on the SLA sub-queue lengths and thread durations, it estimates whether an arriving packet can be dequeued and transmitted to the OLT within its specified delay bounds. The simulation results show that combining a delay prediction-based admission control and PGO-QoS achieve keeping the delay of multi-threaded polling low for high priority classes as well as the overall performance. Furthermore, DC-PGO does not lead to a reduction in the utilization of the LR-EPON. We also adopt the estimation function in the multi-threaded MPCP, compare the performance enhancements obtained by delay-awareness, and show that employment of DC-PGO in LR-EPON is advantageous in terms of packet delay, packet loss ratio, channel utilization and total queue length.

The paper is organized as follows. In Section II, we briefly summarize the related work on DBA in LR-EPON. In Section III, we revisit our previously proposed provisioning framework, PGO-QoS that forms a basis to our
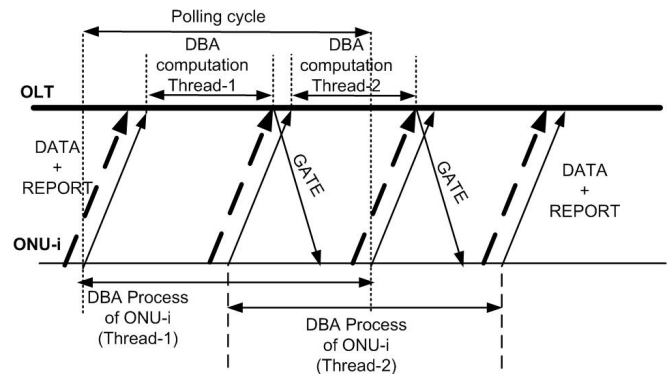

Figure 2. Polling ONUs with two threads [24].

proposal, and we present our proposed delay constrained enhancement, DC-PGO, in detail. Section IV presents numerical results and related discussions. We conclude our paper and give future directions in Section V.

II. RELATED WORK

In the literature, several solutions have been proposed to overcome the performance degradation problem in LR-EPON. A comprehensive survey of the bandwidth distribution solutions in LR-PONs can be found in [23]. Song et al. have proposed multi-threaded polling in order to reduce the gaps in the upstream channel due to exchanging REPORT and GATE messages between the ONUs and the OLTs [15], [16]. Multi-threaded polling is built on top of the conventional MPCP-based inter-leaved polling however, in multi-threaded polling, the OLT polls the ONU requests through multiple threads. Thus, an ONU (say ONU-i) does not have to wait the GATE ($GATE_i^k$) message of the last REPORT message (REP_i^k) to send a request for an incoming user packet since a GATE message that belongs to another polling thread ($GATE_i^{k+1}$) will arrive before $GATE_i^k$. Hence, the request can be sent through the REPORT message of the $(k+1)^{th}$ thread (REP_i^{k+1}). Figure 2 illustrates a scenario of one complete polling cycle which was presented in [24]. In the figure, the OLT polls the ONUs by two parallel threads. The whole polling cycle emulates two interleaved bandwidth distribution processes leading to two short sub-cycles of the main polling cycle. In [15], [16], it is shown that by the employment of multi-threaded polling, average packet delay of the limited DBA in LR-EPON can be reduced significantly until the load gets heavier to almost full utilization of the upstream feeder channel. Skubic et al. further enhanced the multi-threaded polling by proposing a coordination scheme between the multiple polling threads [24] so that over-granting/late-granting the ONUs is avoided and uplink utilization is improved as well.

In [25], the authors propose a bandwidth allocation scheme for LR-EPON where at the beginning of each granting cycle, the OLT determines the idle upstream timeslots in the next cycle and credits one or both of the ONUs whose REPORT messages are causing the

gap. In [26], an adaptive polling scheme is proposed for LR-EPON in order to differentiate various classes of service packets. This scheme is further improved to utilize the upstream gaps through inserted polling cycles [26]. In [27], a fair online distribution of the excessive bandwidth at each polling cycle is introduced in order to overcome the instability of the bandwidth distribution beyond certain critical loads. In [28], the authors have proposed a GATE-Driven bandwidth distribution scheme where the OLT uses the information collected from the REPORT messages and determines when to send the next GATE message. As stated in [29], this scheme converges to a multi-server polling system in long-term. In [30], we have proposed an adaptive threshold-based reporting scheme on top of the multi-threaded polling to reduce average packet delay. In [21], [31], we have proposed an enhancement to the multi-threaded polling, namely Periodic GATE Optimization (PGO) and its Quality of Service (QoS)-aware adaptation PGO-QoS [20]. PGO adopts multi-threaded polling, and it periodically formulates an integer linear programming (ILP) model in order to determine how to credit the overloaded ONUs at each thread until the next formulation period.

III. DELAY-CONSTRAINED ADMISSION CONTROL AND DBA IN LONG-REACH EPON

The proposed mechanism is mainly based on our previously proposed scheme, Periodic GATE Optimization with Quality of Service Awareness (PGO-QoS). Hence, in this section, we start with a brief description of PGO-QoS, and then, we proceed with our proposed delay-constrained admission control scheme, Delay-Constrained Periodic GATE Optimization (DC-PGO). For detailed explanation and performance evaluation of PGO-QoS, the reader is referred to [21].

A. Periodic GATE Optimization (PGO) Revisited

In [21], we have proposed Periodic GATE Optimization (PGO) and its quality of service (QoS)-aware adaptation (PGO-QoS) as an enhancement to multi-threaded polling. PGO-QoS consists of two modules, namely the burstification module running at the ONUs and the bandwidth distribution module running at the OLT.

Burstification module (i.e., intra-ONU scheduling) determines the de-queuing proportion for the SLA queues (sub-queues) at each ONU. For a scenario with three SLA classes, the packets are expected to be dequeued with respect to the dequeuing proportion of $r_1 : r_2 : r_3$ where r_c denotes the component of the proportion for the SLA queue-c, and priority of SLA class-c is greater than the priority of SLA class-d when $c > d$. Burstification module at the ONU periodically updates the dequeuing proportion components, and $\sum_c r_c = R$ where $R \geq 10$. ONU periodically monitors the sub-queue lengths. De-queuing proportion update starts by checking the highest priority queue length, and if the queue length have been increasing, the corresponding component in the de-queuing

proportion is marked to be incremented. In this case, in order to keep the sum of the dequeuing components (R) constant, it attempts to decrement the de-queueing component of a lower priority class. Increment/decrement continues with the lower priority class components. The details of this procedure can be found in [21]. Once, the de-queuing proportions are obtained, each ONU produces a polynomial value as shown in Eq. 1 where X is an arbitrarily large integer. The polynomial value increases dramatically with longer high-priority sub-queues while low-priority sub-queues slightly increase the polynomial value. In other words, an ONU which produces a larger polynomial value is supposed to have more high priority packets to be transmitted in comparison to an ONU with a smaller polynomial value. Each ONU appends this polynomial value to the REPORT message at the end of each update period so that the OLT knows the class-based distribution of the packets at the corresponding ONU.

$$P_i(X) = \sum_{c=0}^{C-1} X^c r_c^i \qquad (1)$$

Bandwidth distribution module of PGO-QoS is almost the same as PGO itself in [31] with a slight difference by taking the polynomial into account. The OLT periodically builds an Integer Linear Programming (ILP) formulation in order to determine the appropriate credits for the overloaded ONUs during the next period at each polling thread. Overloaded ONU refers to an ONU whose last request at thread k (R_i^k) exceeds the minimum guaranteed bandwidth (maximum allowed timeslot), i.e., $R_i^k > W_{max}$. Last bandwidth demands received through each thread are used as the input of the formulation. The objective of the ILP formulation is to minimize the optimized grant of each ONU at each thread as seen in Eq.2 where Λ_i^k stands for the optimized grant of ONU-i at thread k. Optimized grant denotes the granted bandwidth to an overloaded ONU by satisfying the fairness among the SLA classes as well as the polling sub-cycles.

$$minimize \quad \sum_k \sum_i \Lambda_i^k \qquad (2)$$

$$R_{excess}^k = \sum_{i \epsilon Q}^{N} (W_{max} - R_i^k) \qquad (3)$$

The optimization model formulates the following major constraints: i) The excessive bandwidth at thread k (R_{excess}^k as shown in Eq. 3), ii) Limiting the total allocated bandwidth for the overloaded ONUs (Q : Set of overloaded ONUs) and the lightly loaded ONUs (L : Set of lightly loaded ONUs) above by the maximum cycle byte time (T_{max}), iii) Setting the minimum guaranteed bandwidth to the ONUs to the maximum allowed timeslot, and differentiation between each peer of an ONU pair with respect to the last requests and the polynomial values reported by them. Formulation of the constraints is straightforward except the one given in Eq. 4 hence, here we only explain this constraint. According to the equation,

the OLT aims to issue more grants for the ONUs that have longer queue lengths and more number of high priority packets.

$$\Lambda_i^k - \frac{R_i^k \cdot P_i(X)}{R_j^k \cdot P_j(X)} \cdot \Lambda_{j_{j \neq i}}^k \geq 0, \quad \forall k \wedge R_i^k < R_j^k \quad (4)$$

In Eq. 5, Λ_i^k is the optimized GATE value of ONU-i for thread k at the last optimization solution, $P_i(X)$ denotes the polynomial value sent by ONU-i, and R_i^k stands for the bandwidth demand of ONU-i at thread k. Whenever an ONU is overloaded, until the next ILP formulation period, it is granted by using the formulation in Eq. 5 where Q denotes the set of overloaded ONUs. Thus, the ONU is granted the maximum allowed bandwidth and a portion of the total excessive bandwidth which is proportional with its calculated credit value for the corresponding thread k.

$$G_{i \epsilon Q}^{(k)} = \left\{ W_{Max} + \sum_{j \epsilon Q} R_{j_{excess}}^k \cdot \frac{(\Lambda_i^k - W_{Max})}{\sum_{j \epsilon Q} (\Lambda_j^k - W_{Max})} \right\} \quad (5)$$

B. Delay Constrained Periodic GATE Optimization (DC-PGO)

PGO-QoS was designed to work with multiple SLA queues however, since packets may arrive with pre-specified delay bounds, it calls for a control scheme in order to admit or drop the user packets upon arrival. Since the upstream channel is a contention domain, the delay experienced by an arriving packet can be affected by the dynamic profile of the incoming traffic of the corresponding ONU as well as the other ONUs. Thus, some of the packets are likely to be marked as *lost* at the destination since they are not able to arrive within the required delay bounds. In order to utilize bandwidth more efficiently, ONUs call for an admission control scheme which returns the estimated delay of an arriving packet and determines to drop/admit the packet based on the delay estimation. We add this mechanism to PGO-QoS and name it Delay-Constrained Periodic GATE Optimization (DC-PGO). Fig. 3 illustrates the block diagram of an ONU running the burstification and admission control schemes of the proposed framework.

In DC-PGO, the admission control unit of an ONU uses the sum of the sub-queue lengths (Q_c), maximum allowed bandwidth (W_{max}) and the time difference between two successive threads (Δt_{REP}) in order to formulate the estimated delay (D_{est}). As seen in Eq. 6, admission control module of DC-PGO assumes that the corresponding ONU will be granted W_{max} until the packet is dequeued. By dividing the total sub-queue lengths by the maximum allowed timeslot, it estimates an approximative number of sub-cycles to wait. Then, by simply multiplying the estimated number of sub-cycles with the time difference between the last two REPORT message departures, estimated delay (D_{est}) of an arriving packet is obtained.
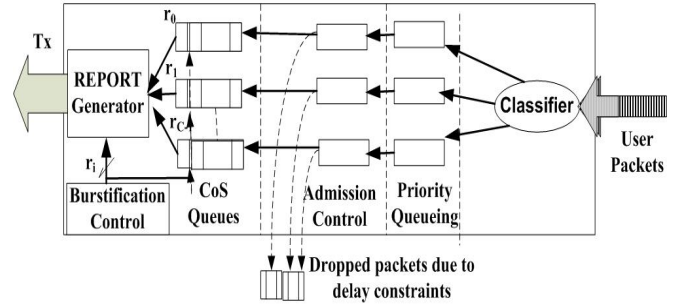
Figure 3. ONU block diagram for DC-PGO.

An average grant of W_{max} seems to be a naïve assumption since whenever the ONU is lightly loaded ($\sum_k Q_c \leq W_{max}$), the ONU is granted the requested bandwidth to transmit $\sum_k Q_c$ bytes. However, the DBA module of DC-PGO credits the overloaded ONUs based on the results of the periodically run ILP formulation. As stated in the previous subsection, the enhancement introduced by the DBA module of DC-PGO (i.e., PGO-QoS) is to determine a heterogeneous distribution of the excessive bandwidth among the ONUs. Thus, Λ_i^k denoting the bandwidth grant for ONU-i at thread k, the DBA module already guarantees $\Lambda \geq W_{max}$ for the overloaded ONUs. Hence, considering the dynamic profile of the incoming traffic, the assumption of an average grant of W_{max} is reasonable. It is worth to note that the success of the delay estimation process can be enhanced by the employment of further efficient methods such as data mining, pattern recognition or linear regression techniques.

As seen in Algorithm 1, each arriving packet is classified with respect to the SLA specifications that also include the delay requirements of its corresponding SLA class c (Θ^c). The estimated delay (D_{est}) for the arriving packet is compared to the delay bound of its SLA class (Θ^c). If $D_{est} \leq \theta^c$, the packet is admitted and enqueued in the appropriate CoS queue (i.e., sub-queue), and its bandwidth request is issued by the next REPORT message. Otherwise, the packet is not admitted to its CoS queue and dropped since it is assumed to be possibly marked as a lost packet at the destination due to violation of the delay bound.

$$D_{est} = (\lfloor \frac{\sum_k Q_c}{W_{max}} \rfloor + 1) \cdot \Delta_{REP} \quad (6)$$

Consolidation of PGO-QoS and the admission control scheme defined above is expected to enhance the delay performance of the LR-PON for the following reasons. DC-PGO aims to keep the SLA queues available for the arriving packets. Hence, packet loss is mostly due to the violation of the delay bounds although the system experiences packet losses due to buffer overflow as well. Packet delay is a function of the queueing, granting and dequeuing delays. Employment of a look-ahead mechanism to admit the incoming packets is expected to result with shorter buffers which lead to shorter queueing and dequeuing delays. Besides, DBA module of DC-

Algorithm 1 Admission control of DC-PGO

1: $\{C$: Number of SLA classes$\}$
2: $\{\theta^c$: Delay requirement of class-c, $\theta^c \epsilon \Theta\}$
3: $\{$Wait for packet arrival$\}$
4: **if** (new packet (p) arrived) **then**
5: $\quad c \leftarrow p.class$
6: $\quad D_{req} \leftarrow \theta^c$
7: $\quad D_{est} \leftarrow (\frac{\sum_{c=0}^{C-1} Q_c}{W^{max}} + 1). \cdot \Delta t_{REP}$
8: $\quad$**if** ($D_{est} \leq D_{req}$) **then**
9: $\quad\quad Q_c.enqueue(p)$
10: $\quad$**else**
11: $\quad\quad$Drop(p)
12: $\quad$**end if**
13: **end if**

PGO aims to reduce the granting delays for all packets. Moreover, co-operation of the burstification and the DBA modules further reduces the delay for the high priority classes. Furthermore, due to the same reasons, DC-PGO introduces improved transparency to the changes in the SLA scenarios as the network load gets heavier as we present in the next section.

IV. NUMERICAL RESULTS

Performance evaluation of DC-PGO is done by discrete event simulation implemented in Visual C++ while the periodic optimization results of the DBA module are provided by CPLEX. The LR-EPON consists of 16 ONUs that are connected to the OLT via feeder fiber of 100km. User traffic capacity is assumed to be 100Mbps while the fiber link is assumed to offer 1 Gbps capacity. ONUs are assumed to have total buffer capacities of 1MB. Incoming packets size is assumed to be distributed between 64B and 1500B. To be coherent with the previous work [21], OLT builds the ILP formulation upon receiving every 10^4 packets. Number of SLA classes (C) is assumed to be three where the priority order is as follows: $SLA_{class_1} < SLA_{class_2} < SLA_{class_3}$. In order to be coherent with the realistic scenarios, user packets are distributed with respect to the proportion of 2:1:1. Thus, the cheapest class has the highest density. Initial thread cycle is assumed to be 0.3ms while the OLT polls the ONUs by three threads as in [16], [21]. DC-PGO runs multi-threaded polling as a basis, and in order to present its enhancement to multi-threaded polling (MT), we also adapt the admission control mechanism into MT.

Two different delay requirement sets (Θ) are assumed and tested under DC-PGO where $\Theta = \{\theta^1, \theta^2, \theta^3\}$.

Delay Set-1: $\Theta = \{150ms, 75ms, 5ms\}$
Delay Set-2: $\Theta = \{120ms, 50ms, 3ms\}$

We initially, evaluate the delay performance of DC-PGO as illustrated in Fig. 4. As seen in the figure, under both scenarios, combining the admission control scheme at the tail of the input queues and PGO-QoS in the burstification and the DBA modules enhances the overall packet delay performance of multi-threaded polling.
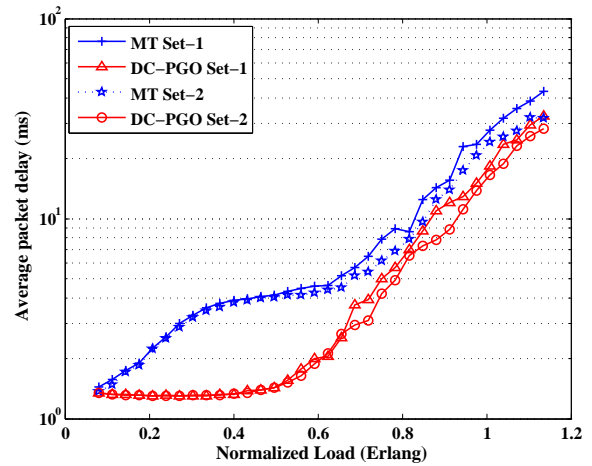
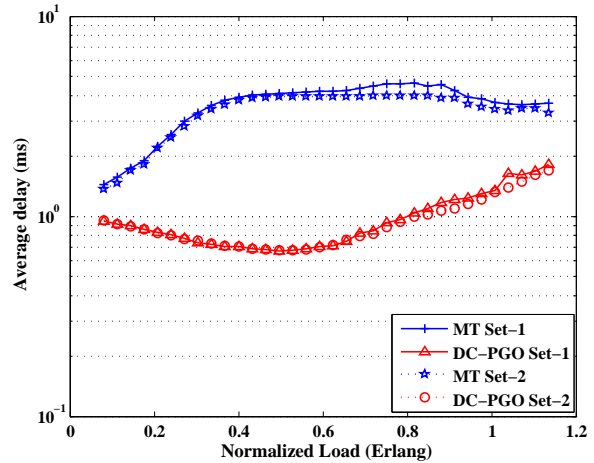Figure 4. Average packet delay enhancement by DC-PGO under both delay constraint sets.

Figure 5. Average packet delay enhancement for SLA class-3 by DC-PGO under both delay constraint sets.

Besides, employment of the second scenario, leads to reduction for both MT and DC-PGO under moderate and heavy loads since arriving packets have lower bounds under the second scenario. This phenomenon can also be seen in Fig.5-7 where the average delays for the packets of SLA_{class_3}-SLA_{class_1} are represented, respectively.

Fig.5 illustrates the delay performance of DC-PGO and MT under both scenarios for the packets of SLA_{class_3}. For each scenario, DC-PGO enhances the performance of MT for the packets of this class. Beyond the moderate loads, setting lower delay bounds for the arriving packets helps reducing the average delay for SLA_{class_3} under both schemes. Hence, the admission control scheme adopted by MT and DC-PGO ensures delay-awareness. Fig. 6 illustrates the same performance evaluation results for the packets of SLA_{class_2}.

Since burstification and DBA modules of DC-PGO prioritize SLA_{class_3} and SLA_{class_2}, starting from the moderate loads, it introduces longer delays to the packets of SLA_{class_1} when compared to MT as seen in Fig. 7.
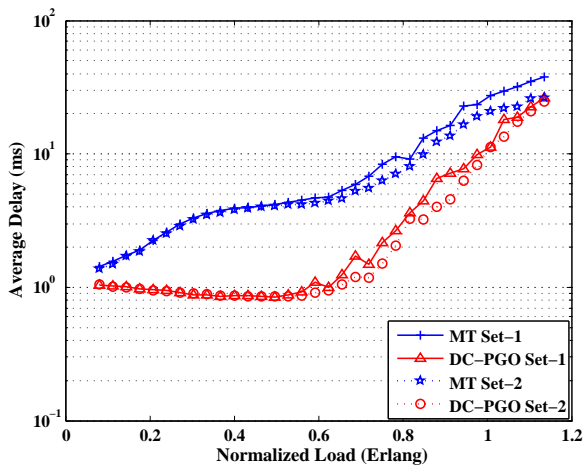
Figure 6. Average packet delay enhancement for SLA class-2 by DC-PGO under both delay constraint sets.
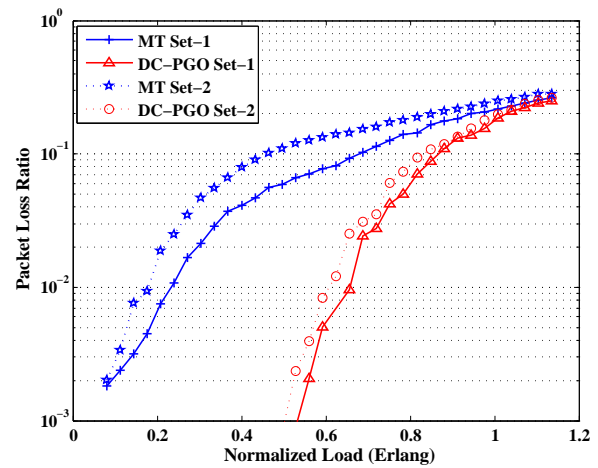

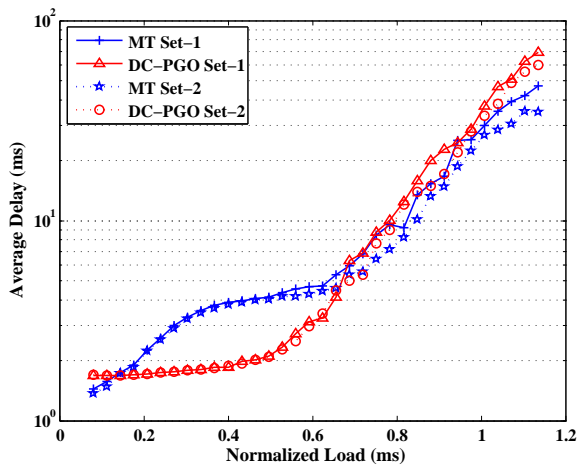Figure 8. Average packet drop ratio under DC-PGO and MT.

Figure 7. Average packet delay for SLA class-1 under DC-PGO and MT.
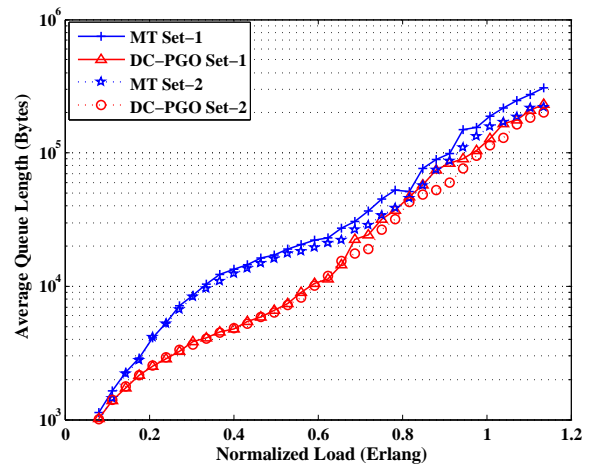

Figure 9. Average queue length under DC-PGO and MT.

However, in reality, it is reasonable for DC-PGO (and for any differentiated provisioning scheme) to treat the low-priority packets according to the best effort service strategy. Hence, the behavior in the figure does not mask the advantageous aspects of DC-PGO.

In Fig. 8, average packet drop probability under DC-PGO and MT is presented for both scenarios. The results in the figure are consistent with those in the previous figures. First, in the second scenario, both schemes drop more packets when compared to their performance in the first scenario. Since the delay bounds are lower in Delay-Set-2, packets are dropped earlier due to delay bound violation which results with increased packet delay. Beyond 1.0 Erlang, the network gets heavily loaded hence, other than the delay bound violation, buffer overflow arises as another reason for packet losses. Hence packet loss performances of DC-PGO and MT coincide under heavy loads. On the other hand, DC-PGO leads to lower packet delay until the network load of 1.0 Erlang in both scenarios. The reason for dropping less packets

in DC-PGO is two-fold: First, burstification and DBA modules of DC-PGO leads to reduced overall packet delay as we have seen in Fig. 4. Hence, when compared to MT with limited DBA, DC-PGO is more likely to meet the delay specifications. Thus, introducing reduced overall delay is one of the factors which also reduces the packet drop probability. The second factor affecting the packet loss probability is the total buffer occupancy. Periodically optimized crediting mechanism at the OLT assists the overloaded ONUs to burst their buffers in order to minimize the granting delays which results in reduced occupancies at the input buffers. Fig. 9 illustrates the total queue length behavior under DC-PGO and MT for both delay set scenarios. In both scenarios, DC-PGO succeeds in keeping the queue length below MT due to the reasons mentioned above. Thus, reduced buffer occupancy arises as the second factor for reduced packet loss probability.

Fig.10 compares the channel utilization performance of DC-PGO to that of MT under the two delay sets. As seen in the figure, DC-PGO is not affected significantly by the change in the contract scenario (delay requirement set) in
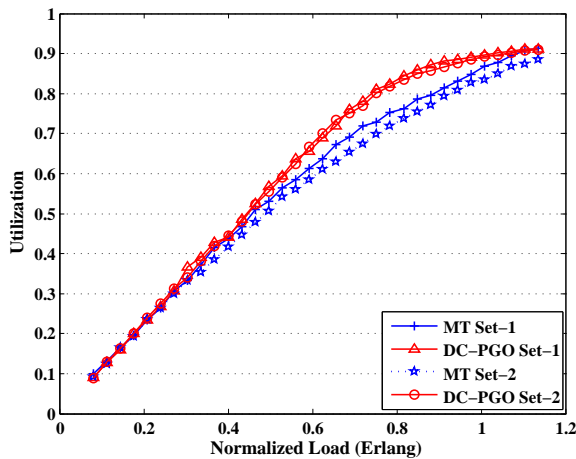
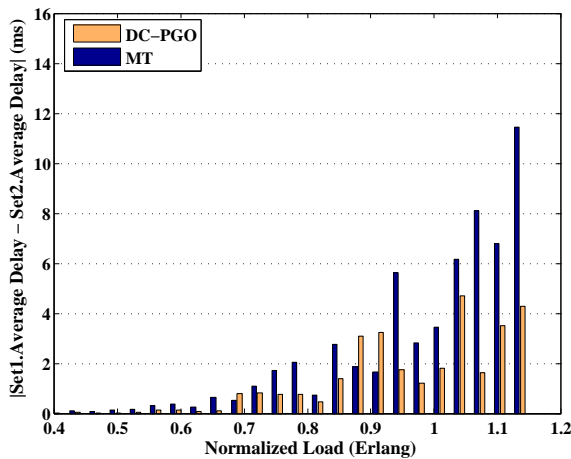Figure 10. Average channel utilization under DC-PGO and MT.

Figure 11.   Transparency of DC-PGO to the change in the contract scenario.

terms of utilization while MT leads to reduced utilization under Delay-Set-2 scenario where packet delay requirements of the three SLA classes are lower than those under the Delay-Set-1 scenario. As we have already shown in Fig. 8, DC-PGO does not show a significant change in packet loss probability performance since at the OLT, it aims to adapt the credits of the overloaded ONUs in order to minimize the granting delay. Hence, channel utilization of DC-PGO seems to be more transparent to the change in the contract scenario. The second phenomenon is that DC-PGO does not lead to a reduced utilization while reducing the average packet delay. On the contrary, under each scenario, starting from 0.4 Erlang until 1.0 Erlang network load, it leads to enhanced utilization for both delay requirement scenarios.

We have clearly seen that DC-PGO demonstrates transparency in terms of overall delay and utilization performance when the delay requirement scenario changes in Fig. 4 and Fig. 10. In Fig. 11, by presenting statistical data, we illustrate the transparency of DC-PGO and MT to the change in the delay requirement scenario. The y-axis

in the figure denotes the absolute difference between the average delay per packet under Delay-Set-1 and Delay-Set-2 scenarios. As seen in the figure, MT without PGO-QoS leads to a maximum average delay difference of 11.5ms while DC-PGO introduces a maximum average delay difference of 4.5ms.

V. Conclusion

Long-Reach Ethernet PON (LR-EPON) suffers from long packet delays due to increased feeder distance hence, new solutions have been proposed in the literature to replace the conventional bandwidth distribution mechanisms. In this article, we have presented a modified version of our previously proposed bandwidth distribution scheme, namely Periodic GATE Optimization with Quality of Service Awareness (PGO-QoS). PGO-QoS has two modules, namely the dynamic bandwidth allocation (DBA) module running at the OLT in order to minimize the granting delay per ONU and the burstification module running at each ONU to differentiate de-queuing process at the SLA sub-queues. We have called the proposed modified version Delay-Constrained Periodic GATE Optimization (DC-PGO). DC-PGO runs in an environment where the packets arriving at an ONU belong to differentiated Service Level Agreement (SLA) classes. Thus, each arriving packet has a specific delay requirement. Hence, in DC-PGO, we have presented an admission control scheme that runs for each arriving packet. The packets are enqueued if they are forecasted to arrive at the OLT within their delay bounds. Otherwise, they are dropped in order to reserve space for the arriving packets in the related sub-queues. We have also modified the multi-threaded (MT) polling which forms a basis for DC-PGO as well as its successor PGO-QoS so that MT runs the same admission control for the arriving packets with differentiated delay requirements. We have evaluated the performance of DC-PGO in comparison to that of MT by employing two delay requirement set scenarios for three SLA classes. Through simulations, we have shown that DC-PGO introduces reduced average delay per packet as well as reduced average delay for the packets of the high priority service classes. Furthermore, simulation results verify that DC-PGO leads to reduced packet loss and consequently better utilization until the heavy network loads. The simulation results further show that DC-PGO is more transparent to the change in delay requirement set as the average delay and utilization performances are less affected by the change in the packet delay bounds.

Currently, we are extending this study by adapting DC-PGO into survivable LR-EPON architectures to guarantee both enhanced delay performance and reliability.

References

[1] J. Zheng and H. T. Mouftah, *Optical WDM Networks: Concepts and Design Principles*.   Wiley-IEEE Press, Hoboken, NJ, 2004.

[2] H. Naser and H. T. Mouftah, *Broadband Access Networks, Chapter 7: Dynamic Bandwidth Allocation for Ethernet Passive Optical Networks*. Shami A., Maier M., Assi C., Eds.; Springer, 2009, pp. 151–167.

[3] D. Shea and J. Mitchell, "Long-reach optical access technologies," *IEEE Network*, vol. 21, no. 5, pp. 5–11, 2007.

[4] R. Davey, D. Nesset, A. Rafel, D. Payne, and A. Hill, "Designing long reach optical access networks," *BT Technology Journal*, vol. 24, pp. 13–19, 2006.

[5] K. Ennser, M. Zannin, and S. Taccheo, "Extending reach of passive optical networks through optical amplification," in *International Conference on Transparent Optical Networks,(ICTON)*, 28 2009-July 2 2009, pp. 1–4.

[6] L. Gutierrez, M. de andrate, and S. Sallent, "New trends on optical access networks: DBAs for 10G EPON and Long-Reach PON," in *European Conference on Networks and Optical Communications*, June 2009, pp. 487–494.

[7] H. Song, B.-W. Kim, and B. Mukherjee, "Long-reach optical access," in *Broadband Access Networks*, A. Shami, M. Maier, and C. Assi, Eds., 2009.

[8] ——, "Long-reach optical access networks: A survey of research challenges, demonstrations, and bandwidth assignment mechanisms," *IEEE Communications Surveys & Tutorials*, vol. 12 issue 1, pp. 112–123, First Quarter 2010.

[9] R. P. Davey, D. B. Grossman, M. Rasztovits-Wiech, and D. B. Payne, "Long-reach passive optical networks," *IEEE/OSA Journal of Lightwave Technology*, vol. 27 no 3, pp. 273–291, February 2009.

[10] D. P. Shea and J. E. Mitchell, "A 10-Gb/s 1024-way-split 100-km long-reach optical-access network," *IEEE/ OSA Journal of Lightwave Technology*, vol. 25, no. 3, pp. 685–693, Mar. 2007.

[11] "IEEE 802.3ah - Ethernet in the First Mile working group archives," [Online] http://www.ieee802.org/3/efm.

[12] G. Kramer, B. Mukherjee, and G. Pesavento, "IPACT: A dynamic protocol for an ethernet PON (EPON)," *IEEE Communications Magazine*, vol. 40 (2), pp. 74–80, 2002.

[13] M. Mcgarry, M. Reisslein, and M. Maier, "Ethernet passive optical network architectures and dynamic bandwidth allocation algorithms," *IEEE Communications Surveys Tutorials*, vol. 10, no. 3, pp. 46–60, 2008.

[14] J. Zheng and H. T. Mouftah, "A survey of dynamic bandwidth allocation algorithms for ethernet passive optical networks," *Optical Switching and Networking*, vol. 6 issue 3, pp. 151–162, July 2009.

[15] H. Song, A. Banerjee, B.-W. Kim, and B. Mukherjee, "Multi-Thread Polling: A Dynamic Bandwidth Distribution Scheme in Long-Reach PON," in *IEEE Global Telecommunications Conference, 2007*, 2007, pp. 2450–2454.

[16] H. Song, B.-W. Kim, and B. Mukherjee, "Multi-thread polling: A dynamic bandwidth distribution scheme in long-reach PON," *IEEE Journal on Selected Areas in Communications*, vol. 27 issue 2, pp. 134–142, February 2009.

[17] K. Kanonakis and I. Tomkos, "Offset-based scheduling with flexible intervals for evolving GPON networks," *IEEE/OSA Journal of Lightwave Technology*, vol. 27 no 15, pp. 3259–3268, August 2009.

[18] D. Shea and J. Mitchell, "Architecture to integrate multiple pons with long reach dwdm backhaul," *Selected Areas in Communications, IEEE Journal on*, vol. 27, no. 2, pp. 126–133, 2009.

[19] K. Prince, A. V. Osadchiy, and I. T. Monroy, "WiMAX Radio-on-Fibre in 118-km Long-Reach PON with Deployed Fibre," in *35th European Conference on Optical Communication (ECOC)*, Sep. 2009.

[20] B. Kantarci and H. Mouftah, "Periodic GATE Optimization with QoS-awareness for Long-Reach Passive Optical Networks," in *IEEE Symposium on Computers and Communications (ISCC)*, 2010, pp. 879–884.

[21] B. Kantarci and H. T. Mouftah, "Periodic GATE optimization (PGO): A new service scheme for long-reach passive optical networks," *IEEE Systems Journal*, vol. 4/4, pp. 440–448, Dec. 2010.

[22] ——, "On SLA-constraints in dynamic bandwidth allocation for long-reach passive optical networks," in *International Conference on Transparent Optical Networks (ICTON)*, June 2010, Tu.B1.3.1 - Tu.B1.3.7.

[23] ——, "Bandwidth distribution solutions for performance enhancement in long-reach passive optical networks," *Communications Surveys Tutorials, IEEE*, vol. PP, no. 99, pp. 1 –20, 2011.

[24] B. Skubic, J. Chen, J. Ahmed, B. Chen, L. Wosinska, and B. Mukherjee, "Dynamic bandwidth allocation for long-reach PON: overcoming performance degradation," *Communications Magazine, IEEE*, vol. 48, no. 11, pp. 100–108, Nov. 2010.

[25] N. Merayo, T. Jimenez, P. Fernandez, R. Duran, R. M. Lorenzo, I. deMiguel, and E. Abril, "A bandwidth assignment polling algorithm to enhance the efficiency in QoS long-reach EPONs," *European Transactions on Telecommunications*, [Online] http://dx.doi.org/10.1002/ett.1449, November 2010.

[26] N. Merayo, J. T, R. J. Duran, d. M. I. Fernandez, P., R. M. Lorenzo, and E. J. Abril, "Adaptive polling algorithm to provide subscriber and service differentiation in a Long-Reach EPON," *Photonic Network Communications*, vol. 19, pp. 257–264, 2010.

[27] J. R. Ferguson, M. Reisslein, and M. McGarry, "Online excess bandwidth distribution for Ethernet passive optical networks," *Journal of Optical Networking*, vol. 8, pp. 358–369, April 2009.

[28] N. Antunes, C. Fricker, P. Robert, and J. Roberts, "GATE-Driven Dynamic Wavelength and Bandwidth Allocation for WDM-EPONs," in *IEEE Global Telecommunications Conference*, 2010, pp. 1–5.

[29] ——, "Upstream traffic capacity of a WDM EPON under online GATE-driven scheduling, internal report, 2010."

[30] B. Kantarci and H. T. Mouftah, "Bandwidth Distribution with Adaptive Threshold-based Optical Burst Assembly in Long-Reach EPON," in *OSA Advanced Photonics Congress*, 2011.

[31] B. Kantarci and H. Mouftah, "Periodic GATE Optimization (PGO) in Long-Reach Passive Optical Networks," in *25th Queen's Biennial Symposium on Communications (QBSC)*, May 2010, pp. 230–233.

Burak Kantarci is currently a postdoctoral fellow at the School of Electrical Engineering and Computer Science of the University of Ottawa. He received the M.Sc, and Ph.D degrees in Computer Engineering at Istanbul Technical University (ITU) in 2005 and 2009, respectively. He received the Siemens Excellence Award in 2005 for his studies in optical burst switching. During his Ph.D study, he was a visiting scholar under the supervision of Prof. Mouftah at the University of Ottawa (2007-2008). He has co-authored over four dozen refereed papers in established journals and conferences, and contributed three book chapters. His research interests are energy-efficient network planning, broadband access networks, WDM networks, optical switching, survivable network design, green communications and cloud computing.

Hussein T. Mouftah joined the School of Information Technology and Engineering (SITE) of the University of Ottawa in 2002 as a Tier 1 Canada Research Chair Professor, where he became a University Distinguished Professor in 2006. He has been with the ECE Dept. at Queen's University (1979-2002), where he was prior to his departure a Full Professor and the Department Associate Head. He has six years of industrial experience mainly at Bell Northern Research of Ottawa (became Nortel Networks). He served IEEE ComSoc as Editor-in-Chief of the IEEE Communications Magazine (1995-97), Director of Magazines (1998-99), Chair of the Awards Committee (2002-03), Director of Education (2006-07), and Member of the Board of Governors (1997-99 and 2006-07). He has been a Distinguished Speaker of the IEEE Communications Society (2000-07). Currently he serves IEEE Canada (Region 7) as Chair of the Awards and Recognition Committee. He is the author or coauthor of 7 books, 49 book chapters and more than 1000 technical papers, 12 patents and 140 industrial reports. He is the joint holder of 12 Best Paper and/or Outstanding Paper Awards. He has received numerous prestigious awards, such as the 2008 ORION Leadership Award of Merit, the 2007 Royal Society of Canada Thomas W. Eadie Medal, the 2007-2008 University of Ottawa Award for Excellence in Research, the 2006 IEEE Canada McNaughton Gold Medal, the 2006 EIC Julian Smith Medal, the 2004 IEEE ComSoc Edwin Howard Armstrong Achievement Award, the 2004 George S. Glinski Award for Excellence in Research of the U of O Faculty of Engineering, the 1989 Engineering Medal for Research and Development of the Association of Professional Engineers of Ontario (PEO), and the Ontario Distinguished Researcher Award of the Ontario Innovation Trust. Dr. Mouftah is a Fellow of the IEEE (1990), the Canadian Academy of Engineering (2003), the Engineering Institute of Canada (2005) and the Royal Society of Canada RSC: The Academy of Science (2008).

Energy Efficient Optical Networks with Minimized Non-Renewable Power Consumption

Xiaowen Dong, Taisir El-Gorashi and Jaafar M. H. Elmirghani

School of Electronic and Electrical Engineering, University of Leeds, LS2 9JT, United Kingdom

Abstract- Recent studies have shown that the Information and Communication Technology (ICT) industry is responsible for about 2% of the global emission of CO_2 and this percentage is expected to increase as the internet expands in bandwidth and reach. In this paper we propose a hybrid-power IP over WDM network where renewable energy is used to reduce the CO_2 emission of IP over WDM networks. A Linear Programming (LP) model and a novel heuristic are developed to minimize the non-renewable power consumption in the "hybrid-power" IP over WDM network. The performance of the network is studied considering two topologies, the NSFNET and the USNET. Compared with routing in the electronic layer, the results show that routing in the optical layer coupled with using renewable energy significantly reduces the CO_2 emissions of the IP over WDM network by up to 73% for the NSFNET and 69% for the USNET, and the proposed heuristic has little impact on the QoS. We also develop an LP model to identify the impact of the location of nodes employing renewable energy on the non-renewable power consumption of the network. The results show that the optimum location of nodes employing renewable energy is determined according to the output power of the renewable energy sources and the power consumption of the nodes.

I. INTRODUCTION

In the last ten years, the bandwidth of the Internet has grown by at least 50 to 100 times leading to a significant increase in the power consumption of networks. Further bandwidth growth between 40% and 300% is predicted in the next 3 years [1] as a result of the growing popularity of bandwidth intensive applications. Today the power consumption of networks is a significant contributor to the total energy demand in many developed countries; for example, in 2005 the energy used by the Telecom Italia network was more than 2TWh which is about 1% of the total Italian energy demand [2]. In the winter of 2007, British Telecom became the largest single power consumer in the UK accounting for 0.7% of the total UK's power consumption [3]. Therefore, with the increase in data rates, the bottleneck facing the Internet's expansion will probably become its power consumption. In practice, 228 grams of CO_2 approximately are produced by a network component that consumes 1kWh of traditional electricity [4]. If the network can be designed such that it dispenses with 1kW non-renewable power consumption, then this will lead to a significant reduction in CO_2 emissions of about 2 tones every year, a family vehicle typically emits 150g/km CO_2.

Recently significant research efforts have been focused on developing energy efficient networks. Gupta *et al.* [5] pioneered the introduction of the concept of "greening the internet" in 2003. Most of the existing work on energy saving has considered local adaptation by implementing hardware-based techniques, such as sleep cycles and rate adaptation. In [5], it is proposed to save power by allowing network interfaces and other components to sleep when they are idle. In [6] two power saving schemes are proposed. In the first scheme, traffic is shaped into small bursts at the edge nodes to allow downstream line cards to sleep in between packet bursts. The second scheme is based on the fact that operating devices at lower frequencies and/or voltages can significantly reduce power consumption. The latter scheme is considered as an important step towards power-proportional networking hardware.

Power consumption and heat dissipation are increasingly becoming primary objectives in router design. In [7], the authors discuss the use of optics in routers to scale capacity and reduce power consumption. In [8] methods are investigated to decrease power consumption in interconnection fabrics. A case study of power demands of standard router platforms is provided in [9] where a generic model for router power consumption is developed.

In [10] the authors focused on saving energy in local area Ethernet networks. An IEEE 802.3 Energy Efficient Ethernet Study Group was established in November 2006 [11] to standardize the Adaptive Link Rate (ALR) concept to reduce direct energy use of Ethernet links. In [12] the authors have considered energy-aware traffic engineering where power consumption is taken into account in addition to the standard traffic engineering objectives. In [13] a novel energy reduction approach at the network level is proposed where the load dependent power consumption information of the communication equipment is taken into account when taking traffic-engineering decisions. A group known as "Green Grid" was also formed to increase energy efficiency in data centres [14].

Power consumption of backbone networks has been receiving increasing focus for two reasons. First, the percentage that backbone networks are responsible for of the total network power consumption is expected to significantly increase with the growing popularity of bandwidth intensive applications such as high-definition IPTV. In addition, as the power consumption of the backbone network is often limited to a few locations, heat dissipation becomes an important issue to consider. In [15] lightpath bypass in the optical layer is implemented to reduce power consumption in the IP over WDM network to reduce the number of IP router ports required. A Mixed Integer Linear Programming (MILP) optimization model and two heuristics are implemented to minimize power consumption.

In this paper, we focus on reducing the CO_2 emissions of backbone IP over WDM networks by proposing a "hybrid-power" IP over WDM architecture where the power supply of the network is composed of non-renewable energy and renewable energy. A LP optimization model for the hybrid-power IP over WDM architecture and a new heuristic are set up to minimize the non-renewable power consumption. Issues including how to use renewable energy (solar in this work) more effectively, how to reduce the non-renewable
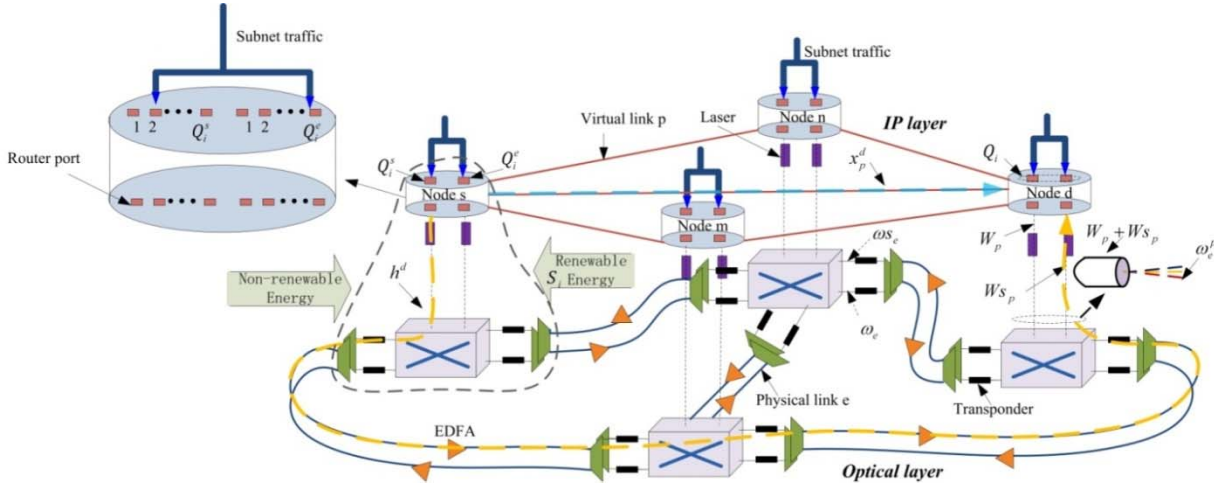
Fig.1. Structure of the hybrid-power IP over WDM network

power consumption of transponders (the second most power consuming device in a node), and how to select the location of nodes using renewable energy are considered.

The remainder of this paper is organized as follows: In Section II, the LP optimization model for the hybrid-power IP over WDM network and the new heuristic for minimizing the non-renewable power consumption are introduced. Results that evaluate the non-renewable power consumption of the IP over WDM network considering the NSFNET and the USNET topologies are presented in Section III. Finally, the paper is concluded in Section IV.

II. HYBRID-POWER IP OVER WDM NETWORK

Similar to IP over WDM networks, the hybrid-power IP over WDM network is composed of an IP layer and an optical layer. However, the difference is that the power supply of this new network is mixed being composed of non-renewable energy and renewable energy. In this case, the total CO_2 emission of an IP over WDM network will be reduced if a portion of the non-renewable power consumption is replaced by renewable energy. Therefore, the problem becomes that associated with minimizing the non-renewable power consumption of the hybrid-power IP over WDM network.

A. Linear Programming Mathematical Model

In [15], a MILP model was developed for minimizing the total power consumption of IP over WDM networks. We have formulated a model that builds on these concepts but is focused on minimizing the non-renewable power consumption by employing renewable energy in the hybrid-power network [16], [17], [18]. In this LP model, we assume the network has the topology $G = (N, E)$ with N nodes and E physical links. The nodes that have access to renewable energy can also be powered by non-renewable energy to guarantee QoS when the renewable energy output becomes low. The renewable energy can power the ports and transponders in a node. Fig.1 gives the details of the hybrid-power IP over WDM network. The total non-renewable power consumption of the network is composed of:

1) Non-renewable power consumption of router ports without access to renewable energy

$$\sum_{i \in N} PR \cdot \left(Q_i^e + \sum_{p \in P} \delta_{ip} \cdot W_p \right)$$

2) The non-renewable power consumption of EDFAs

$$\sum_{e \in E} PE \cdot E_e \cdot f_e$$

3) The non-renewable power consumption of router ports that have access to renewable energy (the non renewable energy may be used for example to guarantee control at all time)

$$\sum_{i \in N} PRS \cdot \left(Q_i^s + \sum_{p \in P} \delta_{ip} \cdot Ws_p \right)$$

4) The non-renewable power consumption of transponders that have access to renewable energy (again the non renewable energy may be used for example to guarantee control at all time) and the transponders without access to renewable energy.

$$\sum_{e \in E} (PT \cdot \omega_e + PTS \cdot \omega s_e)$$

The LP model that minimizes the non-renewable power consumed is defined as follows:

Objective: minimize

$$\sum_{i \in N} PR \cdot \left(Q_i^e + \sum_{p \in P} \delta_{ip} \cdot W_p \right) + \sum_{e \in E} PE \cdot E_e \cdot f_e$$
$$+ \sum_{i \in N} PRS \cdot \left(Q_i^s + \sum_{p \in P} \delta_{ip} \cdot Ws_p \right) \quad (1)$$
$$+ \sum_{e \in E} (PT \cdot \omega_e + PTS \cdot \omega s_e)$$

Subject to:

$$\sum_{p \in P} x_p^d = h^d \quad \forall d \in D, \quad (2)$$

$$\sum_{d \in D} x_p^d \le (W_p + Ws_p) \cdot B \quad \forall p \in P, \quad (3)$$

$$\sum_{p \in P} (\delta_{ip} \cdot W_p + \delta_{ip} \cdot Ws_p) + Q_i \le \nabla^i \quad \forall i \in N, \quad (4)$$

$$\sum_{e \in E} \delta_{ep} \cdot \omega_e^p = W_p + Ws_p \qquad \forall\, p \in P, \tag{5}$$

$$PR \cdot \left(Q_i^s + \sum_{p \in P} \delta_{ip} \cdot Ws_p \right) + \sum_{e \in E} PT \cdot \omega s_e \cdot \delta_{ie} \le S_i \tag{6}$$
$$\forall\, i \in N,$$

$$\sum_{p \in P} \omega_e^p \le W \cdot f_e \qquad \forall\, e \in E, \tag{7}$$

$$Q_i^e + Q_i^s = Q_i \qquad \forall\, i \in N, \tag{8}$$

$$\sum_{p \in P} \omega_e^p = \omega_e + \omega s_e \qquad \forall\, e \in E \tag{9}$$

The variables and parameters of the equations above are defined in Table 1.

The aim of the objective function (Equation (1)) is to minimize the non-renewable power consumption of the hybrid-power IP over WDM network. Equation (2) and Equation (5) represent the flow conservation constraint in the IP layer and the optical layer. Equation (3) ensures that the traffic flow on each virtual link does not exceed its capacity. The term ($W_p + Ws_p$) represents the total number of wavelength channels on each virtual link powered by either non-renewable energy or renewable energy. Equation (4) ensures that the limit on the number of router ports in each node is not exceeded. Equation (6) ensures that the renewable power consumption of router ports and transponders is not larger than the maximum output power of the renewable energy source in each node. Equation (7) and Equation (9) give the limit on the number of wavelength channels in each physical link e. Equation (8) ensures that for each node the total number of router ports assembling data is equal to the number of ports using non-renewable energy and the number of ports using renewable energy.

Table 1

Parameters (pa) and variables (ve) used for LP model

$E(Pa)$	Physical link set in optical layer,
$P(Pa)$	Virtual link set in IP layer,
$D(Pa)$	Traffic demand set between node pairs,
$\delta_{ip}(Ve)$	If node i belongs to virtual link p, δ_{ip} is '1', otherwise it is '0'
$\delta_{ie}(Ve)$	If node i belongs to physical link e, δ_{ie} is '1', otherwise it is '0'
$\delta_{ep}(Ve)$	If virtual link p starts at physical link e, δ_{ep} is '1', otherwise it is '0'
$PR(Pa)$ and $PE(Pa)$	Non-renewable power consumption of a router port and an EDFA respectively, both use non-renewable energy.
$PRS(Pa)$	Non-renewable power consumption of a router port that has access to renewable energy.
ω_e (Ve) and ωs_e (Ve)	Number of wavelength channels on physical link e in the optical layer which use non-renewable energy and renewable energy respectively.
W_p (Ve) and	Number of wavelength channels on virtual

Ws_p(Ve)	link p in the IP layer which use non-renewable energy and renewable energy respectively.
Q_i^e (Ve) and Q_i^s (Ve)	Number of ports which are powered by non-renewable energy or renewable energy for data aggregation in node i.
x_p^d (Ve)	Traffic demand d between node pairs on virtual link p.
ω_e^p (Ve)	Number of wavelength channels of virtual link p on physical link e.
f_e(Ve)	Number of fibers on physical link e.
$E_e(Pa)$	Number of EDFAs on each fiber on physical link e.
$PT(Pa)$ and $PTS(Pa)$	Non-renewable power consumption of a transponder that has access to non-renewable energy only or has access to renewable energy respectively.
$W(Pa)$	Number of wavelengths in a fiber.
Q_i (Pa)	Number of ports for assembling data.
$\nabla^i(Pa)$	Maximum number of ports in node i.
$S_i(Pa)$	The maximum output power of the renewable energy source in node i.
$h^d(Pa)$	Traffic demand d between node pairs.
$B(Pa)$	Capacity of each wavelength.

B. Heuristic Approach

In the multi-hop bypass heuristic proposed in [15] bandwidth utilization is improved by allowing traffic demands between different source-destination pairs to share capacity on common virtual links (lightpaths). Improving the wavelength bandwidth utilization results in fewer virtual links, and therefore, fewer IP router ports and lower power consumption. However, in the hybrid-power IP over WDM network architecture as we assume that renewable energy sources are available to a limited number of nodes, implementing the Multi-hop bypass heuristic which is based on shortest-path routing will only minimize the total power consumption not taking into account whether this power comes from renewable or non-renewable sources. To minimize the utilization of non-renewable power, we propose a new heuristic where the traffic flows are allowed to traverse as many nodes as possible that use renewable energy to ensure that in addition to reducing the total number of IP router ports and transponders, the non-renewable energy consumption is minimized. This constraint may increase the propagation delay, however to maintain QoS, only the two shortest-path routes are considered. Due to the changing traffic pattern and the fact that the output power of renewable energy sources varies during different times of the day, the routing paths are dynamic. The new heuristic is known as Renewable Energy Optimization hop (REO-hop). The flowchart of the heuristic is shown in Fig. 2.

In this heuristic, all the node pairs are reordered based on their traffic demands from highest to lowest and an empty virtual link topology G is created. A node pair is then retrieved from the ordered list, and its traffic demand is routed over virtual topology G so that it traverses the maximum number of nodes that use renewable energy. As mentioned, only the two shortest-path routes are considered, i.e. the two shortest-path

routes are compared in terms of the number of nodes that use renewable energy and the one with the maximum number is selected. If sufficient free capacity is available on the virtual topology, the selected route is accommodated and the remaining capacity on all the virtual links is updated. If the selected route with the maximum number of nodes using renewable sources is not available, the other route is selected. In case the virtual topology cannot accommodate both routes, a new direct virtual link is established between the node pair. Two virtual links are computed, one is a path with the maximum number of nodes that use renewable energy, and the other is the shortest-path route. The two virtual links are compared and the one with lower non-renewable power consumption is selected and is established. If the non-renewable power consumption is the same for both paths, the shortest path is selected in order to minimize the propagation delay. The new virtual link is added to the virtual topology G. The above process is repeated for all the node pairs. When all the traffic demands are routed on the virtual topology G, the objective function (Equation (1)) is used to calculate the total non-renewable power consumption of the network.
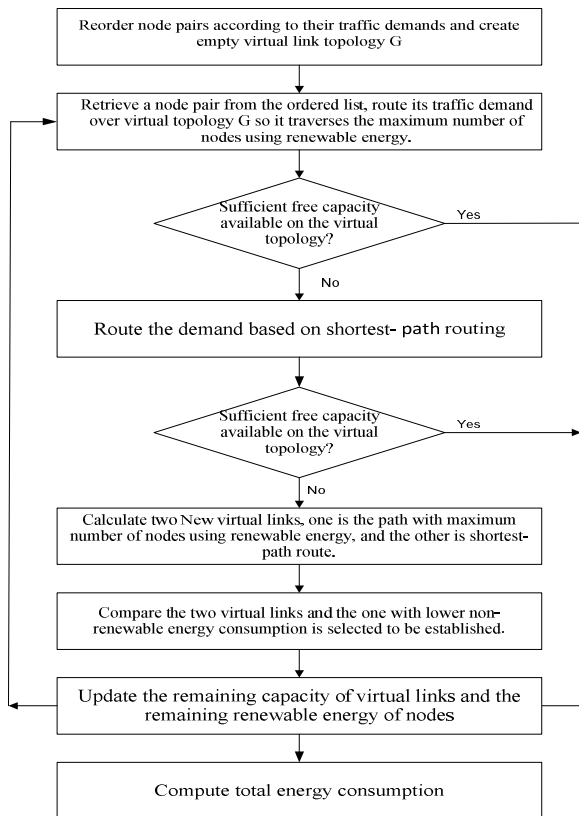

Fig.2. The Flowchart of the REO-hop heuristic

III. SIMULATION AND RESULTS

In [16] and [17] we have evaluated the impact of the REO-hop heuristic on the non-renewable power consumption of IP over WDM networks considering the NSFNET topology, depicted in Fig.3(a). The NSFNET network consists of 14 nodes and 21 bidirectional links. In this paper we investigate the hybrid power IP over WDM architecture in a larger topology and compare it to the NSFNET network. We consider the USNET network, depicted in Fig.3(b), with 24 nodes and
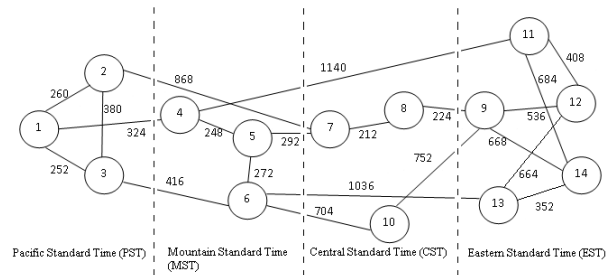
43 bidirectional links.

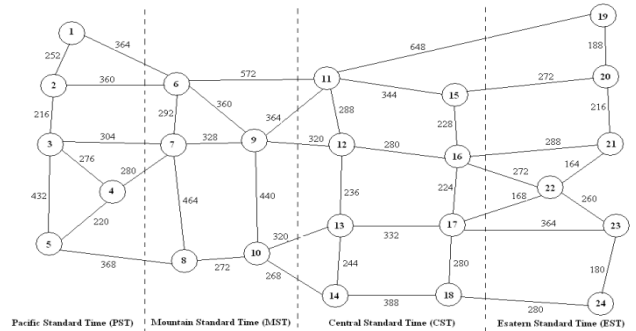
Fig.3(a). The NSFNET topology with time zones

Fig.3(b). The NSFNET topology with time zones

As mentioned in Section II, solar energy is used as the renewable energy source. As both the NFSNET and USNET topologies cover the US, different parts of the networks fall in different time zones, i.e., the nodes will experience different levels of solar energy and traffic demands at any given point in time. There are four time zones, Eastern Standard Time (EST), Central Standard Time (CST), Mountain Standard Time (MST) and Pacific Standard Time (PST). There is an hour time difference between each time zone and the next, we use EST as the reference time. Note that time zones dictate habits and therefore network utilization and traffic demands are different from one time zone to the other. To compare the two topologies, we consider the same traffic demand for both of them. Fig. 4 shows the average traffic demand during different hours of the day [19].

The average traffic demand between each node pair ranges from 20 Gb/s to 120 Gb/s and the peak occurs at 22:00 in these traffic profiles. We assume that the traffic demand between each node pair in the same time zone is random with a uniform distribution and no lower than 10 Gb/s.

The geographical location of nodes affects the sunset and sunrise time, and therefore has impact on the solar energy generated in each node. The solar power available to a node in the NSFNET and the USNET topologies [20] are shown in Fig. 5(a) and Fig. 5(b), respectively. Table II and Table III give the details of the solar output power of each node in the NSFNET and the USNET topologies, respectively. The solar output power is non-zero from 6:00 to 22:00 and the maximum output power occurs at 12:00. Table IV shows the simulation environment parameters in terms of number of wavelengths, wavelength capacity, distance between two neighbouring EDFAs, and power consumption of different components in these two networks. Some of the parameters are similar to those in [15] which are derived from Cisco's 8-slot CRS-1 data sheets [21].

TABLE II
SOLAR OUTPUT POWER OF EACH NODE IN NSFNET (20 kW MAXIMUM OUTPUT POWER)

Node ID	1	2	3	4	5	6	7	8	9	10	11	12	13	14
	SR: 05:43	SR: 05:14	SR: 05:16	SR: 05:54	SR: 05:27	SR: 05:55	SR: 05:51	SR: 05:39	SR: 05:17	SR: 05:53	SR: 05:18	SR: 05:41	SR: 06:27	SR: 05:30
Time (EST)	SS: 20:04	SS: 21:02	SS: 19:34	SS: 20:40	SS: 20:41	SS: 20:10	SS: 20:53	SS: 20:47	SS: 20:24	SS: 19:56	SS: 20:30	SS: 20:29	SS: 20:30	SS: 20:59
00:00	0 kW	0 kW	0 kW	0 kW	0 kW	0 kW	0 kW	0 kW	0 kW	0 kW	0 kW	0 kW	0 kW	0 kW
02:00	0 kW	0 kW	0 kW	0 kW	0 kW	0 kW	0 kW	0 kW	0 kW	0 kW	0 kW	0 kW	0 kW	0 kW
04:00	0 kW	0 kW	0 kW	0 kW	0 kW	0 kW	0 kW	0 kW	0 kW	0 kW	0 kW	0 kW	0 kW	0 kW
06:00	0 kW	0 kW	0 kW	0 kW	0 kW	0 kW	0 kW	0 kW	0 kW	0 kW	2 kW	0.5 kW	0 kW	0.5 kW
08:00	0 kW	0 kW	0 kW	0 kW	2 kW	0.5 kW	0.5 kW	2.5 kW	6 kW	2 kW	6 kW	6 kW	4.5 kW	6 kW
10:00	1.5 kW	2 kW	2 kW	7 kW	6 kW	6 kW	6 kW	6 kW	13 kW	6 kW	13 kW	13 kW	13 kW	13 kW
12:00	10 kW	10 kW	10 kW	13 kW	13 kW	13 kW	13 kW	18 kW	18 kW	18 kW	20 kW	20 kW	20 kW	20 kW
14:00	18 kW	18 kW	18 kW	18 kW	20 kW	20 kW	20 kW	18 kW	18 kW	18 kW	13kW	13kW	13kW	13kW
16:00	18 kW	18 kW	18 kW	18 kW	18 kW	18 kW	18 kW	13kW	13kW	13kW	7.5 kW	7.5 kW	7.5 kW	7.5 kW
18:00	13kW	13kW	13kW	18 kW	13 kW	13 kW	13 kW	8 kW	8 kW	8 kW	5 kW	5 kW	5 kW	5 kW
20:00	8 kW	8 kW	8 kW	8 kW	8 kW	8 kW	8 kW	3kW	3kW	2 kW	2 kW	2 kW	2 kW	2 kW
22:00	2.5 kW	3 kW	0.5 kW	4 kW	2 kW	0.5 kW	3 kW	0 kW	0 kW	0 kW	0 kW	0 kW	0 kW	0 kW

(SR: Sunrise, SS: Sunset. SR time and SS time are given in the node's local time in June)

TABLE III
SOLAR OUTPUT POWER OF EACH NODE IN USNET (20 kW MAXIMUM OUTPUT POWER)

Node ID	Time(EST)	0:00	2:00	4:00	6:00	8:00	10:00	12:00	14:00	16:00	18:00	20:00	22:00
1	SR:5:12 SS: 21:09	0 kW	0 kW	0 kW	0 kW	0 kW	6 kW	13 kW	18 kW	18 kW	13 kW	8kW	4 kW
2	SR:5:27 SS: 21:01	0 kW	0 kW	0 kW	0 kW	0 kW	6 kW	13 kW	18 kW	18 kW	13 kW	8kW	4 kW
3	SR:5:44 SS: 20:10	0 kW	0 kW	0 kW	0 kW	0 kW	6 kW	13 kW	18 kW	18 kW	13 kW	8kW	2 kW
4	SR:5:56 SS: 21:02	0 kW	0 kW	0 kW	0 kW	0 kW	6 kW	13 kW	18 kW	18 kW	13 kW	8kW	4 kW
5	SR:5:42 SS: 20:08	0 kW	0 kW	0 kW	0 kW	0 kW	6 kW	13 kW	18 kW	18 kW	13 kW	8kW	2 kW
6	SR:5:27 SS: 20:47	0 kW	0 kW	0 kW	0 kW	0.5 kW	6 kW	13 kW	20 kW	18 kW	13 kW	8kW	0.6 kW
7	SR:5:57 SS: 21:01	0 kW	0 kW	0 kW	0 kW	0 kW	6 kW	13 kW	20 kW	18 kW	13 kW	8kW	3 kW
8	SR:5:18 SS: 19:34	0 kW	0 kW	0 kW	0 kW	0.8 kW	6 kW	13 kW	20 kW	15 kW	8 kW	3kW	0 kW
9	SR:5:32 SS: 20:31	0 kW	0 kW	0 kW	0 kW	0.5 kW	6 kW	13 kW	20 kW	15 kW	8 kW	3kW	0.8 kW
10	SR:6:01 SS: 20:17	0 kW	0 kW	0 kW	0 kW	0 kW	6 kW	18 kW	20 kW	15 kW	8 kW	2kW	0.5 kW
11	SR:5:55 SS: 21:02	0 kW	0 kW	0 kW	0 kW	0.5kW	8 kW	13 kW	18 kW	15 kW	8 kW	5 kW	0 kW
12	SR:6:12 SS: 21:06	0 kW	0 kW	0 kW	0 kW	0.6kW	8 kW	13 kW	18 kW	15 kW	8 kW	5 kW	0 kW
13	SR:6:13 SS: 20:46	0 kW	0 kW	0 kW	0 kW	0.5kW	8 kW	13 kW	18 kW	15 kW	8 kW	4 kW	0 kW
14	SR:6:35 SS: 20:37	0 kW	0 kW	0 kW	0 kW	0.5kW	8 kW	13 kW	18 kW	15 kW	8 kW	4 kW	0 kW
15	SR:5:27 SS: 20:33	0 kW	0 kW	0 kW	0 kW	1.5kW	8 kW	13 kW	18 kW	15 kW	8 kW	4 kW	0 kW
16	SR:5:46 SS: 20:18	0 kW	0 kW	0 kW	0 kW	1.3kW	8 kW	13 kW	18 kW	15 kW	8 kW	4 kW	0 kW
17	SR:5:54 SS: 20:11	0 kW	0 kW	0 kW	0 kW	1kW	7 kW	13 kW	18 kW	15 kW	8 kW	4 kW	0 kW
18	SR:6:00 SS: 20:04	0 kW	0 kW	0 kW	0 kW	1kW	7 kW	13 kW	18 kW	15 kW	8 kW	4 kW	0 kW
19	SR:5:08 SS: 20:41	0 kW	0 kW	0 kW	1.8 kW	5 kW	15 kW	20 kW	18 kW	13 kW	8 kW	2 kW	0 kW
20	SR:5:14 SS: 20:31	0 kW	0 kW	0 kW	1.5 kW	5 kW	15 kW	20 kW	18 kW	13 kW	8 kW	2 kW	0 kW
21	SR:5:25 SS: 20:32	0 kW	0 kW	0 kW	1 kW	4.5 kW	13 kW	20 kW	18 kW	13 kW	8 kW	2 kW	0 kW
22	SR:5:43 SS: 20:38	0 kW	0 kW	0 kW	0.8 kW	4.3 kW	13 kW	20 kW	18 kW	13 kW	8 kW	2 kW	0 kW
23	SR:5:54 SS: 20:28	0 kW	0 kW	0 kW	0 kW	4 kW	13 kW	20 kW	18 kW	13 kW	8 kW	2 kW	0 kW
24	SR:6:19 SS: 20:34	0 kW	0 kW	0 kW	0 kW	4 kW	13 kW	20 kW	18 kW	13 kW	8 kW	2 kW	0 kW

(SR: Sunrise, SS: Sunset. SR time and SS time are given in the node's local time in June)
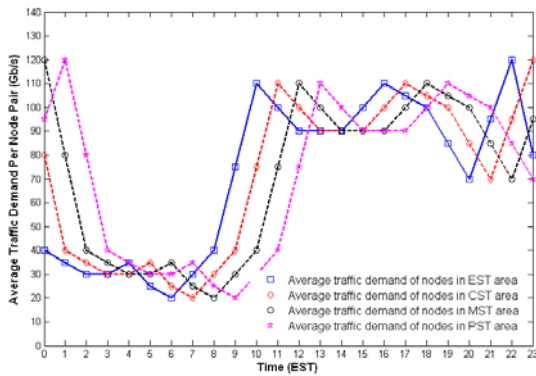
Fig.4. Average traffic demand in different time zones
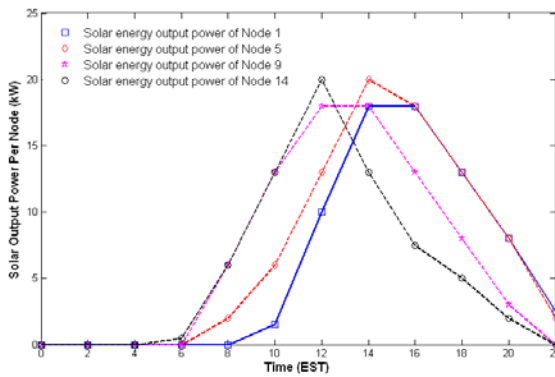

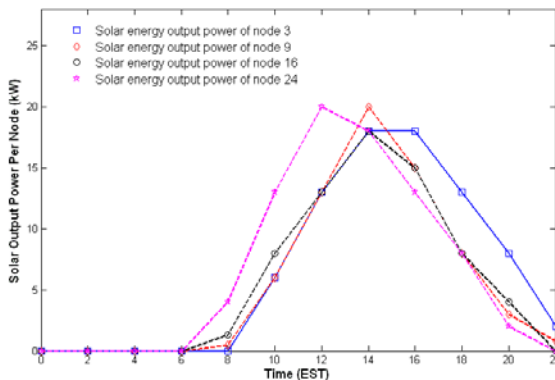Fig.5(a). Solar power in different nodes in different time zones in the NSFNET

Fig.5(b). Solar power in different nodes in different time zones in the USNET

TABLE IV
INPUT DATA FOR THE SIMULATION

Distance between two neighboring EDFAs	80 km
Number of wavelength in a fiber (W)	16
Capacity of each wavelength (B)	40 Gb/s
Non-renewable power consumption of a router port (PR)	1000 W
Renewable power consumption of a router port (PR^s)	1000 W
Non-renewable power consumption of a router port that has access to renewable power (PRS)	0 W
Non-renewable power consumption of a transponder (PT)	73 W
Renewable power consumption of a transponder (PT^s)	73 W
Non-renewable power consumption of a transponder that has access to renewable power (PTS)	0 W
Non-renewable power consumption of an EDFA (PE)	8 W

A.   Non-renewable Power Consumption of the Network

To compare the non-renewable power consumption of the

two topologies, we assume that node sets (4, 5, 6, 7 and 9) and (1, 4, 6, 7, 19, 20 and 22) are initially selected to employ solar energy in the NSFNET and the USNET Topologies, respectively. In Section III.B we will study the optimization of the location of nodes employing solar energy.

Typically a one square meter silicon solar cell can produce about 0.28 kW of power [22]. We assume that the maximum solar energy available to a node is 20 kW, therefore a total solar cell area of about 100 m^2 is required.

The AMPL/LPSOLVE software is used to solve the LP problem. Five different cases are considered: 1) Non-bypass heuristic without renewable energy, 2) Non-bypass heuristic with renewable energy, 3) Multi-hop-bypass heuristic without renewable energy 4) Multi-hop-bypass heuristic with renewable energy, and 5) REO-hop heuristic with renewable energy.

Load is one of the factors that influence equipment power consumption. Different power versus traffic profiles are proposed in the literature to provide an accurate description of the dependency between equipment power consumption and traffic load [9]. Adaptive Link Rate (ALR) schemes allow equipment to introduce functions (such as sleep cycles and transmission rate adaptation) so as to save power when traffic is not at its peak [6]. Fig.6 shows different power profiles for telecommunication equipment. We consider the 'On-off' power profile [9] that assumes that equipment has two power states (on and off), i.e. the equipment consumes full power when switched-on, and the 'Cubic' power profile which is typically used in equipment that uses Dynamic voltage Scaling (DVS) and Dynamic Frequency Scaling (DFS) [9]. Other power profile exist including 'Linear' power profile: [9], [23], 'Log10' power profile [24], [25] and 'Log100' power profile.

Fig.7(a) and Fig.7(b) show the total non-renewable power consumption of the NSFNET and the USNET, respectively under the on-off and cubic power profiles. The power consumption of the non-bypass approach without solar power under the on-off power profile gives the upper bound on the non-renewable power consumption. Compared to the non-bypass approach with solar power under the on-off profile, both of the Multi-hop-bypass and REO-hop heuristics have reduced the non-renewable power consumption for both the NSFNET and the USNET topologies. For both topologies, the REO-hop heuristic with solar power under the on-off power profile outperforms the Multi-hop-bypass when the solar power is significant and the traffic demand is high (between 6:00 and 22:00).

Furthermore, the REO-hop heuristic outperforms the Multi-hop-bypass heuristic for both topologies from 0:00 to 6:00 when there is no solar power and the traffic demand is low as the REO-hop heuristic tries to route demands on virtual links with sufficient capacity rather than using shortest-path routing as with the Multi-hop-bypass heuristic.

Introducing the cubic power profile has resulted in reducing the total non-renewable power consumption under the REO-hop heuristic by 54% and 58% for the NFSNET and the USNET, respectively compared to the upper bound. Further CO_2 reductions can be introduced by deploying solar power in all the nodes in the network. Compared to the upper bound, the

REO-hop heuristic under the cubic power profile and when all nodes have access to solar power has achieved an average non-renewable power reduction (CO_2 reduction) of 58% and 60% for the NFSNET and the USNET, respectively.
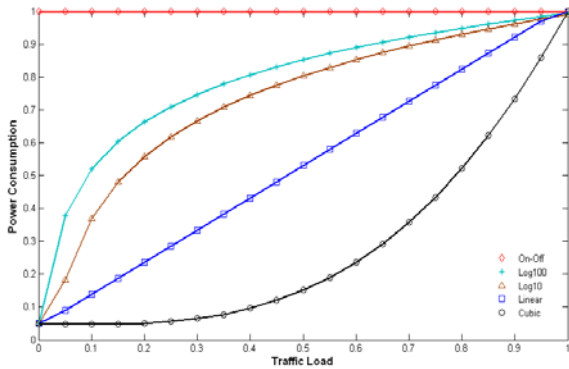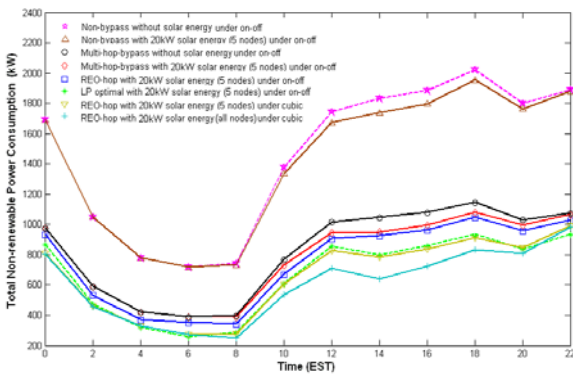

Fig.6. Different power profiles

Fig.7(a).The total non-renewable power consumption of different heuristics under different power profiles with and without solar power for the NSFNET
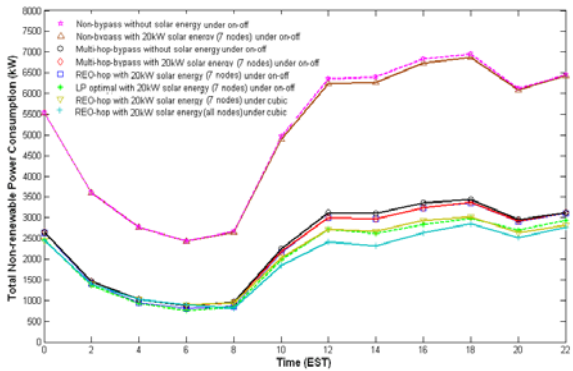

Fig.7(b). The total non-renewable power consumption of different heuristics under different power profiles with and without solar power for the USNET

In Fig.8 we examine the impact of different values of the maximum solar output power available per node (40 kW, 60 kW and 80 kW) on the total non-renewable power consumption of the two topologies. A solar cell area of up to 300 m^2 is needed to generate such values. Solar cell with such surface area can be practically built in a typical core routing node location. Increasing the maximum solar power output per node has linearly reduced the total non-renewable power consumption under different algorithms. In both topologies, using the REO-hop heuristic has resulted in higher reduction in the total non-renewable power consumption compared to the Multi-hop heuristic.
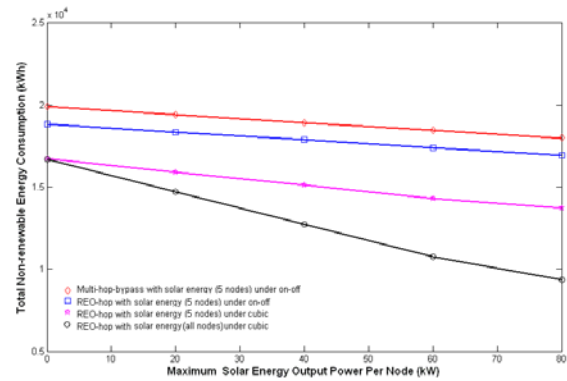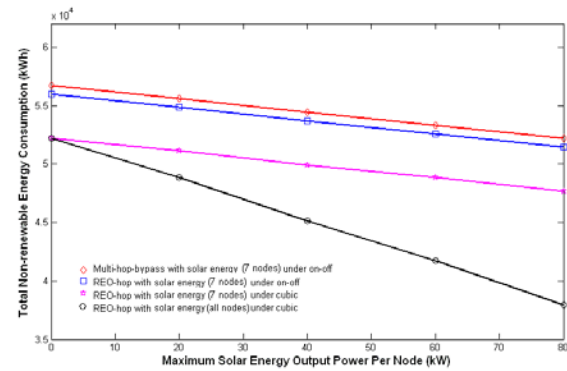

Fig.8(a). The total non-renewable energy consumption in a 24 hour period for different values of the maximum solar energy output under different heuristics and power profiles in the NSFNET

Fig.8(b). The total non-renewable energy consumption in a 24 hour period for different values of the maximum solar energy output under different heuristics and power profiles in the USNET
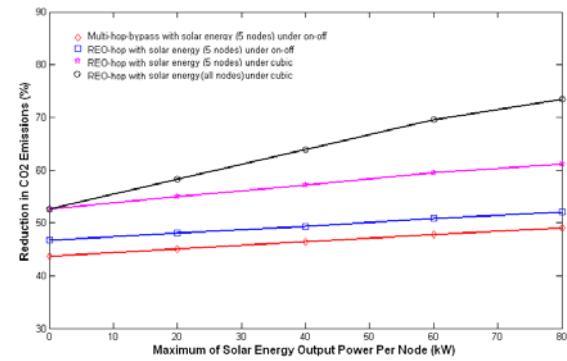

Fig.9(a). Reduction in CO_2 emissions in a 24 hour period under different heuristics in the NSFNET
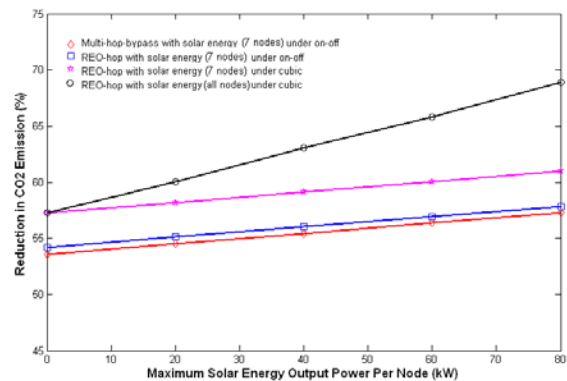

Fig.9(b). Reduction in CO_2 emissions in a 24 hour period under different heuristics in the USNET

Similar trends to those observed in Fig.8(a) and Fig.8(b) are

observed for the reduction in CO_2 emissions in Fig.9(a) and Fig.9(b). Compared to the upper bound "non-bypass without solar energy", the total CO_2 emissions of the NFSNET during a 24 hour period (Fig.9(a)) have been reduced by about 47%~52% under the REO-hop-bypass heuristics with 5 nodes employing 20kW solar power considering the on off power profile and by about 53%~73% with all nodes employing 80kW solar power considering the cubic power profile. As mentioned in Section I, about 228 grams CO_2 are produced through the consumption of 1kWh of non-renewable energy. Therefore by using the REO-hop heuristic with all nodes employing 80kW solar power under the cubic power profile we will be able to reduce the CO_2 emissions of the NSFNET by about 1900 tones every year.

In Fig.9(b), the total CO_2 emissions of the USNET during a 24 hour period have been reduced by about 57%~69% under the REO-hop heuristic when all nodes employ 80kW solar power considering the "cubic" power profile. The annual CO_2 emissions reduction in this case is about 4600 tones.

We can see from Fig.9(a) and Fig.9(b) that the REO-hop heuristic has resulted in higher reductions in the non-renewable energy consumption of the USNET compared to the NSFNET when there is not any solar energy or only few nodes employing solar energy. This can be understood if we remember that the REO-hop heuristic is based on bypass and reduces the non-renewable energy consumption mainly by reducing the number of the ports in intermediate nodes between source node and destination node. Given that the average hop number is 1.5 and 2.0 in the NSFNET and the USNET, respectively, the REO-hop heuristic will result in higher reductions in the number of ports in intermediate nodes in the USNET and therefore a higher percentage of reductions in the non-renewable energy consumption in the USNET.

As the REO-hop heuristic routes demands dynamically based on the output power of solar power sources in nodes and the available capacity, the propagation delay under the REO-hop heuristic is expected to increase compared to the Multi-hop-bypass heuristic which routes traffic based on the shortest path. However, as the REO-hop heuristic routes demands using only the two shortest-path routes, the propagation delay (Fig.10) has not increased significantly (the increase is less than 0.3 ms, i.e. less than 10%) maintaining the QoS.
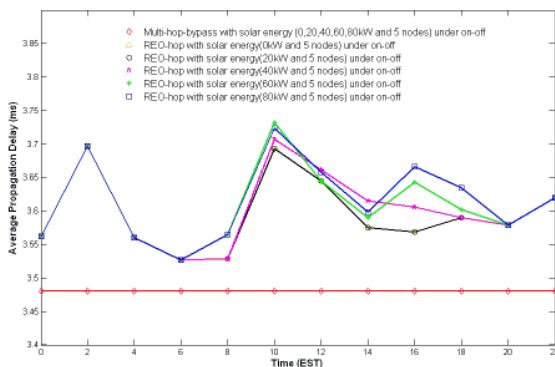

Fig.10(a). Average propagation delay of the REO-hop and the Multi-hop-bypass heuristics in the NSFNET
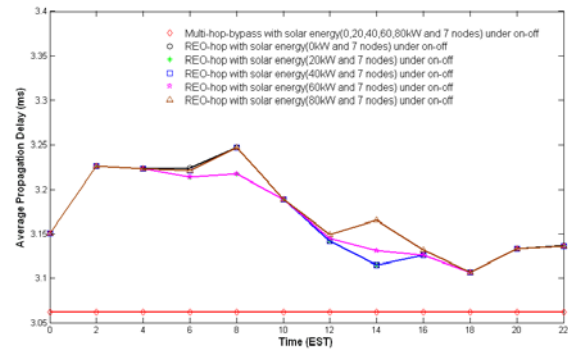

Fig.10(b). Average propagation delay of the REO-hop and the Multi-hop-bypass heuristics in the USNET

B. Location of Nodes Employing Renewable Energy

In the previous results, we have randomly selected nodes to use renewable energy. To investigate the impact of the location of nodes that have access to renewable energy on the total non-renewable power consumption, a new LP model is developed with the objective of optimizing the selection of nodes that use renewable energy such that the non-renewable power consumption savings are maximized. The new LP model is subject to the same constraints in Section II.A, except that Equation (6) is replaced with Equation (11) and a new constraint is added (Equation (12)).

In this model we consider time as a variable. Therefore, t is added to all the variables in Table I where t is the time point of time set T.

The new LP model is defined as follows:

Objective: maximize

$$\sum_{t \in T} \sum_{i \in N} \left(PR^s \cdot \left(Q_{it}^s + \sum_{p \in P} \delta_{ipt} \cdot Ws_{pt} \right) + \sum_{e \in E} PT^s \cdot \omega s_{et} \cdot \delta_{iet} \right) \quad (10)$$

Subject to:

Equations: (2) (3) (4) (5) (7) (8) (9) (10)

(Every variable in the equations above has had the time variable t augmented)

$$PR^s \cdot \left(Q_{it}^s + \sum_{p \in P} \delta_{ipt} \cdot Ws_{pt} \right) + \sum_{e \in E} PT^s \cdot \omega s_{et} \cdot \delta_{iet}$$
$$\leq S_{it} \cdot \varepsilon_i \quad (11)$$
$$\forall \, i \in N, t \in T$$

$$\sum_{i \in N} \varepsilon_i = Ns \quad (12)$$

where $\varepsilon_i = 1$ if node i uses renewable energy, otherwise $\varepsilon_i = 0$, and Ns is the total number of nodes with access to renewable energy.

Equation (11) ensures that the renewable power consumption in each node is within the maximum output power of its associated renewable energy source at any time of the day. Equation (12) implies that the total number of nodes that use renewable energy is limited to Ns which is set in advance.
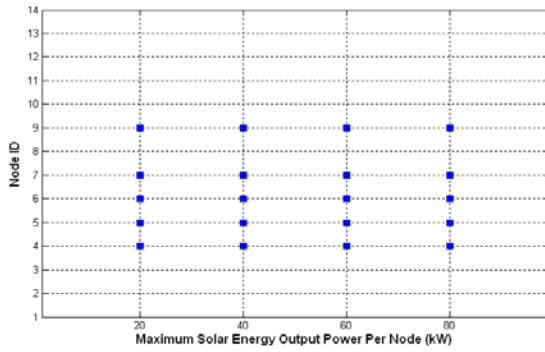
Fig.11(a). Optimal location of nodes with access to renewable energy under different values of the maximum solar energy per node for the NSFNET topology
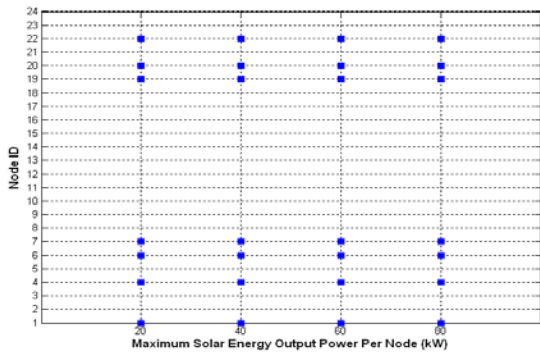

Fig.11(b). Optimal location of nodes with access to renewable energy under different values of the maximum solar energy per node for the USNET topology
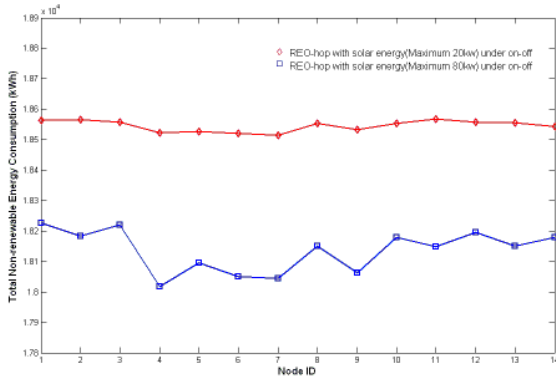

Fig.12(a). The total non-renewable energy consumption of the NSFNET topology in a 24 hour period with different nodes using renewable energy
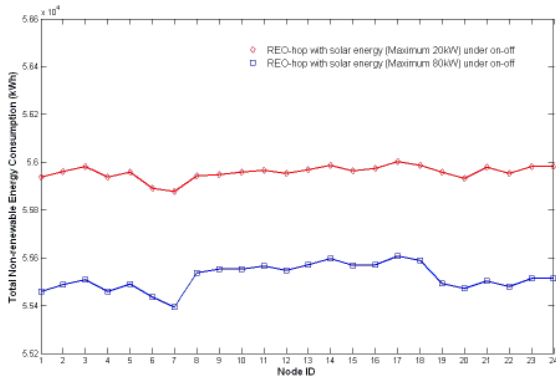

Fig.12(b). The total non-renewable energy consumption of the USNET topology in a 24 hour period with different nodes using renewable energy
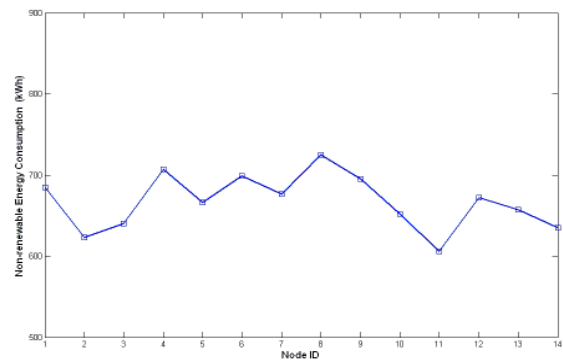

Fig.13(a). The non-renewable energy consumption of the NSFNET nodes in a 24 hour period under the REO-hop heuristic without solar energy
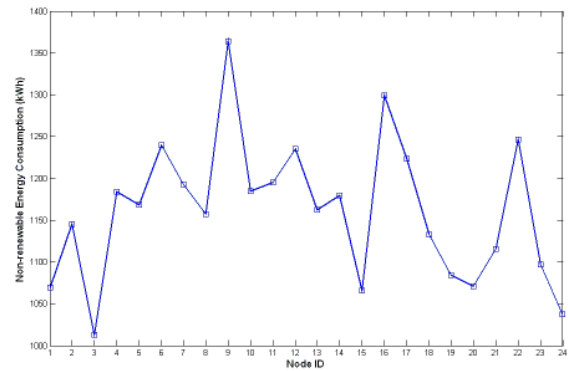

Fig.13(b). The non-renewable energy consumption of the USNET nodes in a 24 hour period under the REO-hop heuristic without solar energy

The optimization results of the NSFNET and the USNET are given in Fig.11(a) and Fig.11(b), respectively under different values of the maximum renewable energy output power (20kW to 80kW) and the on-off power profile, assuming Ns=5 in NSFNET and Ns=7 in USNET. We can see that the optimal node selections do not change.

To verify the optimization results in Fig.11, we evaluate the total non-renewable power consumption of the REO-hop heuristic in a 24 hour period where we consider only a single node to use renewable energy. We evaluate the performance under different values of the maximum solar power per node. While for the NSFNET topology (Fig.12(a)) the total non-renewable consumption is lower when the nodes in the centre of the network (4, 5, 6, 7, and 9) use renewable energy, nodes distributed through the network (1, 4, 6, 7, 19, 20 and 22) in the USNET topology (Fig.12(b)) result in a lower total non-renewable consumption.
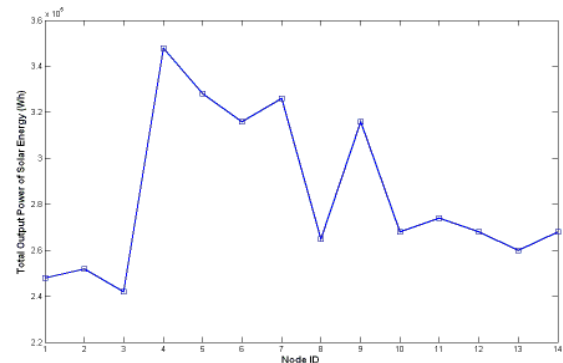

Fig.14(a). The solar energy output power of the NSFNET nodes in a 24 hour period
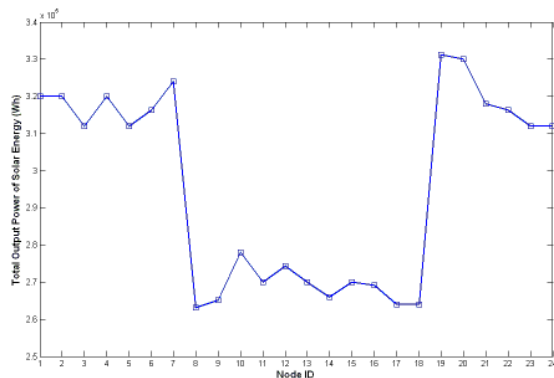
Fig.14(b). The solar energy output power of the USNET nodes in a 24 hour period

The impact of deploying renewable energy at a node depends on its power consumption and geographical location. Deploying renewable energy at nodes where more traffic flows go through and higher solar energy is available is expected to have more impact on reducing the total non-renewable power consumption of the networks. Fig.13 shows the non-renewable power consumption of both topologies under the REO-hop heuristic without solar power considering the on-off power profile. Fig14 shows the output power of the solar energy of each node (maximum output power is 80kW) in both topologies. Nodes at the center of NSFNET topology (Fig.13(a)) consume more non-renewable energy and have higher total solar output power (Fig.14(a)) compared to other nodes. Therefore deploying renewable energy in these nodes will result in higher reductions in the total non-renewable power consumption of network. Similarly, in the USNET network nodes with the highest non-renewable power consumption (Fig.13(b)) and the highest output solar power (Fig.14(b)) are selected to deploy solar power.

IV. Conclusions

In this paper, we have investigated the use of renewable energy in IP over WDM networks to reduce the non-renewable energy consumption and consequently CO_2 emissions. We have developed a LP optimization model and proposed an efficient heuristic based on the Multi-hop-bypass heuristic, known as REO-hop, to optimize the use of renewable energy in the hybrid-power IP over WDM architecture. We have investigated the LP model and the REO-hop heuristic considering two topologies, the NSFNET and the USNET. For both topologies, the REO-hop heuristic has reduced the non-renewable power consumption compared to the Multi-hop-bypass by up to 73% and 69% for the NSFNET and USNET, respectively while maintaining QoS. Furthermore another LP optimization model has been developed to optimize the selection of nodes that employ renewable energy. The results show that the optimum location of nodes employing renewable energy is selected according to the output power of the renewable energy sources and the power consumption of nodes.

Acknowledgements

The authors would like to acknowledge funding from the

References

[1] C. Bianco, F. Cucchietti and G. Griffa, "Energy consumption trends in the next generation access networks – a teleco perspective," (INTELEC 2007), Rome, Italy, Sept. 2007, pp. 737-742.

[2] Telecom Italia Website, "The Environment", URL: http://www.telecomitalia.it/sostenibilita2006/English/B05.html

[3] BT Press, "BT announces major wind power plans," Oct. 2007, http://www.btplc.com/News/Articles/Showarticle.cfm?ArticleID=dd 615e9c-71ad-4daa-951a-55651baae5bb.

[4] BT Website, "Wind farms to power BT," 2009, http://www.btplc.com/sharesandperformance/Annualreportandrevie w/Shareholdermagazine/May2009/windfarms.htm?Terms=380,4305

[5] M. Gupta and S. Singh, "Greening of the Internet," in *Proc.ACM SIGCOMM*, Aug. 2003.

[6] S. Nedevschi, L. Popa, G. Iannaccone, Y. Ratnasamy, and D. Wetherall. "Reducing Network Energy Consumption via Sleeping and Rate-Adaptation," In *NSDI*, 2008.

[7] I. Keslassy, S. Chuang, K. Yu, D. Miller, M. Horowitz, O. Solgaard, and N. McKeown, "Scaling internet routers using optics," in *Proceedings of ACM SIGCOMM '03*, Karlsruhe, Germany, August 2003.

[8] A. Wassal and M. Hasan, "Low-power System-level Design of VLSI Packet Switching Fabrics," *IEEE Transactions on Computer-Aided Design of Integrated Circuits and Systems*, vol. 20, no. 6, June 2001.

[9] J. Camilo C. Restrepo, C. Gruber, C. M. Machuca, "Energy Profile Aware Routing" In *First International Workshop on Green Communications IEEE International Conference on Communications (ICC),* June 2009, Dresden, Germany

[10] K. J. Christensen, C. Gunaratne, B. Nordman, and A. D. George, "The next frontier for communications networks: power management," *Computer Commun.*, vol. 27, pp. 1758–1770. Aug. 2004.

[11] The Green Grid, http://www.thegreengrid.org/pages/ overview.html.

[12] J. Chabarek, J. Sommers, P. Barford, C. Estan, D. Tsiang, S. Wright, "Power Awareness in Network Design and Routing," *INFOCOM,* pp. 457-465, 2008.

[13] N. Vasic and D. Kostic, "Energy Aware Traffic Engineering," in *Proceedings of the 1st Int'l Conf. on Energy-Efficient Computing and Networking (E-ENERGY)*, 2010.

[14] IEEE 802.3 Energy Efficient Ethernet Study Group, http://grouper.ieee.org/groups/802/3/eee_study/index.html.

[15] G. Shen and R. S. Tucker, "Energy-Minimized Design for IP Over WDM Networks," *Optical Communication and Networking*, vol.1, pp. 176-186, 2009.

[16] X. Dong, T. El-Gorisha and J.M.H. Elmirghani, "IP over WDM Networks Employing Renewable Energy Sources," *Journal of Lightwave Technology*, vol. 29, pp. 3-14, 2011

[17] X. Dong, T. El-Gorisha and J.M.H. Elmirghani, "Renewable Energy in IP over WDM Networks," *ICTON 2010*, pp.1-8, 2010, Germany

[18] X. Dong, T. El-Gorashi, J.M.H Elmirghani, "Green IP Over WDM Networks With Data Centers", *IEEE/OSA Journal of Lightwave Technology* vol. 29 , Issue: 12, pp. 1861 – 1880.

[19] Y. Chen and C. Chou, "Traffic Modeling of A Sub-network by using ARIMA," *Info-tech and Info-net, Proceedings, ICII-2001.* vol. 2, pp. 730-735, 2001.

[20] H. Wang, H. Yang and H. Wu, "A Fine Model for Evaluating Output Performance of Crystalline Silicon Solar Modules," *Photovoltaic Energy Conversion, IEEE 4th World Conference*, vol. 2, pp. 2189-2192, 2006.

[21] Cisco CRS-1 specification data sheet, http://www.cisco.com.

[22] J. Zhao, A. Wang, P. P. Altermatt S. R. Wenham and M. A. Green, "24% Efficient Silicon Solar Cells," *Photovoltaic Energy Conversion, Twenty Fourth. IEEE Photovoltaic Specialists Conference,* vol. 2, pp. 1477-1480, 1994

[23] T. T. Ye, "Analysis of power consumption on switch fabrics in network routers," proceedings of the 39th Design Automation Conference, New Orleans, pp. 524-529, U.S.A, June 10-14, 2002.

[24] R. Hays, "Active/Idle Toggling with Low-Power Idle," presentation at IEEE802.3az Task Force Group Meeting, January 2008.

[25] IEEE802.3az, Energy Efficient Ethernet Study Group, http://www.ieee802.org/3/az/index.html.

Xiaowen Dong received a B.E. degree in electronic engineering from Southwest Jiaotong University, Chengdu, China, in 2005. From 2005 to 2007, he worked as a wireless communication system engineer in Wuhan Research Institute (WRI), Wuhan, China. In October 2008, he received an M.E. degree with First Class Honours in electronic engineering from National University of Ireland, Maynooth, Ireland. Currently, he is a Ph.D. student in electronic and electrical engineering at University of Leeds. His research interests include energy aware networks, high-effect routing method and protocols in optical communication.

Taisir El-Gorashi received a BSc (Hons) First Class in electrical and electronic engineering from University of Khartoum, Sudan, and an M.Sc. degree (Distinction) in photonic and communication systems from University of Wales Swansea, UK in 2004 and 2005, respectively. In 2010 she obtained a Ph.D. degree in optical networking form University of Leeds, UK. Currently she is a post-doctoral research associate in the School of Electronic and Electrical Engineering, University of Leeds. Her research interests include next generation optical network architectures and green ICT

Jaafar Elmirghani received a BSc (Hons) First Class in Electrical Engineering from the University of Khartoum, Sudan in 1989 and the PhD in 1994 from the University of Huddersfield, UK for work on optical receiver design and synchronization. He is the Director of the Institute of Integrated Information Systems and Professor of Communication Networks and Systems within the School of Electronic and Electrical Engineering, University of Leeds, UK. He joined Leeds in 2007 and prior to that (2000–2007) as chair in optical communications at the University of Wales Swansea he founded, developed and directed the Institute of Advanced Telecommunications and the Technium Digital (TD), a technology incubator/spin-off hub. He has provided outstanding leadership in a number of large research projects at the IAT and TD. He has co-authored *Photonic switching Technology: Systems and Networks*, (Wiley) and has published over 300 papers. He has research interests in optical systems and networks and signal processing. Dr. Elmirghani is Fellow of the IET, Fellow of the Institute of Physics and Senior Member of IEEE. He was Chairman of IEEE Comsoc Transmission Access and Optical Systems technical committee and was Chairman of IEEE Comsoc Signal Processing and Communications Electronics technical committee, and an editor of IEEE Communications Magazine. He was founding Chair of the Advanced Signal Processing for Communication Symposium which started at IEEE GLOBECOM'99 and has continued since at every ICC and GLOBECOM. Dr. Elmirghani was also founding Chair of the first IEEE ICC/GLOBECOM optical symposium at GLOBECOM'00, the Future Photonic Network Technologies, Architectures and Protocols Symposium. He chaired this Symposium, which continues to date under different names. He received the IEEE Communications Society Hal Sobol award, the IEEE Comsoc Chapter Achievement award for excellence in chapter activities (both in 2005), the University of Wales Swansea Outstanding Research Achievement Award, 2006 and the IEEE Communications Society Signal Processing and Communication Electronics outstanding service award, 2009.

Target Tracking Approximation Algorithms with Particle Filter Optimization and Fault-Tolerant Analysis in Wireless Sensor Networks

Xiang Gao
School of Microelectronics, Xidian University, Xi 'an, China
Email: xgao@mail.xidian.edu.cn

Yintang Yang[1], Duan Zhou[2], Jianxian Zhang[1,2] and Changchun Chai[1]
[1] School of Microelectronics, Xidian University, Xi 'an, China
[2] School of Computer Science and Technology, Xidian University, Xi 'an, China
Email: ytyang@xidian.edu.cn, zhouduan3788@126.com, {jxzhang, ccchai}@ mail.xidian.edu.cn

Abstract—**In order to process target tracking approximation with unknown motion state models beforehand in a two-dimensional field of binary proximity sensors, the algorithms based on cost functions of particle filters and near-linear curve simple optimization are proposed in this paper. Through moving target across detecting intersecting fields of sensor nodes sequentially, cost functions are introduced to solve target tracking approximation and velocity estimation which is not similar to traditional particle filters that rely on probabilistic assumptions about the motion states. Then a near-linear curve geometric approach is used to simplify and easily describe target trajectories that are below a certain error measure. Because there maybe some sensor nodes invalid in practice, so a fault-tolerant detection is applied to avoid the nodes' reporting fault and also improve accuracy of tracking at the same time. The validity of our algorithms is demonstrated through simulation results.**

Index Terms—**particle filters, cost function, target tracking, fault tolerant**

I. INTRODUCTION

In Wireless Sensor Networks (WSN), binary proximity sensors are able to be tasked to report outputs 1 when a motion target is within the proximity, and 0 otherwise. This simple sensing model is of both practical interest and information processing for several reasons. Firstly, simplified binary outputs based on the quantization rule [1] from sensors are able to save the large number of data transmission to fusion centre. Secondly, WSN fulfill the sensors' location deployment based on the minimal sensor' sensing capability [2] so that sensors ensure communication connection each other during the target tacking. Finally, this simple model permits the derivation of performance of abstraction, so tracking algorithms are designed under the assigned error and are achieved through auxiliary near-linear curve simplification approach.

However, the classical target tracking algorithm is often formulized as a Kalman filtering problem about gaussian models or a particle filtering issue about not-gaussian and not-linear models. The Kalman filter and the Extended Kalman filter (EKF) are presented and derived to solve the given systems dynamic models under linear and Gaussian state systems as well as non-linear and non-Gaussian state functions respectively [3]. The Kalman filter could be able to converge the systems to a steady state and convey the last system measurement to the novel state estimate. However, EKF using the frame of linear filter to solve non-linear systems results in the state linearization. Hence, EKF is not an optimal approach to obtain the target trace in this problem. The particle filters based on recursive Bayesian filters could be applied to any state transition or measurement model, so they are greatly superior to the EKF and currently applied to solve non-linear systems [4]. At the same time, many different modified particle filters are proposed. A new Gaussian sum particle filter is used to perform the sensors selection and the tracking is propagated among the fixed sensor nodes [5], while the multi model auxiliary particle filter [6] is presented to track the target among the mobile sensor nodes. When there are multiple targets in systems dynamics, a multi-modal particle filter with fast tracking capability is introduced to track multi-target trace [7].

Above these filtering algorithms, the authors adopt differently filters to handle sampled information obtained from the assumptions of given or known individual system dynamic mathematical models and probabilities, which are related to the system states and the observations. Meanwhile, in order to sample the information, sensors are able to process different sensing properties, such as radar, acoustic, magnetic, and so on [8]. While an assumption is proposed that the target states' models are unknown in advance and sensors have the simplest function of reporting the target within their sensing regions, the common filtering algorithms are not suitable in this situation.

In this paper, we assume the tracking conditions without any sensing information about orientation, speed or other attributes of the target, and also, there are no probabilistic assumptions and system models used. However, cost reference particle filters [9, 10], which make use of user-defined cost functions measure the quality of state signal estimates according to the given system state-space mathematical models, could be introduced to solve the problems of no probabilistic assumptions. And then, our emphasis is on utilizing geometric features of neighbor sensors' common sensing areas to establish limits of candidate paths and target moving boundaries according to sensors' sensing disks partition [11] and the idea of minimalist approach [12] respectively. A particle filtering algorithm is used to clean up influences of roughly detecting information and limits of the boundaries. So Cost-Function Particle Filters based on Piece-wise Linear Curve (CPF-PLC) is designed for getting preferable target tracking and velocity estimation. In the meantime, a fault-tolerant analysis based on [13, 14] is added to target tracking considering the practical application.

II. The Geometric Description of Sensing Disks

For simplicity, the authors assume that the sensing region of each sensor is disk, and sensors are deployed uniformly which could keep communication coverage of the whole networks. Sensing binary information is transmitted by dynamic hierarchy routing protocol [15]. All sensors are assumed to detect an object correctly in their effect sensing regions and incorrect detections are avoided by fault-tolerant algorithms proposed [16].

An example is proposed to express the model of target's movement across these sensing disks and some geometric features are also defined as follows.
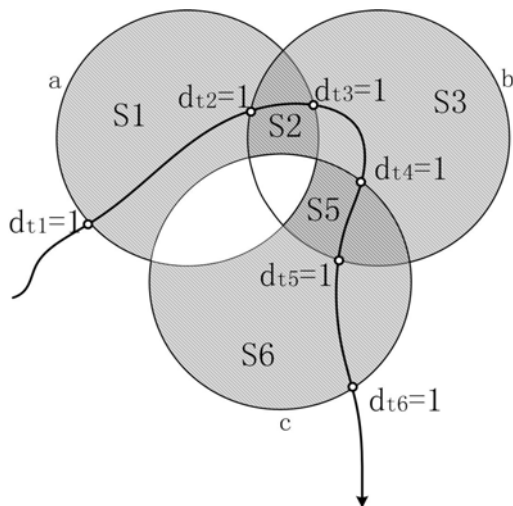

Figure 1.　The geometry of target trajectories across three sensors' sensing disks

The shaded areas S_i are target's location over time intervals t_k with constant sensing information, and the sensing binary boundary signals of sensor a, b and c are defined by d_{tk} in Fig. 1. The located boundary curves

$B_j (j = 1, 2 \cdots)$ of the moving target in each shaded area are stamped by d_{tk} in time t_k order and target tracking algorithms in this paper will use these geometric features to restrain particle sampling limits and tendency of tracking estimation.

III. Tracking with Geometric Filtering

In this section, the algorithm of CPF-PLC is described in detail. When target tracking obtained by Cost-Function Particle Filtering (CPF), a posterior near-linear curve simplified algorithm is proposed to improve the target's velocity estimation and also clean up special errors between true target trajectories and estimate paths.

A. Definition of Cost Function

In order to estimate target position $X_{0:t}$ which is two-dimensional vector including x and y coordinates and couldn't be able to makes use of any Probability Distribution Functions(PDF), a cost function is defined to deduce a posteriori state PDF $P(X_{0:t} | Y_{1:t})$ according to sampling quality observations in S_i.

The idea of this cost function is derived from [9].The candidate paths (called particles) are created in terms of samples at each time instant t by the previous candidate paths at time instant t-1. At any time, t, there are M particles within the current S_i, for the lth particle denoted by X_t^l. At the next time instant t+1, N particles are chosen uniformly at random from the current S_i for lth particle denoted by X_{t+1}^l particle. So there are MN increments between the position X_t^l and X_{t+1}^l, and also MN particles. The increment Y_{t+1} is defined as:

$$Y_{t+1} = \left\| X_{t+1}^l - X_t^l \right\| . \tag{1}$$

We assume that target trajectories are low-frequency variation with respect to the target moving trend in each S_i. Therefore, when sampling time difference is shorter between t and t+1, the value of Y_{t+1} is able to be regarded as the approximate vector velocity at time t+1. Sampling weights are abstracted from the cost function that penalizes changes in the vector velocity. These weights will depend on the former observation Y_t at time instant t to estimate this potential punishment and void bad samples. Based on a prediction of the changes vector velocity from Y_t, a cost function is given by

$$R(X_t | Y_{t+1}) = \left\| Y_{t+1} - Y_t \right\| . \tag{2}$$

B. Cost-Function particle filtering algorithm

This section describes CPF on the basis of above the definitions.

First step: selection of the most promise particles, namely resampling process.

The proposed resampling technique proceeds sequentially in a manner similar to the Sample Important Resampling (SIR) method[17] and initial costs are assigned zero. Given a set of MN increments at time

instant t, where M particles X_{t-1}^M are from time instant t-1 and N particles X_t^N are chosen from M particles uniformly at time instant t respectively. According to (2), let the particles $\{X_t^m, Y_t^{(m)}\}_{m=1}^{MN}$ sorted based on their predicted costs $R_t^{(m)}$ in descending order and the first M of MN particles are replicated N times which is to avoid sample impoverishment. The weights are defined as:

$$\omega_t^m \propto \lambda(R_t^{(m)}), \tag{3}$$

where λ is a monotonically decreasing function which is defined as $\lambda(R_t^{(m)}) = \dfrac{1}{(R_t^{(m)})^2}$. The new particle streams are $\{\overline{X_t^m}, \overline{R_t^{(m)}}\}_{m=1}^{MN}$ at time instant t.

Second step: choose M particles from $\overline{X_t^m}$ with the best cost $\overline{R_t^{(m)}}$. For $m = 1, \cdots MN$, let

$$\overline{Y_{t+1}^m} = \left\| X_{t+1}^m - \overline{X_t^m} \right\|, \tag{4}$$

where $X_{t+1}^m (m = 1, \cdots N)$, and m are the samples at time t+1 for the first step. So the costs at time t+1 are expressed as:

$$R^{(m)}(X_{t+1} \mid Y_{t+1}) = \left\| \overline{Y_{t+1}^m} - Y_t^m \right\| \tag{5}$$

and ω_{t+1}^m is obtained by (3).

Third step: estimation of the position X_{t+1} . There are many ways to estimate X_{t+1} at time instant t+1, such as:

$$\overline{X_{t+1}} = \sum_{m=1}^{MN} X_{t+1}^m \omega_{t+1}^m . \tag{6}$$

C. Near-Linear Curve Simplification Algorithm

In this paper, there is no any probabilistic assumption or target motion state information used. The target tracking estimated by CPF may omit and exceed the boundary limits about each S_i when the estimate trajectories stab across B_j. So a posterior near-linear curve simplification algorithm named Piece-wise Linear Curve (PLC) from [18] is proposed to solve the problems. Through PLC, the velocity estimate error ε is able to be bounded in a reasonable range and then it is helpful to improve velocity re-estimation at the same time.

The description of PLC in detail is seen from [18]. Hence, the estimate trajectories of the target obtained from CPF are viewed as a polygonal curve C which is composed of line segments of vertices $\overline{X_{0:t}}$. The aim is to minimize the maximum number of vertices $\overline{X_{0:t}}$ of curve C to get a simplified curve C' so that the error between C and C' is under an assigned error measure φ . Then, average diameter d of each S_i is able to be computed by [11,19]. This value of d means that the segment length of estimate trajectories in each S_i is lower than d at least. Therefore, following conclusions are obtained:

Conclusion 1: when φ is equal to d, the velocity estimate error ε could be optimized and be lower than an upper bound at least with d-simplification of curve C.

Proof. Conclusion is given that $\varepsilon \le \dfrac{\sqrt{2}d}{X_t X_{t+k}}$, and the detailed proof process is seen from [19]. At the same time, it is known that the size of C' with d-simplification of curve C is at most the size of C'' with $d/2$-simplification of curve C proved in [18]. So the error of ε will become smaller with the increment of k, which leads to increment of the length of $\overline{X_t X_{t+k}}$ when C is a monotone curve. In section III-A, target trajectories have been assumed as the low-frequency variation. Consequently, the curve C here is able to be viewed as the monotone curve approximatively. Then, the differences of true trajectories and estimate paths are d at least, and therefore, when C' is determined as a d-simplification of C, ε is lower than a certain upper bound at least.

Conclusion 2: the intervals of sampling time in CPF must be shorter than that of the target across the two adjacent B_j

Proof. Because PLC is to clean up overlength segments during the estimation of CPF and conclusion 1 clarifies that C' is a d-simplification of C at least, there is one particle at least in each S_i so that sampling time is must shorter the differences between t_k and t_{k+1}. The shorter sampling time, the more accurately target trajectories are estimated because of the more sampling particles.

The algorithm of PLC is described as follows:

Algorithm : PLC
1. $C' = \phi$;
2. for all $\overline{X_t}(t = 1, 2, ...)$ do $k = t + 1$
3.   if $\delta(\overline{X_t X_k}, C) > \varphi$ then $t = k$ -1 and $k = t + 1$
4. $C' \leftarrow C' \cup \overline{X_t}$;
5.   else
6. $t = t + 1$ and $k = t$;
7.   end if
8. end for

The function of $\delta(\cdot)$ denotes the error of the segment $\overline{X_t X_k}$ with respect to C under the error measure φ .

D. Sensor Nodes Fault-tolerant Models

Considering some sensor nodes invalid about their reporting of the tracking information, a fault-tolerant detection algorithm is introduced to modify their fault reporting and improve the tracking accuracy according to [13]. The fault sensor nodes are corrected by Bayesian probabilities estimation of their neighbor nodes, which could report correct binary proximity when the target moves in or out of the nodes' sensing disks. Define $E_i(a, K)$ as the output result of K neighbor nodes which make the same decision "a" around senor node i. If senor node i could be corrected as the decision "a" by K neighbor nodes, PDF is expressed:

$$P(D_i = a \mid E_i(a, K)) = \frac{K}{N} , \qquad (7)$$

where N is the number of the total neighbor nodes around senor node i.

According to Bayesian estimation, the probability that the sensor node can make a decision about whether to disregard its own sensor reading S_i in the face of the evidence $E_i(a, K)$ from its neighbor nodes is:

$$P_{aaK} = P(D_i = a \mid S_i = a, E_i(a, K)) = \frac{(1-p)K}{(1-p)K + p(N-K)} , \quad (8)$$

where p is the sensor node fault probability is uncorrected.

Let g_K be the probability that exactly K of node i's N neighbor nodes are not faulty,

$$g_K = \binom{N}{K}(1-p)^K p^{(N-K)} . \qquad (9)$$

The average number of errors after the fault-tolerant analysis:

$$\alpha = \left[\sum_{K=0}^{N} P_{aaK} g_{N-K} p + (1 - \sum_{K=0}^{N} P_{aaK} g_K)(1-p) \right] n , \qquad (10)$$

where n is total number of senor nodes in WSN.

To make the value α minimum, the threshold of probabilities Θ is defined as:

$$\Theta = \frac{(1-p)(K-1)}{2p + (K-1)} . \qquad (11)$$

The detailed proof is seen from [13, 14].

IV. SIMULATION RESULTS

The simulation tests are carried out to evaluate the performance of our algorithm of CPF-PLC. The whole algorithm is written in matlab. Our general experimental setup simulated a 150 x 150 unit field, including 25 sensors in a regular 5 x 5 grid with the distance of 24 units. The sensing radius for each sensor is set to 45 units. The number of sampling particles is 100. A similar negative spin curve is created to simulate the target trajectories. We also introduce the algorithm of Occam track [19] to compare with our algorithm. Occam track is to get the longest segments as estimate trajectories which cross the most B_j and is a pure geometric algorithm. At the same time, the probability p is set to 0.2, and each node can only communicate with its immediate neighbor node in each cardinal direction. So each node has four neighbor nodes at most when this node is located in central area of WSN.

Fig. 2(a) shows that original sensor nodes aren't modified by fault tolerant detection. The star points presented in Fig. 2(a) stand for the error nodes uncorrected from original sensor faults. However, the corrected sensor faults are shown in Fig. 2(b), where the star points with circle are not corrected nodes which are errors before detection and the dot points with circle are new errors introduced and the rest points denote correct sensor nodes. So through the detection, the sensor faults

reduce by three sensor faults from five sensor faults from Fig. 2(a), which can improve performance of the tracking.
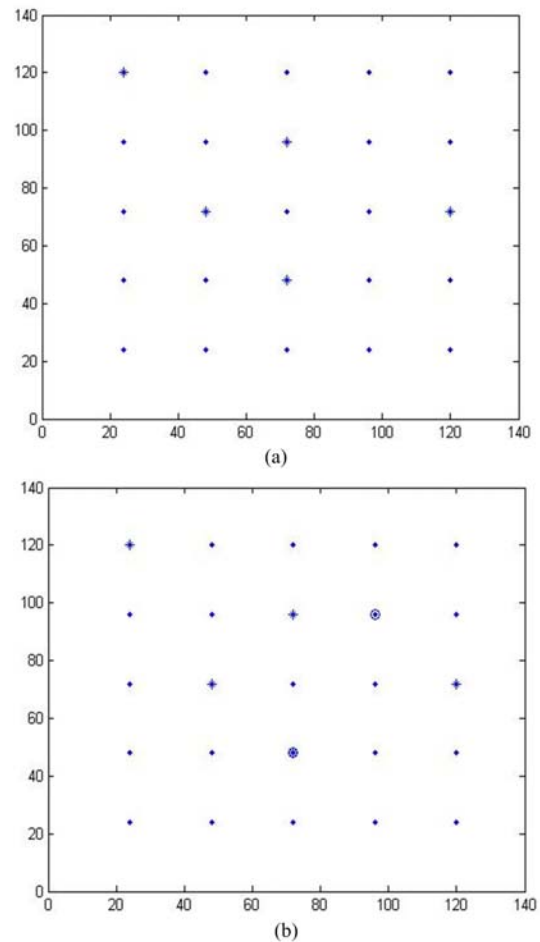

Figure 2. Compare between uncorrelated sensor faults and corrected sensor faults after fault tolerant detection

Real lines stand for the target trajectories and dotted lines present the estimate trajectories using different tracking algorithms in Fig. 3. The deployment of the sensor nodes with fault tolerant detection in Fig. 3(a) and (b) is the same as that in Fig. 2(b). The cross points with circle stand for failure nodes in Fig. 3(a) and (b). However, the sensor nodes are correct sensor nodes in Fig. 3(c) and (d). Because CPF-PLC track makes use of the particle filtering, the accuracy of estimation is higher than that in Occam track essentially. At the same time, CPF-PLC track also adopts a posterior clean up process which can reduce estimation errors in inflexion of the trajectories from the results. Average segment is about 3d through simulations. So the results from Fig. 3 shows that the performance of CPF-PLC is well on solving some special trajectories and could obtain a better approximation on target tracking. At the same, the tracking accuracy of Fig. 3(a) and (b) with fault tolerant are less than that of Fig. 3(c) and (d) without fault tolerant (namely without sensor faults) respectively. The reason is obviously that the error sensor nodes affect the performance of the tracking. Hence, if we want to improve the accuracy of the tracking, the measure to be taken is that more correct and effective sensor nodes are

deployed in around of the error nodes so that the applications about WSN can't be affected by sensor faults.
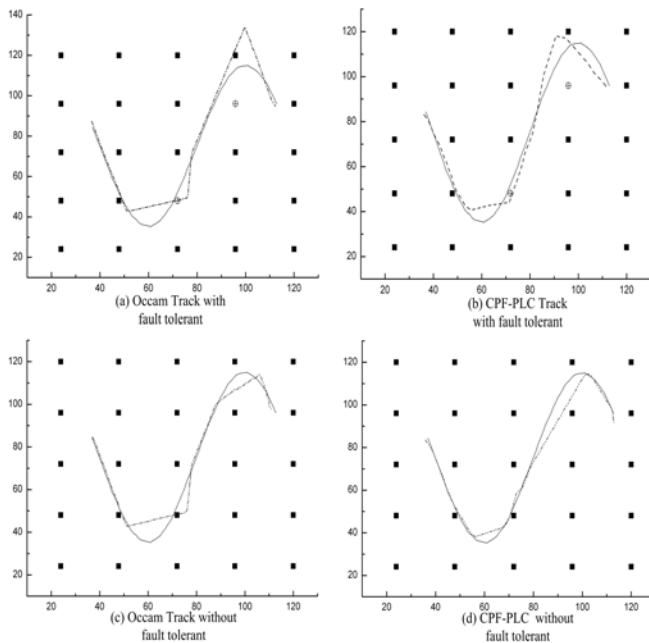

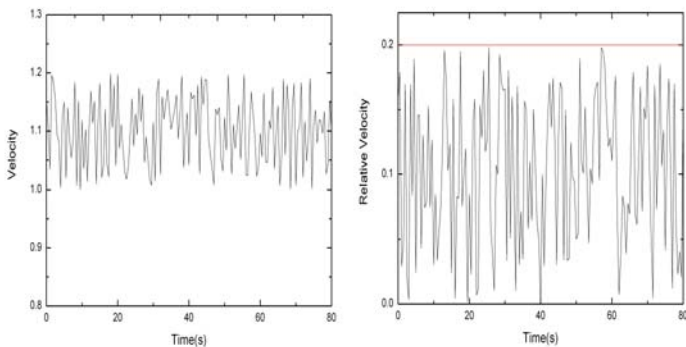Figure 3. Compare between two tracking algorithms with or without fault tolerant

Figure 4. Velocity estimation by CPF-PLC

In Fig. 4, the velocity is estimated by CPF-PLC track without fault tolerant. The results shows that the velocity is kept approximate value 1.1 unites to wing fluctuation and the relative velocity is lower than the value 0.2 unites, which means that the velocity estimate error ε is about 20%. Then the results from figure 3 show that average segment is about $3d$. These data represent that our algorithm keeps a good performance according to collusion 1 and this algorithm presents the robust estimation.

V. CONCLUSION

In this paper, we present two sub-algorithms for target tracking so that they become an effective and accurate estimation about the trajectories and velocity. Hence, CPF-PLC is designed to achieve this aim and avoids that estimate trajectories across B_j is out of pre-ordained

order, while this situation might appear in occam track of [19]. Particle filters can present large number of robust samples, so it is able to estimate the better trajectories. Then a near-linear curve approach is used to simplify and easily describe target trajectories under a certain error so that the velocity estimate error ε is given the upper bound at least. The simulation results prove our conclusions.

REFERENCES

[1] Y. Rauan, P. Willett, A. Marrs, F. Palmieri and S. Marano, "Practical fusion of quantized measurements via particle filtering," *IEEE Transactions on Aerospace and Electronic Systems*, Vol.44, No.1, pp15-29, 2008.
[2] X.Gao, Y.T.Yang and D.Zhou, "Coverage of communication-based sensor nodes deployed location and energy efficient clustering algorithm in WSN," *Journal of Systems Engineering and Electronics*, Vol.21, No.4, pp 698-704, Aug.2010.
[3] M.I. Ribeiro, "Kalman and Extended Kalman Filters: Concept, Derivation and Properties," http://users.isr.ist.utl.pt/~mir/pub/kalman.pdf, 2004.
[4] N.J. Gordon, D.J. Salmond and A.F.M. Smith, "Novel approach to nonlinear/non-Gaussian Bayesian state estimation," *IEE Proceedings of Radar and Signal Processing*, Vol.140, No.2, pp 107-113, Apr.1993.
[5] Z. Yan, B.Y. Zheng, L.Xu and S.T. Li, "Collaborative tracking via particle filter in wireless sensor networks," *Journal of Electronics (China)*, Vol.25, No.3, pp 311-318, May 2008.
[6] L. Mihaylova, D. Angelova, D.R. Bull and C.N. Canagarajah, "Localization of Mobile Nodes in Wireless Networks with Correlated in Time Measurement Noise," *IEEE Transactions on Mobile Computing*, Vol.10, No.1, pp 44-53, 2010.
[7] J. Madapura and B. Li, "Multi-target tracking based on KLD mixture particle filter with radial basis function support," *IEEE International Conference on Acoustics, Speech and Signal Processing*, pp 725-728, 2008.
[8] C. Meesookho, S. Narayanan and C.S. Raghavendra, "Collaborative classification applications in sensor networks," *In Proceedings of the Workshop on Sensor Array and Multichannel Signal Processing*, pp 370-374, 2002.
[9] M.F. Bugallo, J. Miguez and P.M. Djuric, "Positioning by Cost Reference Particle Filters: Study of Various Implementations," *The International Conference on Computer as a Tool, 2005. EUROCON 2005*, pp 1610-1613.
[10] P.M. Djuric, M. Vemula and M.F. Bugallo, "Target Tracking by Particle Filtering in Binary Sensor Networks," *IEEE Transactions on Signal Processing*, Vol.56, No.6, pp 2229-2238, 2008.
[11] P. Agarwal and M. Sharir, Handbook of Computational Geometry, Netherlands: J.-R. Sack and J. Urrutia, 2000.
[12] J. Aslam, Z. Butler, F. Constantin, V. Crespi, G. Cybenko and D. Rus, "Tracking a moving object with a binary

sensor network," *Proceedings of ACM SenSys*, pp 150-161, 2003.

[13] B. Krishnamachari and S. Iyengar, "Distributed Bayesian algorithms for fault-tolerant event region detection in wireless sensor networks," *IEEE Transactions on Computers*, Vol.53, No.3, pp 241-250 2004.

[14] C. Qingchun, L. Kam and F. Pingzhi, "Comments on "Distributed Bayesian algorithms for fault-tolerant event region detection in wireless sensor networks," *IEEE Transactions on Computers*, Vol.54, No.9, pp 1182-1183, 2005.

[15] Y.T. Yang, X. Gao, C.C. Chai and J.X. Zhang, "Novel Dynamic Routing Algorithm for Energy Optimization in WSN," *Journal of Xidian University*, Vol.37, No.5, 777-782, Oct. 2010.

[16] B. Krishnamachari and S. Iyengar, "Distributed Bayesian algorithms for fault-tolerant event region detection in wireless sensor networks," *IEEE Transactions on Computers*, Vol.53, No. 3, 241-250, 2004.

[17] B. Ristic, S. Arulampalam and N. Gordon, *Beyond the Kalman Filter: Particle Filters for Tracking Applications*, Boston : Artech House, 2004.

[18] P.K. Agarwal, S. Har-Peled, N.H. Mustafa and Y.S. Wang, "Near-Linear Time Approximation Algorithms for Curve Simplification," *Algorithmica*, Vol.42, No.3-4, pp 203-219, 2005.

[19] N. Shrivastava, R. Mudumbai, U. Madhow and S. Suri, "Target tracking with binary proximity sensors," *ACM Transactions on Sensor Networks*, Vol. 5, No. 4, pp 30:1-30:33, 2009.

Xiang Gao wsa born in Jiangsu province in 1982. He received B.S. degree from Nanjing Normal University in 2004,and received Ph.D.degree in Microelectronics and Solid State Electronics at Xidian University, Xi'an China, in 2011. His current research interests include Wireless Sensor Networks, Target Tracking and Network on Chip System.

Yintang Yang received his B.S. and M.S. degrees in Microelectronics and Solid State Electronics at Xidian University, Xi'an, China in 1982 and 1984, respectively, and received the Ph.D. degree at Xi'an Jiaotong University in 1999.

He is currently a Professor and Ph. D supervisor with School of Microelectronics. His research interests include VLSI technology, new semiconductor materials and devices, microelectronics reliability technology and network-on-chip.

Duan Zhou received her Ph.D. degree in Computer Application Technology from School of Computer Science and Technology, Xidian University, Xi'an, China in 2009.

She is currently a Processor with School of Computer Science and Technology of Xidian University. Her research focuses on embedded system, computer control, design of integrate circuit and globally asynchronous locally synchronous (GASL) circuits.

Jianxian Zhang received his B.S. and M.S. degrees in computer science and technology at Xidian University, Xi'an, China in 2005 and 2008, respectively. He is currently working toward the Ph.D. degree in Microelectronics and Solid State Electronics in School of Microelectronics, Xidian University, Xi'an, China.

His research focuses on communication-centric design methodologies for large-scale system on chip, with emphasis on modeling, analysis, and energy optimization for network-on-chip architectures.

Changchun Chai received his his B.S. degree in Semiconductor Device and Physics at Tsinghua University and M.S. degree in Semiconductor Physics and Device at Xidian University in 1983 and 1990, respectively, and received the Ph.D. degree in Microelectronics and Solid State Electronics at Xidian University in 1999.

He is currently a Professor and Ph. D supervisor with School of Microelectronics. His research interests include VLSI technology, new semiconductor materials and devices, microelectronics reliability technology.

Design of Wireless Sensor Network-Based Greenhouse Environment Monitoring and Automatic Control System

Yongxian Song

School of Electronic Engineering, Huaihai Institute of Technology, Lianyungang, China
Email: soyox@126.com

Juanli Ma, Xianjin Zhang and Yuan Feng

School of Electronic Engineering, Huaihai Institute of Technology, Lianyungang, China
Email: soyox@163.com

Abstract—In view of the characteristics of greenhouse environment monitoring system, a system scheme based on wireless sensor network (WSN) is presented, which adopts Atmega128L chip and CC2530 that is a low power RF chip from TI to design the sink node and sensor nodes in the WSN. The monitoring and management center can control the temperature and humidity of the greenhouse, measure the carbon dioxide content, and collect the information about intensity of illumination, and so on. And the system adopts multilevel energy memory. It combines energy management with energy transfer, which makes the energy collected by solar energy batteries be used reasonably. Therefore, the self-managing energy supply system is established. In addition, the nodes deployment method and time synchronization problem are analyzed in detail. The system can solve the problem of complex cabling with the advantages of low power consumption, low cost, good robustness, extended flexible and high reliability. An effective tool is provided for monitoring and analysis decision-making of the greenhouse environment.

Index Terms—wireless sensor networks, AVR single chip microcomputer, greenhouse, time synchronization, nodes deployment

I. INTRODUCTION

The greenhouse agriculture is developing very fast with the increasing demand of fresh vegetables in the large and medium cities. It is a kind of place in which it can change the plant growth environment, create optimum condition for plant growth, and keep out of the environment changes and the influence of atrocious weather [5-6]. On the basis of making full use of natural resources, greenhouse monitoring system obtain the optimum condition of plant growth by changing the factors of greenhouse environment such as temperature, humidity, intensity of illumination, carbon dioxide content and so on, and the purpose is to increase crop yield, improve its quality, regulate growth cycle, improve economic benefit. Greenhouse monitoring system is a complex system, the different kinds of parameter in the greenhouse needs automatic monitoring, information processing, real-time control and on-line optimizing.

In recent years, the greenhouse industry has got greater progress, and improved agricultural labor productivity. However, we have quite big difference with developed country in control system area. On the one hand, the introduction costs of foreign advanced control system are too high, and most of them are not suitable for the national conditions of our country; on the other hand, The vast majority of existing control technology and equipment are backward in the domestic, equipment types is too simple, environmental regulation is limited, and it is difficult to popularize application. Therefore, the greenhouse control system that adapt to the development of China's greenhouse production would be developed [20-21].

At present, the greenhouse cable monitoring system is relatively mature, the network topology structure evolved from that of centralized to that of distributed, for example, RS485 based measurement and control system is a centralized structure and Field-bus (CAN BUS, PROFIBUS, LONWORKS, and so on) based measurement and control system is a distributed structure. Although the system's functions are more and more decentralized and the system has more and more distance [18-20], the most of greenhouse data acquisition systems adopt the wired collection way which is factitious or prewired. The workload is increased and real-time and validity of the data cannot be guaranteed by means of artificial. The monitoring control system which adopts the wired collection way is influenced by geographic position, physical circuit and complex environment and it is bounded clearly. With the appearance of low cost, low power dissipation sensor and the development of wireless communications technical, it is time to construct wireless greenhouse monitoring system, this will have great real-significance to realize agricultural modernization [2-4]. According to the requirement of collecting greenhouse environmental message quickly and accurately, this paper explores deeply at some aspects, such as greenhouse

environmental message collection, dispose, transmission, release and so on, and the greenhouse monitoring system based on WSN is introduced. Lots of the Sensor Nodes are deployed randomly in the monitoring area, the tiny Sensor Nodes which have the ability of wireless communication and data-handling constitutes the distributed intelligence monitoring net which can complete the appointed mission by self-organization network, and use the synergic way to achieve perception, collection and handle the environmental message covered by the net, then use the multi-hop way to transfer the detecting data from Sensor Node to Management Node by Sink Node link. Contrarily, by means of Management Node, user could proceed to deploy and supervise, publish and monitor assignment, collect monitoring data for WSN [1]. This system has high practical value to realize information and automation of large-scale greenhouse monitoring and improve work efficiency.

II. THE OVERALL STRUCTURE OF THE SYSTEM

The greenhouse environment monitoring system based on WSN includes monitoring centre, sensor nodes and control equipments. Sensor nodes are deployed in greenhouse wherever, and preside periodic collection greenhouse environmental message and transmit to control centre, it is constituted by Sink Node, Relay Node and Sensor Node. These data are handled and analyzed when control centre gains, then relevant decisions are made and send control message to greenhouse control equipment, which regulate greenhouse environment parameters to obtain best growth environment for crops. Modern greenhouse has very large size, and which adopt hierarchical system structure. Supposed that greenhouse is rectangular area, the measurement system overall structure is shown in Fig.1.

The greenhouse was divided into several same area of greenhouse, each measurement and control area is managed by a base station, and is divided into many virtual grids and is non-overlapping. A number of sensor nodes are deployed in virtual grid and make a cluster, each cluster includes a cluster head (sink node) and some cluster member nodes. Cluster head generated from the member nodes through cluster head election algorithm, and cluster member nodes compose of sensor nodes which can collect environmental data and control nodes which can control actuators and adjust environmental parameters. Control node does not participate in cluster head election, it obtain command which the monitoring center send from cluster head node and execute corresponding control operation. The star network composed of Cluster head nodes, sensor nodes and control nodes, it mainly complete data acquisition and control of greenhouse environment. The data which is collected is transmitted directly from sensor nodes to cluster head, the cluster nodes transferred data to the base station by way of multiple hops, at last, the base station transferred each cluster head node data which is packaged to the monitoring center. Base station is relay station between the monitoring center and greenhouse WSN nodes, the network control is realized by managing all the

nodes of single greenhouse measurement and control area. The monitoring center is not only total console of more greenhouse network, but also data center of measurement and control system of the greenhouse network , and take charge of control and management of the entire system.
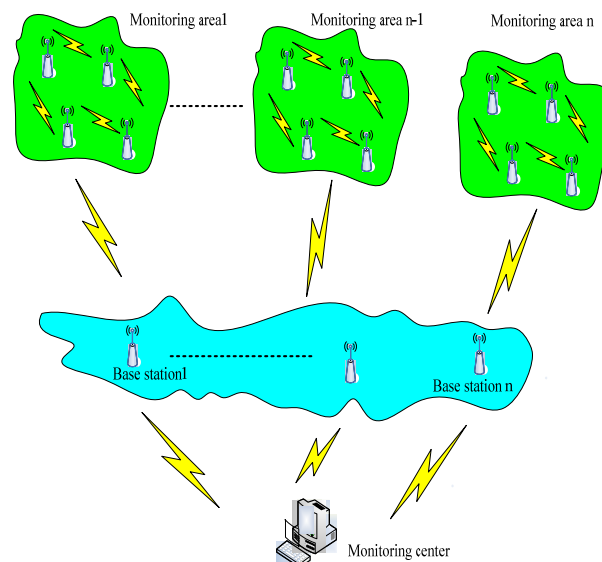

Figure.1The system structure of Greenhouse WSN measurement and control

III. GREENHOUSE WIRELESS SENSOR NETWORK NODES DESIGN

Sensor network nodes are objects which are deployed in study areas of WSN, in order to collect and forward information, and accomplish specified task. Therefore, every Sensor Node has not only collect and process data, but also the function of wireless communication. Greenhouse wireless sensor network monitoring system consists of two types of nodes, sensor nodes and sink nodes. Sensor nodes consist of processor module, wireless communication module, power supply module, sensor module and position setting switch which set physical location information of itself. Sink nodes consists of processor module, wireless communication module, continuous power supply module and serial interface communication module.

A. Sensor node module design

Sensor nodes mostly make up of processor module, wireless communication module, sensor module, switch of position setting and energy supply module. Its structure is shown in Fig.2. Sensor module is in charge of information collection and data conversion in monitoring area, according to the application requirements, it can select temperature sensor, humidity sensor, light sensor, carbon dioxide concentration sensor and so on. Processor module takes charge of controlling the operation of all the sensor nodes, storing and disposing the collection data of the node or forwarded by other nodes; Wireless communication module is responsible for wireless communication, exchanging control information and

transceiver acquisition data between this node and other nodes. Position setting switch is used to set a sensor node specific physical location in greenhouses. Energy supply module can provide energy which the work need for sensor node, in the paper, we adopt solar self-supply module for node power supply.
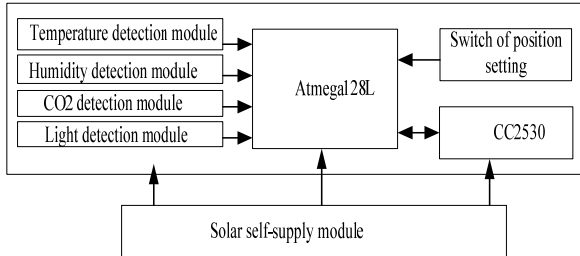

Figure.2   Sensor node structure chart

B.   Sink node module design

Sink node mainly complete the sensor nodes data gathering and fusion within communication network, and realize ascending and descending communication protocol conversion. It released monitoring task of management nodes, and the data collected is forwarded to the external network through a serial port. It is not only an enhanced sensor node, but also special gateway device which hasn't monitoring function and only has wireless communication interface. Its structure is shown in Fig.3. It consists of power system, memory module, processor module, node communication module, serial interface communication module and so on. Because sink nodes need to handle a lot of data of sensor nodes, and have longer work time and shorter sleep time, energy of battery cannot enough to energy consumption of sink node, therefore, the project of solar power self-powered module of sink nodes is adopted in the paper.
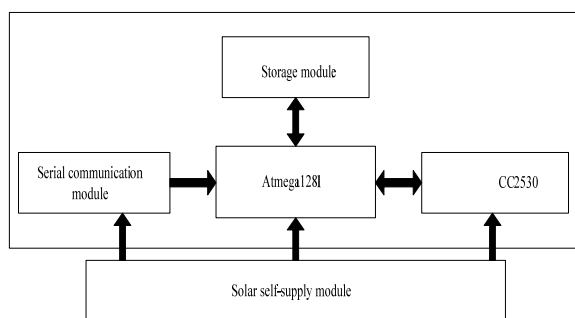

Figure.3. Sink node structure chart

C.   Solar power collection and energy management module

In order to solve the problem of energy supply of sensor nodes, we adopted solar energy supply system in the paper, and the structure is shown in Fig. 4. Fig.4 show that power supply module have energy collector, energy storage, backup energy memory, power management and control section. Energy collector consists of solar panels, and is responsible for transforming the solar energy into electrical energy; energy storage includes the main level

of energy stored, consists of super-capacitor, it is responsible for storing the collected solar energy and supply power for wireless sensor nodes; back-up energy memory formed by a lithium battery, in the practical application, Lithium-polymer battery is adopted to supply power in the long absence of light or in case of emergency for the system; power management and control section are responsible for monitoring the primary and secondary energy memory and energy state of back-up energy memory, according to state, energy memory is used to supply for the system and control solar energy to add energy for itself. In this system, the polymer lithium battery capacity is 300mA.h, in practical applications, according to actual situation, chose adequate capacity battery [11]. Power supply performance test that sensor nodes continuously work for 1d is shown in Fig.5.
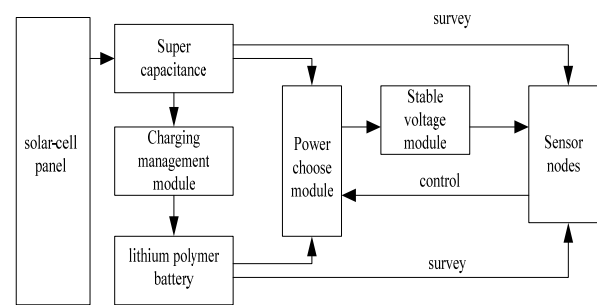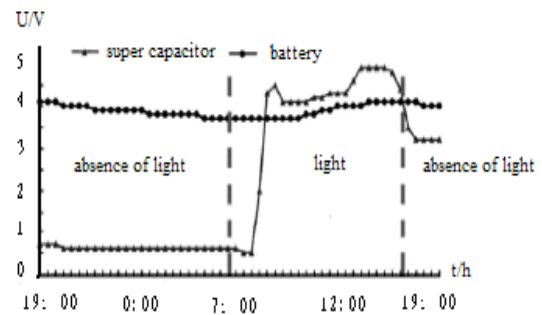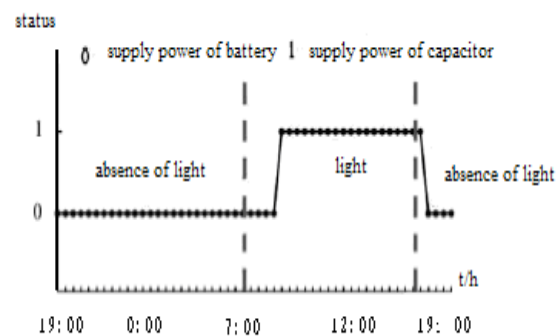

Figure.4. Solar self-supply module structure

(a) The voltage curve of super-capacitors and polymer lithium battery

(b) Power supply switch

Figure.5 Power supply test of sensor node

IV. SYSTEM SOFTWARE DESIGN

A. Software Design

Modular design thought is adopted in system software program which mainly composed of data collection system of the greenhouse and wireless control systems. The data acquisition system uses wireless sensor nodes to collect information of the surroundings, and transfer data to the sink node by means of combining the wireless network; then sink nodes sent the data which are fused to the controller; in the same time, the sink node receives instructions from controller, and forwards the command to the sensor node again. The workflow of system software is shown in Fig.6.
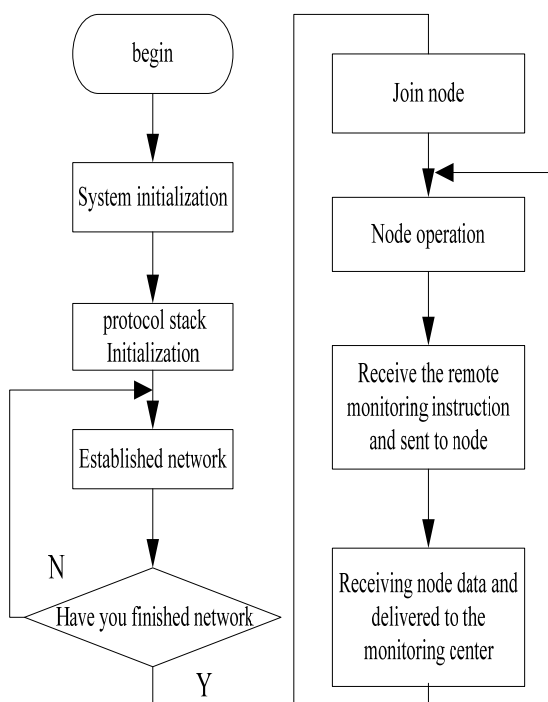

Figure.6 System software flowchart

B. Problem of nodes deployment

Integration of sensor technology, data processing and communications technologies such as wireless sensor networks has been great attention by all researchers, it also is moving node intelligence, miniaturization and large-scale network of direction, but as a distributed system, the support of a reasonable node deployment and time synchronization is very necessary. In a distributed system, different Sensor Node has its own local clock, temperature changes and the different environment will make the node clock frequency drift. Even if each node achieves time synchronization at a time, after it has longer work hours, due to frequency drift, the node will accumulate a certain clock skew, and it is inconsistent with the clock of reference node. Therefore it needs to have a good time synchronization mechanism to ensure clock synchronization between each node and the reference nodes. Especially in sensor networks, time division multiple access (TDMA) and multi-node data fusion technology all need a good time synchronization mechanism.

1. Cluster network formation

Existing WSN clustering algorithm, LEACH is a clustering algorithm which is more mature and commonly used [12], but it is the uniform clustering, some nodes of the low energy at the edge region may also be selected as cluster head, at this time their energy will soon be exhausted, and bring about that the network can not function properly, so this paper adopt non-uniform cluster head election algorithm based on LEACH to form a cluster structure of the network.

2. Cluster head selection

A fully distributed mechanism is adopted, the sensor's working process is divided into periodic rounds, each round consists of two stages, that is, cluster the establishment phase and stable phase. Algorithm can guarantee that have bigger probability to take node which has a large residual energy as the cluster head, and it extends the network lifetime. Suppose that threshold is $T(n)$, and nodes generate a random number between 0 and 1, if $T(n)$ is smaller than the random number, it is the cluster head node of current round. The settings of $T(n)$ are as follows.

$$T(n) = \begin{cases} \lambda \cdot \dfrac{q}{1-q\left(r \bmod (1/q)\right)}, n \in G \\ 0 \qquad\qquad\qquad\qquad, else \end{cases},$$

$$\lambda = \frac{E\_node}{E_0}$$

Where, and E_node are the energy of the current node; E_0 is the node's initial energy; q is the percentage of cluster head node desired of all nodes; r is the current round number; G is the nodes muster which do not become a cluster head nodes in the final $1/q$ round.

3. Cluster formation

After cluster head is chosen, the network is organized into the breadth-first spanning tree topology, and the root node is based on time reference node. Each node has a jump distance variable level which arrive the time reference node, the level value of the only time reference node is 0, other nodes are infinite. According to the following two steps to establish topology: the first step, the time reference node sends packets of topology establishment, if the node received is the cluster head node, then the level is set to 1, otherwise, do not respond. The second step, the cluster head node sends packets of topology establishment to the ordinary node, for the node receiving packets of i layer, first, i is compared with itself level, if i is less than the level, their level will be set $i+1$, otherwise, it is discarded. The process is repeated until all nodes have been given the appropriate level. It is worth noting that if an ordinary node receives

more than one nodes group, and it grade equals to its parent nodes, then compared with their power level, and selected the strongest power node as its parent node. After cluster head selection is completed and breadth-first spanning tree topology is established, the network is divided into multiple clusters and each cluster consists of a number of cluster member nodes and a cluster head.

C. Synchronization algorithm design

Considering the sources of the time synchronization error in the wireless sensor network, and in order to solve the problems that have large amount of information in general method of synchronization, a method based on an exchange of information is proposed, and maintain the entire cluster node synchronous by compensating each node for the cluster head node. After the cluster head nodes complete the synchronization in pairs to nodes in cluster, and time synchronization accuracy is maintained by making the cluster head node estimate the time to offset of each node. The system mainly analyzes the node synchronization process in the cluster, and takes the cluster head node as the third party node, that is, the synchronization for other nodes is completed by the cluster head node. In each synchronization cycle, synchronization process will be divided into two phases, the first stage is parameter estimation, it need to complete two tasks, namely, the initial synchronization of the node and the necessary parameters are estimated and stored by an exchange of information. The second stage is the time maintenance phase, after the initial synchronization is completed, the time clock of nodes in cluster is compensated regular or irregularly though the cluster head node. Compensation procedure is as follows.

(1) Complete time synchronization in pairs between each node in cluster and the cluster head node.

(2) The cluster head nodes send synchronization messages to each node.

(3) The cluster head node synchronization message is received by each node, each node sends the estimated values of the frequency offset to the cluster head, and send the local time at the same time.

(4) The cluster head nodes receive the message, and fill out the "time synchronization table."

(5) The cluster heads periodically calculate the time offset, and send to each node, each node corrects the time after receiving.

(6) Complete a synchronization cycle and repeat steps 1 to 5.

V. EXPERIMENT AND SIMULATION

A. Experimental verification

The nodes that we use are shown in Figure 7, the sensor nodes are placed in the greenhouse environment, in experiment, we selected three common nodes and a gateway node. Three common nodes are connected with the sensors, respectively. The gateway node is connected with computer together through the serial port.
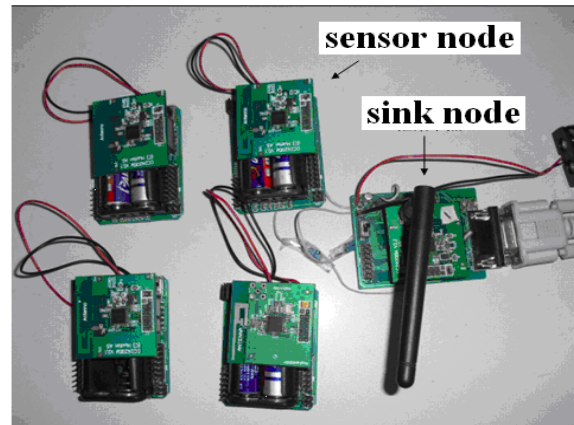

Figure.7 Physical map

In the system, we validates the feasibility of the system through data collection, and selects three nodes to make the data acquisition test of the 10 default temperature, set temperature is 8, 11, 12, 15, 18, 22, 23, 25, 27, 30, respectively, the test temperature data of each node is shown in Fig.8. By analyzing the measured temperature data, it shows that each sensor node respond better to temperature changes, and the sensor nodes only have some original error. The changes of humidity can be measured by the same method. The right collecting and transmitting of temperature and humidity data shows that the system is reliable and feasible.
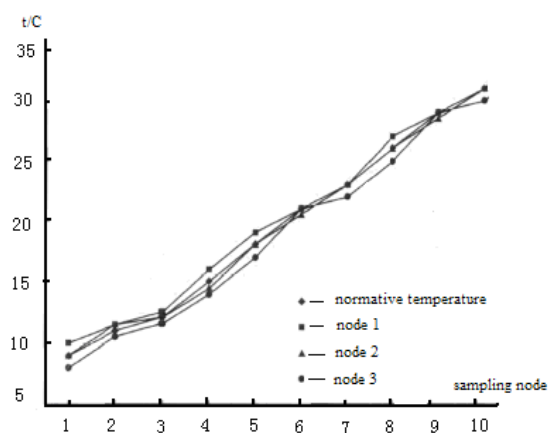

Figure.8 The test pattern of node temperature data

B. The simulation results and analysis

The synchronization algorithm that was proposed in the paper is evaluated by simulation tool NS2. First, the configuration of NS2 is as follows: Double diameter ground propagation model, gain omnidirectional antenna model, IEEE802.15.4MAC layer protocol and so on, and the module such as communication energy, the packet type, MAC timestamp type and track type and so on are modified, and Compared with TSPN algorithm, Set up the simulation environment to be the 50m×50m square area, we deployed 100, 120, 140, 160, 180, 200, 220, 240, 260 nodes, respectively, and the wireless communication distance is set as 10 m, the algorithm in the paper and TPSN algorithm are simulated respectively. The entire

network adopt clustering algorithm to cluster. The simulation results are shown in Fig.9. Fig.9 show that the proposed algorithm requires much less synchronization overhead than TPSN, mainly because the cluster head node requires only one exchange of information in a synchronous cycle, thus it reduces overhead, the advantage is more obvious when the nodes are more.
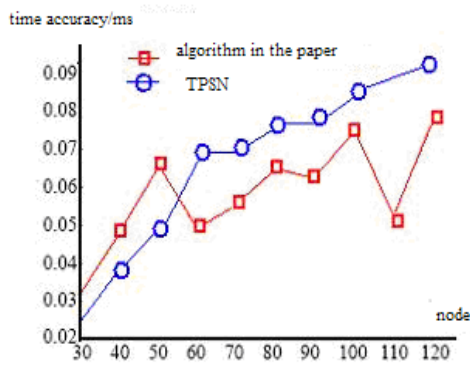

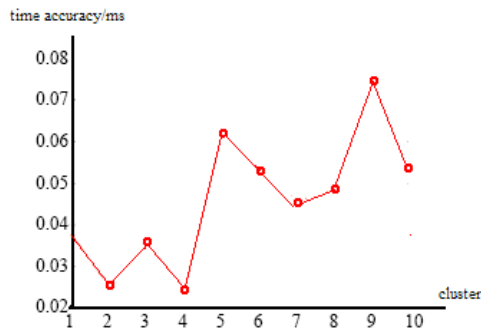Figure 10 Compared with TPSN time accuracy chart

Figure.11 The average synchronization accuracy of each cluster

VI.   CONCLUSION

According to the characteristics of the modern greenhouse production, the wireless sensor networks is applied to greenhouse measurement and control system in the paper, and combine wireless sensor network technology and greenhouse control technology to achieve automatic adjustment of the entire greenhouse system. In the hardware side, the wireless sensor network nodes mainly consist of control chip Atmega128L and wireless transceiver chip CC2530. In the software side, modular design thought is adopted, the deployment of sensor nodes is in-depth analyzed, and proposed a synchronization method based on time error compensation, achieved the synchronization in a certain error range by the few exchange of information. The synchronization efficiency are greatly improved, the node energy overhead is reduced. However, because the frequency deviation is estimated by the node, the time accuracy will be influenced by the frequency offset estimation, and the frequency offset estimate is researched the next step. From the simulation results, it can be seen that the algorithm is better than TPSN in

energy costs and synchronization accuracy, so the system has a very good value.

REFERENCES

[1]   Wang Zhu, Wang Qi ,Hao Xiaoqiang. The Design of the Remote Water Quality Monitoring System based on WSN[C]. The 5th International Conference on W ireless Communications, Networking and Mobile Computing 2009, 1-4.
[2]   Du Xiaoming, Chen Yan.The Realization of Greenhouse Controlling System Based on Wireless Sensor Network[J].JOURNAL OF AGRICULTURAL MECHANIZATION RESEARCH, 2009(6): 141-144.
[3]   Qiao Xiaojun, Zhang Xin, Wang Cheng, et al. Application of the wireless sensor networks in agriculture[J], Transactions of the CSAE,2005, 9(21):232-234.
[4]   S.L. Speetjens, H.J.J. Janssen, etc. Methodic design of a measurement and control system for climate control in horticulture[J]. COMPUTERS AND ELECTRONICS IN AGRICULTURE, 2008, (64):162-172.
[5]   Wang Linji.The Design of Realizing Change Temperature Control in Greenhouse by PLC [J].ELECTRICAL ENGINEERING, 2008, 5：81-83.
[6]   Liu Yanzheng, Teng Guanghui, Liu Shirong.The problem of the control system for Greenhouse Climate[J].CHINESE AGRICULTURAL SCIENCE BULLETIN. 2007,23：154-157.
[7]   C. Y. Wan, S. B. Eisenman, A. T. Campbell, et al. Overload traffic management for sensor networks[J]. ACM Transactions on Sensor Networks, 2007, 3, Article No. 18 .
[8]   G. S. Ahn, E. Miluzzo, A. T. Campbell, et al. Funneling-MAC: A Localized, Sink-Oriented MAC For Boosting Fidelity in Sensor Networks[C]. Proceedings of the 4th international conference on Embedded networked sensor systems. New York: ACM, 2006: 293-306.
[9]   Li Nan, Liu Chengliang, Li Yanming, Zhang Jiabao, Zhu Anning. Development of remote monitoring system for soil moisture based on 3S technology alliance[J]. Transactions of the CSAE，2010，26（4）: 169-173.
[10]   Wang Zhu, Wei Debao, Wang Ling. Design of Greenhouse Temperature and Humidity Monitoring System Based on WSN[J]. Instrument Technique and sensor. 2010(10): 45-48.
[11]   Li Nan, Liu Chengliang,Li Yanming, et al. Development of remote monitoring system for soil moisture based on 3S technology alliance[J]. Transactions of the CSAE, 2010, 26(4): 169-174.
[12]   W.B. Heinzelman, A.P. Chandrakasan, H. Balakrishnan. An Application Specific Protocol Architecture for Wireless Micro-sensor Networks [J]. IEEE Transaction on Wireless Communications, 2002, (10): 660-670.
[13]   Liu Lijuan, Wang Xu. Time-Offset Compensation Based Time Synchronization Approach for Wireless Sensor Network[J]. Chinese Journal of Spectroscopy Laboratory, 2011, 1(28): 41-45.
[14]   J.H. Tarng, B.W. Chuang, PC. Liu. A relay node deployment method for disconnected wireless sensor networks:Applied in indoor environments[J]. Journal of Network and Computer Applicatons. 2009.32:652-659.

[15] Y.C. Wang, Y.C. Tseng. Distributed Deployment Schemes for Mobile Wireless Sensor Networks to Ensure Multilevel Coverage[J]. IEEE TRANSACTIONS ON PARALLEL AND DISTRIBUTED SYSTEMS. 2008.19(9):1280-1294.

[16] P. Gajbhive, A. Mahajan. A Survey of Architecture and Node deployment in Wireless Sensor Network[C]. 1st International Conference on the Applications of Digital Information and Web Technologies, ICADIWT 2008: 426-430.

[17] W.T. Xu, X.H. Hao, C.L. Dang. Connectivity Probability Based on Star Type Deployment Strategy for Wireless Sensor Networks[C].Proceedings of the 7th World Congress on Intelligent Control and Automation. 2008:1738-1742.

[18] Wu FeiQing, LiBin Zhang, Fang Xu, et al. Design of a control system for glass greenhouses based on the CAN-bus[C]. Proceedings of the 4th International Symposium on Precision Mechanical Measurements, 2008.

[19] Pérez IG,AJ Calderón Godoy. Greenhouse automation with programmable controller and decentralized periphery via field bus[C]. Proceedings of the IEEE 2009 International Conference on Mechatronics, 2009.

[20] Yu Guoqing, Zhanyou Sha,Mingwei Cai. Agricultural environment information monitoring instruments based on integrated intelligent sensors[C]. Proceedings of the Remote Sensing and Geoscience for Agricultural Engineering, 2009.

[21] Fitz-Rodríguez E, C Kubota, GA Giacomelli, et al. Dynamic modeling and simulation of greenhouse environments under several scenarios: A web-based application[J].Computers and Electronics in Agriculture, 2010, 70(1):105~116.

[22] Kolokotsa D., G. Saridakis, K. Dalamagkidis, et al. Development of an intelligent indoor environment and energy management system for greenhouses[J].Energy Conversion and Management, 2010:155~168.

Yongxian Song was born in xuzhou,on April 1,1975. He r eceived the B.S. degree in Applied Electronic Technology from Hu aihai Institute of Technology, Lianyungang,China, in 1997, and the M.S degree in Control Theory and Control Engineering from Jiangsu university, Zhenjiang, China , in 2006. From 2009 to now, He is studing for Ph.D degree in Control Theory and Control Engineering from Jiangsu university, Zhenjiang, China. Since 2006, he has beeen a teacher in Huaihai Institute of Technology, Lianyungang,China. His current research interests include signal processing ,intelligent control, and industrial control .

Juanli Ma female, lecturer, born in 1976, 1995-1999 studied at Gansu University of Technology, studying electrical automation, and obtained a bachelor degree. 2004-2007 studied at the Northwestern Polytechnical University, studying control theory and control engineering and obtained a Master degree in Engineering. From1999 to now, she has been working in the Huaihai Institute of Technology.

Xianjin Zhang was born in suqian, in1975. He received the B.S. degree in Applied Electronic Technology from Guilin University of Electronic Techonlogy, Guilin, China, in 1998, and the M.S degree in Power Electronic and Control Engineering from Nanjing University of Aeronautics & Astronautics, Nanjing, China, in 2005. Since 2005, he has been a teacher in Huaihai Institute of Technology, Lianyungang,China. His current research interests include electric and electronical converting technique.

Yuan Feng. was born in lianyungang ,on March 28,1978. He received the B.S. degree in Computer hardware and application from Huaihai Institute of Technology, Lianyungang, China, in 1999. and the M.S degree in Industrial Control from Nanjing University of Science, Nanjing, China, in 2007. From 1999 to now, he has beeen a teacher in Huaihai Institute of Technology, Lianyungang,China. His current research interests include signal processing, Computer Control Technology.

A Research on HCCA Mechanism of Wireless LAN Access

Hua Liang
Hunan International Economics University, Chang sha , China
e-mail: hualianglc@qq. com

Feng Zeng
School of Software, Central South University, Changsha, China
e-mail: fengzeng@csu.edu.cn

Abstract—**Analyzed the quality of service (Qos) scheduling mechanism of IEEE802. 11e, discussed the simple scheduling algorithm (Simple Scheduler) and its deficiencies exist in supporting variable bit-rate service (VBR). And then proposed a improved algorithm which adapts to the real time VBR service. The algorithm can dynamically adjust the service interval and the TXOP of per flow. Finally, implement the algorithm on NS2. Compared with the HCCA, simulation results show that our mechanism effectively improved the delay and transmission efficiency.**

*Index Terms*一**wlan; service interval; duration**

I. INTRODUCTION

Wireless LAN (WLAN) technology provides a simple, flexible deployment solution, and it's gradually being used as access points in the report hall, offices, schools. However, with the increasing application of multimedia services (voice, streaming audio / video, telephone conferencing, Internet gaming), these applications require a certain foundation of quality of service (Qos).

The TXOP method which is proposed in IEEE 802. 11e HCCA sample scheduler [1] can only apply to CBR type of business, instead of VBR. So there are many literatures exploring ways to improve the HCCA VBR type of business that can be transmitted in the HCCA mode. The authors in [2] propose a method that uses TSPEC delay in the delay bound limit parameter to set the token rate and bucket size of the final size and then estimates the parameters of Queue Size Each SI TXOP assigned to the number of workstations to reduce the packet loss rate. References [3, 4, 5] propose to use the Queue Size of the IEEE 802. 11e MAC Header to estimate the next TXOP number assigned by the SI to workstations, furthermore, the TXOP will assign duration time according to the actual traffic generated by each SI work station. Reference [9] proposes PRBAC admission control algorithm, making use of the so-called long-term average real rate as the improved basis to control admission parameters, use the instantaneous actual rate to calculate the TXOP time assigned to each site, which is more accurate to the actual situation.

According to the analysis above, this paper combines the advantages of the methods proposed in references [3, 4, 5], and proposes an algorithm based on twice allocation. It uses a more efficient way to dynamically allocate transmission time in service cycle; besides, TXOP duration time is assigned based on the true traffic in each station. Through this method, when the traffic load is relatively light, the sites are able to increase the Qos by increase TXOP duration time; When the traffic is over loaded, each station can respond quickly. We give a brief introduction on the mechanism of HCCA in the IEEE802. 1le and analyze the HCCA execution and the calculating method. According to the disadvantage listed in references [3] [4] [5], we design an effective traffic Scheduler, which allocates the network resources according to the actual traffic load on each site, the allocation method is dynamic in traffic self-adjust, ensures a more optimal allocation scheme; simulation results show that the algorithm can effectively improve the network throughput, and reduce the packet loss rate.

II. THE ACCESS MECHANISM OF IEEE802. 11E HCCA

IEEE 802. 11e standard provides a quality guarantee for the transmission of real-time data (Voice, Video) in WLAN. The centralized co-ordination function in the traditional 802. 11MAC standard cannot provide real-time services, the prime reason is when the station is polled, it can only send a frame once a time, and with no priority. Now IEEE introduces the 802. 11e standard [1] which introduces a new Qos mechanism: HCF (Hybrid Coordination Function), which contains two modes, namely EDCA (Enhanced Distributed Channel Access) and HCCA (HCF Controlled Channel Access), EDCA can only be used in CP (Contention Period) , while HCCA can be used both in CP and CFP (Contention-Free Period), EDCA is basically an improved mechanism for DCF, and HCCA is basically an improved mechanism for PCF. Moreover, HCCA transfer protocol defines a time parameter which is called TXOP (Transmission

opportunity), QSTA (Qos Station) can transmit multi data in the time limited by TXOP, which addresses the post-problem that one data frame can be transmitted once a time. HCCA TXOP is calculated according to TSPEC (Traffic Specification) sent by each QSTA, then use the CF-Poll frame to transmit to each QSTA.

TSPEC (Traffic Specification) is a added information element in 802. 11e standard. QSTA describes the Qos properties of data flow based on TSPEC, such as TS info, Mean Data Rate, Medium time, etc. , the format is shown in Table 1 (in bytes).

Table 1 TSPEC frame structure

Bytes :3	2	2	4	4	4	4	4
Ts Info	Nominal MSDU	Maximum MSDU Size	Minimum Service Interval	Maximum service Interval	Inactivity Interval	Suspension Interval	Service Start Time
4	4	4	4	4	4	2	2
Minimum Data Rate	Mean Data Rate	Peak Data Rate	Maximum Burst Size	Delay Bound	Minimum PHY Rate	Surplus Bandwidth Allowance	Medium Time

III. SCHEDULER

A. Pre-Scheduler

In IEEE802. 11e agreement, we defined a basic HCCA scheduler, the simple Scheduler. The basic idea is that: "At regular time intervals, HC allocates a fixed length of time QSTA. This simple scheduler uses a few traffic parameters required by the protocol and several transmission control parameters derived from the parameters to scheduling [1]. " These parameters are as follows:

• Service interval: The time cycle of obtaining TXOP twice in a row. In the HCCA scheduler, any QSTA have the same period of service. Service intervals can be calculated through the following two ways: one is to analyze the traffic meeting the maximum delay bound, to acquire the minimum interval time; two, with the given beacon interval, to calculate the usable factor, and get maximum service interval smaller than the results from the first step scheduler. If there are new traffics being added to the scheduler queue, the service interval needs to be updated. For example: Beacon Interval = 100 ms, the answers for Maximum Service Interval of three workstations are 80 ms, 70 ms, 60 ms, then 50ms is chosen (because 50 can be divided by 100, and is the largest number smaller than 80, 70 and 60) .

• The number N_i: QAP decides how much required traffic stream is distributed to each QSTA according to the need of TSPEC from QSTAs. The used QAP TSPEC parameters include: Mean Data Rate (ρ_i) and Nominal MSDU Size (L_i). Therefore, traffic stream i produces the number N_i of MSDUs in SI:

$$N_i = \left\lceil \frac{S_i * \rho_i}{L_i} \right\rceil \qquad (1)$$

• TXOP duration time: using the following parameters such as Minimum Physical Rate(R_i), Maximum MSDU Size(M) and Overhead in Time Unit(O) from TSPEC, to calculate the TXOP that should be distributed to TRAFFIC STREAM i.

$$TXOP_i = Max\left(\frac{N_i \times L_i}{R_i} + O, \frac{M}{R_i} + O \right) \qquad (2)$$

• Fig. 1 shows according to the TSPEC demand of three QSTA, distributing circulating TXOP service in SI:
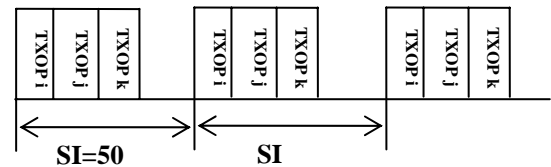

Figure. 1 QSTAi , QSTAj, QSTAk during the round robin scheduling in SI services TXOP

• According to the above mentioned Sample Scheduler, new traffic stream can be transferred. If SI has served k traffic streams in the system, and other QSTA requests for the (k+1)th service demand for traffic stream, if the following inequality holds, the ingoing traffic stream will be transferred normally, otherwise it will be rejected:

$$\frac{TXOP_{k+1}}{SI} + \sum_{i=1}^{K} \frac{TXOP_i}{SI} \leq \frac{T - Tcp}{T} \qquad (3)$$

• This scheduler is simple and easy to realized, but the interval time between SI and TXOP is static, it's only suitable to transfer the business of CBR, instead of VBR. Most multi-media traffic stream have the feature of VBR, so it's important to improve the adaptability to VBR.

IV. THE DYNAMIC SCHEDULER OF VBR.

In IEEE802. 11e, the bandwidth allocation scheme is to give every traffic stream a fixed TXOP, and uses the average data transfer rate to estimate the amount of data generated by a workstation during a SI, so it's only suitable to transfer CBR data streams. Because in each SI, the amount of data and the number of packets of VBR is not fixed, it is difficult to predict the size and the actual number of packets generated by the next node. In order to overcome the defects of the simple algorithm, we propose a new scheduling mechanism, which can dynamically adjust the SI of QSTA to schedule the data stream of sites

and make the scheduling scheme more efficient. The detail process is as follows:

A. *The Computation of SI*

TXOP Limit represents the maximum time which is used by some site to send data, so TXOP Limit is related to the frame size and the number of frames which can be transmitted(N_i). Here, N_i is not a fixed value, it directly affect the transmission opportunities of data. So it is particularly critical to compute the minimum time interval value of all the traffic in each node, i. e. the interval between two successful periods of service. HC (Hybrid coordinator) find out the maximum value of SI in each TS (Traffic Stream), and then select the minimal one which is called m. The value which is smaller than m and is a submultiple of the beacon interval is selected as the scheduled SI.

B. *Determine the next poll time*

Given QSTA is polled at the time t, and the last poll time t_i, if they satisfy the following condition, the procedure will go on to the next step, or enter the wait.

$$t \geq t_i + mSI_i \qquad (4)$$

- In Controlled Access Phase (CAP), just as shown in Fig. 2, if the polled station cannot complete its transmission in the previous SI, it will send a Null frame, and notice the value of T_i to the next poll so that it can be reallocated. Otherwise some additional delay will be arosen, therefore, we adopt the following algorithm to avoid the unnecessary delay.

$$mSI_{new\ i} = mSI_i + T_{i-1} - T_i \qquad (5)$$

Here, T_{i-1} denotes the last visit duration time of one station, T_i denotes the current TXOP duration time. So, if the previous values of SI and mSI are known, then the mSI of next poll can be calculated. The same procedure goes on till every traffic stream has been polled.
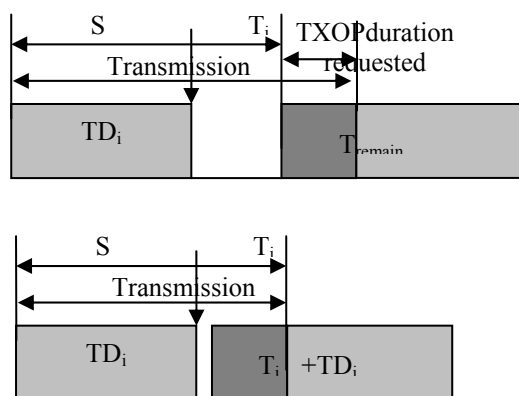

Figure. 2. TXOP duration mSI improvement

Each site obtains the authority to access the channel and transmit its data in the TXOP time which is defined in HCCA of IEEE802. 1le standard, and get access to the channel. In this case, if we use the control method mentioned above, it will generate unnecessary delays which causes the loss of transmission opportunities. To avoid that, our algorithm adaptively adjusts the bias deviation between the actual time and the expected time. Therefore, the twice allocation algorithm can flexibly

control the TXOP duration of data transmission and improve the transmission efficiency of each site.

C. *Calculate the duration time of TXOP Tdi*

$$TDi = Max\ (\frac{\frac{mSI_i \times \rho_i}{L_i} \times Li}{Ri} + O, \frac{Mi}{Ri} + O) \qquad (6)$$

Here, TD_i denotes the duration time of QSTAi's TXOP, R_i denotes the minimum physical bit rate, M denotes the maximum MSDU (e. g. 2304 bytes), O denotes extra cost (e. g. IFSs, ACK CF-Poll）.

Finally using the access control scheduler to determine whether the new TS can be transferred or not. If TD_{k+1} satisfies the following equation, then the new traffic stream can be transferred, otherwise it will be refused.

$$\frac{TD_{K+1}}{SI} + \sum_{i=1}^{K} \frac{TD_i}{SI} \leq \frac{T-Tcp}{T} \qquad (7)$$

Here, k denotes the current quantity of TS, k+1 denotes the new arrival TS, T denotes the interval of beacon, T_{cp} denotes the transmission time of EDCA business.

V. EMULATION AND RESULT ANALYSIS

We'll discuss the impact on network performance of the algorithms mentioned above through simulation. In order to improve the Qos performance of audio data transmission in WLAN, we'll explore the impact of the improved HCCA algorithm on network performance. In the Experiment, the average delay of data transmission, packet loss rate, throughput and TXOP transmission efficiency are chosen as the metrics to evaluate Qos. As for the throughput, it can be calculated by using the amount of bytes that is received divides by the sum of the time it takes; transmission delay is defined as the time starting from the source sends the frame to the destination receives the frame, packet loss rate is defined as the ratio of the number of lost packets and the total number of packets. We perform the simulation with NS simulator. In our simulation, G. 711 Voice signals is used, its parameters are listed in Table 2.

Table2 TSPEC parameters

TSPEC Parameters	G. 711 Voice
Mean Data rate（Kbps）	83
Delay Bound(bytes)	60
Nominal MSDU Size(bytes)	212
Maximum delay(ms)	40
Maximum Burst Size(bytes)	576
Peak Data Rate （Kbps）	83
Minimum PHY Rate （Mbps）	12
Minimum Service Interval(ms)	20
Maximum Service Interval(ms)	30

The simulation results are shown in Fig. 3. As shown in Fig. 3 (a), because of the extra cost of computation on a variety of load data flow, IEEE802. 1le simple scheduling algorithm (Simple Scheduler) achieves a lower average delay. But the delay of our improved algorithm still meets

the requirements of Qos. Compared with the benefits of our algorithm, a little higher delay is acceptable. Fig. 3 (b) shows that when the number of sites more than five, the packet loss rate of the improved algorithm is between 0. 8% and 1. 5%; with the growth in the number of sites, the packet loss rate of original algorithm will increase rapidly, and when the number of sites is 11, packet loss rate achieves 50%. As we can see in Fig. 3 (c), when the number of sites is more than five, owing to the use of the fixed TXOP duration, the increase of throughput in the traditional algorithm is not remarkable. While the

improvement on throughput and loss rate of the improved algorithm mainly benefits from the accurate allocation of transmission opportunities, which is based on the queue size of each data stream. Finally, as can be seen from Fig. 3 (d), because the TXOP is calculated according to requirements, so the utilization ratio achieves 90%, which obtains about a 20% improvement than that of the basic algorithm in IEEE802. 1le. Based on the above analysis, we can draw a conclusion that our algorithm brings a greater improvement on the Qos performance of the system.
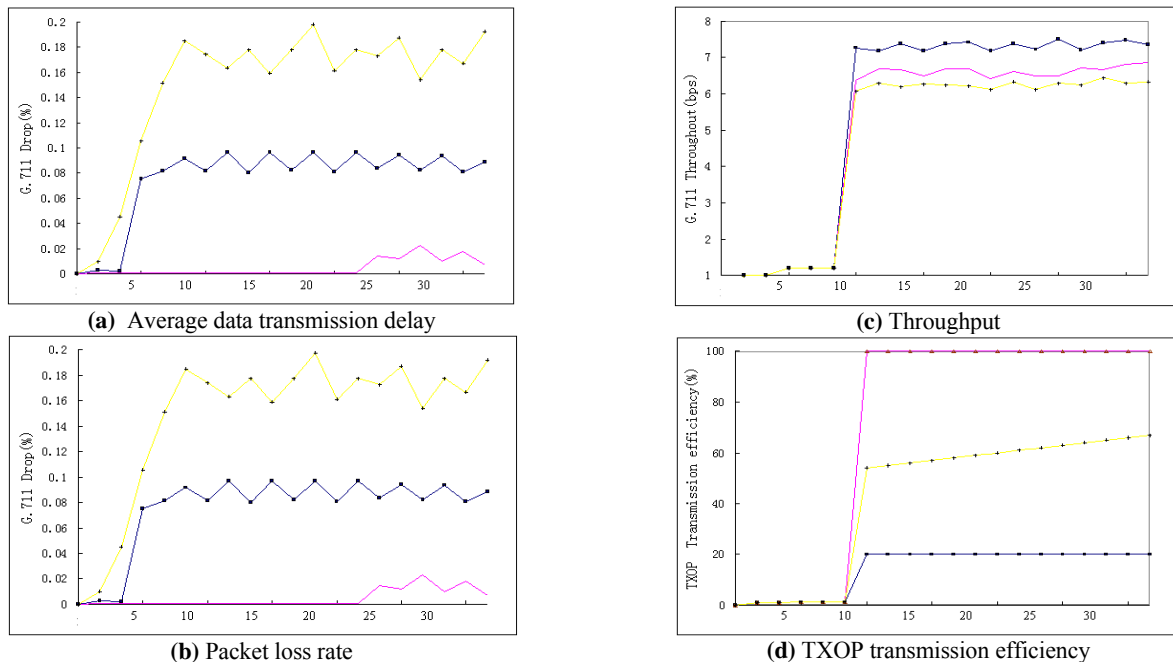

(a) Average data transmission delay

(c) Throughput

(b) Packet loss rate

(d) TXOP transmission efficiency

Figure. 3 Simulation results

VI. CONCLUSION

This essay mainly explore the problems that multimedia business have met in the process of transferring in WLAN, According to the HCCA simple scheduler, it raised a scheduler of distributing network resources dynamically according to each site's traffic stream, and flexibly manage the TXOP duration time of traffic transfer in the second distribution scheduler, to further improve the transfer efficiency on each site. Thus, it only improves the efficiency of WLAN lines, but also meets the need of real time business Qos.

REFERENCES

[1] IEEE Std. 802. 11e-2005, Part 11: Wireless LAN medium access control(MAC) and physical layer (PHY) specifications Amendment 8: medium access control (MAC) quality of service enhancements, Nov. 2005.

[2] Skyrianoglou, D. ; Passas, N. ; Salkintzis, "ARROW: An Efficient Traffic Scheduling Algorithm for IEEE 802. 11e HCCA", IEEE Transactions on Wireless Communications, vol. 5, no. 12, December 2006 Page(s):3558 - 3567

[3] Bin Muhamad Noh, Z. A. ; Takahiro Suzuki; Shuji Tasaka" A Packet Scheduling Scheme for Audio-Video Transmission with IEEE 802. 11e HCCA and its

[4] Bin Muhamad Noh, Z. A. ; Takahiro Suzuki; Shuji Tasaka" Packet scheduling for user-level QoS guarantee in audio-video transmission by IEEE 802. 11e HCCA" TENCON 2007-2007 IEEE Reqion 10 Conference.

[5] Kyung Mook Lim; Kang Yong Lee; Kyung Soo Kim; Seong-Soon Joo, "Traffic Aware HCCA Scheduling for the IEEE 802. 11e Wireless LAN" Multimedia and Expo, 2007 IEEE International Conference on 2-5 July 2007 Page(s):963- 966.

[6] Higuchi, Y. ; Foronda, A. ; Ohta, C. ;Yoshimoto, M. ; Okada, Y. ;"Delay Guarantee and Service Interval Optimization for HCCA in IEEE802. 11e WLANs", Wirelss Communications and Networking Conference, 2007. WCNC 2007. IEEE.

[7] Milhim, A. D. ;Yaw-Chung Chen;"An Adaptive Polling Scheme to Improve Voice Transmission over Wireless LAN"s". computer Systems and Applications, 2007. AICCSA '07. IEEE/ACS International Conference on 13-16 May 2007 Page(s):146 – 152.

[8] Deyun Gao, Jianfei Cai and Liren Zhang, "Physical Rate Based Admission Control Admission Control for HCCA in IEEE 802. 11e WLANs, " Advanced Information Networking and Applications, TAIWAN 2005. 19th International Conference Volume 1, pp. 479-485.

Application-Level QoS Assessment" Communications, 2006. APCC'06. Asia-Pacific Conference.

[9]   M. Barry, A. T. Campbell, and A. Veres, "Distributed Control Algorithm for service Differentiation in Wireless Packet Networks, "Proc. IEEEINFOCOM'01, vol. 1, Anchorage, AK, 2001, pp. 52-90

[10]   Nan Guo, Chen Chen , Chang Xing. Dynamic TXOP Assignment for Fairness(DTAF)in IEEE802. 11 e WLAN under Heavy Load Conditions. Parallel and Distributed Computing, Applications and Technologies, 2006. PDCAT'06. Seventh International Conference on De. . 2006 Page(s):80-85.

[11]   A. Zambon, R. Personal. QoS Enhancement with Dynamic TXOP Allocation in IEEE 802. 1 1e. Andreadis Indoor and Mobile Radio Communications, 2007. PIMRC 2007. IEEE 18th International Symposium on 3-7 Sept. 2007 Page(s):1-5.

Hua Liang, received his B. Eng. degree in computer science in 2000 from Hunan Normal University, M. Eng. degree in software engineering in 2009 from Central South University. His main research interests include wireless network and QoS routing.

Feng Zeng received his PhD degree in computer science in 2010 in Central South University. His research interests are in QoS mechanism for IP network, web service, and wireless network. He is a member of China Computer Federation.

Traffic Driven Epidemic Spreading in Homogeneous Networks with Community Structure

Fei Shao[1,2,3]

1. Jiangsu Information Analysis Engineering Laboratory, Nanjing, China
2. Center for Control and Intelligence Technology, Nanjing University of Posts & Telecommunications, Nanjing, China
3. School of Information Technology, Jinling Institute of Technology, Nanjing, China
Email: shaofei@jit.edu.cn

GuoPing Jiang[2]

2. Center for Control and Intelligence Technology, Nanjing University of Posts & Telecommunications, Nanjing, China
Email: jianggp@njupt.edu.cn

Abstract—**To understand the effect of the community structure on the epidemic propagation in homogeneous networks, a model of pseudo-random network is presented with adjustable community structure and constant average degree. In the scenario that the propagation is driven by reaction processes from nodes to all neighbors, pronounced community structure can reduce the epidemic propagation velocity. While in the situation that epidemic pathway is defined by traffic flows, the epidemic spreading in networks with pronounced community structure is obviously accelerated instead. When it is extended to the SIS model with traffic flows, the epidemic threshold is found to be proportional to the inverse of the average betweenness. Simulation results have confirmed the theoretical predictions.**

Index Terms—epidemic spreading, community structure, epidemic threshold, traffic flow

I. INTRODUCTION

Since the seminal work on the small-world phenomenon by Watts and Strogatz [1] appeared in Nature in 1998 and on scale-free networks by Barabási and Albert [2] one year later in Science, the study of complex networks has attracted the dramatically increasing interest. The ultimate goal is to understand how the network effects influence dynamical processes taking place upon it. It is shown that complex networks can be classified into two distinct groups depending on their structure properties. The first one is homogeneous complex networks, represented by the exponentially bounded networks [3-4]. A typical example of an exponential network is the random graph model of Erdös and Rényi [4]. Recent studies indicate that many social, biological, and communication systems such as the Internet and the World Wide Web are not homogeneous as the above mentioned model, but have a scale-free topology, exhibiting a power-law degree distribution that is the probability that a node has k connections follows the distribution $P(k) \sim k^\gamma$, where γ ranges between 2 and 3. In homogeneous networks, generally we can assume that each node has roughly the same number of links which means the degrees of all the nodes are almost the same. Nevertheless, in the heterogeneous networks, linking is very often preferential which makes a wide range of degree distributions.

On the basis of the former theoretical study, lots of applications have been made especially on the epidemic spreading [5-9]. In the past few years, lots of large-scale international epidemics among human, animal, and plant caused an enormous amount of damage and loss. Since those disease outbreaks in biological systems can be viewed as the spreading of an epidemic on complex networks, how to control the epidemic spreading is one of the hot topics of recent research of dynamical processes taking place in complex networks. Many models have been proposed to characterize the epidemic spreading on complex networks. In those most extensively studied models, an individual is represented by a node which can be classified in three states: susceptible (which will not infect others but may be infected), infected (which is infective) and recovered (which has recovered from the disease and has immunity). Assume that a susceptible node will be infected by a certain infected one during one time step with probability v, and the recovering rate of infected ones is δ. Then the effective spreading rate λ is defined as $\lambda = v/\delta$ for the disease. Without lack of generality, we set can set $\delta = 1$, since it only affects at the definition of the time scale of the disease propagation.

With the further development of studies on complex networks, another common feature is found in many networks, community structure, the tendency for nodes to divide into subsets within which node-node connections are dense but between which connections are sparser. The impact of community structure on information transfer is

investigated [10] and a novel routing strategy based on community structure which enhance the packet delivery capability is proposed [11-12]. And the community network is found to have a smaller threshold of epidemic outbreak and more prevalence to keep the outbreak endemic with a broader degree distribution [13]. But nowadays, some communication equipment or software are found to be much more likely to make a connection with the nodes with common or similar characteristics while the total links are equal or close to their same limit. For example, in QQ platform, the most popular IM program in Mainland China, there will be at most 1000 friends for a certain QQ ID which is more likely to link with its relatives, classmates and colleagues. The impact that community structure has on epidemic spreading in the homogeneous network are not only of theoretical interest, but also of practical significance.

In this article, considering the emergence of community structure, the authors propose a model to explore the impact of community structure on epidemic spreading in the homogeneous network. Epidemic spreading are investigated in both scenarios that the propagating from nodes to all neighbors and epidemic pathway driven by traffic. The epidemic threshold is analyzed through comparative analysis and simulations based on different parameters and different community structure. Furthermore, it helps adopt appropriate immunization strategies to minimize the risk of epidemic outbreaks.

II. MODELS

The classical SIS model [6-7], which is often used for these in which the infected nodes will return to the susceptible state again, does not take into account the possibility of nodes removal due to death or acquired immunization, and thus nodes run stochastically through the cycle susceptible → infected → susceptible. It is generally used to study epidemics leading to endemic states with a stationary average density of infected nodes. But while investigating the dynamical behaviors in the very early stage of epidemic outbreaks, this case corresponds to the simplified SI model [9], for which infected nodes remain always infective and spread the infection to susceptible neighbors with spreading rate λ. The SI model can be viewed as the limit of the SIS model when the recovering rate $\delta=0$, representing diseases from which recovery is impossible.

In the previous epidemic spreading model which assumes that each node's infectivity is strictly equal to its degree, each infected node will contact every neighbor once within onetime step. In this paper, we also investigate the propagation process driven by traffic flows along the shortest path. The traffic-driven epidemic spreading model can be described as follows: all the nodes can create packets with addresses of destination, receive packets from other nodes, and route packets to their destinations; at each time step, an information packet is generated at every node with probability β, with randomly chosen sources and destinations and all the packets are forwarded one step toward their destinations

through the shortest path; each node has unbounded packet delivery capability for simplicity which means congestion cannot arise in the model; a packet, upon reaching its destination, is removed from the system; a susceptible node has a probability λ of becoming infected every time it receives a packet from an infected neighbor. (When we calculate the epidemic threshold of SIS model, the probability λ is the effective spreading rate while the recovering rate is fixed to 1.)

To know the influence of community structure on epidemic spreading, we employ the modularity measure which is proposed in [14]. Consider a particular division of a network into m communities. Let us define an $m \times m$ symmetric matrix $\mathbf{E}$ whose element e_{ij} is the fraction of all edges in the network that link nodes in community i to nodes in community j. The modularity measure, Q, is defined as follows:

$$Q = \sum_i (e_{ii} - a_i^2), \qquad (1)$$

where a_i is the sum of e_{ij} for a certain j, that is $a_i = \sum_j e_{ij}$. Different divisions lead to different Q where the maximum of them is named as Q_{max}. The higher the modularity Q_{max} is the stronger community structure the network has.

The homogeneous networks, such as ER random graphs and WS small world networks, have highly peaked degree distribution which means most nodes have approximately the same degree. In the homogeneous networks with community structure, the average degree is not any more a meaningful characterization of the network properties. We introduce the betweenness b_i to estimate the possible packets passing through a node i under a given routing strategy. The most widely used betweenness measure is that of Freeman [15-16], usually called shortest path betweenness which is defined as

$$b_i = \sum_{s,t} \frac{\sigma(s,i,t)}{\sigma(s,t)}, \qquad (2)$$

where $\sigma(s,i,t)$ is the number of shortest paths between nodes s and t that pass through node i and $\sigma(s,t)$ is the total number of shortest paths between node s and t and the sum is over all pairs s, t of all distinct nodes. This may be normalized by dividing through the number of pairs of nodes not including i, which is $(n-1)*(n-2)/2$.

To this end we are required to be able to construct homogeneous networks with controllable community structure. A model of pseudo-random network is employed since all other properties such as average node degree will be equivalent to fully random networks except the controllable varying strength of community structure. These networks are comprised of n nodes which are split into m communities of n/m nodes each. Each node has on average Z_{in} edges connecting it to nodes of the same community and Z_{out} edges to nodes of other communities. While Z_{in} is varied, the value of Z_{out} is chosen to keep the total average degree constant, and set

to $<k>$. As Z_{in} is increased, the communities become better defined and easier to identify.

III. SIMULATIONS AND ANALYSIS

We employ a family of pseudo-random networks with $n=128$ nodes in each network which are divided into $m=4$ communities with $n/m=32$ nodes in each community. The average degree is set to $<k>=16$ while $Z_{in}= 8$ for a random network with modularity $Q_{max}=0.2533$, $Z_{in}=12$ for a network with community structure whose modularity Q_{max} is 0.4907, and $Z_{in} =15$ for a network with pronounced community structure whose modularity Q_{max} is up to 0.6976. And the average betweenness $<b>$ is 0.0157, 0.0172 and 0.0235 consequently. In all simulations, we generate 100 instances, and the result is the average of the 100 instances. What's more, the propagation is computed averaging over 100 different starting configurations in a certain instance.

A. Epidemic Spreading in Homogeneous Networks

It is proved that in homogeneous networks, each node has approximately the same degree which makes it possible to use mean-field theory to obtain approximate results [9]. In this case the system is completely defined by the number of infected node $I(t)$, and the reaction rate equation for the density of infected nodes $i(t)=I(t)/n$ (where n is the total number of nodes) reads as

$$\frac{di(t)}{dt} = \lambda * <k> *i(t)*(1-i(t)). \quad (3)$$

Equation (3) states that the average density of newly infected nodes is proportional to the spreading rate λ, the density of susceptible nodes that may become infected, $1-i(t)$, and the probability of infected nodes in contact with any susceptible one. The homogeneous mixing hypothesis considers that this last term is the product of the number of links emanating from each node $<k>$ and the average density of infected nodes $i(t)$. Obviously, the formula considers that all nodes have the same number of neighbors $<k>$; i.e., it assumes a perfectly homogeneous network. And each node's infectivity, measured by its possibly maximal contribution to the propagation process within one time step, is strictly equal to its degree.

Numerical simulations are performed on the pseudo-random networks mentioned above to produce the results as shown in Fig. 1.
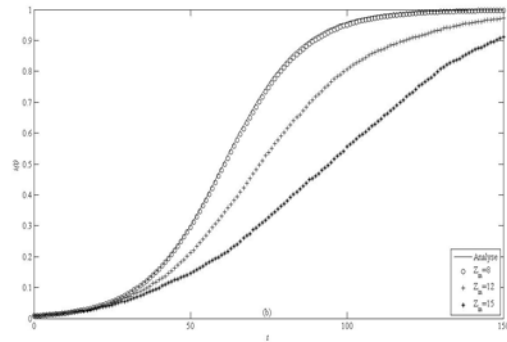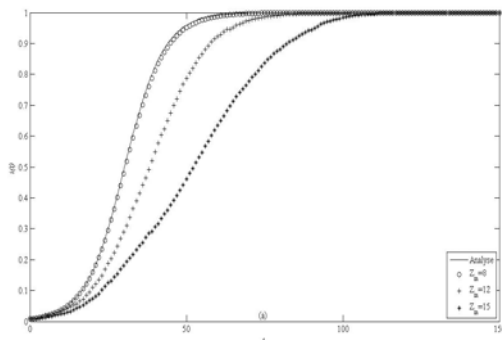

Figure 1.   Average density of infected nodes $i(t)$ versus time t. The solid curve denotes theoretical prediction and the circle, plus, and star denote the case of $Z_{in}=$ 8, 12, and 15 respectively. (a).The spreading rate λ is 0.01 (b).The spreading rate λ is 0.005

Fig. 1(a) and 1(b) exhibit the average density of infect nodes for different Z_{in}. While Z_{in} is set to 8, the network is a traditional random network as mentioned in [4]. In both scenarios, our simulations agree well with the theoretical predication of (3). When Z_{in} increase from 8 to 12 and 15, the modularity Q_{max} is 0.2533 to 0.4907 and 0.6976 consequently which means more pronounced community structure. The epidemic propagation velocity is smaller in networks with stronger community structure which is different from the previous study [13]. In the networks with pronounced community structure, the infected seed is more likely to infect the one in the same community because there are more edges linked with the node in the same community than the others. After a short while, the new infected node will find that most of its neighborhoods are infected because they are in the same community. Therefore, the community structure slows down the epidemic propagation. Comparing Fig. 1(a) and 1(b), we can find that the effect of community structure slowing down the epidemic propagation is especially obvious when the epidemic spread at lower rate.

B. Traffic Driven Epidemic Spreading in Homogeneous Networks

In the traffic driven epidemic spreading model, we can also obtain approximate results of the density of infected nodes $i(t)$ using mean-field theory as follows:

$$\frac{di(t)}{dt} = \lambda * \beta * n* <b> *i(t)*(1-i(t)). \quad (4)$$

Equation (4) states that the average density of newly infected nodes is proportional to the spreading rate λ, the density of susceptible nodes that may become infected, $1-i(t)$, the probability of a packet passing through a link pointing to an infected node, $i(t)$, the total number of packets, $\beta * n$, and the fraction of packet passing through node which is equal to the average betweenness, $<b>$. Equation (4) can be solved with the initial condition $i(t)_{t=0} = i_0$,

$$i(t) = \frac{i_0}{i_0 + e^{-\lambda * \beta * n* <b> *t} - i_0 * e^{-\lambda * \beta * n* <b> *t}} . \quad (5)$$

At small times, the density of infected nodes is very small, we can get that

$$i(t) \approx i_0 * e^{\lambda * \beta * n* <b> * t} . \qquad (6)$$

The above calculations imply that the density of infected nodes is proportional to the spreading rate λ and the packet generation rate β in a given network. And if the network has pronounced community structure, which means the greater average betweenness, the density of infected nodes is higher. In other words, the epidemic spreading in networks with pronounced community structure is obviously accelerated.
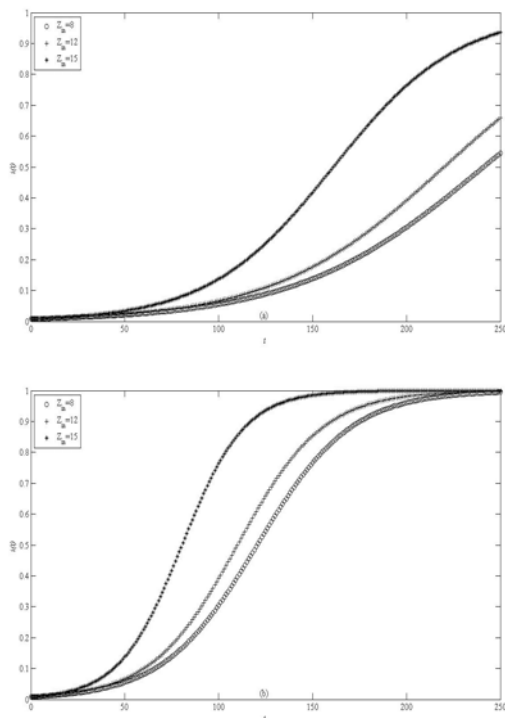

Figure 2. $i(t)$ versus t for different Z_{in}. The packet generation rate β is 1. (a). λ=0.01 (b). λ=0.02

Fig. 2(a) and 2(b) exhibit the relationship of the density of infected nodes and the spreading rate λ which agree well with (6). In both scenarios, the increase of the density of infected nodes is companied with the increase of Z_{in}, as well as the community structure. By comparing Fig. 2(a) and Fig. 2(b), we discover that the lower the spreading rate is, the more obvious the effect is.
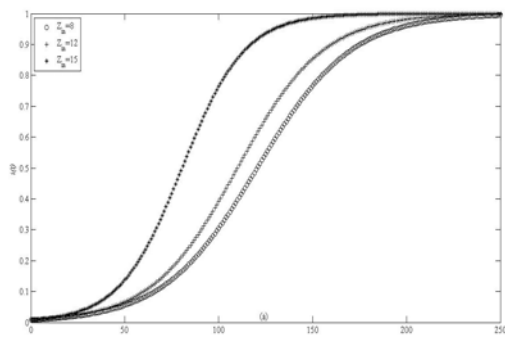

Figure 3. $i(t)$ versus t for different Z_{in}. λ=0.01. (a). β=2 (b). β=3

Fig. 3(a) and 3(b) exhibit the relationship of the density of infected nodes and the packet generation rate. There is only slight difference that can be ignored between Fig. 3(a) and Fig. 2(b) where only one of the two parameters (the spreading rate and the packet generation rate) is doubled. It also confirms the validity of (6). Also in both scenarios, strengthening the community structure will result in the increase of the density of infected nodes. By comparing Fig. 2(a), 3(a) and 3(b), we can also observe that the lower the packet generation rate is, the more obvious the effect is.

In the traffic driven epidemic spreading model, the nodes with higher betweenness are more likely to be infected since they are given more opportunities to receiving packets from infected nodes. And if they are infected, they are more able to spread the epidemics. They can be called the 'super spreader' [17-18] because the node with great infectivity in an epidemic contact network. So the epidemic spreading in networks with pronounced community structure is accelerated.

C. Epidemic Threshold in Traffic Driven Epidemic Spreading in Homogeneous Networks

Finally, we extend it to SIS model with traffic flows, the only thing is to add the decaying item, which is proportional to the product of the curing rate γ (we set it to 1 for simplicity) and the average density of infected nodes $i(t)$. So in SIS model, the equation is

$$\frac{di(t)}{dt} = -i(t) + \lambda * \beta * n* <b> *i(t) * (1-i(t)) \quad (7)$$

The ultimate purpose is the general prediction of a nonzero epidemic threshold, λ_c, which is the simple criterion for finding optimal immunization strategies [19-22]. If the value of λ is above the threshold, the epidemic spread and become persistent. On the contrary, below it, the epidemics die out and endemic states are impossible. After imposing the stationary condition of (7), $di(t)/dt$=0, we obtain the equation of the epidemic threshold:

$$\lambda_c = \frac{1}{\beta * n* <b>} . \qquad (8)$$

Figure 4.   *i(t)* versus *t* for different Z_{in}. β=1. The results denote the case of different spreading rate λ (from bottom to top) as labeled in the figures. (a). Z_{in} = 8 (b). Z_{in} = 12 (c). Z_{in} = 15
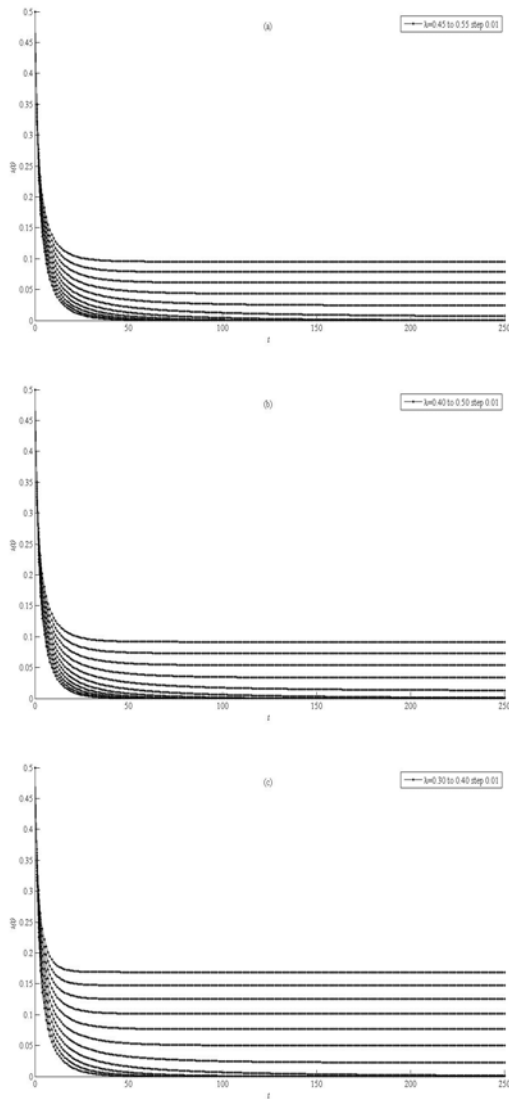

Figure 5.   *i(t)* versus *t* for different Z_{in}. β=1. The results denote the case of different spreading rate λ (from bottom to top) as labeled in the figures. (a). Z_{in} = 8 (b). Z_{in} = 12 (c). Z_{in} = 15

Fig. 4(a), 4(b) and 4(c) exhibit the epidemic threshold λ_c of the different networks. In Fig. 4(a), when the spreading rate λ is lower than 0.49, the infected nodes disappear. And while it is up to 0.50, the infections can proliferate on the network. It is in good agreement with analytical finding of the (8), λ_c=1/(1*128*0.0157)= 0.4976. And the predication of (8) for Z_{in} = 12 and Z_{in} = 15 is 0.4542 and 0.3324 consequently.   One can see clearly from Fig. 4(a), 4(b) and 4(c) that the simulation results agree very well with the analytic results.

To find the influence of packet generation rate on the threshold, we change β from 1 to 2 to get the simulation results as shown in Fig. 5. When the packet generation rate is doubled, the predication of (8) is 0.2488, 0.2271, and 0.1662 which also agree well with the simulation results.
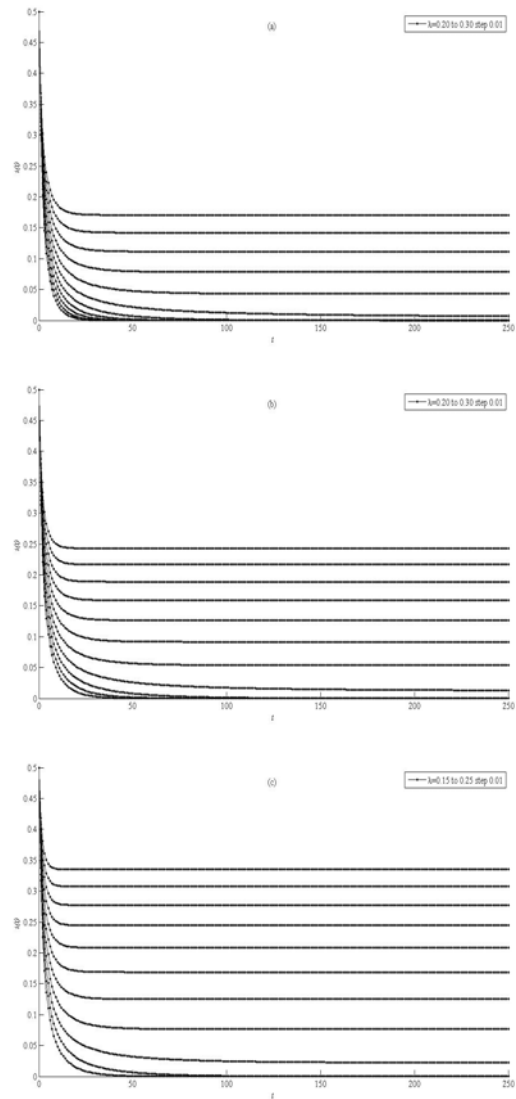
IV. CONCLUSIONS

Aiming at the influence of community structure on epidemic spreading, we have computed both analytically and numerically the conditions for the emergence of an epidemic outbreak in homogeneous network in both scenarios that the propagating from nodes to all neighbors and epidemic pathway driven by traffic. Two distinct results are achieved due to the different models: community structure is proved to have a positive effect reducing epidemic propagation velocity in the traditional model while it can accelerate the epidemic propagation in the traffic driven model. Additionally, the analytical results of the epidemic threshold value are obtained, which agree well with the numerical simulations. The results indicate that the epidemic threshold is proportional to the inverse of the average betweenness and the packet generation rate in a given homogeneous network. It is of

practical importance to adopt appropriate immunization strategies to control the epidemic spreading.

REFERENCES

[1] Watts D J, and Strogatz S H, Collective dynamics of 'small-world' networks. *Nature*, 393(1998),440-442.
[2] Barabási A L, and Albert R, Emergence of Scaling in Random Networks. *Science*, 286(1999),509-512.
[3] Erdös P, and Rényi A, On Random Graphs. *Publicationes Mathematicae*, 6(1959),290-297.
[4] Erdös P, and Rényi A, On the Evolution of Random Graphs. *Publications of the Mathematical Institute of the Hungarian Academy of Science*, 5(1960),17-61.
[5] Bailey N T J, The Mathematical Theory of Infectious Diseases and Its Applications, New York, Hafner Press, 1975.
[6] Anderson R M, and May R M, *Infectious Diseases of Humans*, Oxford, Oxford University Press, 1991.
[7] Hethcote H W, The mathematics of infectious diseases. *SIAM Review*, 42(2000), 599-653.
[8] Murray J D, *Mathematical Biology*, Springer-Verlag, Berlin, 1993.
[9] Barthélemy M, Barrat A, Pastor-Satorras R, and Vespignani A, Velocity and Hierarchical Spread of Epidemic Outbreaks in Scale-Free Networks. *Phys. Rev. Lett.*, 92:17 (2004), 178701.
[10] Danon L, Arenas A, Guilera A D, Impact of community structure on information transfer. *Phys. Rev. E*, 77:3 (2008), 036103.
[11] Shao F, Jiang G P, Optimal Traffic Routing Strategy Based on Community Structure. *Acta Phys. Sin.*, 60:7 (2011), 078902 (in Chinese)
[12] Shao F. An Optimal Routing Strategy Based on Community Structure in Scale-Free Networks. *Journal of Computational Information Systems*, 7:4 (2011), 1181-1189

[13] Liu Z H, and Hu B B, Epidemic spreading in community networks. *Europhys. Lett.*, 72(2005), 315-321
[14] Newman M E J, Girvan M. Finding and evaluating community structure in networks. *Phys. Rev. E*, 69:2 (2004), 026113.
[15] Freeman, L. C. A set of measures of centrality based upon betweenness. *Sociometry*, 40(1977), 35–41.
[16] Freeman, L. C. Centrality in social networks: Conceptual clarification. *Social Networks*, 1(1979), 215–239.
[17] Bassetti S, Bischoff W E, Sherertz R J, Are SARS superspreaders cloud adults? *Emerging Infectious Diseases*, 11:4(2005), 637-838.
[18] Small M and Tse C K, Clustering model for transmission of the SARS virus: application to epidemic control and risk assessment. *Physica A*, 351(2005), 499-511.
[19] Pastor-Satorras R, and Vespignani A, Epidemic spreading in scale-free networks. *Phys. Rev. Lett.*, 86(2001), 3200-3203.
[20] Pastor-Satorras R, and Vespignani A, Immunization of complex networks. *Phys. Rev. E* 65(2002), 036104.
[21] Dezsö Z, and Barabási A L, Halting viruses in scale-free networks. *Phys. Rev. E* 65(2002), 055103.
[22] Castellano C, and Pastor-Satorras R, Thresholds for epidemic spreading in networks. *Phys. Rev. Lett.*, 105(2010), 218701.

Fei Shao was born in Jiangsu, China, in 1978. He received the Bachelor Degree from Jiangsu University of Science and Technology in 1998, Master degree in Computer Application Technology from Nanjing University of Technology, Jiangsu, China in 2003. Since 2008, he has been pursuing his Dr. Degree in the School of Computer Science & Technology at Nanjing University of Posts & Telecommunications. From 2010 to now, he is an associate professor at the School of Information Technology, Jinling Institute of Technology and working for Jiangsu Information Analysis Engineering Laboratory. His current research interests include information security and complex dynamical networks.

Guoping Jiang, Professor and Ph.D supervisor of Nanjing University of Posts and Telecommunications. His research interests include chaos synchronization and control, chaos-based communication, and complex dynamical networks.

Co-occurrence Relation of DNS Queries Based Research on Botnet Activities

Zhiwen Wang, Lu Liu
MOE KLINNS Lab and SKLMS Lab
Xi'an Jiaotong University, Xi'an, P.R. China
Email: wzw@mail.xjtu.edu.cn, yacht2005@gmail.com

Abstract—**As a new platform for launching attacks collectively, botnets have been considered as the leading security threat to the Internet in the literature. Previous works focus on how to detect zombies via some of the behavioral patterns of botnets. However, it's an important and challenging task to track the network activities of the zombies so as to have an insight into the global view of "what those zombies do" besides "who those zombies are" since it's an exclusively nature of botnets to stay stealthy when conducting various malicious activities as long as possible. In this paper, an improved approach is proposed to handle this new problem based on co-occurrence relation of DNS queries with full consideration of the spatial and temporal properties of botnet activities. The approach excludes noise made by NAT, and distinguishes domains with co-occurrence relation by botnet activities from them by normal user activation, according to the spatial dimensions and time dimensions. Then, we validate the approach using DNS traffic in real network. The experimental result shows it can eliminate the NAT interference, significantly reduce the amount of data and improve the discovery of unknown botnet domain exceptionalness, we analysis main factors whish impact the approach, and then proposed treatment strategies correspondingly.**

Index Terms—**co-occurrence relation of DNS queries, botnet, tracking in network, NAT**

I. INTRODUCTION

Botnet is a group of infected hosts (zombies) that are controlled by botmaster. The zombies receive and execute commands send by botmaster. Typically attacks include DDos, Information stolen, fishing, spam, click fraud, etc, so that botnets are considered as serious threat on Civil Internet [1], Industrial production control system[2] and MILNET "One-to-many" command and control[3] is the essential difference between botnets and other attack technology like traditional virus, Trojans and back door programs. "Large scale, organized, high controllable, stealthy, long-term latent" are the typical features of botnets.

The hot spot on botnet research is botnets detection. The purpose of botnet detection is to find zombies via some of the behavioral patterns of botnets such as signatures [4-6]. Recent years, some research institutes detecting botnets through some approaches without signatures. Sonalysts collects and classifies traffic, then calculates the scores of threat among hosts[7]. Yuanchen He mines malicious domain from meanings and statistically informative features[8]. Xin Hu detects botnets focusing on single and double fast-flux domains[9]. However, the interactive between botmaster and zombies is a dynamic procedure, so that the behavioral patterns of botnets we have found will be updated in time and then lose efficacy. So it's an important and challenging task to track the network activities of the zombies so as to have an insight into the global view of "what those zombies do" besides "who those zombies are" and find more up-to-date features of botnets.

In previous researches we know the behavioral patterns of botnets detection are mainly IP and domains of C&C servers. We will tracking botnets activates dynamically and comprehensively via domains of C&C servers. Currently among the research of botnets based on domain names, Ricardo in University of Pittsburgh detects C&C Servers by abnormal DDNS[10], and detects bots using Bayesian approach based on the similarity of their DNS traffic[11]. But the complex mathematics can't take them in use in large scale network. This paper focus on tracking botnet activities based on co-occurrence relation of DNS queries[12]. This paper makes the following main contributions. (1) We evaluate the applicable range and defects of the scoring method based on co-occurrence relation of DNS queries, find this method does not apply to the network existing NAT, and cannot distinguish the difference of co-occurrence relation of DNS queries by botnet activities from them by normal user activation since the oversight of the feature persistent. (2) We propound a proved scoring method and apply to the botnet tracking. The method not only can overcome interference caused by NAT, but also can dynamically tracking botnets effectively and reliably via taking group and persistence of botnets into condition. (3) We analysis main factors whish impact the approach, and then make feasibility analysis correspondingly.

II. CO-OCCURRENCE RELATIONS OF DNS QUERIES

Let a query from a host to a domain be $q = (h, d)$, and $Q = \{q_1, q_2, q_3, \cdots\}$ be the set of queries. For a set of DNS query D, if there exists a related set of DNS query D' and a related set of hosts H, for each

$h \in H$, $d \in D$, $d' \in D'$, such that $(h,d) \in Q$, $(h,d') \in Q$, then we call there is a co-occurrence relation of DNS queries between set D' and D, and D' is the co-occurrence domain set. In large distributed applications, co-occurrence relation of DNS queries reflects the visiting pattern of participant hosts, so that it provides a connection way for finding unknown domains related.

We track 23 botnets include Zeus, Srizbi, etc for a long time and find that botnets with whether centralized or distributed structure, or with whether IRC or HTTP protocol, all have the following characters:
- Group dynamics in spatial dimension. Bots are controlled by same botmaster, and they receive same commands and visit related website with same pattern.
- Persistence in temporal dimension. Bots access relevant servers (including control server, the update server, etc.) in duration so that they can keep controlled by botmaster. Many different domain names will be used in a botnet's life cycle, and zombies will access them persistently, receiving the attacker's command and control, and to ensure stealthy and reliability.
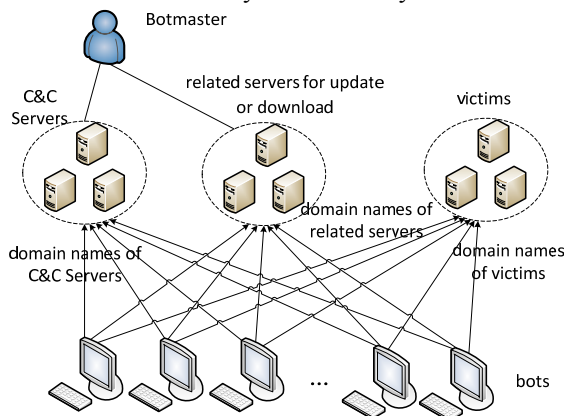

Figure 1.   co-occurrence relation of DNS queries in botnet behaviors

Figure 1 shows the process that bots visit different sorts of domain name: first, they visit C&C server and receive commands; then, bots query related domain name from the commands to visit related server, they will update zombie program, download malware, upload the theft of information and so on; then, bots query domain names which they will attack. So zombies in a same botnet must have the same or similar visiting pattern of domain names since they are controlled by same botmaster.

Therefore, queries zombies made have clear co-occurrence relation: Domain names of botnets we have known can be act as the given domain name set, such as capture income command and control domain name; And domain names of botnets unknown can be act as co-occurrence domain set, such as related domain name for update or download and domain names of victims.

III. TRACKING BOTNET ACTIVITIES BASED ON CO-OCCURRENCE RELATION OF DNS QUERIES

There are two key issues when we use the approach tracking botnet based on co-occurrence relation of DNS queries:

(1) how to find the co-occurrence relation domain names;

(2) how to make a distinction of co-occurrence relation domain names between botnets and others.

To issue 1, a score method on co-occurrence relation is used, and we take domain names with high score as candidate. To issue 2, we first need to eliminate NAT IP, and then distinguish co-occurrence relation domain names by botnets from those by other network behaviors through typical characters of botnets which are group dynamics in spatial dimension and persistence in temporal dimension.

A. *Score method on co-occurrence relation of DNS queries*

K. Sato proposes a score method in [6] based on the assumption "If two domain names are resolved by the same host frequently and one is black, the other is also black." above, the method can be expressed as follows:

$$\begin{cases} S(d) = \left(\sum_{d_b \in D_B} C(d_b, d) \right) * W(d) \\ C(d_i, d_j) = \dfrac{\sum_{\{h | d_i \in D_h \wedge d_j \in D_h\}} 1/|D_h|}{\left|\{h \mid d_i \in D_h \vee d_j \in D_h\}\right|} \\ W(d) = \dfrac{\left|\{h \mid h \in H_I \wedge d \in D_h\}\right|}{\left|\{h \mid h \in H \wedge d \in D_h\}\right|} \end{cases} \quad (1)$$

Where H_I denotes set of infect hosts, H denotes set of query hosts, D_h denotes set of domain names host h requests, D_B denotes set of black domain names we have known; $C(d_i, d_j)$ represents a degree of co-occurrence relation between d_i and d_j, $W(d)$ represents a correction about domain names in queries sent by infected heavy user. And the total score $S(d)$ is the sum of the degree of domain name d and each $d_b \in D_B$ through a correction by $W(d)$. Then, choose some of the highest rating scores in the domain name as a malicious domain name to expand the domain name list by calculating the scores of all of domain names the infect hosts visited.

B. *Analysis on the score method*

We test and analysis the result of the score acquired by formula (1) in real network environment for a long time and find that there are two problems:

(1) We find that it will seriously affect the validity of this method when uses NAT technology in the network environment. NAT technology has been widely used in the Internet, and it can make multiple hosts through a NAT share a single IP address to access Internet. And K. Sato's domain co-occurrence score method ignores the

existence of NAT. Experimental results show that if NAT exists, the method of confidence and performance will be severely affected, in particular in:

- Too many domain names of misinformation. If there has one infect host in NAT, then all the domain names other hosts within NAT visited will be determined to the domain names to be measured, which making a high number of domains to be measured; especially when there are many hosts in the NAT, it will lead to a sharp increase in the number of domains to be measured.

- The score of domain name of inaccuracy. For a domain name d to be measured, whether there has host infect or not in the NAT, the result score will be different with actual situation for the base of calculation like the number of hosts and black domain names which have co-occurrence relation with d are inaccurate. Therefore, we should filter queries by NAT in order to get a better result.

(2) This method does not take into account the inherent features of botnets that group dynamics and persistence, so that making it difficult to distinguish co-occurrence relation domain names by botnets from those by other network behaviors. Since the local characteristics of each botnet are different, so we need to study each botnet's domain access separately, and then find related unknown malicious domain name correspondingly. Meanwhile, we should observe the traffic in a long time since zombies visit domain names of botnets persistently but online time uncertainty. So we take the parameter observation time into consider. The longer the observation time is, the more obvious the tracking effects are.

C. Improvement on the score method

In order to track the behavior of the botnet better, domain names were based on insufficient analysis of the current scoring method, we conducted three improvements based on insufficient analysis of the score method:
- filtering queries by NAT;
- spatial refinement;
- the introduction of observation time

a) Filtering queries by NAT

In order to eliminate the influence by NAT, the most effective way is to filter queries by hosts behind NAT. and the key point to accomplish this is recognition the IP of NAT host. Because the mechanism of precise methods to identify NAT all need particular protocol support, and scalability is poor; To take full advantage of existing DNS traffic, the paper design a simple identification method based on the statistical properties of DNS traffic.

Suppose random variable X_{ij} denotes the number of domain names which host i queried in time period j ($j = 1, 2, 3, \cdots$), the observation value is x_{ij} . If we observed t time periods continuously, then the average number of domain names which host i queried per period is $\overline{x_i} = \sum_{j=1}^{t} x_{ij} / t$. If $\overline{x_i} > M_k$, we consider this host as a NAT. Where the threshold M_k is upper percentile for random variables X_{ij} , that is, $P\{X_{ij} > M_k\} = k$, $k \in (0,1)$. Recognition parameters k can be determined according to the actual network environment.

b) Spatial refinement of co-occurrence relation of DNS query for analysis

Spatial refinement means we will analysis and process the co-occurrence relation of DNS queries of each botnet independently. Suppose that there are N sets of botnet feature, botnet B_b among them has n domain names we have known, the set of them is $Z_b = \{d_1, d_2, \cdots, d_n\}$. We define the set of DNS queries as $R = \{r_1, r_2, r_3 \cdots\}$, the element $r = (t, h, p, d)$ contains the feature information, where t represents request time, h represents the host who request the query, p represents resource records, and d represents the domain name requested. We define two operators $\Phi(r)$ and $\Gamma(r)$ to get host requested and domain name to request., if a host sends a DNS request to any domain names in Z_b , then: the host are considered as a zombie of botnet B_b , the set of them is $H_b = \{h_1, h_2, \cdots, h_m\}$, that is, $\forall h \in H_b \rightarrow \exists d \in Z_b \wedge \exists r \in R \wedge \Phi(r) = h \wedge \Gamma(r) = d$; the unknown domain names requested by zombies of B_b are considered as the set of co-occurrence domain names to be measured $C_b = \{d_1, d_2, \cdots, d_k\}$, that is, $\forall d \in C_b \rightarrow d \notin Z_b \wedge \exists h \in H_b \wedge \exists r \in R \wedge \Phi(r) = h \wedge \Gamma(r) = d$.

We define the score $S_b(d)$ of domain name d to be measured in botnet B_b as:

$$
\begin{cases}
S_b(d) = \left(\sum_{d_b \in Z_b} C(d_b, d) \right) * W(d) \\
C(d_i, d_j) = \dfrac{\sum_{\{h | d_i \in D_h \wedge d_j \in D_h\}} 1 / |D_h|}{\left| \{h \mid d_i \in D_h \vee d_j \in D_h\} \right|} \\
W(d) = \dfrac{\left| \{h \mid h \in H_b \wedge d \in D_h\} \right|}{\left| \{h \mid h \in H \wedge d \in D_h\} \right|}
\end{cases} \quad (2)
$$

According to formula (2), calculate all the co-occurrence scores of domain names to be measured in C_b of botnet B_b , some with higher scores are selected as the extension malicious domain names of botnet B_b

c) Observation time of co-occurrence relation of DNS query for analysis

Introducing observation time means we will analysis and process the co-occurrence relation of DNS queries in a long observation according to the feature persistence of botnet. We divide the observation into several small time windows with same timespan. If there are multiple time windows, the score of the domain name to be mearured in each of them is higher, and there is more possibility the domain name is an unknown domain of botnet.

Suppose timespan of the window is T, for each time window t, calculate the co-occurrence score of domain name d to be measured of botnet B_b using formula (2) respectively. Then we can get the set of the co-occurrence score of domain name d to be measured of botnet B_b in each time window: $S(d, B_b) = \{S_b(d, t_1), S_b(d, t_2), \cdots S_b(d, t_x)\}$. Then we can calculate the average co-occurrence score of d as $\overline{S_b}(d) = (S_b(d, t_1) + S_b(d, t_2) + \cdots + S_b(d, t_x))/x$, and find the max co-occurrence score of d as $S_{b\max}(d) = \max(S_b(d, t_i))$. Then we can get the improved $S_b(d)$ with observation time as:

$$S_b(d) = \frac{\overline{S_b}(d)}{\max(\overline{S_b}(d_i))} \cdot \alpha + \frac{S_{b\max}(d)}{\max(S_{b\max}(d_i))} \cdot (1 - \alpha),$$
$$\alpha \in (0, 1). \qquad (3)$$

Where $\max(\overline{S_b}(d_i))$ denotes the maximum of the average co-occurrence score of all domain names to be measured of botnet B_b, $\max(S_{b\max}(d_i))$ denotes the maximum of the max co-occurrence score of all domain names to be measured of botnet B_b, α denotes the scaling factor which can reflect the percentage of the average score and the max score in the practical network. When research botnet, if α equals 1, peak of the co-occurrence score will be ignored, and apply to the network with many zombies and the feature persistence shown obviously; if α equals 0, the co-occurrence score method will degenerate into the dimension without observation time; for the network that the frequency of zombie behaviors not clear, always set α larger but not 1, so that can highlight the persistence of botnet without missing the queries requested by zombies which keep in touch with botmaster not frequently. So, the co-occurrence score $S_b(d)$ will distributes between 0 and 1. If the value is the larger, there is more possibility queries about the domain name that caused by botnet.

In the score method with observation time, the timespan T directly reflects the persistence feature of botnet and the value effected by two factors: (1) the number of zombies. If the number of zombies take large part of all hosts in the network, then the value T can be small since there are stable number of zombies online almost at any time; (2) the frequency of connection between zombies and botmaster. If the frequency of connection is higher, the value T can be smaller. but on the premise that valuable data can be got in each time window.

IV. VALIDATION AND ANALYSIS

A. Data Preprocessing

We use DNS server's inlet dataflow of Xi'an Jiaotong University as data source (about 4M/s) to get the initial data set R. After capturing data for over 1 year, about 83 million records per day on average, we find out that most of them are normal DNS queries. In order to adapt to large-scale network and improve computing performance, we need to preprocess the initial data.

a) Data Reduction

We use "domain name white list" to filter data, which will reduce the amount of data to 15%~25% and remove a large number of noise for data analysis. "Domain name white list" is a list of domain names which are irrelevant to botnet detection. These are mainly three types of domain names in white list: common domain names, misconfigure domain names and program frequently query domain names. Program frequently query domain names are frequently queried by defective programs or free programs or malwares but are irrelevant to botnet.

b) Data Collection

We do some further statistical work on data set R, we calculate the number of query hosts of each domain name in $R = \{r_1, r_2, r_3 \cdots\}$ to get the data set $R_s = \{s_1, s_2, s_3, \cdots\}$. The elements of it are four-dimensional arrays $s = (t, h, d, n_{all})$. n_{all} represents the number of queries of domain name d sent by host h on date t. This work can reduce data set without loss of valid information and highlights the statistical characteristics. The reduced data set is about 3.5 million records per day.

We collect DNS data flow on the outlet of campus network of Xi'an Jiaotong University from 2010/6/1 to 2010/6/21 and preprocess the initial data to get a reduced data set R_D as our experimental data set.

B. Experiment and Evaluation Result

a) Influence of NAT host to domain co-occurrence score

In this section, we simulate a network which contains NAT hosts. We use one day's data flow of a real network of 10,000 hosts as data source, and select 101 hosts from one subnet as a NAT network. Then we add simulated visit data of botnet domain names and compare the domain co-occurrence scores of the two.

We assume that there are 15 botnet domain names (5 known and 10 unknown) and 10 zombies, and do 4 experiments on the conditions that there are 0/1/5/10 zombies in NAT network. In order to simulate more realistically, we also consider the situation in which

zombies may not visit botnet domains due to network problems, program crashes or system stability problems. So the rule of generating simulated visit data of botnet domain names is defined as: select some hosts in both NAT and non-NAT network and each host visit more than 3 of 15 botnet domain names randomly.
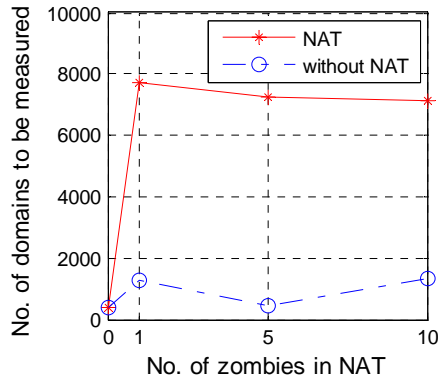

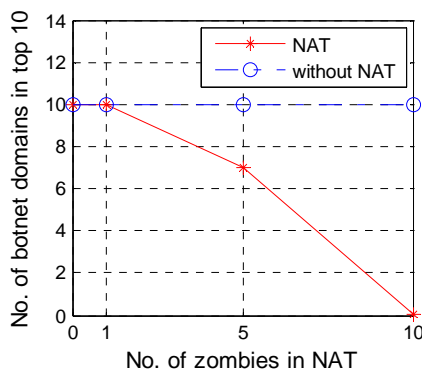Figure 2.   number of domain names candidate with change of number of bots in NAT

Figure 3.   number of botnet domains in co-occrrence scores Top 10 with change of number of bots in NAT

We calculate the domain co-occurrence score from experiments and use Equation 3 to normalize the result to [0, 1], and find out that if there are NAT hosts in network and there are zombies in NAT hosts, then (1): the numbers of domain names before and after the removal of NAT visits are of great difference – nearly 4 times, as is shown in Figure 2;(2) the degree of confidence of malicious domain names calculated by domain co-occurrence score is low if don't remove NAT host's visit, and the degree of confidence is lower while the number of NAT host is increasing, as is shown in Figure 3. Under extreme condition, if all 10 zombies are in NAT network, it will report that there are 1317 domain names whose co-occurrence score are the same and highest, and that means the method is ineffective. Actually, this situation is not impossible because hosts in the same NAT subnet is more probably effected with the same malware[13].

So, this paper is going to analyze the probability distribution of domain co-occurrence score in conditions of different number of zombies in NAT subnet.

There are no zombies in NAT subnet, as is shown in Figure 4(a). The number of domains candidate   is constant, and domain co-occurrence score of one domain

changes little, and the probability distribution of domain co-occurrence score changes little.

There are 1 zombie in NAT subnet, as is shown in Figure 4(b). The influnce to domain co-occurrence score is little because the one zombie in NAT subnet is always regarded as 1 whether it is in NAT or not, and domain co-occurrence score is a little lower because of the noise data generated by other hosts in NAT subnet.

There are 5 zombies in NAT subnet, as is shown in Figure 4(c). This will influence the domain co-occurrence score largely because there are zombies in and out of NAT subnet, the co-occurrence score is lower, and the noise data generated by other hosts in NAT subnet will influence the score too. In this case, the degree of confidence is lower.

There are 10 zombies in NAT subnet, as is shown in Figure 4(d). In this case, all zombies are regarded as one host which will lose the group characteristics, and the large noise generated by other hosts in NAT subnet influence the co-occurrence score largely and make it totally ineffective.
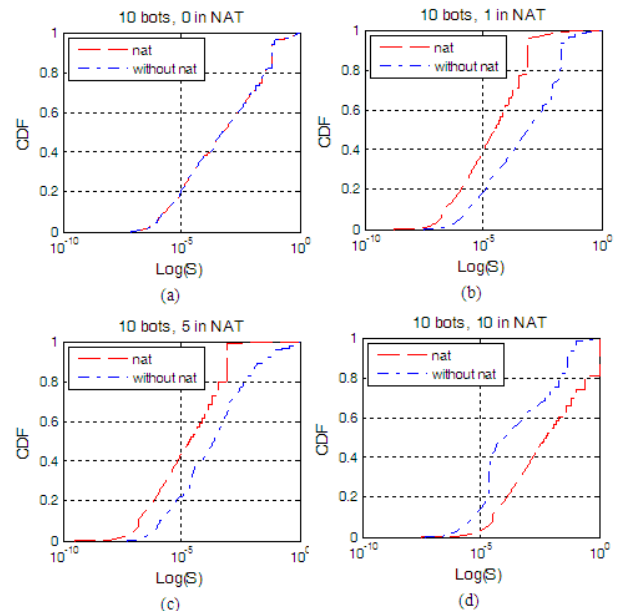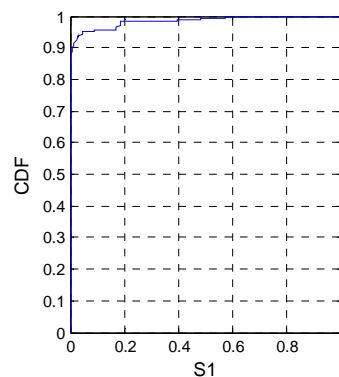

Figure 4.   probability distribution of domain co-occurrence rate with change of number of bots in NAT or without NAT

b)   probability distribution of domain co-occurrence scores of botnets

c) Comparison of Improved co-occurrence score and original method

In this section, we use botnet domain names captured by honeynet to do experiments. We select a botnet which contains many zombies, B_1, and its feature domain names are {ircd.zief.pl, proxim.ircgalaxy.pl, proxima.ircgalaxy.pl}.

We set the time window T as large as 1 day because the number of zombies in education network is small, and set the scale factor α to 0.8 because there are not large scale botnet communication behavior in education

network, and set the NAT identifiable parameter k to 0.95.

Then calculate co-occurrence score $S_1(d_i)$, and the probability distribution is shown in Figure 5. It can be seen that over 95% of domains candidate co-occurrence score are less than 0.2, so we can just focus on very few domain names. We calculate co-occurrence score $S(d_i)$ with original method, and use Equation 3 to set scale factor α to 0, then compare it with improved method. The result is shown in Table 1.

Table 1 Comparison of co-occurrence scores with two methods

Improved method（Number of domains candidate:2115）				Original method（Number of domains candidate:25383）			
Score	Domain Number	Domain Type	Statistics	Score	Domain number	Domain Type	Statistics
1	1	Malicious		1	1	Malicious	
0.948537431	1	Malicious		0.736523725	6	Malicious	
0.891123038	5	Malicious		0.736523725	12	Normal	
0.791713638	1	Malicious	Malicious:15 Normal:20	0.672123485	5	Malicious	Malicious:20 Normal:33
0.570833635	2	Malicious		0.499201044	1	Malicious	
0.483080101	17	Normal		0.263476275	7	Malicious	
0.393204733	3	Normal		0.263476275	19	Normal	
0.305277408	4	Malicious		0.245507908	2	Normal	
0.247863015	1	Malicious					

From Table 1, we can draw the following conclusions.
- With the improved method, the number of domains candidate reduces largely, which will improve computing performance.
- With the improved method, the number of domain names whose co-occurrence scores are larger than 0.2 is 35, 42.9% of which are malicious, meanwhile with the original method, the number of domain names whose co-occurrence scores are larger than 0.2 is 53, %37.7 of which are malicious. So the improved method is better than original one in terms of malicious domain detection percentage. But in terms of detection number, the improved method is less than original one. There are 13 domain names that are detected with both methods, the reason why there are 7 domain names that are detected with original method but are not detected with improved method is that, these domain names only appear in one time window and are relevant to only one zombie, which do not match the group and persistent characteristics of botnet..
- In the result with improved method, the domain names whose score are the same also have the same type, but in the result with original method, the domain names whose score are the same contain both malicious and normal domain names. For example, there are 6 malicious and 12 normal domain names in the 18 domain names whose score are 0.736523725. This shows that the improved method represents the relativity of domain names and group characteristics of botnet better than original one.

In the comparison above, we can use the following rules to detect the domain names whose score is larger than 0.2 whether they are malicious:
- It is announced by security organization as malicious domain or it has malicious URL.
- It has the same second-level domain with known malicious domains, and this second-level domain is not a dynamic DNS provider.
- It has the same prefix with known malicious domains.
- There is no information in search engine about this domain, and it has the same IP address with known malicious domains.

C. Influence factors of co-occurrence score method

There are mainly 3 influence factors of co-occurrence score method: the number of known malicious domains, the number of zombies and online time of zombies. For a given botnet, the more known malicious domains and zombies are, the more the obvious group characteristic is, and the higher the degree of confidence of co-occurrence is. Meanwhile, the longer the online time is, the higher the probability of interaction of zombies and bot master is, and the more obvious the persistent characteristic is, and the higher the degree of confidence of co-occurrence is. In Experiment, we find out a botnet B_2, which has 1 zombie in campus network, and its detection result is shown in Table 2. The result shows that when there are too few zombies in a botnet, the spatial characteristic of the botnet is not obvious. In this case, although we can detect the domain of the botnet, it contains more normal

domains, and this failed to meet the purpose of tracking botnet.

Table2 Sore of Botnet B_2 which has only 1

zombie($S_2(d_i) > 0.5$)

Score	Domain #	Domain Type	Statistics
1	1	Normal	
1	5	Malicious	
0.797601085	1	Normal	Normal:13
0.696537831	1	Normal	Malicious:5
0.590373473	1	Normal	
0.539773744	9	Normal	

V. CONCLUSION

This paper focuses on the network visit behavior of zombies, analyzes the shortage of domain co-occurrence score method by K. Sato, and presents a new method of removing NAT hosts and using domain co-occurrence score to trace botnet. We consider the group and consistent characteristic of botnet, and do further analysis on its spatial characteristics to separate different botnets. Also we introduce score analysis on time dimension to separate the co-occurrence behavior of botnet domains and normal domains. In order to test the validity and reliability of the improved method of co-occurrence score, we use DNS query data flow of Xi'an Jiaotong University as data source to trace botnet, and the experimental result shows that the improved method can detect malicious domain names better. At last, this paper introduces strategies for 3 influence factors of co-occurrence: the number of known malicious domains, the number of zombies and online time of zombies.

The detection method mentioned in this paper requests a stability characteristic of botnet domain name, but in fact there are some botnet whose co-occurrence behavior are hard to detect because their domain names changes very frequently (such as Conficker). So, we are going to expand this method to host co-occurrence behavior in order to trace more botnets.

ACKNOWLEDGMENT

REFERENCES

[1] Vitaly Kamluk. The botnet ecosystem. .(2009-12). http://www.securelist.com/en/analysis?pubid=204792095

[2] Boldizsar Bencsath. Stuxnet. (2010-11). http://www.crysys.hu/courses/gain_adatbiztonsag/stuxnet-material.pdf

[3] D. Dagon, G. Guofei and C. P. Lee, and L. Wenke. A Taxonomy of Botnet Structures Computer Security Applications Conference(ACSAC). Twenty-Third Annual, 2007, p. 325-339. , 2007

[4] J. Goebel, T. Holz. Rishi: Identify bot contaminated hosts by IRC nickname evaluation. Cambridge MA: USENIX Workshop on Hot Topics in Understanding Botnets (HotBots'07), 2007

[5] Konrad Rieck, Guido Schwenk, Tobias Limmer, Thorsten Holz, Pavel Laskov. Botzilla: Detecting the "Phoning Home" of Malicious Software. Lusanne, Switzerland: 25th Symposium On Applied Computing (SAC), Track on Information Security Research and Applications, 2010

[6] Peter Wurzinger, Leyla Bilge, Thorsten Holz, Jan Goebel, Christopher Kruegel, Engin Kirda. Automatically Generating Models for Botnet Detection. Saint Malo, France: European Symposium on Research in Computer Security (ESORICS'09), 2009

[7] McCusker,O., Kiayias, A., Walluck, D., and Neumann, J., A Combined Fusion and Mining Strategy for Detecting Botnets, Proceedings of the 2009 Cybersecurity Applications and Technologies Conference for Homeland Security（CATCH '09）, 2009

[8] Yuanchen He, Zhenyu Zhong, Sven Krasser, Yuchun Tang. Mining DNS for Malicious Domain Registrations. Collaborative Computing: Networking, Applications and Worksharing (CollaborateCom), 2010 6th International Conference, 2010

[9] Xin Hu, Matthew Knysz, Kang G. Shin. Measurement and Analysis of Global IP-Usage Patterns of Fast-Flux Botnets. Shanghai, China: 30th IEEE International Conference on Computer Communications (IEEE INFOCOM 2011), April 2011

[10] R. Villamar´ın -Salomon and J. C. Brustoloni, Identifying botnets using anomaly detection techniques applied to DNS traffic.. Las Vegas, Nev, USA,: the 5th IEEE Consumer Communications and Networking Conference, pp. 476-481, January 2008.

[11] R. Villamar´ın-Salomon and J. C. Brustoloni. Bayesian bot detection based on dns traffic similarity. New York, NY, USA: Proceedings of the 2009 ACM Symposium on Applied Computing(SAC '09) pages 2035–2041, 2009. ACM.

[12] Kazumichi Sato, keisuke Ishibashi. Extending Black Domain Name List by Using Co-occurrence Relation between DNS queries.. San Jose, CA: 3rd USENIX Workshop on Large-Scale Exploits and Emergent Threats (LEET '10), 2010

[13] M. Patrick Collins , Timothy J. Shimeall , Sidney Faber , Jeff Janies , Rhiannon Weaver , Markus De Shon , Joseph Kadane.. Using uncleanliness to predict future botnet addresses. California, USA: Proceedings of the 7th ACM SIGCOMM conference on Internet measurement, October 24-26, 2007

Zhiwen Wang Hunan Province, China. Birthdate: May, 1973. is Computer Architecture Ph.D, graduated from department of Computer Science and Technology of Xi'an JiaoTong. And research interests on high-performance network, network management and survivability of information system.He is a associate professor of Dept. Computer Science and Technology of Xi'an JiaoTong University.

Lu Liu Shaanxi Province, China. Birthdate: Oct, 1987. is Computer Science and Technology, master candidate, Xi'an Jiaotong University. And research interests on network security, botnet detection and tracking.

A New Attack Detection in Large Scale Network based on Entropy

Qin Qia, Zhiwen Wang
Xi'an Jiaotong University, Xi'an, P.R. China
Email: qxia@ctec.xjtu.edu.cn, wzw@mail.xjtu.edu.cn

Abstract—**Intrusion Detection System (IDS) typically generates a huge number of alerts with high false rate, especially in the large scale network, which result in a huge challenge on the efficiency and accuracy of the network attack detection. In this paper, an entropy-based method is proposed to analyze the numerous IDS alerts and detect real network attacks. We use Shannon entropy to examine the distribution of the source IP address, destination IP address, source threat and destination threat and datagram length of IDS alerts; employ Renyi cross entropy to fuse the Shannon entropy vector to detect network attack. In the experiment, we deploy the Snort to monitor part of Xi'an Jiaotong University (XJTU) campus network including 32 C-class network (more than 4000 users), and gather more than 40,000 alerts per hour on average. The entropy-based method is employed to analyze those alerts and detect network attacks. The experiment result shows that our method can detect 96% attacks with very low false alert rate.**

Index Terms— **Network Security; IDS; Shannon Entropy; Renyi Cross Entropy**

I. INTRODUCTION

Network attacks are defined as the operations that disrupt, deny, degrade, or destroy information resident in computer networks or the networks themselves. In recent years, more and more network attacks threatened the reliability and QoS of Internet,compromised the information security and privacy of users. KSN (Kaspersky Security Network) recorded 73 million Internet browsers attacks on their users in 2009, and that number skyrocketed to 580,371,937 in 2010 [1]. Symantec reported that they recorded 3 billion attacks from their global sensor and client [2].

Intrusion Detection System (IDS) is used to monitor and capture intrusions into computer and network systems which attempt to compromise their security [3]. With the development of networks, a large number of computer intrusions occur every day and IDSs have become a necessary addition to the security infrastructure of nearly every organization. However, IDSs still suffer from two problems: 1) large amount of alerts. In fact, more than 1 million alerts are generated by Snort each day in our research; 2) high false alerts rate. Gina investigated the extent of false alerts problem in Snort using the 1999 DARPA IDS evaluation data, and found that 69% of total generated alerts are considered to be false alerts [4]. These problems result in a huge challenge on the efficiency and accuracy of the network attack detection.

Several methods have been applied to resolve the problems of large amount of alerts and high false rate. Pietraszek used the adaptive alert classifier to reduce false alerts, which is trained with lots of labeled past alerts [5]. Whereas, it is difficult to label large volume alerts generated in large-scale network. In order to reduce the false alarms, Mina propose the extend DPCA to standardize the observations according to the estimated means [6]. Spathoulas and Katsikas propose a post-processing filter based on the statistical properties of the input alert set [7]. Cisar employ EWMA to detect attacks by analyzing the intensity of alerts [3]. In our research, 32 C-class subnets are monitored by Snort and more than 1 million alerts are generated every day. Therefore, we propose a method to spot anomalies which is more tolerable for the operator rather than reduce false alerts.

In information theory, entropy is a measure of the uncertainty associated with a random variable, which is widely used to analyze the data and detect the anomalies in information security. Lakhina *et al* argue that the distributions of packet features (IP addresses and ports) observed in flow traces reveal both the presence and structure of a wide range of anomalies. Using entropy as a summarization tool to analyze traffic from two backbone networks, they found that it enables highly sensitive detection of a wide range of anomalies, augmenting detections by volume-based methods [8]. Brauckhoff ind that entropy-based summarizations of packet and flow counts are affected less by sampling than volume-based method in large networks [9]. A. Wagner and B Plattner applied entropy to detect worm and anomaly in fast IP networks [10].

Relative entropy and Renyi cross entropy can be used to evaluate the similarity of different distributions. Yan *et al* use a traffic matrix to represent network state, and use Renyi cross entropy to analyze matrix traffic and detect anomalies rather than Shannon entropy. The results show Renyi cross entropy based method can detect DDoS attacks at the beginning with higher detection rate and lower false rate than Shannon entropy based method [11]. Gu *et al* proposed an approach to detect anomalies in the network traffic using Maximum Entropy estimation and relative entropy [12]. The packet distribution of the

benign traffic was estimated using Maximum Entropy framework and used as a baseline to detect the anomalies.

In this paper, an entropy-based method is proposed to detect network attack. The Shannon entropy and Renyi cross entropy are employed to analyze the distribution characteristics of alert features and detect network attack. The experimental results under actual network data show that this method can detect network attack quickly and accurately.

The rest of the paper is organized as follows: the method is introduced in Section 2, and the experimental results are shown in Section 3. Section 4 is the conclusion and future work.

II. METHODOLOGY

In this paper, Snort is used to monitor the network and five statistical features of the Snort alert are selected. The Shannon entropy is used to analyze the distribution characteristics of alert that reflect the regularity of network status. When the monitored network runs in normal way, the entropy values are relatively smooth. Otherwise, the entropy value of one or more features would change. The Renyi cross entropy of these features is calculated to measure the network status and detect network attacks.

A. Snort Alert and Feature Selection

Each Snort alert consists of tens of attributions, such as *timestamp*, *source IP address* (*sip*), *source port*, *destination IP address* (*dip*), *destination port*, *priority*, *datagram length* and *protocol*, etc. Suppose there are *n* alerts generated in time interval *t*. The alerts set in time interval *t* is denoted as *Alert*(*t*) = {*alert*$_1$, *alert*$_2$, …, *alert*$_n$}.

Assuming there are *m* distinct *sip* and *k* distinct *dip* in *Alert*(*t*), we can generate the distinct source IP addresses set (*SIP*) and distinct destination IP addresses set (*DIP*):

$$SIP = \{sip_1, sip_2, …, sip_m\},$$
$$DIP = \{dip_1, dip_2, …, dip_k\}.$$

Suppose the number of alerts come from *sip*$_i$ is *snum*$_i$, and the number of alerts send to *dip*$_i$ is *dnum*$_i$. The alert number of each source IP (*SNUM*) and destination IP (*SNUM*) can be calculated:

$$SNUM = \{snum_1, snum_2, …, snum_m\},$$
$$DNUM = \{dnum_1, dnum_2, …, dnum_k\}.$$

There are 4 default priorities of Snort alert: 1, 2, 3 and 4. The threat severity gradually weakens from 1 to 4(*high*, *medium*, *low*, *info*). In order to strengthen the threat degree of high severity alerts, the threat degree of the *alert*$_i$ is denoted as *threat*$_i$=5^(4-*priority*$_{alerti}$) in present work. Suppose the threat degree sum of all alerts come from *sip*$_i$ is *sthreat*$_i$, and the threat degree sum of all alerts send to *dip*$_i$ is *dthreat*$_i$. The *threat degree of each source IP* (*STHREAT*) and *destination IP* (*DTHREAT*) can be calculated:

$$STHREAT = \{sthreat_1, sthreat_2, …, sthreat_m\},$$
$$DTHREAT = \{dthreat_1, dthreat_2, …, dthreat_k\}.$$

The datagram length is the size of the packet that breaks the alarm rules of Snort. We search the distinct datagram length of all alerts, and generate the datagram length set

$$DGMLEN = \{dgmlen_1, dgmlen_2, …, dgmlen_x\},$$

where *x* is the number of the distinct datagram length of all alerts. Suppose the number of alerts whose datagram length equal to *dgmlen*$_i$ is *dgmNum*$_i$. The alert number with different datagram length can be calculated:

$$DGMNUM = \{dgmNum_1, dgmNum_2, …, dgmNum_x\}.$$

Above 5 features (*SNUM*, *DNUM*, *STHREAT*, *DTHREAT*, *DGMNUM*) are selected to evaluate the alerts and detect attacks.

B. Shannon Entropy-based Feature Analysis

Shannon entropy is used as measures of information and uncertainty [13]. For a dataset $X = \{x_1, x_2, x_3, …, x_n\}$, each data item *x* belongs to a class $x \in C_x$. The entropy of *X* relative to C_x is defined as

$$H(X) = -\sum_{i=1}^{n} p_i \log_2 p_i \tag{1}$$

where p_i is the probability of x_i in *X*.

The distribution characteristics of *SNUM*, *DNUM*, *STHREAT*, *DTHREAT* and *DGMNUM* are analyzed using Shannon entropy. The entropies of *SNUM* and *DNUM* in time interval *t* can be calculated

$$H(Sip_t) = -\sum_{i=1}^{m} (snum_i/n) \cdot \log(snum_i/n) \tag{2}$$

$$H(Dip_t) = -\sum_{i=1}^{k} (dnum_i/n) \cdot \log(dnum_i/n) \tag{3}$$

The entropy of *STHREAT* and *DTHREAT* can be calculated:

$$H(Sthreat_t) = -\sum_{i=1}^{m} \frac{threat\_of\_sip(i)}{sum\_threat} \cdot \log\left(\frac{threat\_of\_sip(i)}{sum\_threat}\right) \tag{4}$$

$$H(Dthreat_t) = -\sum_{i=1}^{m} \frac{threat\_of\_dip(i)}{sum\_threat} \cdot \log\left(\frac{threat\_of\_dip(i)}{sum\_threat}\right) \tag{5}$$

where *threat_of_sip*(*i*) is the threat sum of the alerts from *sip*$_i$, *threat_of_dip*(*i*) is the threat sum of the alerts to *dip*$_i$, and *sum_threat* is the threat sum of all the alerts in *ALERTS* which can be calculated using

$$sum\_threat = \sum_{i=1}^{n} threat_i \tag{6}$$

The entropy of datagram length is

$$H(Dgmlen_t) = -\sum_{i=1}^{x} (dgmNum_i/n) \cdot \log(dgmNum_i/n) \tag{7}$$

After calculating the entropies of above features, we can use an entropy vector $V(t) = [H(Sip_t), H(Dip_t), H(Sthreat_t), H(Dthreat_t), H(Dgmlen_t)]$ to represent the network status of time interval *t*.

C. Renyi Cross Entropy-based Attack Detection

The Renyi entropy, a generalization of Shannon entropy, is a measure for quantifying the diversity, uncertainty or randomness of a system. The Renyi entropy of order α is defined as

$$H_\alpha(P) = \frac{1}{1-\alpha} \log_2 \sum_r p_r^{\alpha} \tag{8}$$

where $0 < \alpha < 1$, *P* is a discrete stochastic variable, and p_r is the distribution function of *P* [14]. Higher values of α, approaching 1, giving a Renyi entropy which is increasingly determined by consideration of only the highest probability events. Lower values of α,

approaching zero, giving a Renyi entropy which increasingly weights all possible events more equally, regardless of their probabilities. The special case $\alpha\to1$ gives the Shannon entropy. The Renyi cross entropy of order α is derived as

$$I_{\alpha}\left(p,q\right)=\frac{1}{1-\alpha}\log_2\sum_r\frac{p_r^{\alpha}}{q_r^{\alpha-1}}\qquad(9)$$

where p and q are two discrete variables, p_r and q_r are their distribution functions [14]. If α=0.5, the Renyi cross entropy is symmetric, which means $I_{\alpha}(p,q)=I_{\alpha}(q,p)$. In the rest of the paper, when referring to the cross entropy we mean the symmetric case

$$I_{0.5}\left(p,q\right)=2\log_2\sum_r\sqrt{p_rq_r}\qquad(10)$$

The Renyi cross entropy is used to fuse the values of different features. As mentioned above, we use an entropy vector $V(t)=[H(Sip_t),\ H(Dip_t),\ H(Sthreat_t),\ H(Dthreat_t),\ H(Dgmlen_t)]$ to represent the network status of time t, thus the network status can be viewed as a time series of entropy vector $V(1),\ V(2),\ …,\ V(t)$. Before calculating Renyi cross entropy, $V(t)$ is unitized to

$$\overline{V}(t)=[\overline{H}(Sip_t),\overline{H}(Dip_t),\overline{H}(Sthreat_t),\overline{H}(Dthreat_t),\overline{H}(Dgmlen_t)]\quad(11)$$

where

$$\begin{aligned}\overline{H}\left(Sip_t\right)&=H\left(Sip_t\right)\big/H_{sum}\\\overline{H}\left(Sthreat_t\right)&=H\left(Sthreat_t\right)\big/H_{sum}\\\overline{H}\left(Dip_t\right)&=H\left(Dip_t\right)\big/H_{sum}\qquad(12)\\\overline{H}\left(Dthreat_t\right)&=H\left(Dthreat_t\right)\big/H_{sum}\\\overline{H}\left(Dgmlen_t\right)&=H\left(Dgmlen_t\right)\big/H_{sum}\end{aligned}$$

and $Hsum=$ $H(Sip_t)+H(Dip_t)+H(Sthreat_t)+H(Dthreat_t)+H(Dgmlen_t)$.

To determine if there is any change in the network at time t compare with previous time t-1, we use (13) to calculate the Renyi cross entropy of $\overline{V}(t)$ and $\overline{V}(t-1)$

$$I_{0.5}\left(\overline{V}(t-1),\overline{V}(t)\right)=2\log_2\sum_r\sqrt{p_r(t-1)\cdot p_r(t)}\qquad(13)$$

To test whether there is a change, we use

$$\left|I_{0.5}\left(\overline{V}(t-1),\overline{V}(t)\right)\right|\begin{array}{c}Change\\ \substack{>\\<}\quad\eta\\ NoChange\end{array}\qquad(14)$$

The choice of threshold η is network dependent and it can be set as experience. Since our purpose is to detect network attack, it is not enough to compare network status of time t to its previous time t-1, unless we make sure that no attack occurs in time t-1. Thus, the average of the latest n normalized Shannon Entropies is employed to replace the t-1, called $\overline{V}(t,n)$

$$\overline{V}(t,n)=\frac{1}{n}\sum_{i=1}^n\overline{V}(t-i)\qquad(15)$$

Then, we calculate the Renyi cross entropy of $\overline{V}(t)$ and $\overline{V}(t,n)$,

$$I_{0.5}\left(\overline{V}(t,n),\overline{V}(t)\right)=2\log_2\sum_r\sqrt{p_r\left(\overline{V}(t,n)\right)p_r\left(\overline{V}(t)\right)}\qquad(16)$$

and network attack is detected if its absolute is greater than η.

III. Experiment Results

A. Data Collection

In the research, we have used Snort to monitor 32 C-class subnets in the Xi'an Jiaotong University campus network for two weeks, which include more than 4,000 users. In this paper, we select the alerts gathered in 2010-12-6. There are 862,284 alerts with 65 signatures, which come from 42,473 distinct source IP addresses and send to 11,790 distinct destination IP addresses.

As shown in Fig.1, four statistical features of alerts display the trend as the people living customs and habits (the time interval set as 5 seconds). Few alerts are generated in the middle night; then, more alerts are detected from 8:00 to 10:00 when students get up successively; the alerts keep the same trend from 10:00 to 23:30; the alerts collapse at last 30 minutes, since network constraint due to the dormitory administrating rules.

At the same time, the statistical features change abruptly in some time intervals. In general, these abnormal upheavals are the sign of the faults or network attacks.

We select two alerts sets in different time period as training and test data set:

Training data set includes 170,516 alerts generated from 10:00 to 14:00. These alerts come from 13,148 IP addresses and send to 7,570 IP addresses. By analyzing these alerts manually, we identify 87 host scan attacks, 5 port scan attacks, 1 DoS attack and 1 host intrusion.

Test data set includes 578,389 alerts generated from 14:00 to 23:30. These alerts come from 29,327 IP addresses and send to 10,590 IP addresses. By analyzing these alerts manually, we identify 203 host scan attacks, 7 port scan attacks, 6 DoS attack, 3 host intrusion and 1 worm attack.

B. Entropy-based Attack Detection

The training data is evaluated by Shannon entropy, as shown in Fig. 2 (a). We remove the alerts associated to true attacks, which called as *Attack Alert*. The remainders are called as *Flase Alert*. We re-evaluate the *Noise Alert* in the training data set, as shown in Fig. 2 (b). The Shannon entropies are relatively smooth when no attack occurs; otherwise, one or some of the values would change abruptly.

Although the Shannon entropies reflect the regularity of network status, it is difficult to detect attack directly by using five fixed thresholds. Because the Shannon entropy value varies with the activities of end users even the network runs in normal way. In our experiment, the Renyi cross entropy is used to fuse the Shannon entropy of five statistical features to detect attack. As shown in Fig. 3, we calculate the Renyi cross entropy of the alerts in train data set using (13). It is clearly shown that 1) the Renyi cross entropy will change sharply when the network are attacked, see Fig. 3 (a); 2) the Renyi cross entropy will be close to 0 without the large-scale network attacks and failures, see Fig. 3 (b). Thus, it is easy to detect attack using fixed threshold.
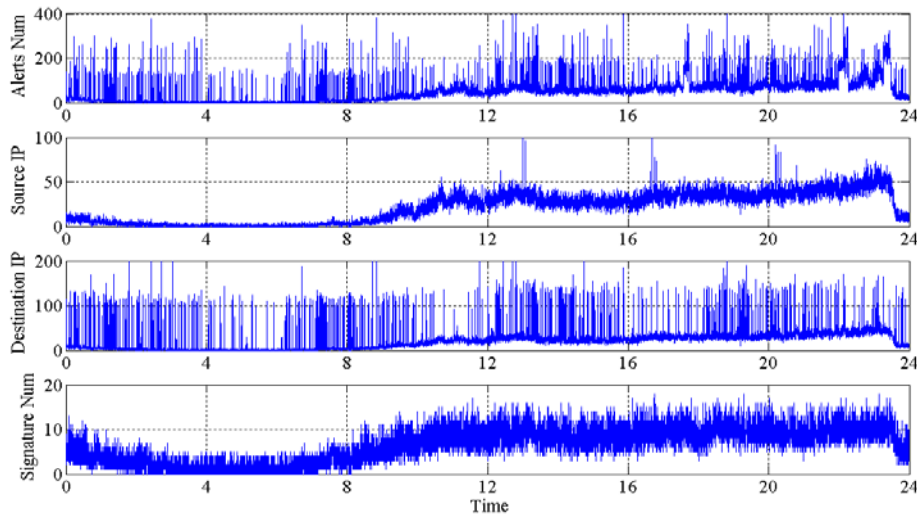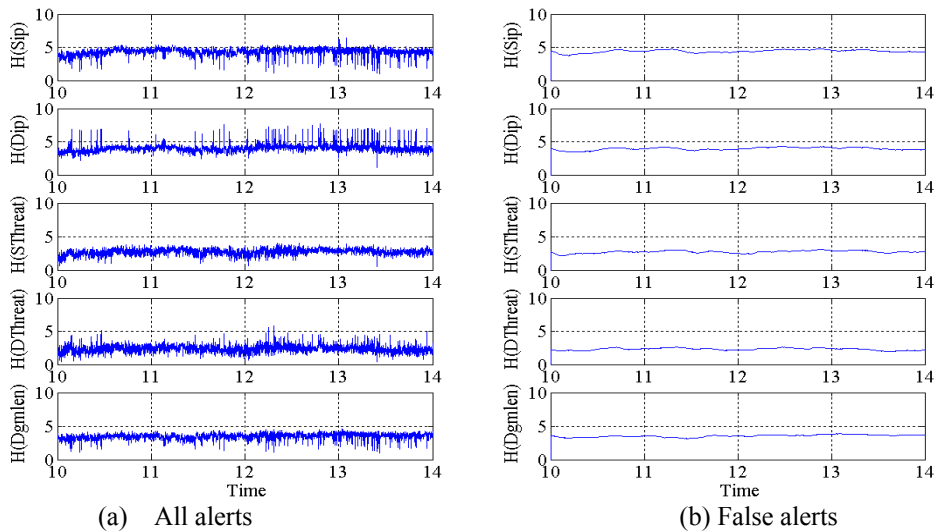
Figure 1. The statistical results of alerts (2010-12-6)

(a)   All alerts

(b) False alerts

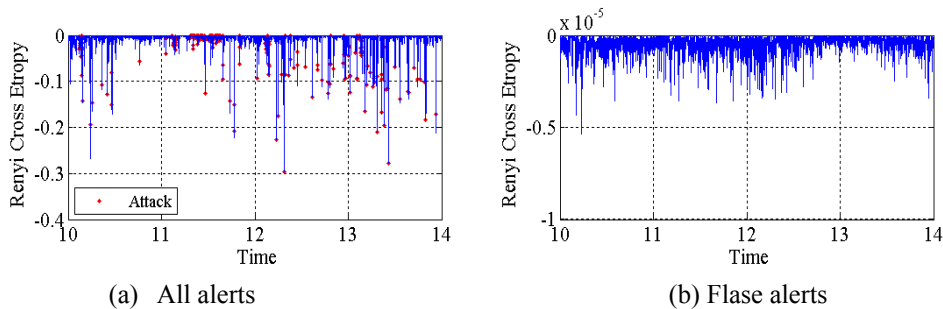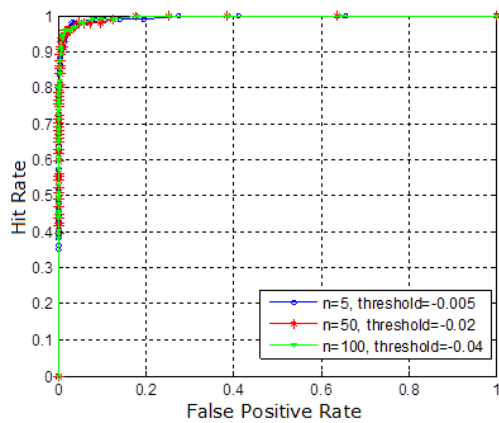Figure 2. Shannon entropy

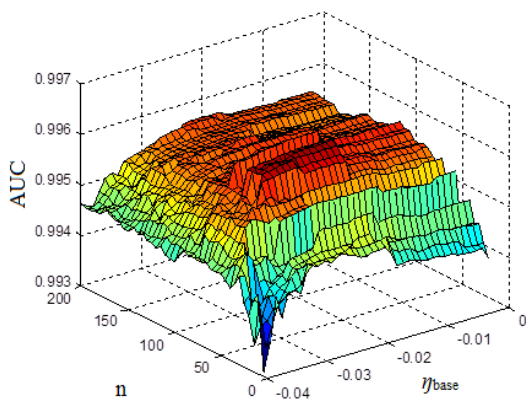(a)   All alerts

(b) Flase alerts

Figure 3. Renyi cross entropy

In the experiments, when η_{detect}=-0.016, 84 attacks can be detected from 94 attacks with 11 false detections. 81 host scan attacks can be detected from 87 host scans. The missed scan attacks last for a relative long time and with small scan density. 1 port scan is detected from 5 port scans. 1 host intrusion and 1 DoS attack are detected successfully.

According to (15) and (16), the n and η are important for the accuracy of attack detection. In the experiments, we set η_{base} = {-0.001, -0.002, -0.003, … , -0.04} and n =

{5, 10, 15, … , 200}. For each combination of η_{base} and n, the training data is analyzed in the following method. Firstly, each $V(t)$ is unitized to $\overline{V}(t)$ using (11) and (12); Secondly, the Shannon entropy can be calculated using (15). Its unitized form is $\overline{V}(t,n)$. Finally, $\overline{V}(t)$ is compared with $\overline{V}(t,n)$ using (16) to calculate Renyi cross entropy value.

(a) ROC

(b) AUC

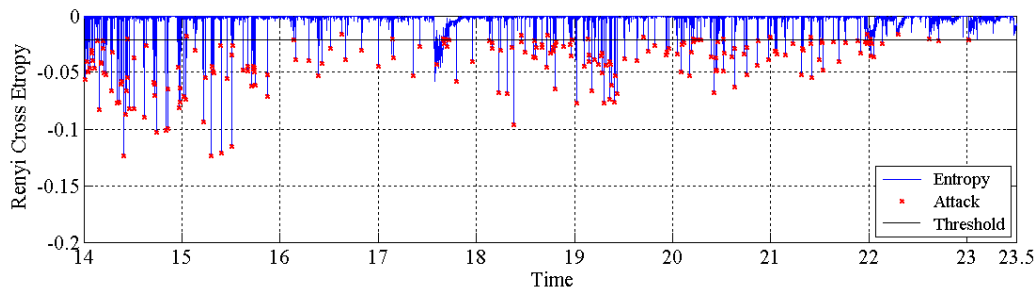Figure 4 Detection result on training data set

In the experiment, ROC (Receiver Operating Characteristic) is used to describe the detection results. ROC is a graphical plot of true positive rate and false positive rate [15]. Fig. 4(a) shows the ROC curve of detection results in training data, where the size of NTS n and base threshold η_{base} equals (5, 0.005), (50, 0.02) and (100, 0.04) separately. When detection threshold η_{detect} comes to 0, almost all the time intervals are detected as network attack. Thus, the detection false positive rate and hit rate are both near 100%. A detection result with high hit rate and low false rate is considered to be a good result. In this case, the ROC curve is plotted at the top left corner, and the AUC value (Area Under ROC Curve) has large value. In this paper, we use AUC value to evaluate the detection results. The best combination of n and η_{base} can be obtained using training data. As shown in Fig. 4(b), the AUC values of all the combinations are calculated, and the highest AUC is 0.9962 when n=95 and η_{base}=-0.022.

C.   Testing

The test data set is analyzed to detect the attacks using entropy-based method. As shown in Fig. 5, 211 attacks can be detected from 220 attacks (detection rate is as high as 96%) with 8 false detections. 197 host scan attacks can be detected from 203 host scans. 4 port scans are detected from 7 port scans. 3 host intrusions, 1 worm attack and 6 DoS attacks are detected successfully.

Figure 5. Attack detection results on test data set

IV.   CONCLUSION

In this paper, a new network attack detection method based on entropy is proposed. The source IP, destination IP, alert treat and alert datagram length are selected from tens of Snort alert attributions. The Shannon entropy is used to analyze the alerts to measure the regularity of current network status. The Renyi cross entropy is employed to fuzz the Shannon entropy on different features to detect network attacks.

In the experiments, the network traffic of more than 4000 users in 32 C-class network are monitored using Snort. 748905 alerts, generated from 10:00 to 23:30 Dec. 6 2010, are selected and separated into training data set and test data set. The experiments show that the Renyi cross entropy value is near 0 when the network runs in normal, otherwise the value will change abruptly when attack occurs. The attack detection rate of entropy method is as high as 96% with only 8 false alerts.

In next step, more alerts from different time segments will be collected to test our method and an attack classification method will be considered.

REFERENCES

[1]. A. Gostev, "Kaspersky Security Bulletin. Malware Evolution 2010," Kaspersky, 2011.

[2]. M. Fossi, G. Egan, K. Haley, E. Hohnson, T. Mack and A. Et, "Symantec Global Internet Security Threat Report Trends for 2010," Symantec, 2011.

[3]. P. Cisar, S. Bosnjak and S. M. Cisar, "EWMA Algorithm in Network Practice," *International Journal of Computers, Communications & Control*, vol.5, pp. 160-170, 2010.

[4]. G. C. Tjhai, M. Papadaki, S. M. Furnell and N. L. Clarke, in Lecture Notes in Computer Science (including subseries Lecture Notes in Artificial Intelligence and Lecture Notes in Bioinformatics), Turin, Italy, 2008, pp. 139-150.

[5]. T. Pietraszek, "Using Adaptive Alert Classification to Reduce False Positives in Intrusion DetectionRecent Advances in Intrusion Detection," vol.3224, pp. 102-124, 2004.

[6]. J. Mina and C. Verde, "Fault detection for large scale systems using Dynamic Principal Components Analysis with adaptation," *International Journal of Computers, Communications & Control*, vol.2, pp. 185-194, 2007.

[7]. G. P. Spathoulas and S. K. Katsikas, in 2009 16th International Conference on Systems, Signals and Image Processing, IWSSIP 2009, Chalkida, Greece, 2009.

[8]. A. Lakhina, M. Crovella and C. Diot, in Computer Communication Review, New York, United States, 2005, pp. 217-228.

[9]. D. Brauckhoff, B. Tellenbach, A. Wagner, M. May and A. Lakhina, in Proceedings of the ACM SIGCOMM Internet Measurement Conference, IMC, Rio de Janeriro, Brazil, 2006, pp. 159-164.

[10].A. Wagner and B. Plattner, in Proceedings of the Workshop on Enabling Technologies: Infrastructure for Collaborative Enterprises, WET ICE, Linkoeping, Sweden, 2005, pp. 172-177.

[11].R. Yan and Q. Zheng, "Using Renyi cross entropy to analyze traffic matrix and detect DDoS attacks," *Information Technology Journal*, vol.8, pp. 1180-1188, 2009.

[12].Y. Gu, A. McCallum and D. Towsley, "Detecting anomalies in network traffic using maximum entropy estimation," in *Proc. 2005 Proceedings of the 5th ACM SIGCOMM conference on Internet Measurement*, pp. 32.

[13].C. E. Shannon, "A mathematical theory of communication," *SIGMOBILE Mob. Comput. Commun. Rev.*, vol.5, pp. 3-55, 2001.

[14].C. E. Pfister and W. G. Sullivan, "Renyi entropy, guesswork moments, and large deviations," *IEEE Transactions on Information Theory*, vol.50, pp. 2794-2800, 2004.

[15].A. P. Bradley, "The use of the area under the ROC curve in the evaluation of machine learning algorithms," *Pattern Recognition*, vol.30, pp. 1145-1159, 1997.

Qin Qia Shan'xi Province, China. Birthdate: May, 1973. She get her master degree of Computer Architecture from Xi'an JiaoTong University in 2003. And current research interests on high-performance network, network management and survivability of information system. As chief editor, she has published 3 textbooks about computer network. Now She is a senior lecturer of Dept. Computer Science and Technology of Xi'an JiaoTong University.

Zhiwen Wang Associate professor, Hunan Province, China. Birthdate: May, 1973. is Computer Architecture Ph.D, graduated from department of Computer Science and Technology of Xi'an JiaoTong. And research interests on high-performance network, network management and survivability of information system.He is a associate professor of Dept. Computer Science and Technology of Xi'an JiaoTong University.

A Dynamic Length Mechanism for Unite Frame on MAC Layer of FCS Based on UWB

Jun Wang
Shenyang University of Chemical Technology, Shenyang, 110142, China
Email: wj_software@hotmail.com

WeiRu Chen
Shenyang University of Chemical Technology, Shenyang, 110142, China
Email: wangjundmu2010@gmail.com

Abstract—**The UWB (Ultra Wide Band) technology can play an effective role in FCS (Fieldbus Control System). But the channel acquisition time of UWB is high, and a lot of packets are short in FCS. So the efficiency of FCS based on UWB will significantly reduce. In this paper, a CSMA/CA protocol with D-UF (Dynamic Length Mechanism for Unite Frame) is proposed. The characteristics of UWB and size of data packets in FCS are taken into account in the CSMA/CA protocol with D-UF. First, the characteristics of UWB and FCS are discussed, and the slot utilization of CSMA/CA protocol is analyzed in different FCS. Finally, the packet assembly policy is designed. At the same time, the performance of the CSMA/CA protocol with D-UF is evaluated in FCS based on UWB by modeling and simulation. Simulation results show that the CSMA/CA protocol with D-UF is effective to increase slot utilization, and improve throughput, and reduce average delay in the FCS based on UWB. It is useful to engineer for designing the FCS based on UWB.**

Index Terms—**dynamic length, FCS, UWB, CSMA/CA**

I. INTRODUCTION

According to the FCC (Federal Communications Commission) regulations, the center frequency of UWB (Ultra Wide Band) is higher than 20%, and its bandwidth is wider than 500MHz. This technology has been used for radar applications and experimental work for over half a century, but it was not allowed to apply in civilian areas. In 2002, the FCC changed the rules that the UWB technology is allowed to use in civilian areas. In 2003, the first FCC-certified commercial system was installed [1].

The UWB technology is a radio technology that is based on modulation of short-nanosecond and low-energy pulse. Since the UWB uses pulse technology, it is capable of being detected in a longer range than other signal forms. Pulse signals can tend to penetrate solid objects, and its effect is better than continuous wave signals. For example, the UWB is used for ground penetrating radar. This characteristic makes the UWB have greater potential for industrial automation applications than exciting other technology. Some bandwidth types are showed in Table I.

TABLE I.
SOME BANDWIDTH TYPES

Type	Center frequency / Bandwidth
Narrowband	≤1%
Broadband	%1≤…≤20%
UWB	≥20% or Bandwidth ≥500Mbps

Fig. 1 shows the comparison of power spectral density between the UWB communication signal and other communication signals:
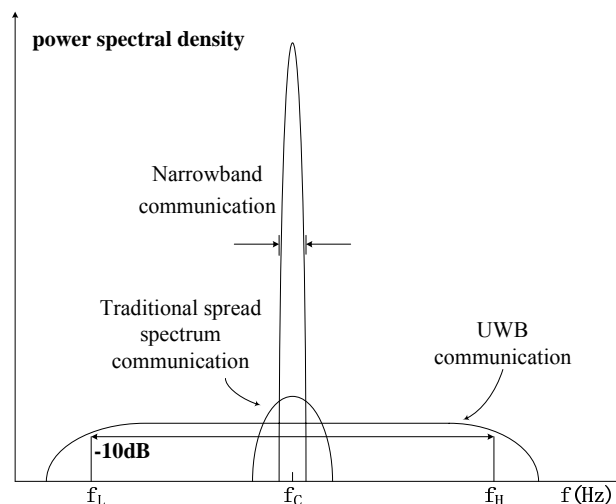

Figure 1.   The comparison of power spectral density between the UWB communication signal and other communication signals.

So far, a lot of researches on UWB technology primarily pay attention to the investigation of behavior in the physical layer [2]. Research has been limited at physical layer of the network protocol stack, and did not relate to higher layers. Previous researches on the DLL (Data Link Layer, it includes MAC and DDL) did not almost consider RF (Radio Frequency) technology that is

used on physical layer. So these research achievements are not suitable for the characteristic of the UWB technology. For instance, one of drawbacks of the UWB technology is that the channel acquisition time is high in its current state. It is a critical challenge that a receiver usually needs tens of micro-seconds or even tens of milliseconds to synchronize with transmitted signals when UWB system is designed, known as timing acquisition problem [3]. At the same time, owing to a lot of short packets in the FCS applications [4-6], the performance of delay and slot utilization will be declined in FCS based on UWB. Hence, we must take into account characteristics of UWB and size of data packet in FCS, and design a new MAC protocol or mechanism for the FCS based on UWB.

Lu et al [7] researched the impact of acquisition time and solved timing acquisition problem by aggregating multiple upper-layer packets into a larger frame. It is a good idea. We introduce to the idea of aggregating multiple upper-layer packets, and design a dynamic length mechanism for unite frame on MAC layer in FCS based on UWB in this paper. The discussion of this topic takes the following structure. Section II analyses some characteristics of typical FCS, and calculates slot utilization when the CSMA/CA protocol is used in the MAC layer of the FCS based on UWB. Section III proposes a dynamic length mechanism for unite frame on MAC layer of FCS based on UWB. In section IV, simulation model is structured, and simulation results are

presented and discussed. Conclusions are provided in section V.

II. SLOT UTILIZATION OF THE CSMA/CA PROTOCOL IN FCS BASED ON UWB

This section will analyze some characteristics of typical FCS and size of their packets, and calculate slot utilization when the CSMA/CA protocol is used in the MAC layer of different typical FCS.

A. FCS Characteristic

Fieldbus is becoming more popular in industrial control systems. Now, some automation systems use the fieldbus technology. Fieldbus, in a first approximation, is a local area network, and it dedicates to connection between sensors, actuators and controllers. They may provide real-time communication in fieldbus control system. The real-time communication is required for manufacturing industry, robots, power plants, cars, trains, aircrafts, building automation applications, and so on.

There are hundreds of different fieldbus protocols in all around the world. Different countries and businesses have established different standards of FCS. The IEC61784 standard classifies fieldbuses into eight types [8-9]. The characteristics of popular fieldbuses are showed in Table II [10]. The size of data packets is almost short in these popular fieldbuses, and this is a distinct characteristic in the FCS applications.

TABLE II
PERFORMANCE AND CHARACTERISTICS OF POPULAR FIELDBUSES

Fieldbus Name	Management Standard	Data Packet Size	MAX Node Number
Interbus-S	DIN 19258	1~512B	256node
WorldFIP	IEC 1158-2	128B	256node
Lon Works	ASHRAE of BACnet	228B	32000node/domain
DeviceNet	ISO 11898 and 11519	1~8B	64node
Profibus-DP, PA	DIN 19245	244B	127node
Fieldbus Foundation	ISA SP50/IEC TC65	1~251B	2~32segment

B. Slot utilization of the CSMA/CA protocol in different types FCS based on UWB

The slot utilization is defined as follow [3]:

$$\mathrm{S}U = \frac{T_d}{T} \qquad (1)$$

Let T_d denote the transmission time of data packet. T is all time for sending a data packet, include the channel acquisition time, the transmission time of RTS/CTS packet, and so on.

The basic wireless MAC protocol is the carrier sense multiple access with collision avoidance protocol (usually known as CSMA/CA protocol), and it has distributed coordination function. Unlike CSMA/CD protocol (carrier sense multiple access with collision detection protocol), the CSMA/CA protocol tries to avoidance collisions before they happen. The CSMA/CD protocol deals with collision by detection. If a node want to transmit a data packet, it will first transmit a short control

packet-RTS (Request To Send), which will include the source address, destination address, and duration time of the following transaction (include transmission time of the data packet and the respective packets-ACK). The destination node will respond (if the medium is free) with a response control packet-CTS (Clear To Send), which will include the same information. The slot configuration of CSMA/CA protocol is showed in Fig.2.
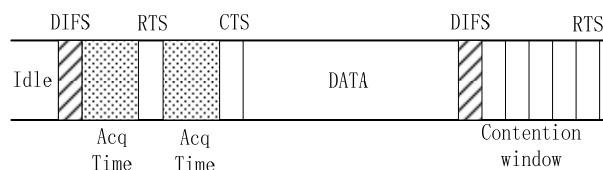

Figure 2.   The slot configuration of CSMA/CA protocol.

Let T_d, T_a and T_r denote the transmission time of data packet, the channel acquisition time and the transmission time of RTS/CTS packet respectively. T_s is the minimum time required to sense carrier (also defined as DIFS in the 802.11 protocol), and T_c is the slot time of contention. When the CSMA/CA protocol is used in the MAC protocol of different typical FCS, the slot utilization is approximately given by (2) [3].

$$SU = \frac{T_d}{T} = \frac{T_d}{T_d + 2T_a + 2T_r + T_s} \qquad (2)$$

The extreme size of data packets in several typical FCS is as follow:
1) Interbus-S: 512B
2) WorldFIP: 128B
3) Lon Works: 228B
4) DeviceNet: 8B
5) Profibus-DP, PA: 244B
6) Fieldbus Foundation: 251B

If the speed of data transmission is 11Mbps and T_a =0.01ms, T_r=0.015ms, T_s =0.005ms.

The transmission time of data packet T_d in different typical FCS is as follows:
1) Interbus-S:

$$T_d = \frac{512 \times 8}{11 \times 10^6} \approx 0.372ms$$

2) WorldFIP:

$$T_d = \frac{128 \times 8}{11 \times 10^6} \approx 0.093ms$$

3) Lon Works:

$$T_d = \frac{228 \times 8}{11 \times 10^6} \approx 0.166ms$$

4) DeviceNet:

$$T_d = \frac{8 \times 8}{11 \times 10^6} \approx 0.006ms$$

5) Profibus-DP, PA:

$$T_d = \frac{244 \times 8}{11 \times 10^6} \approx 0.177ms$$

6) Fieldbus Foundation:

$$T_d = \frac{251 \times 8}{11 \times 10^6} \approx 0.183ms$$

The slot utilization of CSMA/CA protocol in different typical FCS is as follows:
1) Interbus-S:

$$\because T_d + 2 \times T + T_a + 3 \times T_s + T_D$$
$$= 0.4 + 2 \times 0.015 + 0.01 + 3 \times 0.005 + 0.01$$
$$= 0.465ms$$
$$\therefore n = 3$$
$$\frac{T_d}{3 \times TS} = \frac{0.4}{3 \times 0.2} \approx 66.7\%$$

2) WorldFIP:

$$\because T_d + 2 \times T + T_a + 3 \times T_s + T_D$$
$$= 0.2 + 2 \times 0.015 + 0.01 + 3 \times 0.005 + 0.01$$
$$= 0.265ms$$
$$\therefore n = 2$$
$$\frac{T_d}{2 \times TS} = \frac{0.2}{2 \times 0.2} \approx 50\%$$

3) Lon Works:

$$\because T_d + 2 \times T + T_a + 3 \times T_s + T_D$$
$$= 0.2 + 2 \times 0.015 + 0.01 + 3 \times 0.005 + 0.01$$
$$= 0.265ms$$
$$\therefore n = 2$$
$$\frac{T_d}{2 \times TS} = \frac{0.2}{2 \times 0.2} \approx 50\%$$

4) DeviceNet:

$$\because T_d + 2 \times T + T_a + 3 \times T_s + T_D$$
$$= 0.2 + 2 \times 0.015 + 0.01 + 3 \times 0.005 + 0.01$$
$$= 0.265ms$$
$$\therefore n = 2$$
$$\frac{T_d}{2 \times TS} = \frac{0.2}{2 \times 0.2} \approx 50\%$$

5) Profibus-DP, PA:

$$\because T_d + 2 \times T + T_a + 3 \times T_s + T_D$$
$$= 0.2 + 2 \times 0.015 + 0.01 + 3 \times 0.005 + 0.01$$
$$= 0.265ms$$
$$\therefore n = 2$$
$$\frac{T_d}{2 \times TS} = \frac{0.2}{2 \times 0.2} \approx 50\%$$

6) Fieldbus Foundation:

$$\because T_d + 2 \times T + T_a + 3 \times T_s + T_D$$
$$= 0.2 + 2 \times 0.015 + 0.01 + 3 \times 0.005 + 0.01$$
$$= 0.265ms$$
$$\therefore n = 2$$
$$\frac{T_d}{2 \times TS} = \frac{0.2}{2 \times 0.2} \approx 50\%$$

The maximal size of data packet in above FCS is commonly 512B. If the speed of data transmission is 50Mbps and T_a =1ms, then T_d is 0.08192ms. Because the slot time is very low, T_r and T_s may be neglected. Under the circumstances, the slot utilization of CSMA/CA protocol is as follows:

$$\frac{T_d}{T_d + 2T_a + 2T_r + T_s} = \frac{0.08192}{0.08192 + 2 \times 1 + 0 + 0} \approx 3.9\%$$

Evidently, the high channel acquisition time effected on performance of CSMA/CA protocol in the FCS based

on UWB. So we design a dynamic length mechanism for unite frame to alleviate impact of channel acquisition time.

III. THE DYNAMIC LENGTH MECHANISM FOR UNITE FRAME

Because the channel acquisition time of UWB is high, and a lot of packets are short in FCS, we introduce to a dynamic length mechanism for unite frame on MAC layer of FCS based on UWB.

A. The Design of unite frame

We define a new type of data packet, called *unite frame*. Unlike the existing data packet, a *unite frame* may consist of multiple upper-layer data packets, and those data packets are transmitted as one unit. A frame contains only one upper-layer data packet in MAC of IEEE 802.11. This approach of assembling multiple upper-layer data packets may significantly reduce the synchronization overhead in the FCS based on UWB. But we must classify incoming upper-layer data packets and manage buffers effectively so that to reduce the assembly time of *unite frame*. The data packet is classified by the destination address and the priority level of data packets in the FCS based on UWB. The incoming upper-layer data packets can be classified and put into $D \times P$ matrix queue buffer, where D is the total number of destination addresses including possible broadcast and multicast addresses, and P is the total number of priority level of data packets in the FCS based on UWB. We will assemble *unite frame* quickly by above $D \times P$ matrix queue buffer.

B. Realization of dynamic length mechanism for unite frame

Because of interference on industrial environment, wireless communication is not very stable. If the size of *unite frame* (UF) is too large, the probability of interference is greater than short frame on industrial environment. It would generate retransmission phenomenon repeatedly, and the performance of overall channel utilization and average delay is not improved. On the other hand, the buffer maybe not has a number of packets for sending to the same destination at time. The FCS often require real-time, some data packets have to wait until system assembles a UF for the specified size. Regardless of the size of UF, the channel utilization will be low still. The major challenge in an assembly mechanism of UF is that how to merge packets in $D \times P$ matrix queues buffers. Therefore, taking into account the above problem, the size of UF is designed dynamically in this paper.

We define S_{max} and S_{min}, and they respectively represent the maximum size and the minimum size of UF. The maximum size of UF can not larger than S_{max}. When the buffer has no data packets of same destination address, and the size of the UF is not shorter than S_{min}, the mechanism may assemble data packets of lower priority level in $D \times P$ matrix queues buffer than the first data packet in the UF. The UF may be assembled data packets of different priority level, but the destination address of these data packets is the same.

According to FCS characteristics, the dynamic length mechanism for unite frame on MAC layer of FCS based on UWB are as follows:

First of all, the first data packet of the highest priority level in $D \times P$ matrix queues buffer will be took out, and add to UF. The destination address of the UF will be the same as destination address of that data packet. The data packets of the same destination address and the same priority level are added to the UF until the size of UF equals to S_{max}, or the time is overtime. The UF is sent. If there is no data packets of the same destination address and the same priority level, and the size of UF is larger than S_{min}. The UF will be sent. Otherwise, you may add data packets of the same destination address and lower priority level to the UF until the size of UF equals to S_{min}, or the time is overtime.

It should be emphasized that, S_{min} is the Maximum size of UF, when the UF consists of some data packets of different priority level. The pseudo code of the dynamic length mechanism for unite frame on MAC layer of FCS based on UWB is as follows:

```
While(START)
{  p=0;
   d=0;
  for(;d<=ADD_MAX; d++) //ADDD_MAX is the total
                        number  of  destination
                        addresses      including
                        possible broadcast and
                        multicast addresses.
 {
 for(i=0;p<=  P_MAX;  p++)// P_MAX  is  the total
                        number   of   priority
                        level in the FCS.
  {for(n=0;buffers [d][p][n]!=NULL;n++,i++)
  {send_queue[i]= buffers [d][p][n];
   if (size(send_queue[i])< S_max)
   {send_frame(address,send_queue);//sending  unite
                        frame           to
                        physical      layer
                        by      CSMA/CA
                        protocol.
     ...//processing buffers[d][p][n].
    i=0;
   }
 }//there is no data packets of the same destination
   address and the same priority level in buffer.
  if ( size(send_queue[i])>= S_min)
  {send_frame(address,send_queue);
      ...  //processing schedule_packet.
  }
  else
  { j=p,h=0
  While(j<= P_MAX)
   {
  for(;buffers [d][j][h]!=NULL||(send_queue[i])< S_min)
    {send_packet[i]= buffers[d][j][h];
     h++;
```

```
   i++;
 }
 if (S_min<=(send_queue[i]))
 {
   send_frame(address,send_queue);
    ...//processing  schedule_packet.
  break;
 }
 else
  j++;
 }
              // there is no data packets in the same
              destination address and the different
              priority level in buffer.
 send_frame(address,send_queue);
            ...//processing schedule_packet.
 }
```

```
        }// p= P_MAX
       }// d= ADD_MAX
      }
```

VI. SIMULATION AND RESULTS ANALYSIS

In this section, we evaluate the performance of the dynamic length mechanism for unite frame on MAC layer of FCS based on UWB by simulation. We structured simulation model based on the CSMA/CA protocol with dynamic length mechanism for unite frame (D-UF). Fig.3 shows the simulation model.

We choose 100 nodes and they are located in a 100m×100m area. Table III gives the parameters of the simulation model [11-12].
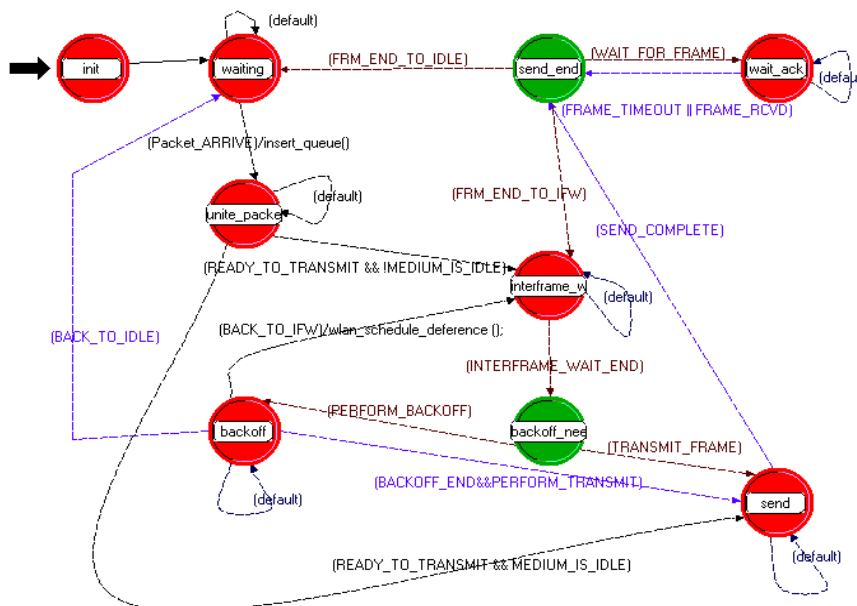
Figure 3. The simulation model.

TABLE III
PARAMETERS AND VALUES

Simulation parameters	Values
Number of nodes	100
Area of network	100 m×100 m
Data packet size	8~2048bytes
Acquisition time	1 ms
RTS	20 bytes
CTS	14 bytes
ACK	14 bytes
Contention slot time	20 μm
Contention window	7,15,31,63
S_{max}	2048 bytes
S_{min}	512 bytes

Fig.4 shows the three major performances: throughput, slot utilization and delay. Clearly, the slot utilization and throughput of CSMA/CA protocol with D-UF is higher than the traditional CSMA/CA protocol. The delay of CSMA/CA protocol with D-UF is lower than the traditional CSMA/CA protocol. Of course, if the data
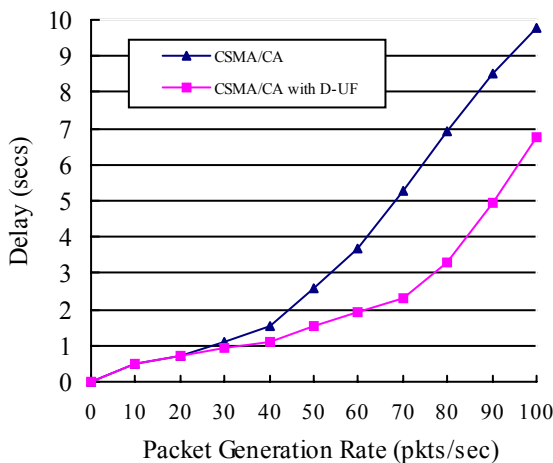
packet size is larger than 2048 bytes, the slot utilization is the same as the traditional CSMA/CA protocol, and the throughput of CSMA/CA protocol with D-UF is lower than the traditional CSMA/CA protocol, and the delay of CSMA/CA protocol with D-UF is higher than the traditional CSMA/CA protocol. But the size of data packets is less than 2048 bytes in FCS.
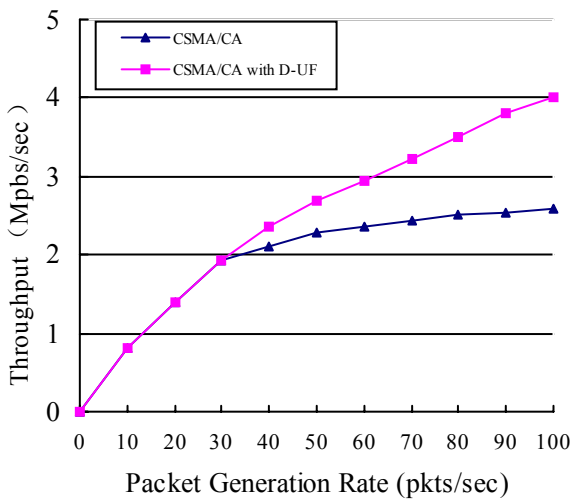
(a)
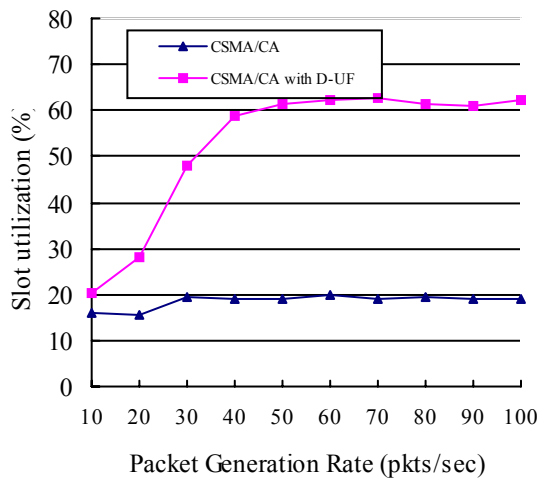
(b)

(c)

Figure 4.   Throughput, slot utilization and delay of two kinds of protocols

Simulation results show that the CSMA/CA protocol with D-UF is more effective than traditional CSMA/CA protocol in the FCS based on UWB.

V. CONCLUSION

The UWB technology is ideally suited for wireless industrial control networks (FCS) in complex and hostile industrial environments. Owing to high channel acquisition time of UWB and a lot of short packets in industrial control system, the efficiency of FCS based on UWB will significantly reduce. We researched the impact of acquisition time and solved timing acquisition problem by aggregating multiple upper-layer packets into a UF. We designed a dynamic length mechanism for unite frame on MAC layer of the FCS based on UWB. The performance on throughput, slot utilization and delay of CSMA/CA protocol with D-UF is better than the traditional CSMA/CA protocol

REFERENCES

[1] Y. Ben-Ezra, M. Ran and B.I. Lembrikov, "Optical transmission of OFDM ultra-wideband signals beyond 40 Gb/s," Journal of Networks, 2010, vol.5, no. 2, pp.140-151.

[2] Raja Jurdak, Pierre Baldi and Cristina Videira Lopes, "U-MAC: A Proactive and Adaptive UWB MediumAccess Control Protocol", Proc IEEE MILCOM, 1998, pp.2111-2124.

[3] J. Ding, L. Zhao, S. Medidi and K. M. Sivalingam, "MAC Protocols for Ultra-Wide-Band Wireless Networks: Impact of Channel Acquisition Time", *Proc IEEE MILCOM*, 1998, pp.59-65.

[4] A. Willig, K. Matheus, and A. Wolisz, "Wireless technology in industrial networks", Proceedings of IEEE, June 2005, vol.93, no. 6, pp.1130–1151.

[5] D. Ma, W. Zhang, and Q.H. Li, "Dynamic scheduling algorithm for parallel real-time jobs in heterogeneous system", Computer and Information Technology. Sept. 2004, pp.462-466.

[6] G. Cena, I.C.Cena, A. Valenzano, "Evaluation of Response Times in Industrial WLANs", IEEE Transactions on Industrial Informatics , Aug. 2007, pp.191-201.

[7] K.J. Lu, D.P. Wu, Y.G Fang, and R.C. Qiu, "On Medium Access Control for High Data Rate Ultra-wideband Ad hoc Networks", Wireless Communications and Networking Conference, March 2005, pp.795-800.

[8] C. Dao Manh, K. Myung Kyun, "Real-Time Communications on an Integrated Fieldbus Network Based on a Switched Ethernet in Industrial Environment", Embedded Software and Systems, vol.4523, 2007, pp.498-509,

[9] P. Matkurbanov, L. SeungKi, A. Valenzano, "A Survey and Analysis of Wireless Fieldbus for Industrial Environments, SICE-ICASE", Oct. 2006, pp5555-5561.

[10] H.C. Ching, K.G. Shin, "Real-time communication in FieldBus multiaccess networks", Real-Time Technology and Applications Symposium, 1995, pp.86-95.
[11] S. Xiao-Ying, Z. Zhen-Chao, "Research of real-time wireless networks control system MAC protocol", Journal of Networks, April 2010, vol.5, no. 5, pp.419-426.
[12] N. Bilel, S. Ye-Qiong, "Performance improvement of CSMA/CA for data gathering scenarios in wireless sensor networks", ComNet 2010, Nov. 2010, pp.1232–1253.

Jun Wang received the B.Sc. and M.Sc. degrees in computer science from the Shenyang Institute of Chemical Technology, PRC in 2001 and 2005, respectively, and the Ph.D. degree from Shenyang Institute of Automation of CAS, PRC in 2009. Currently, he is an associate professor at Shenyang University of Chemical Technology, PRC and leads the Network Engineering Teaching and Research Group in the Department of Computer Science and Technology. Since January 2010, he has been invited as an Academic Visitor (including post-doctoral project as a post-doctor) at De Montfort University, UK.

His research interests include wireless network, software reliability in distributed computing systems and the Internet of things.

Wei-Ru Chen received the B.Sc. and M.Sc. degrees from Northeast University, PRC in 1985 and 1988, respectively. He is currently the head of the Department of Computer Science and Technology Shenyang University of Chemical Technology, PRC.

His research interests include software architecture, software reliability, and data mining.

Cognitive Networks Autonomic Decision-making Approach Based on Influence Diagram

Jin Qi, Shunyi Zhang, Lu Cao, Yanfei Sun, Ling Tan
Nanjing University of Posts and Telecommunications, Nanjing, 210003, China
qijin001@163.com, dirsyz@njupt.edu.cn, glasssnake1989@163.com,
sunyanfei @njupt.edu.cn, cillatan0@163.com

Abstract—The current research focus on the areas such as definition and system structure of cognitive networks (CNs), with the lack of autonomic decision-making theory and approach. In this paper, we proposed an autonomic decision-making approach based on influence diagram for CNs. Utilizing influence diagram to choose and execute the action which maximized the network overall performance can effectively predict the trend in network performance, archive autonomic decision-making and avoid network performance deterioration. The simulation results show that the CNs autonomic decision-making approach given network the abilities of learning, reasoning and autonomic decision-making without any human intervention. As a result, the network cognition has been archived while the network Quality of Service (QoS) has been guaranteed.

Index Terms—Cognitive networks; Influence diagram; QoS; Autonomic decision-making

I. INTRODUCTION

With the rapid development of networks technology, the Internet has already become a huge non-linear dynamic complex system. It faces diverse issues such as multi-service, differences in requirement, dynamic time-varying, and the scarcity of resources, especially, the service diversification and demand differences, which have become the direct driving force to change the traditional Internet application model, QoS requirements and network behavior.

Though currently, the DiffServ and the IntServ architecture, in a certain extent, guarantee QoS, but there are still many problems. First of all, the requirements of different service on QoS parameters such as delay, jitter and packet loss rate are different, and there are lots of difficulties in achieving real-time awareness of service types and distinguishing the service. Next, it lacks of effective methods for reducing serious network burden caused by P2P traffic. In addition, due to lacking of autonomic and intelligence, networks cannot obtain comprehensive knowledge about their own status and behavior. With the increasing complexity of networks, the traditional island style and the static QoS guarantee methods become inefficient and have a passive response to decision-making. Meanwhile, the network is often lack of congestion, low QoS performance. Service transfer and QoS guarantee cannot dynamically adapt to environment. The low utilization of resource of whole network leads to the deterioration of users' requirements of QoS [1, 2]. In

short, the growing complexity of effective management of networks is becoming one of the major challenges.

In this paper, we propose a CNs autonomic decision-making approach based on influence diagram. First, we build a credit evaluation CNs model (CCNM), then we construct influence diagram model (IDM) for CECM, to achieve utility maximization and guarantee QoS. Meanwhile, through the service type credit evaluation mechanism, we limit the complexity of edge routers to make the provision of service-level QoS guarantee possible.

The rest of this paper is structured as follows. Section II presents the related work in CNs. A credit evaluation cognitive networks model is built in Section III. Section IV proposes CNs autonomic decision-making approach based on influence diagram. Simulation results are presented and discussed in Section V. Finally, Section VI concludes this paper.

II. RELATED WORK

At present, the Internet has become increasing complex, difficult to manage and control. Lacking autonomic and adaptive capacity , the ability of Internet perceiving its own status while acquiring its own goals as well as intelligent reasoning is relatively weak [3,4]. CNs, as a potential approach to solve the problems in network, is becoming one of the hottest research issues of Next Generation Networks (NGN) [5, 6, 7].

This section provides an overview of CNs. For further information about CNs, the reader can refer to [8], which provides an excellent overview of the subject.

CNs is an active network with cognitive characteristics, inspired by Cognitive Radio (CR) theory and technology [9]. Its kernel goal is to solve the problem of system structure and application environment complexity rapid increasing caused by heterogeneous and dynamic network access. It provides the decision-making basis for selection of multi-network, channel, routing and service in future communication network, and, at the same time, provides the theoretical basis as well as technical support to guarantee the QoS and end to end goal of seamless smoothing access.

In 2003, the Clarks introduced the concept of knowledge plane (KP) into the network [10]. The KP distribute across the network layers and interact with them to get overall network information which network can utilized to achieve self-configuring, self-healing, self-

optimization and self-protection. Thomas proposed three-tier system architecture of CNs: the behavior target layer, cognitive processing layer and network adjustable software layer [7]. Motorola's FOCALE architecture introduced autonomic management concept into the network, realized cognitive function of the network, whose kernel idea is to enable the network adjust according to the user's requirements and environmental changes through autonomy [11]. Mahonens [12] proposed a cognitive resource management architecture which can interact with communication protocol stack to achieve self-optimization. Dimitrakopoulos demonstrated a method for B3G (Beyond 3G) architecture of the distributed cross-layer re-configuration management approach [13]. Gelenbe utilized a cognitive packet in the process of routing selection which, based on the information of router status collected and carried by the cognitive packet, given the router learning and reasoning abilities as well as optimize routing selection[14]. Autonomic Network Architecture (ANA) and Component-ware for Autonomic Situation-aware Communications and Dynamically Adaptable Services (CASCADAS) are the EU IST FP6 funded network project. The network infrastructure proposed in ANA supports the autonomy between nodes can interconnect flexibly and dynamically reconfigure according to the requirement of users [15]. The kernel goal of CASCADAS is to achieve self-organizing, self-adaptive and communicate situation awareness of its components [16]. EU Seventh Framework Program (FP7) continue supporting researches on the CNs, typical items such as Self-Net, which combines the self-management unit and the feedback control loop together to provide a novel method for the future communication networks [17] .

In General, the current research focus on the areas such as definition and system structure of cognitive networks, it mainly emphasize on the network protocol, cognitive nodes awareness and reconfiguration etc. with the lack of cognitive network QoS theory and technology research. The researches focus mainly on the wireless area [18, 19, 20, 21], and mature on the cognitive core networks research .The more influential is FOCALE architecture proposed by Motorola.

The kernel idea of FOCALE is to adjust the environment according to the users' requirements and environment changes through self-management. In order to change their service and the way of resources provision, the network must be able to change the configuration of network elements properly, namely, calculating the state of network elements and making comparison with the desired state, it can make appropriate adjustment as long as find some difference between them. In addition, in order to adapt the variety network environment, FOCALE can change its function according to the network environment.

FOCALE use double-loop architecture of maintenance loop and adjusting loop. When the current state is the same as the desired state, or the performance of network changes towards the established goals, the maintenance loop will be start and do no adjust. When the network

state deviated from the established goals or does not match with the expected state, enable the adjusting loop. FOCALE can achieve more flexible management through the double-loop architecture. However FOCALE still has many deficiencies：

- Replace the managed network elements by using classes and objects and cannot reflect the state changes in the life cycle, namely, cannot build the network behavior model.
- FOCALE still does not have any mechanism to predict the state of the network or make decisions in advance, makes further process only after a problem emerging in the network. In the core network environment, this approach cannot guarantee QoS of network.

Focus on autonomic decision-making that FOCALE architecture still hasn't achieved yet. We proposed a CCNM in section III.

III. CREDIT EVALUATION COGNITIVE NETWORK MODEL

With the credit evaluation mechanisms of economics and the related theory in artificial intelligence (AI), the CNs function can be realized by building a CCNM in using the method of learning, reasoning and decision making.

A. CCNM Topology

The network topology in CCNM is shown in Fig.1. It mainly consists of edge routers, domain cognitive servers, and central routers.
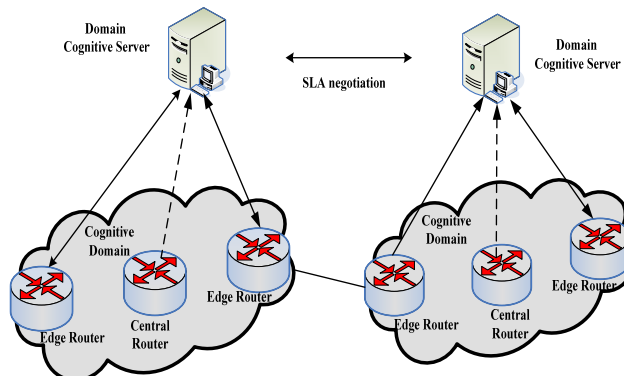

Figure 1. CCNM topology

- Edge Router: Service awareness module is deployed, identify service, and implement the credit penalties for different service based on the policies sent by the domain cognitive servers and mark different DSCP marking for IP packets, the network adjustment will be achieved consequently.
- Cognitive domain server: use the collected information for processing, reasoning, learning and decision making.
- Central Router: collect and upload the packet loss information.
- SLA negotiation: between the cognitive domain servers, the same mechanism as the traditional network.

B. Cognitive Agent for CCNM

This paper propose a cognitive agent which can model the explored environment, choose the best action according to current environment and the utility function, which continues probing, learning and correcting the environment model after the action is implemented. As shown in Fig.2.
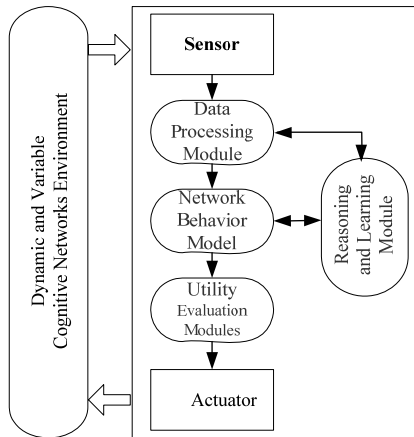

Figure 2. Cognitive agent for CCNM

- Sensor: Count network traffic and packet loss rate, determine the type sign of the IP packet.
- Data Processing Module: Data fusion and processing, produce the samples required by reasoning and learning modules.
- Reasoning and Learning Module: Achieve the network behavior model by reasoning.
- Network Behavior Model: Interact with the reasoning and learning modules to predict the network state.
- Utility Evaluation Module: Map one or more state to a real number used to describe the utility of a certain behavior.
- Actuator: Choose the action which makes the maximum utility values by using the utility function to adjust the network state.

C. Decision-making Model Architecture for CCNM

In this paper, we improve the FOCALE architecture and introduce the credit evaluation mechanism for the decision-making model, as shown in Fig. 3.
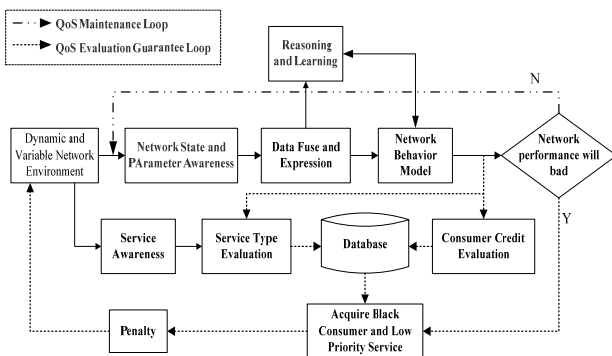

Figure 3. Decision-making model architecture for CCNM

- QoS Maintenance Loop: Start the maintenance loop when the overall performance of the network is predicted well in the next time, only for data collection.
- QoS Evaluation Guarantee Loop: credit evaluation works in two ways, routine and triggered: (1) the routine manner takes the traffic to evaluate credit in network every interval, (2) the triggered manner works once the abnormal is detected. The user will be added into the blacklist and stored into the database when they were found working against the credit. Read the blacklist service from the database and downgrade the corresponding traffic when the overall performance is predicted to be declined.

IV. CNs Autonomic Decision-making Approach Based on Influence Diagram

A. Influence Diagram

Influence diagram, which extends the Bayesian Network by increasing the number of utility nodes and decision nodes, is mostly utilized in decision analysis. Three types of nodes and four types of arcs are included. The three type of nodes are: decision nodes(the square), indicating the decision plans available to the decision maker, chance nodes(the circle), showing random variables, and utility nodes(the diamond), displaying the benefit a decision can bring in-always corresponding a utility function.

The four types of arcs are: (1) relevance arc, connecting two chance nodes or towards from a chance node to a utility node, indicating the function dependence and related probability between them, (2) influence arc, from a decision node to a chance node or a utility node, indicate the effect of the node value the decision node puts on the connected node, (3) information arc, pointing from a chance node to a decision node, indicate the time process and the information the decision maker knows before decision making, (4) no-forgetting arc, from one decision node to another, indicating the strict timing among several decisions that the next decision must be made on the base of the current decision.

B. Building the IDM for CCNM

(1) Determine of Influence diagram node

The traditional definition of the delay, jitter and packet lose rate do not apply to the CNs model proposed in this paper, which should be redefined.

a) *CNs Average Delay.* Suppose there are n paths which each determined by two edge routers, during a time interval T, test the delay on path i every $t(t < T)$, mark the result as d_i, then the average delay of path i within interval T is:

$$\bar{d}_i = \frac{1}{l}\sum_{j=1}^{l} d_{ij} \text{, of which } l = \left\lfloor \frac{T}{t} \right\rfloor \qquad (1)$$

After weighted average, the CNs average delay is:

$$CD = \sum_{i=0}^{n} w_i \overline{d}_i \text{, of which } \sum_{i=0}^{m \times m} w_i = 1 \qquad (2)$$

b) *CNs Jitter.* Suppose the test out delay of path i is d_i, and then the jitter of path i is [22]:

$$J_{ij} = J_{i(j-1)} + (|d_{ij} - d_{i(j-1)}| - J_{i(j-1)})/m \quad (3)$$

$J_{i0} = 0$, considering the complexity, the value of m in this paper is 8. After weighted average, the CNs jitter is:

$$CJ = \sum_{i=1}^{n} w_i J_i \text{, of which } \sum_{i=0}^{m \times m} w_i = 1 \qquad (4)$$

c) *CNs Packet Lose Rate.* During a time interval T, assume the number of lost packets of router i is p_{i_loss} while the number of received packets is $p_{i\_receive}$, then the packet lose rate of router i within interval T is:

$$L_i = \frac{p_{i\_loss}}{p_{i\_receive}} \qquad (5)$$

After weighted average, the packet lose rate of CNs is:

$$CL = \sum_{i=1}^{n} w_i L_i \qquad (6)$$

d) *CNs Input Increment.* Assume the number of IP packets edge router i received from other cognitive domains during a time interval T is $p_{i\_receive}$ while the average of IP packets count by router i is p_{i_length}. Then the input increment within this interval is:

$$CII_t = \frac{I_t - I_{t-1}}{I_{t-1}}$$

$$I_t = \sum_{i=1}^{n} p_{i\_receive} \times p_{i\_length} \qquad (7)$$

e) *CNs Current Load.* During a time interval T, test the queue length of router i, the testing period is t, assume the queue length is l_i while the maxim queue length is l_{i_max}. Then the average queue utilization of router i within the interval T is:

$$\overline{r}_i = \frac{1}{n} \sum_{j=1}^{n} \frac{l_{ij}}{l_{i\_max}} \text{, of which } n = \left\lfloor \frac{T}{t} \right\rfloor \qquad (8)$$

After weighted average, the CNs current load is:

$$CL = \sum_{i=0}^{n} w_i \overline{r}_i \text{, of which } \sum_{i=0}^{m \times m} w_i = 1 \qquad (9)$$

f) *Blacklist Load.* Assume the number of IP packets edge router i received form blacklist service during a time interval T is $bp_{i\_receive}$ while the average length of IP packets count by router i is p_{i_length}. Then the blacklist traffic within this interval is:

$$BL_t = \sum_{i=1}^{n} bp_{i\_receive} \times p_{i\_length} \qquad (10)$$

Here regard the blacklist traffic of time period T as current blacklist load while the blacklist traffic of time period $T+1$ as the future blacklist load.

g) *CNs normalized QoS function.* Combine the formula of power with the overall performance evolution criteria mentioned in reference[23], assume that $\Theta_{i,j}$ is the target of QoS indicator j of service level i while $\Psi_{i,j}$ is the actual value, then the cognitive network normalized QoS function can be described as:

$$\lambda_{i,j} = \frac{\Psi_{i,j}}{\Theta_{i,j}} \qquad (11)$$

$\lambda_{i,j}$ says the user satisfaction, d_i, j_i and l_i, respectively, indicate the normalized network delay, jitter and packet loss rate of service level i of cognitive network. Then, the integrated normalized QoS function can be described as:

$$\lambda_i = \alpha l_i + \beta j_i + \gamma d_i \text{, of which } 0 < \alpha, \beta, \gamma < 1 \text{ and}$$
$$\alpha + \beta + \gamma = 1 \qquad (12)$$

h) *CNs health.* The health of service level i can be described as:

$$CH_i = \frac{T_i^a}{\alpha l_i + \beta j_i + \gamma d_i} \text{, of which } 0 < \alpha, \beta, \gamma < 1$$
$$\text{and} \qquad \alpha + \beta + \gamma = 1 \qquad (13)$$

(2) *Building IDM for CNNM*

This paper, mostly based on the related knowledge about computer network as well as CNs, begin building an IDM form utility nodes [24].

The utility equation of this influence diagram can be described as follows:

$$U(a, CH_1, CH_2, ..., CH_n) = w_1 CH_1 + w_2 CH_2 + ... + w_n CH_n$$
$$= \sum_{i=1}^{n} w_i CH_i \qquad (14)$$

Of which CH_i says the health of service level i, $0 < w_i < 1, and \sum_{i=1}^{n} w_i = 1$ indicate the weight of service i. Thus the father node of utility describes the CNs robustness of each service. Once the father nodes of utility nodes are decided, the next step is to make sure which chance nodes and decision nodes have a direct impact on those father nodes. There are several chance node which might affect the robustness of some service CNs, such as current load(CL), input increment(II), future blacklist load(FBL), whether the special date T, and decision node A. In order to simplify the calculation, the influence diagram has two service levels, as shown in Fig. 4. The node A can either reduce the service level to class 2 or do not handle the case.
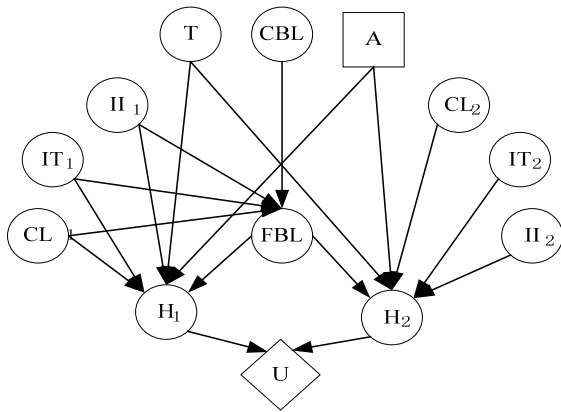
Figure 4.   IDM for CCNM

C. CNs Autonomic Decision-making Approach Based on Influence Diagram

This paper proposed an IDM based autonomic decision-making approach in CNs, of which the basic thought is to archive knowledge presentation, reasoning and learning by utilizing Bayesian Network, to build behavior model of network and to decide the best action though the surrounding based on the influence diagram [25]. The specific steps are as follows:

Step1: Domain cognitive servers perceive the QoS parameters collected by the routers, regard them as training samples, and learn to decide the parameters of Bayesian network.

Step2: In real time cases, cognitive proxy perceive the QoS parameters of routers, namely the value of chance node in influence diagram, utilizing them to instantiate the chance nodes while updating belief through joint tree algorithm.

Step3: Initialize the utility value u to 0, the action value a to null, for each possible action belong to the action set of decision node, do the follow steps:

  a) Instantiate decision node uses this action value.

  b) Calculate the Posterior probability of utility node U's father node H through the Bayesian network inference algorithm as well as the expected value u_i of this action.

If $u_i > u$, a better action can be executed, update u and a : $u = u_i$ and $a = a_i$. If there still actions have not been executed, back to a), else go to Step4.

After every action that belongs to action set A is evaluated, a turn out to be the best action.

Step4: Cognitive proxy execute the action a through an actuator. In fact, this process can be divided into two parts:

  a) Cognitive proxy sends the order executing action a the edge router through appropriate approach.

  b) Edge router, according to action a , changes the policy which service provided, such as reducing the class of users on the blacklist or non-critical service.

Step5: Edge routers continue collecting QoS parameters while uploading them to the domain cognitive server.

  a) If domain cognitive server didn't update the model, namely the parameters of influence diagram, store the parameters in the date base, back to Step2.

  b) If domain cognitive server decides to update the model, back to Step1.

V.   EXPERIMENT AND SIMULATION RESULTS
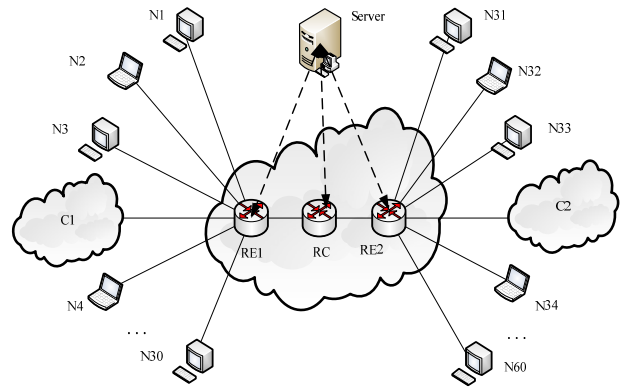
A. NS2 Simulation

Figure 5. Simulation topology

We construct the 'dumbbell' topology simulation environment for CNs as shown in Fig.5. RC represents the central router. RE1 and RE2 represent the edge routers, applying the TSWTCM coloring methods. C1, C2 represent the nodes cloud, applied to simulating the web traffic. N1 …N60, represent the network terminal nodes. The setting of link parameter is shown in Table I. And the setting of background traffic of CNs is shown in Table II.

TABLE I.   SETTING OF LINK PARAMETER

Link	Bandwidth	Delay	Queue schedule	Queue number
RE1↔RC	10M	5ms	dsRED/edge	One physical queue includes 3 virtual queues
RC↔ RE2	10M	5ms	dsRED/edge	
Others	10M	5ms	DropTail	

TABLE II.   SETTING OF BACKGROUND TRAFFIC OF CNS

Traffic name	Produce origin	Traffic direction	Effect
Web traffic	PackMime-HTTP module in NS2 [26]	C1 ↔ C2	C1 models 300 HTTP client servers and 30 HTTP server nodes, and C2 models 70 HTTP server nodes and 200 HTTP clients servers.
FTP	FTP traffic producer in NS2	N32→N2	Interfere traffic
RTP (UDP)	myEvalvid module [27]	N1→N31	DropTail
Random traffic	Traffic generator in NS2	Randomly exceptN1,N2, N32 and N31	Evaluate performance between CNs and TNs

Based on the PHB type of DiffServ and the ITU-T [28] suggestion, this paper divide the service into four classes in CNs model, shown in Table III.:

TABLE III. SERVICE CLASS DIVISION

Service class	The corresponding PHB type of DiffServ	Service type
class 0	EF PHB	Virtual Private Line service
class 1	AF PHB	Guarantee Service
class 2	BE PHB	Best-effort service
class 3	LBE PHB	No guarantee service

Every class has different number of level, the number in level of class0 is easy divided，it can be given different bandwidth according to the requirement of users.Class1 have many level, the divide rule is：

- General users, service classify comply with the IP QoS class divided by ITU-T Y.1514.
- The type of unclear service is viewed as class2.

B. Simulation Results and Analysis

This paper, we only consider the service level of class1 and class2, so the utility equation can be simplified to:

$$U\left(a, H_1, H_2\right) = w_1 H_1 + w_2 H_2 \qquad (15)$$

Compare the different performance between traditional networks (TNs) and CNs in the same background traffic. The TNs in this paper means the traditional DiffServ network, which possess non-cognitive function. CNs means the networks that adopt the CNNM and CNs autonomic decision-making approach based on IDM, which possess a cognitive function.

We adopt Peak Signal-to-Noise Ratio (PSNR) to weigh the performance of the CNs and the TNs. PSNR means the peak signal-to-noise ratio between the recomposed video image and the non-compress video image after the coding and transmission.

We set the value of class1 and class2 in CNs1 $w_1 = 0.6$ and $w_2 = 0.4$, CNs2 $w_1 = 0.8$ and $w_2 = 0.2$.
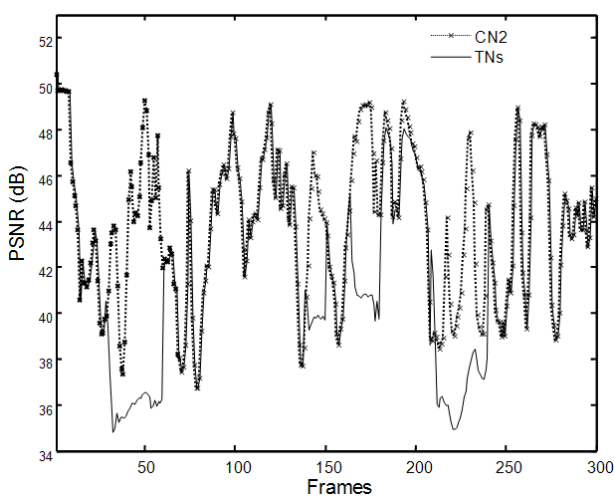

Figure 6. PSNR of RTP after being transmitted by TNs and CNs2

Fig.6. shows the PSNR of RTP video traffic after being transmitted by TNs and CNs2. The declined PSNR value of RTP video traffic transmitted by TNs is much more than CNs2 because of congestion. The reason is the blacklist service level has been declined to class2 in advance when the performance is predicted to be bad by CNs2.

Packet loss still exists due to the heavy network burden thus the PSNR value is influenced, but the extent is smaller than TNs. We can see that CNs autonomic decision-making approach based on IDM provides some QoS guarantee for class1 service, and makes the video quality better guarantee after the network transmission.
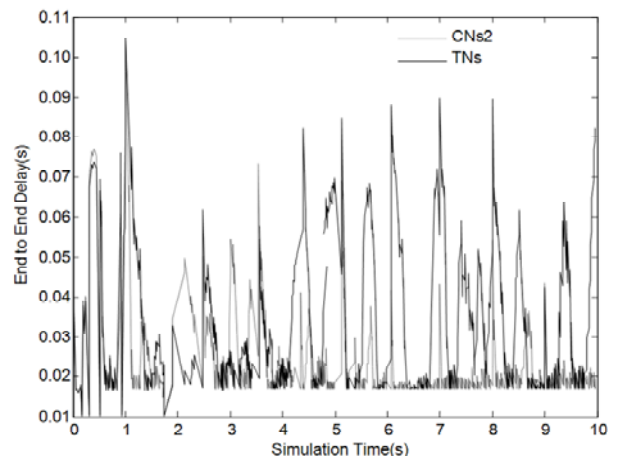

Figure 7. End to end delay of RTP after being transmitted by TNs and CNs2.

Fig.7. shows the end to end delay of RTP video traffic after being transmitted by TNs and CNs2. The X-axis is the beginning time of IP packet transmission, and the Y-axis is the delay of IP packet after network transmission. It can be seen that the delay of RTP video service is obviously improved when the cognitive function is open during network transmission.
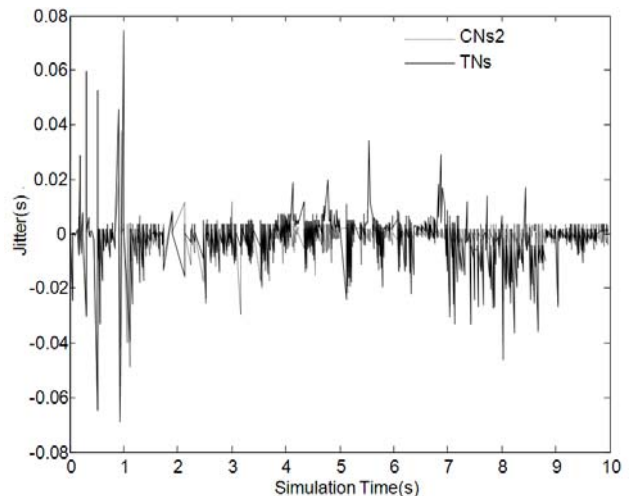

Figure 8. Jitter of RTP after being transmitted by TNs and CNs2

Fig.8. shows the jitter of RTP video traffic after being transmitted by TNs and CNs2. The X-axis is the beginning time of IP packet transmission, and the Y-axis stand for jitter. It can be seen that the jitter of RTP video service is obviously improved when the cognitive function is open during network transmission.
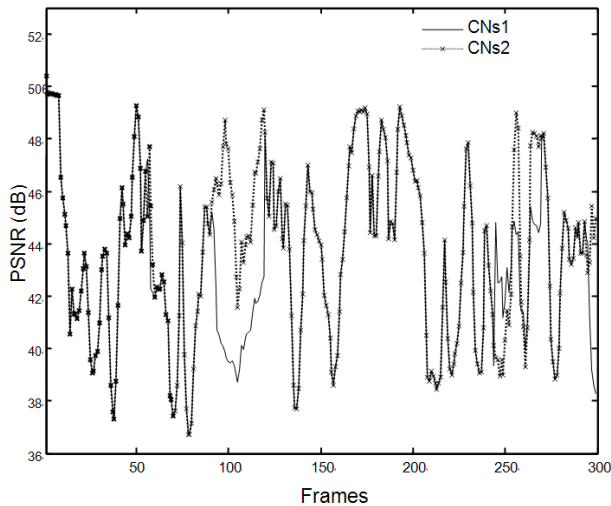

Figure 9. PSNR of RTP after being transmitted by CNs1 and CNs2

Fig.9. shows the PSNR of RTP video traffic after being transmitted by CNs1 and CNs2. It can be seen that the performance of CNs2 is better than CNs1 during QoS guarantee of class2 service. The reason is that the value of class1 and class2 is set $w_1 = 0.6$ and $w_2 = 0.4$ in CNs1 and $w_1 = 0.8$ and $w_2 = 0.2$ in CNs2.
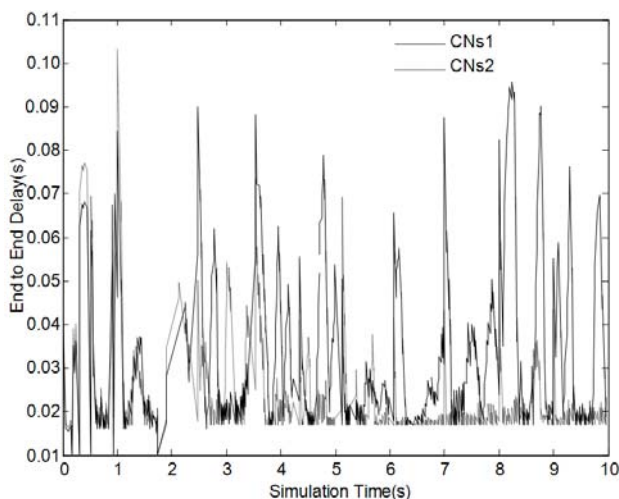

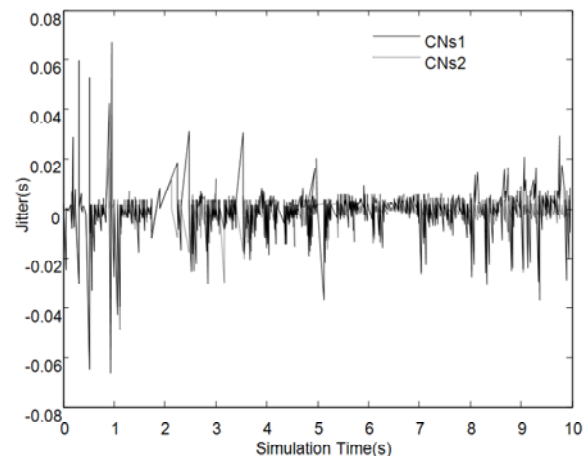Figure 10. End to end delay of RTP after being transmitted by CNs1 and CNs2

Figure 11. Jitter of RTP after being transmitted by CNs1 and CNs2

The meaning of X-axis and Y-axis is the same as Fig.7. and Fig.8. The difference is that Fig.10. describes the end to end delay of RTP video traffic transmitted by CNs1 and CNs2. Fig.11. describes the jitter of RTP video traffic transmitted by CNs1 and CNs2. It can be seen that CNs2 is much more inclined to guarantee QoS of RTP service than CNs1.

In short, both CNs2 and CNs1 are much more inclined to guarantee QoS of RTP service than TNs. With the same structure of influence diagram and utility equation but different weight, CNs2 is much more inclined to guarantee QoS of RTP service than CNs1.

VI. CONCLUSIONS

The proposed CCNM, which refers to the DiffServ architecture, limits the complexity to edge routers, has excellent expansibility. The FOCALE architecture has been expanded while the service type and user credit evaluating mechanism has been introduced, which has excellent flexibility, greatly reduced the cost on the identification of each user and each service. This paper built the influence diagram model for CCNM while proposed a CNs autonomic decision-making approach based on IDM. This approach utilized the parameters of Bayesian network to learn the joint tree algorithm and the other relevant algorithms to achieve CNs self-learning and self-reasoning, and, at the same time, execute the action which maximized the value of utility function, finally achieve CNs autonomic decision-making.

The proposed model for CCNM and the CNs autonomic decision-making approach based on IDM provided a new idea for actual using of CNs theory, for network QoS guarantee, especially, the QoS of service level.

From the CNs QoS requirements, although promising results have been obtained, we are currently investigating some aspects that can be further improved, such as improvement of the relevant Bayesian network structure learning algorithm, through learning the Bayesian network structure form the training examples as well as the combination with other relevant knowledge of this field, achieve a more precise influence diagram model.

REFERENCES

[1] Wojciech B, Andrzej B, Halina Tarasiuk et al. "Provision of end-to-end QoS in heterogeneous multi-domain networks," Annals of Telecommunications, Vol.63, 2008, pp. 559-577.

[2] Chuang Lin, Yuan-Zhuo Wang, Feng-Yuan Ren, "Research on QoS in Next Generation Network", Chinese Journal of Computers, Vol. 31 No. 9, Sept. 2008, pp. 1525–1535.

[3] England U. K, M. Sifalakis, M. Mavrikis, G. Maistros, "Adding reasoning and cognition to the Internet". Proceeding of the 3rd Hellenic Conference on Artificial Intelligence, May, Samos, Greece, 2004.

[4] Ryan W. Thomas, Daniel H. Friend, et.al. Cognitive Networks: Adaptation and Learning to Achieve End-to-End Performance Objectives", IEEE Communications Magazine In Communications Magazine, IEEE, Vol. 44, No. 12. Dec.2006, pp.51-57.

[5] Guy P, Harry P, "Special issue: QoS, control, and security in next generation networks", Telecommunication Systems, Vol.39, No.169, 2008.

[6] Future Internet Design Meeting, FIND2008, http://find.isi.edu,April8-9,2008, Los Angeles,CA.

[7] R.W. Thomas, L.A.DaSilva, A.B. MacKenzie, "Cognitive networks", in: Proc. of the First IEEE International Symposium on New Frontiers in Dynamic Spectrum Access Networks, Baltimore, MD, USA, November 8–11, 2005, pp.352-360.

[8] Carolina Fortuna, Mihael Mohorcic, "Trends in the development of communication networks: Cognitive networks," Comput. Netw. (2009).

[9] S. Paul, J. Pan, and R. Jain, Architectures for the future networks and the next generation Internet: A survey. Computer Communications, Vol.34 pp.2-42, Jan. 2011.

[10] D. D. Clark, C. Partrige, J. C. Ramming, et al. "A knowledge plane for the internet", Proceedings of the SIGCOMM on Applications, technologies, architectures and protocols for computer communications(SIGCOMM 03), Karlsruhe, Germany, Aug.2003.

[11] J. Strassner, "The role of autonomic networking in cognitive networks", in: Q.H. Mahmoud (Ed.), Cognitive Networks: Towards Self-Aware Networks, John Wiley and Sons, Jul.2007.

[12] Petri Mähönen, Marina Petrova, Janne Riihijärvi, Matthias Wellens, "Cognitive wireless networks: your network just became a teenager", Proceedings of IEEE INFOCOM 2006 , Barcelona, Catalunya, Spain, 2006.

[13] G. Dimitrakopoulos, K. Tsagkaris, K. Demestichas, et al, "A management scheme for distributed cross-layer reconfigurations in the context of cognitive B3G infrastructures". Computer Communications, Vol.30, Dec.2007, pp.3807-3822.

[14] E. Gelenbe, R. Lent, A. Nunez, "Self-aware networks and QoS", Proceedings of the IEEE on Evolution of Internet Technologies, Vol.92, Sept. 2004, pp. 1478-1489.

[15] Autonomic Network Architecture. ANA Project [DB/OL]. http://www.ana-project.org, 2010-2-8.

[16] Luciano Baresi, A. D. Ferdinando, Antonio Manzalini and Franco Zambonelli, "The CASCADAS framework for autonomic Communications", Autonomic Communication, 2009, pp.147-168.

[17] A. Kousaridas, N. Alonistioti, "Self-organizing cognitive network elements for next generation communication system", Proceedings of Networking and Electronic Commerce Research Conference Riva Del Garda, Italy, 2009, pp.145-156.

[18] E. Re, G. Gorni, L.S. Ronga, et al, "Flexible and Dynamic Use of Spectrum: The Cognitive Radio Approach. Globalization of Mobile and Wireless Communications", 2011, pp.159-183.

[19] X. Yang, K. Lei, S. Peng, XY. Cao, "Blind Detection for Primary User Based on the Sample Covariance Matrix in Cognitive Radio", Communications Letters, IEEE, Vol.15, Jan.2011, pp. 40-42.

[20] J. Bazerque, G. Giannakis, "Distributed spectrum sensing for cognitive radio networks by exploiting sparsity", IEEE Transactions on Signal Processing, Vol.58(3), 2010, pp.1847.

[21] K. Zeng, P. Paweczak, and D. Cabric, "Reputation-based cooperative spectrum sensing with trusted nodes assistance", Communications Letters, IEEE, Vol.14 (3), Mar. 2010, pp.226-228.

[22] H. Schulzrinne, S. Casner, R. Frederick, et al, "RTP: A Transport Protocol for Real-Time Applications", IETF Technical Report RFC 3550, July 2003.

[23] L. L. Peterson, B. S. Davie. "A System Approach (2nd edition)", Morgan Kaufmann Publisher, Inc, pp.454-457, 2000.

[24] R. A. Howard, J. E, "Metheson. Influence diagrams", Decision Analysis, Vol.2(3) , 2005, pp. 127-143.

[25] Gui song Huang, "Research on QoS Method of Cognitive Network Based on Intelligent Theory", Nanjing, Nanjing University of Posts and Telecommunications, 2011.

[26] Network Simulator Version 2nd. The Ns Mannul [DB/OL]. http://www.isi.edu/nsnam/ns/, 2010-4-20

[27] YD/T 1703-2007. Carrier-class IP QoS architecture. Beijing, China Communications Standards Association,2007.

Jin Qi was born in Shandong, China, in 1983. He received his M.S. degrees from Jiangnan University in China in 2008. He now is a PhD candidate of communication networks in Nanjing University of Posts and Telecommunications. His current research interests include Cognitive Networks, Internet of Things, Network Management and Artificial Intelligence.

Shunyi Zhang was born in Nanjing, Jiangsu, China, in 1944. He is a Professor of Nanjing University of Posts and Telecommunications. He also is a member of the director board for the branch of Chinese Institute of Electronics, and Chinese Institute of Telecommunications. His current interest is in computer Network, IP technology, and Next Generation Network.

Lu Cao was born in Jiangsu, China, in 1989. Her current interest is in Cognitive Networks, IP technology, and Network Management.

Yanfei Sun was born in Shandong, China, in 1976. He is a PhD and associate Professor of Posts and Telecommunications. His current interest is in Communication Networks, IP technology, and Cognitive Networks.

Ling Tan was born in Jiangsu, China, in 1979. She received his M.S. degrees from Nanjing Normal University in China in 2004. He now is a PhD candidate of computer networks in Nanjing University of Posts and Telecommunications. His current research interests include Sensor Networks, Internet of Things, Network Management and Artificial Intelligence.

Multi-amplitude Differential Space-time Block Coding Scheme for Square/Non-Square Code Matrix in MIMO Systems

Xiangbin Yu, Xiaomin Chen,Yuyu Xin, Qiuming Zhu, Dazhuan Xu
Nanjing University of Aeronautics and Astronautics, Nanjing, China
Email: yxbxwy @gmail.com

Abstract—**Differential space-time coding (DSTC) technique has become a good choice when channel estimations are difficult to obtain in multiple antennas system. On the basis of analyzing the existing DSTC schemes, by introducing multi-level quadrature amplitude modulation (MQAM) and matrix transform method, we develop a multi-amplitude differential space-time block coding (STBC) scheme for square or non-square code matrix in MIMO systems, and give the derivation of calculation formulae of the coding advantage in detail. The developed scheme can effectively avoid the performance loss of conventional DSTC schemes based on PSK modulation (i.e. single amplitude DSTC) in high spectrum efficiency. It can be applied to non-square code matrix case, and thus overcomes the shortcoming that existing DSTC schemes are only suitable for square code matrix. Compared with single amplitude DSTC schemes, our scheme has higher spectrum efficiency by carrying information not only on phases but also on amplitudes. Moreover, our scheme has linear decoding complexity, higher coding advantage, and higher code rate for more than two antennas. The simulations results show that the proposed scheme can provide lower BER than the existing single amplitude differential STBC schemes for both square and non-square code matrices.**

Index Terms—**Differential detection; space-time block code; coding advantage; multiple-input multiple-output (MIMO); multi-amplitude modulation**

I. INTRODUCTION

Recently, transmit diversity technique has received considerable attention in multiple-input multiple-output (MIMO) communication systems due to its diversity gain [1-5]. MIMO systems can attain the transmit diversity by employing space-time block coding (STBC) schemes [2-5]. The STBC for two transmit antennas is firstly proposed by Alamouti [4], and then a general framework of space-time block codes by using the orthogonal design theory for different antennae is developed by Tarokh *et al* [3]. The STBC schemes can achieve full transmit diversity with the use of maximum- likelihood (ML) decoding. As a result, it has been adopted as the open-loop transmit diversity scheme in the current 3GPP standards. Considering that the encoding complexity of high-rate multi-antenna STBC schemes, two simple and effective orthogonal STBC schemes are developed in

Refs.[6, 7]. Unfortunately, all these scheme designs are based on the assumption that channel state information (CSI) is perfectly known at the receiver, and unknown at the transmitter, whereas in practice, accurate CSI is difficult to achieve either due to rapid changes in the channel or due to the overhead needed to estimate a large number of parameters such as in a MIMO system [8]. Thus, the differential modulation scheme becomes an attractive alternative.

With differential detection, CSI is not required either at the transmitter or at the receiver. In [9] and [10], Hughs and Hochwald *et al*. independently developed differential unitary space-time coding (DUSTC) schemes based on group codes. These schemes can allow easy realization at the transmitter, but they require group structure and have exponential decoding complexity, which will make their use formidable in practice. In [11], Tarokh *et al*. proposed a simple differential space-time block coding (DSTBC) scheme based on conventional STBC [11], but the scheme is limited in 2 transmit antennas. For this, in a subsequent work, they also proposed a multi-antenna space-time coding scheme for more than 2 transmit antennas [12], but the scheme was still limited in existing STBC structure, and the code-rate is only 1/2, corresponding decoding method is also complex. Afterwards, Ganesan *et al*. presented a differential STBC scheme based on amicable orthogonal design [13]. Compared to the above scheme, the scheme has lower computational complexity, and need not the algebra group structure. By exploiting the rotational invariance of unitary matrices and the property of MPSK modulation, the constellation design for differential space-time modulation is provided in [14]. In [15], the error probability performance of differential orthogonal STBC is analyzed, and the simulation results confirm the accuracy of theoretical analysis. Based on the existing DUSTC, a differential space-time coding design for a MIMO system employing switch and stay combining at the receiver is presented in [16].

Unfortunately, the above schemes basically need to employ the multi-level phase shift-keying (MPSK) constellation, that is, the transmitted symbols are all from the unitary constellation and the corresponding encoded matrix has unit-level. As a result, the minimum distance between symbols become smaller when spectrum

efficiency gets higher, and the minimum product distance between the two encoded matrices also become smaller accordingly, which will bring about the obvious decrease of coding advantage (as defined in [9]) and the loss of system performance. These conclusions can also be achieved from Table I in [9] and Table I in [13]. Considering that multi-level quadrature amplitude modulation (MQAM) scheme has better performance than corresponding MPSK modulation under the same spectrum efficiency, multiple amplitudes DSTBC scheme using MQAM are presented in [17-20], respectively. They obtain better performance than the corresponding DSTBC scheme based on MPSK modulation. However, these schemes are limited to the square STBC scheme (i.e. corresponding code matrix is square) only, which is also main disadvantage in [17]. Moreover, the schemes from Refs.[19-20] are only designed for two transmit antennas and one receive antenna case, the scheme in [18] only suits square STBC with amicable orthogonal design. Motivated by the reason above, by introducing transform matrix and MQAM method as well as simple STBC [7,8] structure, we develop a simple and effective multi-amplitude DSTBC scheme for general STBCs on the basis of Ref.[17], and give specific decoding scheme for multiple receive antennas. The corresponding coding advantage is also analyzed and calculated in detail by means of derivation. The scheme not only suits general STBC schemes with square code matrix, but also can be applied in the case of non-square code matrix, such as the code matrices from 3,5,6,7 transmit antenna, etc. Similarly, it can make use of not only the phase but also amplitude to carry information to improve the spectrum efficiency. Moreover, by using MQAM method, the constellation matrices are no longer limited in unity constellation, they will have different amplitudes, and thus the minimum produce distance will also be increased. As a result, we can improve the performance of pervious code matrix and avoid the performance degradation in high spectrum efficiency. Compared with existing DSTBC based on MPSK modulation, the scheme has lower BER and implementation complexity, and higher spectrum efficiency and coding advantage.

Throughout the paper the superscripts $(\cdot)^T$, $(\cdot)^*$, $(\cdot)^H$ are used to stand for the transpose, complex conjugate, and Hermitian transpose respectively. We denote $E\{ \cdot \}$ and $\mathbf{I}_{N \times N}$ as expectation and $N \times N$ identity matrix, respectively.

II. SYSTEM MODEL

In this section, we consider a wireless multi-antenna communication system with N transmit antennas and K receive antennas operating over a flat and quasi-static Rayleigh fading channel represented by a $N \times K$ fading channel matrix $\mathbf{H}=\{h_{n,k}\}$. The complex element $h_{n,k}$ denotes the channel gain from the n-th transmit antenna to the k-th receive antenna, which is assumed to be constant over a frame of P symbols and varied from one frame to another. The channel gains are modeled as independent complex Gaussian random variables with

zero-mean and variance 0.5 per real dimension. Let V_i be the code matrix with $P \times N$ at time i, then at the receiver, the received signal matrix X_i can be expressed as

$$X_i = \sqrt{\gamma}V_i H + Z_i \qquad (1)$$

where Z_i is $P \times K$ complex Gaussian noise matrix, whose elements are independent, identically distributed (*i.i.d*) complex Gaussian random variables with zero-mean and unit-variance. So at the receiver, the received signal for receive antenna k ($k=1,2,\ldots,K$) can be written as

$$x_{i,t,k} = \sqrt{\gamma} \sum_{n=1}^{N} v_{i,t,n} h_{n,k} + z_{i,t,k} \qquad (2)$$

where the coded symbols from code matrix are normalized to obey $E\{\sum_{n=1}^{N} |v_{i,t,n}|^2\} = 1$, and thus it can ensure that γ is the expected signal-to-noise ratio (SNR). Let the code matrix index be i and time epoch index within the code matrix be t. $\{z_{i,t,k}\}$ are elements of noise matrix Z_i. The structure diagram of a MIMO wireless communication system with N transmit antennas and K receiver antennas is illustrated in Fig.1.
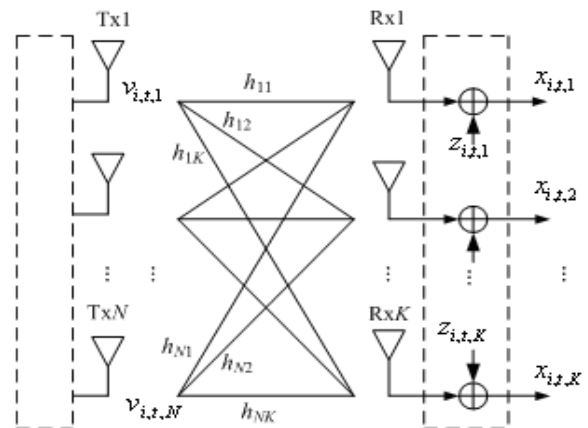

Figure 1. Structure diagram of a MIMO wireless communication system

III. MULTIPLE LEVELS CODE MATRIX

Let L, N and P be positive integers, a conventional STBC is defined by a $P \times N$ dimensional transmission matrix D, every entry of which is linear combination of the L input symbols d_1, $d_2,\ldots,d_L$ and their conjugates d_1^*, $d_2^*,\ldots d_L^*$, and it satisfies the following complex orthogonal condition:

$$D^H D = (\sum_{l=1}^{L}|d_l|^2)I_{N \times N} \qquad (3)$$

where N and P are the numbers of transmit antennas and time slots used to transmit L input symbols, respectively. The input symbols $\{d_l, l=1,\ldots,L\}$ represent the information-bearing binary bits to be transmitted. In a signal constellation such as PSK or QAM having 2^b constellation points, a b binary bits is used to represent a symbol d_l. So a block of Lb binary bits is entered into the STBC encoder at a time. Considering that L symbols are transmitted over P time slots, the rate of the STBC is defined as $R_{STBC} =L/P$ [3,5]. Here, we first consider that

the code matrix of STBC is square, i.e., $N = P$. So $D^H D = DD^H$ in terms of (3).

For convenience of analysis, we define the amplitude of matrix based on Ref.[19]: For a $N \times N$ matrix S, if a nonnegative scalar ρ satisfy the $SS^H = S^H S = \rho^2 I_{N \times N}$, then ρ is defined as the amplitude of matrix S. Let the data symbols $\{d_l, l=1,\dots,L\}$ be taken from the QAM or PSK constellation with unit average energy. Then the code matrix is $G = D / \sqrt{L}$ in terms of [19]. Thus according to (3), we have

$$G^H G = \frac{1}{L} \sum_{l=1}^{L} |d_l|^2 I_{N \times N} = \rho_G^2 I_{N \times N}, \quad G = D/\sqrt{L}. \quad (4)$$

where $\rho_G = \sqrt{\sum_{l=1}^{L} |d_l|^2 / L}$, thus ρ_G is called the amplitude of G based on the above amplitude definition. Then the set of all possible code matrices will form a constellation Ψ [19]. If d_l ($l=1,\dots,L$) is from MPSK symbol, $\rho_G=1$ for all G, and the corresponding Ψ is called a constellation with single amplitude, i.e., it is unitary constellation, the conventional differential space-time coding scheme is based on this. If d_l ($l=1,\dots,L$) is from MQAM, ρ_G will take some discrete values, and Ψ is called a constellation with multiple amplitudes accordingly [19]. Thus G is called multi-level code matrix. The scheme in [19] is based on this, and it is different from other differential code schemes based on unitary code matrix. By introducing multi-amplitude constellation, the information is carried by means of not only the phase but also the amplitude of the code matrix. So the spectral efficiency is effectively improved.

IV. DIFFERENTIAL SPACE-TIME BLOCK CODING BASED ON MULTI-LEVEL CODE MATRIX

At the transmitter, we consider the case of $N \times N$ square code matrices (i.e. $P=N$) firstly. According to Refs.[3,8,9], we have such $N \times N$ matrices for $N=2,4$ and 8. The ith block to be transmitted is a differential code matrix V_i with $N \times N$. At the start of the transmission, the transmitter sends a $N \times N$ identity matrix as initial code matrix V_0 (i.e. $V_0=I_{N \times N}$), which does not carry information. Then the information matrix to be transmitted (i.e. G_i, which is defined by (4) and is from constellation Ψ) is differential encoded, the corresponding differential encoded matrix V_i at time i is obtained as follows:

$$V_i = G_i \overline{V}_{i-1} = G_i V_{i-1} / \rho_{i-1} \quad (5)$$

where $\overline{V}_{i-1}$ is the normalized value of V_{i-1}, ρ_{i-1} is the amplitude of previous differential code matrix V_{i-1}, and $\rho_0 = 1$. From $V_0=I_{N \times N}$ and (5), we have:

$$V_i V_i^H = G_i V_{i-1} V_{i-1}^H G_i^H / \rho_{i-1}^2 = G_i G_i^H \quad (6)$$

Namely V_i has the same amplitude (i.e. ρ_i) with G_i. So,

$$\overline{V}_i \overline{V}_i^H = V_i V_i^H / \rho_i^2 = I_{N \times N} \quad (7)$$

So at time i, $\overline{V}_i$ is unitary matrix and V_i is multi-amplitude matrix. At the receiver, we assume that the channel gains remain constant at two consecutive time blocks, then the received matrix at time i is

$$X_i = \sqrt{\lambda} V_i T H + Z_i \quad (8)$$

where T is our introduced transform matrix, which is identity matrix for square code matrix, and the related explanation will be seen in next section. So the received matrix at time i-1 is written as

$$X_{i-1} = \sqrt{\lambda} V_{i-1} H + Z_{i-1} \quad (9)$$

Substituting (5) and (9) into (8) yields:

$$X_i = \sqrt{\lambda} G_i V_{i-1} H / \rho_{i-1} + Z_i = G_i X_{i-1} / \rho_{i-1} + \tilde{Z}_i \quad (10)$$

where $\tilde{Z}_i = Z_i - G_i Z_{i-1} / \rho_{i-1}$ is a $N \times K$ matrix. Since Z_i and Z_{i-1} are both complex Gaussian random variables with zero mean, $\tilde{Z}_i$ is also a Gaussian random variable with zero mean. Considering that $G_i G_i^H = \rho_i I_{N \times N}$, we can evaluate the variance of $\tilde{Z}_i$ by

$$E\{\tilde{Z}_i \tilde{Z}_i^H\} = (1 + \rho_i^2 / \rho_{i-1}^2) I_{N \times N} \quad (11)$$

Hence, $\tilde{Z}_i$ is a equivalent noise matrix, and its elements are $i.i.d$ complex Gaussian random variables with mean zero and variance $(1 + \rho_i^2 / \rho_{i-1}^2)$.

Based on the above-mentioned analysis, we can obtain the decision matrix by employing ML detector as follows:

$$\hat{G}_i = \arg \min_{G_i \in \Psi} \left\| X_i - G_i X_{i-1} / \rho_{i-1} \right\|^2 \quad (12)$$

In this paper, we assume that the data symbols $\{d_{il}\}$ are from MQAM constellation Φ. Considering that information matrix G_i is defined by (4), its elements are linear combination of L input symbols $\{d_{il}, l=1,2,\dots L\}$ and their conjugates $\{d_{il}^*\}$ in terms of space-time code matrix D_i. Thus the (12) can be equivalent as:

$$\{\hat{d}_{il}\}_{l=1}^{L} = \arg \min_{\{d_{i1},\dots,d_{iL}\} \in \Phi} \left\| X_i - G_i X_{i-1} / \rho_{i-1} \right\|^2$$
$$= \arg \min_{\{d_{i1},\dots,d_{iL}\} \in \Phi} tr\{(X_i - \rho_{i-1}^{-1} G_i X_{i-1})^H (X_i - \rho_{i-1}^{-1} G_i X_{i-1})\} \quad (13)$$

V. DSTBC SCHEME FOR NON-SQUARE MATRIX

A. Encoding scheme

The scheme presented in above section is valid for $N=2$, 4 and 8 transmit antennas, and corresponding code matrix is square. Now we consider the scheme in the case of $N=3$, 5, 6 and 7 transmit antennas, where the code matrix will be non-square matrix. This is also an open problem that needs to be solved in future work in [19]. For simplicity of analysis, we only focus on the 3 transmit antennas case; similar analysis can be extended to other multiple antennas cases. For 3 transmit antennas, we can transmit the first three columns of the differential code matrix of 4 transmit antennas to perform the data

transmission, but the corresponding code matrix is not square. For this reason, we introduce a transform matrix to realize data transmission of 3 antennas as follows:

$$V_{3,i} = V_{4,i}T \tag{14}$$

where $V_{3,i}$ and $V_{4,i}$ denote the transmitted differential code matrices for 3 and 4 transmit antennas, respectively. $V_{4,i}$ is 4×4 square matrix, and $V_{3,i}$ is 4×3 non-square matrix. T is our introduced transform matrix, and used to solve the data transmission in the case of non-square code matrix. Here, T=[1 0 0;0 1 0;0 0 1;0 0 0] is 4×3 matrix for 3 antennas case.

According to the above transform and using Eq.(8), we can implement the data transmission of 3 transmit antennas case by transmitting $V_{4,i}T$. Thus with Eqs.(1) and (8), the corresponding received signal matrix at time i is written by

$$X_i = \sqrt{\gamma}V_{3,i}H + Z_i = \sqrt{\gamma}V_{4,i}\tilde{H} + Z_i \tag{15}$$

where $\tilde{H} = TH$ is an equivalent channel gain matrix. After equivalent transform, T can be absorbed in the channel gain matrix. Considering that $T^HT=\mathrm{I}_{3\times3}$, then $\tilde{H}^H\tilde{H} = H^HT^HTH = H^HH$. Thus, the same diversity performances are obtained. Moreover, after the above transform, we can utilize the previous 4-antenna analysis method to detect the received data for 3-antena systems at the receiver, and the system performance is not affected. From Ref.[3] and [19], we have the information matrix to be transmitted for 4 antennas case:

$$G_{4,i} = \frac{1}{\sqrt{3}}\begin{bmatrix} d_1 & d_2 & d_3/\sqrt{2} & d_3/\sqrt{2} \\ -d_2^* & d_1^* & d_3/\sqrt{2} & d_3/\sqrt{2} \\ \dfrac{d_3^*}{\sqrt{2}} & \dfrac{d_3^*}{\sqrt{2}} & \dfrac{d_2-d_2^*-d_1-d_1^*}{2} & \dfrac{d_1-d_1^*-d_2-d_2^*}{2} \\ \dfrac{d_3^*}{\sqrt{2}} & -\dfrac{d_3^*}{\sqrt{2}} & \dfrac{d_2+d_2^*+d_1-d_1^*}{2} & \dfrac{d_2^*-d_2-d_1-d_1^*}{2} \end{bmatrix} \tag{16}$$

where d_l (l=1,2, 3) denotes d_{il} in fact, we drop the time index i for convenience. Considering that the above code matrix has lots of complex addition and multiplication, here we will use the improved STBC for 3 transmit antennas [8], this STBC has full diversity, the orthogonality and the same rate of 3/4 as H_4 STBC in [3,19]. The improvement is the simpler encoding and decoding of STBC. This STBC code matrix is:

$$H_4' = \begin{bmatrix} d_1 & d_2 & d_3 & 0 \\ -d_2^* & d_1^* & 0 & -d_3 \\ -d_3^* & 0 & d_1^* & d_2 \\ 0 & d_3^* & -d_2^* & d_1 \end{bmatrix} \tag{17}$$

So the corresponding information matrix for 4-antenna is

$$G_{4,i} = H_4'/\sqrt{3} \tag{18}$$

Since 3 symbols are transmitted over 4 time slots, the corresponding scheme will have a code rate of 3/4. Moreover, our proposed scheme is based on the above information matrix, so our scheme has the same rate of 3/4. Thus in the case of 3 or 4 transmit antennas, the code

rate of our scheme is higher than that of the scheme in [14], which can not be used for 3/4-rate STBCs, and only has a code rate of 1/2.

When the number of transmit antennas N=5, we transmit the first five columns of differential code matrix of 8 transmit antennas to perform the corresponding data transmission, which can be realized by introducing 8×5 transform matrix T=[1 0 0 0 0;0 1 0 0 0;0 0 1 0 0;0 0 0 1 0;0 0 0 0 1;0 0 0 0 0;0 0 0 0 0;0 0 0 0 0]. Similar method can be applied in the case of 6 or 7 transmit antennas. Besides, our multiple amplitudes differential STBC scheme may be easily extended in the case of N>8.

Based on the above analysis, we can give a general form of received signal matrix for multi-amplitude DSTBC scheme. Namely, $X_i = \sqrt{\lambda}V_iTH + Z_i$, where T is an identity matrix for square code matrix, and it becomes the above specific transform matrix for non-square code matrix in the case of N=3, 5, 6, 7.

B. Decoding scheme

In this subsection, we give the decoding scheme of the above differential space-time block coding scheme for non-square code matrix. For simplicity, we will focus on 3 transmit antennas and 2 receive antennas case here, and other cases can be analyzed by using similar methods. Let X_i=[$x_{i,11}$, $x_{i,21}$, $x_{i,31}$, $x_{i,41}$; $x_{i,12}$, $x_{i,22}$, $x_{i,32}$, $x_{i,42}$], and X_{i-1}=[$x_{i-1,11}$, $x_{i-1,21}$, $x_{i-1,31}$, $x_{i-1,41}$; $x_{i-1,12}$, $x_{i-1,22}$, $x_{i-1,32}$, $x_{i-1,42}$], then according to Eq.(15), the ML detection corresponding to (13) can be changed as:

$$\{\hat{d}_l\} = \underset{\{d_l\}\in\Phi}{\arg\min} \{|x_{i,11} - (d_1x_{i-1,11} + d_2x_{i-1,21} + d_3x_{i-1,31})\rho_{i-1}/\sqrt{3}|^2$$
$$+|x_{i,21} - (d_1^*x_{i-1,21} - d_3x_{i-1,41} - d_2^*x_{i-1,11})\rho_{i-1}/\sqrt{3}|^2$$
$$+|x_{i,31} - (d_1^*x_{i-1,31} + d_2x_{i-1,41} - d_3^*x_{i-1,11})\rho_{i-1}/\sqrt{3}|^2$$
$$+|x_{i,41} - (d_3^*x_{i-1,21} - d_2^*x_{i-1,31} + d_1x_{i-1,41})\rho_{i-1}/\sqrt{3}|^2 \tag{19}$$
$$+|x_{i,12} - (d_1x_{i-1,12} + d_2x_{i-1,22} + d_3x_{i-1,32})\rho_{i-1}/\sqrt{3}|^2$$
$$+|x_{i,22} - (d_1^*x_{i-1,22} - d_3x_{i-1,42} - d_2^*x_{i-1,12})\rho_{i-1}/\sqrt{3}|^2$$
$$+|x_{i,32} - (d_1^*x_{i-1,32} + d_2x_{i-1,42} - d_3^*x_{i-1,12})\rho_{i-1}/\sqrt{3}|^2$$
$$+|x_{i,42} - (d_3^*x_{i-1,22} - d_2^*x_{i-1,32} + d_1x_{i-1,42})\rho_{i-1}/\sqrt{3}|^2\}$$

We expand the above minimal metric in the right of Eq.(19) and delete the terms that are independent of the transmitted symbols $\{d_l$, l=1,2,3$\}$, then the Eq.(19) is equivalent to

$$\{\hat{d}_l\} = \underset{\{d_l\}\in\Phi}{\arg\min} \{(\frac{\rho_{i-1}^2}{3})(|d_1|^2 + |d_2|^2 + |d_3|^2)\left(\sum_{t=1}^{4}|x_{i-1,t1}|^2 + |x_{i-1,t2}|^2\right)$$
$$-(x_{i-1,11}^*x_{i,11} + x_{i-1,21}x_{i,21}^* + x_{i-1,31}x_{i,31}^* + x_{i-1,41}^*x_{i,41})(\rho_{i-1}/\sqrt{3})d_1^*$$
$$-(x_{i,11}^*x_{i-1,11} + x_{i,21}x_{i-1,21}^* + x_{i,31}x_{i-1,31}^* + x_{i,41}^*x_{i-1,41})(\rho_{i-1}/\sqrt{3})d_1$$
$$-(x_{i-1,12}^*x_{i,12} + x_{i-1,22}x_{i,22}^* + x_{i-1,32}x_{i,32}^* + x_{i-1,42}^*x_{i,42})(\rho_{i-1}/\sqrt{3})d_1^*$$
$$-(x_{i,12}^*x_{i-1,12} + x_{i,22}x_{i-1,22}^* + x_{i,32}x_{i-1,32}^* + x_{i,42}^*x_{i-1,42})(\rho_{i-1}/\sqrt{3})d_1$$

$$-(x_{i-1,21}^*x_{i,11} - x_{i-1,11}^*x_{i,21}^* + x_{i-1,41}^*x_{i,31} - x_{i-1,31}^*x_{i,41}^*)(\rho_{i-1}/\sqrt{3})d_2^*$$

$$-(x_{i,11}^*x_{i-1,21} - x_{i,21}^*x_{i-1,11}^* + x_{i,31}^*x_{i-1,41} - x_{i,41}^*x_{i-1,31}^*)(\rho_{i-1}/\sqrt{3})d_2 \quad (20)$$

$$-(x_{i,22}^*x_{i,12} - x_{i,12}^*x_{i,22}^* + x_{i,42}^*x_{i,32} - x_{i,32}^*x_{i,42}^*)(\rho_{i-1}/\sqrt{3})d_2^*$$

$$-(x_{i,12}^*x_{i-1,22} - x_{i,22}^*x_{i-1,12}^* + x_{i,32}^*x_{i-1,42} - x_{i,42}^*x_{i-1,32}^*)(\rho_{i-1}/\sqrt{3})d_2$$

$$-(x_{i-1,31}^*x_{i,11} - x_{i-1,41}^*x_{i,21} - x_{i-1,11}^*x_{i,31}^* + x_{i-1,21}^*x_{i,41}^*)(\rho_{i-1}/\sqrt{3})d_3^*$$

$$-(x_{i,11}^*x_{i-1,31} - x_{i,21}^*x_{i-1,41} - x_{i,31}^*x_{i-1,11}^* + x_{i,41}^*x_{i-1,21}^*)(\rho_{i-1}/\sqrt{3})d_3$$

$$-(x_{i-1,32}^*x_{i,12} - x_{i-1,42}^*x_{i,22} - x_{i,12}^*x_{i,32}^* + x_{i,22}^*x_{i,42}^*)(\rho_{i-1}/\sqrt{3})d_3^*$$

$$-(x_{i,12}^*x_{i-1,32} - x_{i,22}^*x_{i-1,42} - x_{i,32}^*x_{i-1,12}^* + x_{i,42}^*x_{i-1,22}^*)(\rho_{i-1}/\sqrt{3})d_3$$

Based on Eq.(20), we can divide the above minimal decision metric into three parts, the first part is only a function of d_1, the second part is only a function of d_2, and the third part is only a function of d_3. Thus Eq.(20) is equivalent to these three separate parts. By equivalent transform, the three parts can be further equivalent to minimizing the following three independent decision metrics. Namely, Eq.(19) has following equivalent decision form:

$$\{\hat{d}_1\} = \arg\min_{\{d_1\}\in\Phi}\left|\frac{\rho_{i-1}}{\sqrt{3}}d_1 - \sum_{k=1}^{2}(x_{i-1,1k}^*x_{i,1k} + x_{i-1,2k}x_{i,2k}^* + x_{i-1,3k}x_{i,3k}^* + x_{i-1,4k}^*x_{i,4k})\right|^2$$
$$+\{\sum_{t=1}^{4}|x_{i-1,t1}|^2 + |x_{i-1,t2}|^2) - 1\}(\rho_{i-1}^2/3)|d_1|^2$$

$$\{\hat{d}_2\} = \arg\min_{\{d_2\}\in\Phi}\left|\frac{\rho_{i-1}}{\sqrt{3}}d_2 - \sum_{k=1}^{2}(x_{i-1,2k}^*x_{i,1k} - x_{i-1,1k}x_{i,2k}^* + x_{i-1,4k}^*x_{i,3k} - x_{i-1,3k}x_{i,4k}^*)\right|^2$$
$$+\{\sum_{t=1}^{4}|x_{i-1,t1}|^2 + |x_{i-1,t2}|^2) - 1\}(\rho_{i-1}^2/3)|d_2|^2$$

$$\{\hat{d}_3\} = \arg\min_{\{d_3\}\in\Phi}\left|\frac{\rho_{i-1}}{\sqrt{3}}d_3 - \sum_{k=1}^{2}(x_{i-1,3k}^*x_{i,1k} - x_{i-1,4k}x_{i,2k} - x_{i-1,1k}x_{i,3k}^* + x_{i-1,2k}x_{i,4k}^*)\right|^2$$
$$+\{\sum_{t=1}^{4}|x_{i-1,t1}|^2 + |x_{i-1,t2}|^2) - 1\}(\rho_{i-1}^2/3)|d_3|^2$$
$$(21)$$

By employing the above decoding algorithm, we can obtain the symbols decision variables for the encoding scheme with information matrix being H_4. Namely, for input symbols $\{d_1, d_2, d_3\}$, their decisions are:

$$\{\hat{d}_1\} = \arg\min_{\{d_1\}\in\Phi}\left|\frac{\rho_{i-1}}{\sqrt{3}}d_1 - \sum_{k=1}^{2}[x_{i-1,1k}^*x_{i,1k} + x_{i-1,2k}x_{i,2k}^* - (x_{i-1,3k} + x_{i-1,4k})(x_{i,3k}^* + x_{i,4k}^*)/2\right.$$
$$\left. + (x_{i-1,3k}^* - x_{i-1,4k}^*)(x_{i,4k} - x_{i,3k})/2]\right|^2 + \{\sum_{t=1}^{4}|x_{i-1,t1}|^2 + |x_{i-1,t2}|^2) - 1\}(\rho_{i-1}^2/3)|d_1|^2$$

$$\{\hat{d}_2\} = \arg\min_{\{d_2\}\in\Phi}\left|\frac{\rho_{i-1}}{\sqrt{3}}d_2 - \sum_{k=1}^{2}[x_{i-1,2k}^*x_{i,1k} + x_{i-1,1k}x_{i,2k}^* + (x_{i-1,3k} + x_{i-1,4k})(x_{i,4k}^* - x_{i,3k}^*)/2\right.$$
$$\left. + (x_{i-1,3k}^* - x_{i-1,4k}^*)(x_{i,3k} + x_{i,4k})/2]\right|^2 + \{\sum_{t=1}^{4}|x_{i-1,t1}|^2 + |x_{i-1,t2}|^2) - 1\}(\rho_{i-1}^2/3)|d_2|^2$$

$$\{\hat{d}_3\} = \arg\min_{\{d_3\}\in\Phi}\left|\frac{\rho_{i-1}}{\sqrt{3}}d_3 - \sum_{k=1}^{2}[(x_{i-1,1k} + x_{i-1,2k})x_{i,3k}^*/\sqrt{2} + (x_{i-1,1k} - x_{i-1,2k})x_{i,4k}^*/\sqrt{2}\right.$$
$$\left. + \frac{x_{i-1,3k}^*(x_{i,1k} + x_{i,2k})}{\sqrt{2}} + \frac{x_{i-1,4k}^*(x_{i,1k} - x_{i,2k})}{\sqrt{2}}]\right|^2 + \{\sum_{t=1}^{4}|x_{i-1,t1}|^2 + |x_{i-1,t2}|^2) - 1\}\frac{\rho_{i-1}^2}{3}|d_3|^2$$
$$(22)$$

From the Eqs.(21) and (22), we can see that the calculation complexity of (22) is slightly higher than that of (21), so we will adopt the encoding scheme

with H_4' code for 3 and 4 antennas in simulation. Besides, the above decoding algorithm can be easily extended to more than 2 receive antennas case (i.e $K>2$). When $K>2$, Eq.(21) will be changed as follows:

$$\{\hat{d}_1\} = \arg\min_{\{d_1\}\in\Phi}\left|\frac{\rho_{i-1}}{\sqrt{3}}d_1 - \sum_{k=1}^{K}(x_{i-1,1k}^*x_{i,1k} + x_{i-1,2k}x_{i,2k}^* + x_{i-1,3k}x_{i,3k}^* + x_{i-1,4k}^*x_{i,4k})\right|^2$$
$$+\{\sum_{k=1}^{K}\sum_{t=1}^{4}(|x_{i-1,tk}|^2 + |x_{i-1,tk}|^2) - 1\}(\rho_{i-1}^2/3)|d_1|^2$$

$$\{\hat{d}_2\} = \arg\min_{\{d_2\}\in\Phi}\left|\frac{\rho_{i-1}}{\sqrt{3}}d_2 - \sum_{k=1}^{K}(x_{i-1,2k}^*x_{i,1k} - x_{i-1,1k}x_{i,2k}^* + x_{i-1,4k}^*x_{i,3k} - x_{i-1,3k}x_{i,4k}^*)\right|^2$$
$$+\{\sum_{k=1}^{K}\sum_{t=1}^{4}(|x_{i-1,tk}|^2 + |x_{i-1,tk}|^2) - 1\}(\rho_{i-1}^2/3)|d_2|^2$$

$$\{\hat{d}_3\} = \arg\min_{\{d_3\}\in\Phi}\left|\frac{\rho_{i-1}}{\sqrt{3}}d_3 - \sum_{k=1}^{K}(x_{i-1,3k}^*x_{i,1k} - x_{i-1,4k}^*x_{i,2k} - x_{i-1,1k}x_{i,3k}^* + x_{i-1,2k}x_{i,4k}^*)\right|^2$$
$$+\{\sum_{k=1}^{K}\sum_{t=1}^{4}(|x_{i-1,t1}|^2 + |x_{i-1,t2}|^2) - 1\}(\rho_{i-1}^2/3)|d_3|^2$$
$$(23)$$

According to the above decoding algorithms, our decoding scheme has linear decoding complexity. While for DUSTC based on cyclic group codes, it has exponential decoding complexity, and the decoding of the scheme in [14] is also more complex. So our scheme will be easily implemented due to low complexity. Similarly, our multi-amplitude differential decoding schemes for non-square code matrix with 3 transmit antennas can be easily extended to the code matrix with 5, 6, 7 transmit antennas, etc.

VI. CODING ADVANTAGE

For a constellation constructed from multiple data symbols, a good metric to judge the performance is the square of the minimum distance between two points in the constellation. If the distance is bigger, then the performance is better. Similarly, for the constellation constructed by code matrices, the coding advantage is a good metric to judge the performance of corresponding constellation in terms of the BER analysis in [11] and [12]. By maximizing the coding advantage; the optimal group codes are obtained in [11] and [12]. The coding advantage is defined as in [11]:

$$\Lambda_p = \min_{m\neq s} N \times \Lambda_p(G_m, G_s) \quad (24)$$

where $\Lambda_p(G_m, G_s) = \left\{\det\left((G_m - G_s)^H(G_m - G_s)\right)\right\}^{1/N}$ is minimum product distance between two code matrices G_m and G_s, $\det(\cdot)$ represents determinant operator, N is the number of transmit antennas.

Let G_m and G_s be the information matrices (as defined in (4)) constructed from the data symbols set $\{d_{m1},...,d_{mL}\}$ and $\{d_{s1},...,d_{sL}\}$, respectively, where symbols $\{d_{ml}\}$ and $\{d_{sl}\}$ are both from constellation Φ. Considering that the entries of G_m (i.e. $g_{m,uv}$, u, v are row index and column index of matrix G_m, respectively) are linear combinations of input symbols $\{d_{ml}, l=1,2,...L\}$ and their conjugates, without loss of generality, we can assume that

$$g_{m,uv} = \sum_{l=1}^{L} \mu_{uv} d_{ml} + \sum_{l=1}^{L} \beta_{uv} d_{ml}^{*} \qquad (25)$$

where μ_{uv} and β_{uv} are the constant coefficients used for linear combinations. Similar method can be applied to G_s due to the same definition, and thus its entries has the same form as (25), i.e.,

$$g_{s,uv} = \sum_{l=1}^{L} \mu_{uv} d_{sl} + \sum_{l=1}^{L} \beta_{uv} d_{sl}^{*} \qquad (26)$$

Let matrix $A = G_m - G_s$, and $d_{al} = d_{ml} - d_{sl}$, then the entry of A, a_{uv} is

$$a_{uv} = g_{m,uv} - g_{s,uv} = \sum_{l=1}^{L} \mu_{uv} d_{al} + \sum_{l=1}^{L} \beta_{uv} d_{al}^{*} \quad (27)$$

Thus the matrix A has the same expression form as information matrix G_m (i.e., they have same definition), the only difference is that their input symbols are different, the former symbols are $\{d_{al}\}$, and the latter symbols are $\{d_{ml}\}$. So according to (4), we will have following equation:

$$A^H A = \left(\sum_{l=1}^{L} |d_{al}|^2 / L \right) I_{K \times K} = \left(\sum_{l=1}^{L} |d_{ml} - d_{sl}|^2 / L \right) I_{N \times N} \quad (28)$$

Based on this, we can obtain the minimum product distance $\Lambda_p(G_m, G_s)$:

$$\Lambda_p(G_m, G_s) = \left\{ \det\left(A^H A \right) \right\}^{1/N} = \left(\sum_{l=1}^{L} |d_{ml} - d_{sl}|^2 \right) / L \quad (29)$$

For $G_m \neq G_s$, (29) is minimized when $\{d_{ml}\}$ and $\{d_{sl}\}$ differ in just one symbol, while the other corresponding symbols are same; namely the minimal value corresponds to the minimal distance between constellation points from Φ. Hence, we can evaluate the coding advantage in terms of (24) and (29) as follows:

$$\Lambda_p = \min_{d_{ml}, d_{sl} \in \Phi} (N/L) |d_{ml} - d_{sl}|^2 = (N/L) d_{min} \quad (30)$$

where d_{min} is the minimal distance between constellation points.

TABLE I.

COMPARISON OF CODING ADVANTAGE

Constellation Φ	Coding advantage (N=2, L=2)	Coding advantage (N=3, L=3)	Coding advantage (N=4, L=3)
16PSK	0.1522	0.1522	0.203
16QAM	0.2222	0.2222	0.2963
64PSK	0.0096	0.0096	0.0128
64QAM	0.0408	0.0408	0.0544

Considering that the MQAM method is employed in our scheme, and the minimal distance between constellation points from MQAM is larger than that from MPSK under same spectrum efficiency [23], we can conclude that proposed DSTBC scheme based on MQAM outperforms the corresponding MPSK based DSTBC scheme in terms of Eq.(30). From Eq.(30), we can calculate the coding advantage values of the proposed multi-amplitude DSTBC and MPSK based single amplitude DSTBC respectively, and give their coding advantage comparisons under the same spectrum

efficiency in Table 1. From the Table 1, we can see that the coding advantage of the proposed multi-amplitude DSTBC is indeed higher than that of single amplitude DSTBC, and this superiority becomes more significant with the increase of spectrum efficiency. Hence, the performance of our scheme is obviously superior to the corresponding single amplitude DSTBC scheme, which will also be testified by the following simulations.

VII. SIMULATION RESULTS

In this section, we will evaluate the performance of the developed scheme for multiple antennas systems by computer simulation. The channel is assumed to be quasi-static flat Rayleigh fading. Every data frame includes 480 information bits. The Monte-Carlo method is employed for simulation and Gray code is used to map the data bits to symbol constellations. The number of transmit antennas is set as 2, 3, 4 or 5, and the number of receive antennas is set as 1 or 2. 16PSK and 16QAM are used for the purpose of comparison under the same spectrum efficiency. Similarly, 64PSK and 64QAM are also employed for comparison. In the following figures, xTyR denotes a MIMO system with x transmit antennas and y receive antennas.
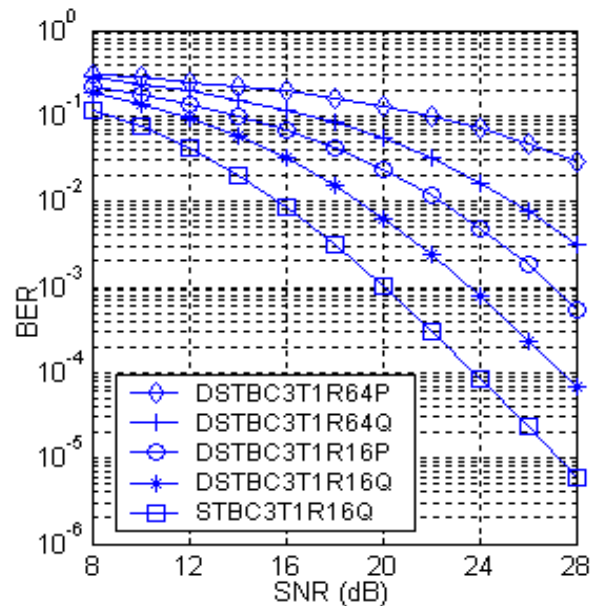

Figure 2. BER against SNR for different DSTBC schemes with 3 transmit antennas and 1 receiver antenna

Fig.2 shows the BER versus SNR for different differential STBC schemes with 3 transmit antennas and 1 receive antenna, where "DSTBC3T1R16Q" and "DSTBC3T1R64Q" represent the proposed multiple amplitudes DSTBC scheme with 16QAM and 64QAM, respectively. "DSTBC3T1R16P" and "DSTBC3T1R64P" denote single amplitude DSTBC scheme with 16PSK and 64PSK modulation, respectively. "STBC3T1R16Q" denote STBC scheme with coherent detection and 16QAM. To maintain the same spectrum efficiency of 4 bit/s/Hz, the 16PSK and 16QAM are used for the conventional single amplitude DSTBC and proposed multiple amplitudes DSTBC, respectively. Meanwhile,

64PSK and 64QAM are also used for single amplitude DSTBC and multiple amplitudes DSTBC respectively for comparison. Thus they obtain the same spectrum efficiency of 6 bit/s/Hz.

It is shown in Fig.2 that our proposed scheme has significant advantage over the conventional single amplitude DSTBC scheme, the "DSTBC3T1R64Q" scheme gives about 6dB gains over "DSTBC3T1R64P" scheme at a BER of 0.03, and the "DSTBC3T1R16Q" scheme achieves about 3 dB gains over "DSTBC3T1R16P" scheme at BER=10^{-3}. When compared to the "STBC3T1R16Q" scheme with coherent decoding, our "DSTBC3T1R16Q" scheme can obtain the same order of antenna diversity, but has performance loss of 3-4dB as expected. However, to implement the coherent STBC scheme, the perfect CSI is required at the receiver, whereas our differential scheme do not need any CSI. Besides, the "DSTBC3T1R16Q" scheme performs better than the "DSTBC3T1R64Q" scheme. It is because when compared with 16QAM scheme, the 64QAM signal constellation points are more densely packed, thus they are more prone to errors in fading channel.
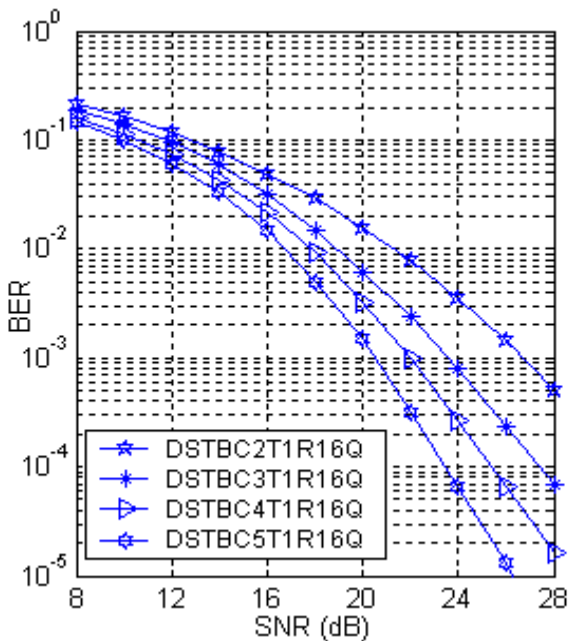

Figure 3.   BER against SNR for multi-amplitude DSTBC schemes with different transmit antennas and 1 receive antenna

In Fig.3, we give the performance comparison of the proposed multi-amplitude DSTBC scheme with different transmit antennas and one receive antennas, 16QAM is employed. "DSTBC2T1R16Q", "DSTBC3T1R16Q", "DSTBC4T1R16Q" and "DSTBC5T1R16Q" represent the multi-amplitude DSTBC scheme with 2, 3, 4 and 5 transmit antennas, respectively. For 5-antenna DSTBC, we use the method similar to 3-antenna DSTBC to encode and decode. From the figure, we can see that our 3-antenna scheme outperforms 2-antenna scheme, but performs worse than 4-antenna scheme. While for our 5-antenna scheme, it can achieve about 2dB gains at a BER of 10^{-4} when compared with 4-antenna scheme. The reason for this is that with the increase of the number of

transmit antennas; the differential STBC scheme with more antennas can obtain higher space diversity gains than that with fewer antennas. The above results are agreement with the expected conclusions. Namely, the scheme with more antennas outperforms the scheme with fewer antennas, which also explains that our schemes for 3 antennas and 5 antennas are valid.
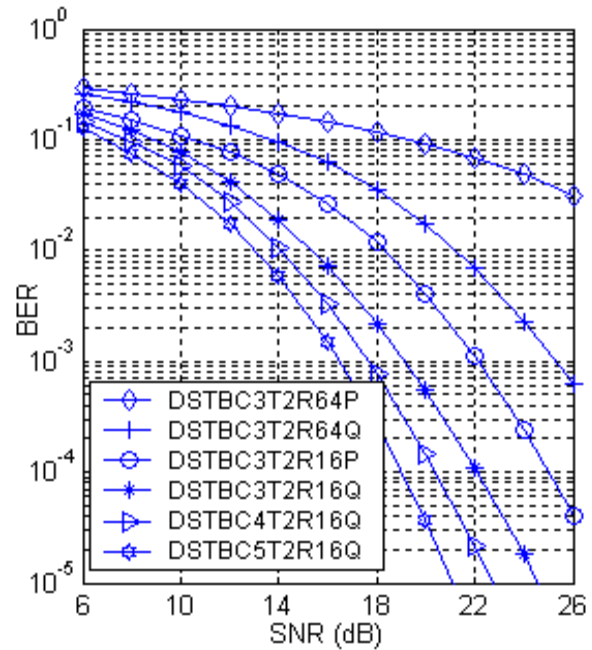

Figure 4.   BER against SNR for different DSTBC schemes with 2 receive antennas

To further comparison, we give the performance comparison of the different DSTBC schemes with two receive antennas in Fig.4. As shown in Fig.4, when 2 receive antennas are employed, the proposed multiple amplitudes DSTBC scheme still performs better than the corresponding single amplitude DSTBC scheme. At a BER of 10^{-4}, the "DSTBC3T2R16Q" scheme gives about 3dB gains over "DSTBC3T2R16P" scheme, and the "DSTBC3T2R64Q" scheme achieves about 7dB gains over "DSTBC3T2R64P" scheme at a BER of 0.03. Moreover, in the case of 2 receive antennas, the multiple amplitudes DSTBC schemes with more transmit antennas still outperforms those with fewer antennas. For our 5-antenna scheme, it can achieve about 2dB gains at a BER of 10^{-5} when compared with 4-antenna scheme, but our 3-antenna scheme performs worse than 4-antenna scheme due to lower space diversity gain. Thus these results are consistent with our expected conclusions, and further testify that the developed schemes for non-square code matrix are effective and reasonable. In addition, compared with the DSTBC schemes in Fig.2 and Fig.3, the corresponding DSTBC schemes in Fig.4 all achieve performance improvement because of using multiple receive antennas, which also further testifies the effectiveness of our given decoding algorithm.

VIII. CONCLUSIONS

By introducing quadrature amplitude modulation and transform matrix method, a multi-amplitude DSTBC scheme for square/non-square code matrix is developed in this paper, and the corresponding coding advantage is derived in detail. The developed scheme can effectively avoid the performance degradation of conventional differential space-time coding scheme based on MPSK modulation in high spectrum efficiency, and overcome the shortcoming that some existing DSTBC schemes only suit square code matrix. Moreover, it can carry information via not only the phase but also amplitude. Thus the system performance and spectrum efficiency are both improved effectively. Theoretic analysis shows that the developed scheme has linear decoding complexity and high coding advantage. Besides, it can obtain higher code rate in the case of more than two antennas. The simulation results show that our multi-amplitude DSTBC scheme has lower BER than the corresponding single amplitude DSTBC under the same spectrum efficiency, and the presented encoding and decoding scheme of the multiple amplitudes DSTBC are also valid.

REFERENCES

[1] C.-B. Chae, A. Forenza , RW. Heath, M. McKay, I. Collings, "Adaptive MIMO transmission techniques for broadband wireless communication systems," *IEEE Commun. Magazine*, vol.48, pp. 112-118, 2010.

[2] H.Jafarkhani, "A quasi-orthogonal space-time block code," *IEEE Trans. on Commun.*, vol.49, no.1, pp.1-4, 2001.

[3] V.Tarokh, H.Jafarkhani, A.R.Calderbank, "Space-time block codes from orthogonal designs," *IEEE Trans. Inform. Theory*, vol.45, no.7, pp.1456-1467, 1999.

[4] S. M.Alamouti, "A simple transmit diversity technique for wireless communications," *IEEE J. Select. Areas Commun.*, vol.16, No.8, pp1451-1458, 1998.\

[5] X.Yu, S-H. Leung, W.H.Mow, W-K Wong, "Performance of variable-power adaptive modulation with space-time coding and imperfect CSI in MIMO Systems," *IEEE Trans. Veh. Technol.*, vol.58, pp. 2115-2120, 2009.

[6] O.Tirhhonen and A.Hottinen "Square-matrix embeddable space-time block codes for complex signal constellations," *IEEE Trans. Inform. Theory*, vol.48, No.2, pp.384-395, 2002.

[7] G.Ganesan and P.Stoica, "Space-time block codes: A maximum SNR approach," *IEEE Trans. Inform. Theory*, vol.47, No.5, pp.1650-1656, 2001.

[8] Chunjun Gao and A.M.Haimovich, "BER analysis of MPSK space-time block codes with differential detection," *IEEE communication letters*, vol.17, no.7, pp.314-316, 2003.

[9] B.L.Hughes, "Differential space-time modulation," *IEEE Trans. Inform. Theory*, vol.46, no.11, pp.2567-2578, 2000.

[10] B.M.Hochwald, W.Sweldens, "Differential unitary space-time modulation," *IEEE Trans. Commun.*, vol.48, no.12, pp. 2041–2052, 2000.

[11] V.Tarokh and H.Jafarkhani, "A differential detection scheme for transmit diversity," *IEEE J. Select. Areas Commun.*, vol.18, no.7, pp.1169-1174, 2000.

[12] H.Jafarkhani and V.Tarokh, "Multiple transmits antenna differential detection from generalized orthogonal designs," *IEEE Trans. Inform. Theory*, vol.47, no.9, pp.2626-2631, 2001.

[13] G.Ganesan and P.Stoica, "Differential modulation using space-time block codes," *IEEE Signal Process. Lett*, vol.19, no.2, pp. 57-60, 2002.

[14] Q.Shi and Q. T. Zhang, "MPSK modulated constellation design for differential space-time modulation," *IEEE Trans. Commun.*, vol.56, no.7, pp. 1038–1042, 2008.

[15] M.Teimouri, N.Rezaee, and A.Hedayat, "Error probability bounds of concatenated channel codes and differential space-time block codes," *IEEE Signal Process. Lett.*, vol.16, no.8, pp 663-666, 2009.

[16] A. B. Narasimhamurthy and C.Tepedelenlioglu, "Differential Space–Time Coded switch and stay Combining," *IEEE Trans. Veh. Technol.,* vol.59, no.7, pp. 3373-3381, 2010.

[17] M. Tao and R.Cheng, "Differential space-time block codes," in Proc. *IEEE Globcom*'01. Nov. 2001, pp.1098-1102.

[18] Z.Chen, G.Zhu, J.Shen and Y. Liu, "Differential space-time block codes from amicable orthogonal designs," in Proc. *IEEE WCNC*'03, Mar. 2003, pp.768-772.

[19] Chan-soo Hwang, Seung Hoon Nam, Jaehak Chung, and Vahid Tarokh,"Differential space time block codes using nonconstant modulus constellations," *IEEE Trans. on signal processing*, vol. 51, pp 2955-2964, Nov. 2003.

[20] Xiang-Gen Xia, "Differentially en/decoded orthogonal space-time block codes with APSK signals," *IEEE Commun. Lett.*, vol.6, pp 150-152, Apr. 2002.

[21] J.G. Proakis, *Digital communications*, 5th ed. New York: McGraw-Hill, 2007.

Xiangbin Yu received his Ph.D. in Communication and Information Systems in 2004 from National Mobile Communications Research Laboratory at Southeast University, China. He has been an Associate Professor with the Nanjing University of Aeronautics and Astronautics since May 2006. Dr.Yu has served as a technical program committee of Globecom 2006, International conference on communications systems 2008 (ICCS'08), ICCS'10, and reviewer of some conferences and journals. He has been a member of IEEE ComSoc Radio Communications Committee (RCC) since May 2007. His research interests include space-time coding, adaptive modulation and space-time signal processing

Xiaomin Chen received the M.S and Ph.D. degrees in Communication and Information Systems from Nanjing University of Aeronautics and Astronautics in 2001 and 2010, respectively. She is currently working as an associate professor at Nanjing University of Aeronautics and Astronautics. Her research interests include MIMO systems, power adaptation, iterative detection and Turbo-blast.

Yuyu Xin is currently working towards the B.S. degree at Nanjing University of Aeronautics and Astronautics, Nanjing, China.

Qiuming Zhu received the M.S degrees in Communication and Information Systems from Nanjing University of Aeronautics and Astronautics in 2005. He is currently working as a lecturer at Nanjing University of Aeronautics and Astronautics. Also, he is pursuing the Ph.D. degree in Communication and Information Systems at Nanjing University of Aeronautics and Astronautics.

Dazhuan Xu received the M.S degrees and Ph.D. in Communication and Information Systems from Nanjing University of Aeronautics and Astronautics in 1986 and 2001, respectively. He is now a full professor in College of Information Science and Technology, Nanjing University of Aeronautics and Astronautics, Nanjing, China. Prof.Xu is a Senior Member of China Institute of Electronics (CIE). His research interests include digital communications, software radio, coding theory, medical signal processing.

Call for Papers and Special Issues

Aims and Scope.

Journal of Networks (JNW, ISSN 1796-2056) is a scholarly peer-reviewed international scientific journal published monthly, focusing on theories, methods, and applications in networks. It provide a high profile, leading edge forum for academic researchers, industrial professionals, engineers, consultants, managers, educators and policy makers working in the field to contribute and disseminate innovative new work on networks.

The Journal of Networks reflects the multidisciplinary nature of communications networks. It is committed to the timely publication of high-quality papers that advance the state-of-the-art and practical applications of communication networks. Both theoretical research contributions (presenting new techniques, concepts, or analyses) and applied contributions (reporting on experiences and experiments with actual systems) and tutorial expositions of permanent reference value are published. The topics covered by this journal include, but not limited to, the following topics:

- Network Technologies, Services and Applications, Network Operations and Management, Network Architecture and Design
- Next Generation Networks, Next Generation Mobile Networks
- Communication Protocols and Theory, Signal Processing for Communications, Formal Methods in Communication Protocols
- Multimedia Communications, Communications QoS
- Information, Communications and Network Security, Reliability and Performance Modeling
- Network Access, Error Recovery, Routing, Congestion, and Flow Control
- BAN, PAN, LAN, MAN, WAN, Internet, Network Interconnections, Broadband and Very High Rate Networks,
- Wireless Communications & Networking, Bluetooth, IrDA, RFID, WLAN, WMAX, 3G, Wireless Ad Hoc and Sensor Networks
- Data Networks and Telephone Networks, Optical Systems and Networks, Satellite and Space Communications

Special Issue Guidelines

Special issues feature specifically aimed and targeted topics of interest contributed by authors responding to a particular Call for Papers or by invitation, edited by guest editor(s). We encourage you to submit proposals for creating special issues in areas that are of interest to the Journal. Preference will be given to proposals that cover some unique aspect of the technology and ones that include subjects that are timely and useful to the readers of the Journal. A Special Issue is typically made of 10 to 15 papers, with each paper 8 to 12 pages of length.

The following information should be included as part of the proposal:
- Proposed title for the Special Issue
- Description of the topic area to be focused upon and justification
- Review process for the selection and rejection of papers.
- Name, contact, position, affiliation, and biography of the Guest Editor(s)
- List of potential reviewers
- Potential authors to the issue
- Tentative time-table for the call for papers and reviews

If a proposal is accepted, the guest editor will be responsible for:
- Preparing the "Call for Papers" to be included on the Journal's Web site.
- Distribution of the Call for Papers broadly to various mailing lists and sites.
- Getting submissions, arranging review process, making decisions, and carrying out all correspondence with the authors. Authors should be informed the Instructions for Authors.
- Providing us the completed and approved final versions of the papers formatted in the Journal's style, together with all authors' contact information.
- Writing a one- or two-page introductory editorial to be published in the Special Issue.

Special Issue for a Conference/Workshop

A special issue for a Conference/Workshop is usually released in association with the committee members of the Conference/Workshop like general chairs and/or program chairs who are appointed as the Guest Editors of the Special Issue. Special Issue for a Conference/Workshop is typically made of 10 to 15 papers, with each paper 8 to 12 pages of length.

Guest Editors are involved in the following steps in guest-editing a Special Issue based on a Conference/Workshop:
- Selecting a Title for the Special Issue, e.g. "Special Issue: Selected Best Papers of XYZ Conference".
- Sending us a formal "Letter of Intent" for the Special Issue.
- Creating a "Call for Papers" for the Special Issue, posting it on the conference web site, and publicizing it to the conference attendees. Information about the Journal and Academy Publisher can be included in the Call for Papers.
- Establishing criteria for paper selection/rejections. The papers can be nominated based on multiple criteria, e.g. rank in review process plus the evaluation from the Session Chairs and the feedback from the Conference attendees.
- Selecting and inviting submissions, arranging review process, making decisions, and carrying out all correspondence with the authors. Authors should be informed the Author Instructions. Usually, the Proceedings manuscripts should be expanded and enhanced.
- Providing us the completed and approved final versions of the papers formatted in the Journal's style, together with all authors' contact information.
- Writing a one- or two-page introductory editorial to be published in the Special Issue.

More information is available on the web site at http://www.academypublisher.com/jnw/.

(Contents Continued from Back Cover)

REGULAR PAPERS